National Library
of Canada

Acquisitions and
Bibliographic Services Branch

395 Wellington Street
Ottawa, Ontario
K1A 0N4

Bibliothèque nationale
du Canada

Direction des acquisitions et
des services bibliographiques

395, rue Wellington
Ottawa (Ontario)
K1A 0N4

Your file Votre référence

Our file Notre référence

NOTICE

The quality of this microform is heavily dependent upon the quality of the original thesis submitted for microfilming. Every effort has been made to ensure the highest quality of reproduction possible.

If pages are missing, contact the university which granted the degree.

Some pages may have indistinct print especially if the original pages were typed with a poor typewriter ribbon or if the university sent us an inferior photocopy.

Reproduction in full or in part of this microform is governed by the Canadian Copyright Act, R.S.C. 1970, c. C-30, and subsequent amendments.

AVIS

La qualité de cette microforme dépend grandement de la qualité de la thèse soumise au microfilmage. Nous avons tout fait pour assurer une qualité supérieure de reproduction.

S'il manque des pages, veuillez communiquer avec l'université qui a conféré le grade.

La qualité d'impression de certaines pages peut laisser à désirer, surtout si les pages originales ont été dactylographiées à l'aide d'un ruban usé ou si l'université nous a fait parvenir une photocopie de qualité inférieure.

La reproduction, même partielle, de cette microforme est soumise à la Loi canadienne sur le droit d'auteur, SRC 1970, c. C-30, et ses amendements subséquents.

Canada

UNIVERSITY OF ALBERTA

A KINETIC STUDY OF THE REDUCTION OF N_2O AND NO BY CO ON A PLATINUM CATALYST USING STEADY-STATE BIFURCATION AND FORCED COMPOSITION CYCLING TECHNIQUES

BY

©

RAMAKANT R. SADHANKAR

A THESIS
SUBMITTED TO THE FACULTY OF GRADUATE STUDIES AND RESEARCH
IN PARTIAL FULFILMENT OF THE REQUIREMENTS FOR THE DEGREE OF
DOCTOR OF PHILOSOPHY

DEPARTMENT OF CHEMICAL ENGINEERING

EDMONTON, ALBERTA
SPRING 1995

National Library
of Canada

Acquisitions and
Bibliographic Services Branch

395 Wellington Street
Ottawa, Ontario
K1A 0N4

Bibliothèque nationale
du Canada

Direction des acquisitions et
des services bibliographiques

395, rue Wellington
Ottawa (Ontario)
K1A 0N4

Your file Votre référence

Our file Notre référence

THE AUTHOR HAS GRANTED AN IRREVOCABLE NON-EXCLUSIVE LICENCE ALLOWING THE NATIONAL LIBRARY OF CANADA TO REPRODUCE, LOAN, DISTRIBUTE OR SELL COPIES OF HIS/HER THESIS BY ANY MEANS AND IN ANY FORM OR FORMAT, MAKING THIS THESIS AVAILABLE TO INTERESTED PERSONS.

L'AUTEUR A ACCORDE UNE LICENCE IRREVOCABLE ET NON EXCLUSIVE PERMETTANT A LA BIBLIOTHEQUE NATIONALE DU CANADA DE REPRODUIRE, PRETER, DISTRIBUER OU VENDRE DES COPIES DE SA THESE DE QUELQUE MANIERE ET SOUS QUELQUE FORME QUE CE SOIT POUR METTRE DES EXEMPLAIRES DE CETTE THESE A LA DISPOSITION DES PERSONNE INTERESSEES.

THE AUTHOR RETAINS OWNERSHIP OF THE COPYRIGHT IN HIS/HER THESIS. NEITHER THE THESIS NOR SUBSTANTIAL EXTRACTS FROM IT MAY BE PRINTED OR OTHERWISE REPRODUCED WITHOUT HIS/HER PERMISSION.

L'AUTEUR CONSERVE LA PROPRIETE DU DROIT D'AUTEUR QUI PROTEGE SA THESE. NI LA THESE NI DES EXTRAITS SUBSTANTIELS DE CELLE-CI NE DOIVENT ETRE IMPRIMES OU AUTREMENT REPRODUITS SANS SON AUTORISATION.

ISBN 0-612-01759-1

Canadä

UNIVERSITY OF ALBERTA
RELEASE FORM

NAME OF AUTHOR: Ramakant Raghunathrao Sadhankar

TITLE OF THESIS: A Kinetic Study of the Reduction of N_2O and NO by CO on a Platinum Catalyst using Steady-State Bifurcation and Forced Composition Cycling Techniques.

DEGREE: Doctor of Philosophy

YEAR THIS DEGREE GRANTED: 1995

Permission is hereby granted to the University of Alberta Library to reproduce single copies of this thesis and to lend or sell such copies for private, scholarly or scientific purposes only.

The author reserves all other publication and other rights in association with the copyright in the thesis, and except as hereinbefore provided neither thesis nor any substantial portion thereof may be printed or otherwise reproduced in any material form whatever without the author's prior written permission.

Sadhanka

8407 - 14th Avenue
Edmonton, Alberta T6K 1X3

Date: February 28, 1995

UNIVERSITY OF ALBERTA

FACULTY OF GRADUATE STUDIES AND RESEARCH

The undersigned certify that they have read, and recommend to the Faculty of Graduate Studies and Research for acceptance, a thesis entitled A KINETIC STUDY OF THE REDUCTION OF N_2O AND NO BY CO ON A PLATINUM CATALYST USING STEADY-STATE BIFURCATION AND FORCED COMPOSITION CYCLING TECHNIQUES submitted by Ramakant Raghunathrao Sadhankar in partial fulfilment of the requirements for the degree of Doctor of Philosophy.

David T. Lynch
Dr. D.T. Lynch

Dr. R.E. Hayes

Dr. L.D. Schmidt

Dr. J. Takats

S.E. Wanke
Dr. S.E. Wanke

Date: FEBRUARY 23, 1995

DEDICATION

This thesis is dedicated to Emmy, Aaron and Leroy

ACKNOWLEDGEMENT

I am thankful to Professor Lynch whose distinguished supervision contributed to the successful completion of this work. My thanks are also due to all those whose timely assistance was indispensable during the experimental work. Walter Boddez and Richard Cooper of Instrument Shop did an excellent job of installing the data acquisition equipment and trouble-shooting the instruments. Keith Faulder and his staff in the Machine Shop helped in fabrication and timely repairs to the equipment. Keith deserves credit for getting all the gas mixtures in time for the experiments. Bob Barton of DACS was very helpful in trouble shooting the data acquisition program and the network problems. I am thankful to Luigi Boccanfuso for writing some of the programs for data-acquisition.

I would also like to thank the Graduate Students in the Chemical Engineering Department for their friendship and the faculty members for their guidance and advice. Finally, I wish to thank my wife, Emmy for her love and support and my children, Aaron and Leroy for their patience over the past four years.

ABSTRACT

The reduction reactions of N_2O and NO by CO over a Pt/Al_2O_3 catalyst have been studied using an external recycle reactor. The N_2O+CO reaction was found to exhibit isothermal steady-state multiplicity at 461-520 K. The steady-state bifurcation behavior has been used to discriminate among four rival mechanisms. Only a kinetic model based on a three-step mechanism and invoking CO self-exclusion from the platinum surface could describe the observed behavior. The model was further tested using transient behavior produced by forced square-wave cycling of CO and N_2O concentrations in the feed. The phase angle between the two square-waves has a pronounced effect on the reaction-rate resonance. Time-average CO conversions as high as five times the steady-state conversion were attained during feed cycling. The model was further modified by incorporating a reaction rate enhancement effect, due to Pt surface phase transition (1x1 ↔ hex), to describe both the transient behavior during feed cycling and the steady-state multiplicity.

The NO+CO reaction also exhibits isothermal steady-state multiplicity at 465-520 K. Generally, the selectivity towards N_2O formation decreased with increasing NO conversion. For the high-conversion steady-states, the N_2O selectivity decreased rapidly with a decrease in the feed $[NO]_o/[CO]_o$ ratio below a critical value of 1.5. It is shown that the N_2O+CO reaction occurs to a significant extent (up to 50%) in the overall NO+CO reaction. The multiplicity behavior and the N_2O selectivity have been described by a seven-step mechanism incorporating the CO self-exclusion effect. The NO+CO reaction also exhibits reaction-rate resonance during variable-phase feed composition cycling. Time-average CO and NO conversions of more than 20 times the steady-state conversions were obtained during feed cycling. The transient results seem to support the seven-step mechanism that was used to describe the steady-state multiplicity. The NO+CO reaction exhibits long-term transients during feed cycling. The number of cycles required to reach cycle-invariance was found to be strongly and inversely dependent on the ratio of the gas-phase capacitance to the surface capacitance.

PREFACE

This thesis is concerned with an examination of the reduction reactions of nitrous oxide and nitric oxide with carbon monoxide. These reactions have been studied because of their importance in automobile catalytic converters. The study involved both experimental and mathematical modelling work. The techniques used for the experimental work involved steady-state bifurcation and forced composition cycling, both of which have been proven to provide a sensitive discrimination among rival reaction mechanisms.

This thesis is organized in a "paper-format" specified in the "Thesis Handbook - A Manual of Regulations and Guide for These Preparation, November 1994" of the Faculty of Graduate Studies and Research. Each of the four chapters following the introductory chapter, namely, Chapters 2-5, is presented in the form of a manuscript without an abstract. The publication details of the manuscripts are given in the footnote of the respective chapter, wherever applicable. The experimental data and the computer programs for mathematical modelling are given in the appendices at the end of the thesis. The bibliography and nomenclature for each chapter appears at the end of the respective chapter. The references to the literature have been cited in the text by italic numerals in parentheses. The citation format is similar to that used by the *Journal of Catalysis*.

This work is supported by the Natural Sciences and Engineering Research Council of Canada. Several individuals helped during the course of this work. Their assistance has been duly acknowledged.

TABLE OF CONTENTS

Chapter

1. Introduction 1
    1.1 Motivation 1
    1.2 Objective 3
    1.3 Methodology 4
    1.4 Outline 4
    1.5 References 5
2. N_2O Reduction by CO: Steady-State Behavior 8
    2.1 Introduction 8
    2.2 Experimental Equipment and Materials 10
    2.3 Results 14
    2.4 Models of Reaction Mechanism 22
        2.4.1 Mechanism 1 23
        2.4.2 Mechanism 2 28
        2.4.2 Mechanism 3 29
        2.4.2 Mechanism 4 30
    2.5 Conclusions 42
    2.6 Notation 42
    2.7 References 44
3. N_2O Reduction by CO: Forced Composition Cycling 48
    3.1 Introduction 48
    3.2 Methods 50
    3.3 Results 54
        3.3.1 Out-of-Phase Cycling 55
        3.3.2 N_2O Phase Lead of 90° and 270° 62
        3.3.3 Variable Phasing of Inputs 66
    3.4 Mathematical Model 70
        3.4.1 CO Self-Exclusion Model 70
        3.4.2 Surface-Phase Transformation Model 77

3.5 Conclusions 88
3.6 Notation 89
3.7 References 92
4. NO Reduction by CO: Steady-State Behavior 95
4.1 Introduction 95
4.2 Methods 97
4.3 Results 9 97
4.3.1 NO Conversion 100
4.3.2 CO Conversion 104
4.3.3 N_2O Selectivity 107
4.4 Discussion 110
4.4.1 Reaction Mechanism 110
4.4.2 Mathematical Model 116
4.4.3 N_2O Selectivity 124
4.5 Conclusions 128
4.6 Notation 129
4.7 References 131
5. NO Reduction by CO: Forced Composition Cycling 134
5.1 Introduction 134
5.2 Methods 136
5.3 Results and Discussion 137
5.3.1 Out-of-Phase Cycling 137
5.3.2 Variable-Phase Cycling 149
5.3.3 Transient Response 154
5.3.4. Kinetic Model 161
5.4 Conclusions 166
5.5 Notation 167
5.6 References 168
6. Summary and Recommendations 170
6.1 N_2O+CO Reaction 170
6.2 NO+CO Reaction 172

6.3 Recommendations for Future Work 175
6.4 References 178
Appendix A Calibration of Mass Flow Controllers 180
Appendix B Experimental Data for the Steady-State Multiplicity of the N_2O+CO Reaction 186
Appendix C MATLAB Programs for Calculating Steady-state CO Conversions for the N_2O+CO Reaction 198
Appendix D Experimental Time-Average CO Conversions for the N_2O+CO Reaction During Feed Composition Cycling 224
Appendix E MATLAB Programs for the N_2O+CO Reaction Feed Cycling 233
Appendix F Steady-state Experimental Data for the NO+CO Reaction 250
Appendix G MATLAB Programs for Steady-State Calculations for the NO+CO Reaction 278
Appendix H Experimental Time-Average Conversions for the NO+CO Reaction During Feed Composition Cycling 288
Appendix I Mathematical Model of the NO+CO Reaction Transient Behavior 302

LIST OF TABLES

Table

2.1 Parameter Values at 499 K for Mechanisms 1 to 4 26
2.2 Temperature Dependence of Parameters for Mechanism 4 33
2.3 Sets of Kinetic Parameters for Mechanism 4 Which Give Similar Predictions 38
3.1 Model Parameters at 499 K 76
3.2 Parameter Values for the Surface-Phase Transformation Model 84
3.3 Comparison of Kinetic Parameters 87
4.1 Effect of Increasing the Value of a Parameter on the Model Predictions 119
4.2 Kinetic Parameters 123
5.1 Conversions During Steady-State and Out-of-Phase Cycling Experiments 145
5.2 Comparison of Model Predictions with Experimental Data for Out-of-Phase Cycling 165

LIST OF FIGURES

Figure

2.1 Recycle Reactor Schematic 11

2.2 Feed System Schematic 13

2.3 Multiplicity Behavior During the Reduction of N_2O by CO at 461-499 K 16

2.4 Multiplicity Behavior During the Reduction of N_2O by CO at 520 K 18

2.5 Dependence of Bifurcation Points on Temperature and Feed Composition 19

2.6 Comparison of Predictions from Mechanisms 1 to 4 to Experimental Bifurcation Points and CO Conversions 25

2.7 Arrhenius-Type Plot of Parameters for Mechanism 4 34

2.8 Predictions from Mechanism 4 at 499 K with Coverage Dependent Adsorption and Desorption Rate Constants 37

2.9 Reaction Rates in the Unique Steady-State Regions 41

3.1 Feed Cycling Strategies 52

3.2 Comparison of Steady-State and Cyclic Operation 53

3.3 Multiplicity Behavior During the Reduction of N_2O by CO at 461-499 K and Predictions of Pt Surface-Phase Transition Model 56

3.4 Dynamic CO_2 Response During 180° Out-of-Phase Feed Composition Cycling 57

3.5 Comparison of Model Predictions to Experimental Data for Time-Average Conversion for Out-of-Phase Cycling 59

3.6 Comparison of Predictions of Time-Average Conversion from Eq. (3.1) to Experimental Data at Low Frequency Out-of-Phase Cycling 61

3.7 Effect of Cycling Frequency on Time-Average Conversions for N_2O Phase Leads of 90° and 270° 63

3.8 Dynamic CO_2 Response for 90° and 270° N_2O Phase Lead 65

3.9 Effect of N_2O Phase Lead on the Time-Average CO Conversion During Cycling 67

3.10 Effect of N_2O Phase Lead on the Dynamic CO_2 Response 69

3.11 Reaction Rate Enhancement Due to CO-Adsorbate

Dependent Pt Surface-Phase Transition 79
3.12 Experimental-Model Comparison of the Steady-State Multiplicity Behavior at 520 K 83
3.13 Experimental-Model Comparison of the Steady-State Bifurcation Boundaries 85
3.14 Arrhenius-Type Plot of the Pt Surface-Phase Transition Model Parameters 86
4.1 NO Conversion Multiplicity for the NO+CO Reaction at 465-505 K 101
4.2 NO Conversion Multiplicity for the NO+CO Reaction at 520 K 103
4.3 CO Conversion Multiplicity for the NO+CO Reaction at 465-505 K 105
4.4 CO Conversion Multiplicity for the NO+CO Reaction at 520 K 106
4.5 Multiplicity of the Rate of N_2O Formation for the NO+CO Reaction at 465-505 K 108
4.6 Multiplicity of the Rate of N_2O Formation for the NO+CO Reaction at 520 K 109
4.7 N_2O Selectivity for the NO+CO Reaction at 465-505 K (High-Rate Branch Only) 111
4.8 N_2O Selectivity for the NO+CO Reaction at 520 K (High-Rate Branch Only) 112
4.9 Arrhenius Plot of Rate Constants 122
4.10 Reactor N_2O Concentration for the High-Conversion Steady-State of the NO+CO Reaction 127
5.1 Time-Average Conversions for Out-of-Phase Feed Cycling 138
5.2 Comparison of Predictions from Eq. (5.1) to Experimental Data at Low Frequencies 140
5.3 Transient Response of Reactor Concentrations for Non-Cycled Feed 144
5.4 Effect of Feed Composition on Number of Cycles Required to Reach Cycle-Invariance 146
5.5 Slow Convergence to Cycle-Invariance at a Frequency of 6 mHz (a) Continuous CO_2 Response, (b) Expanded Views for 10 Cycles 150
5.6 Time-Average Conversions for Out-Of-Phase Cycling with

Time-Average Feed with of 1.2% NO and 1.2% CO 151
5.7 Effect of N_2O Phase Lead on Time-Average Conversions 152
5.8 Transport-Delays in the Response of CO_2, NO and N_2O Analyzers 155
5.9 Dynamic Response During Out-of-Phase Cycling 156
5.10 Dynamic Response for 100° and 270° NO Phase Leads at 2 mHz 160
5.11 Dynamic Response for 100° and 270° NO Phase Leads at 5 mHz 162
5.12 Comparison of Model Predictions with Experimental
Dynamic Response for Out-of-Phase Feed Cycling at 2 mHz 164
A.1 Calibration of Mass Flow Meter for the Total Flow to the Reactor 182
A.2 Calibration of Mass Flow Meter for the Flow of
CO and CO_2 Gas Mixtures 183
A.3 Calibration of Mass Flow Meter for the Flow of
N_2O and NO Gas Mixtures 184
A.4 Calibration of the Auxiliary Mass Flow Meter for
the Flow of CO and CO_2 Gas Mixtures 185

1. INTRODUCTION

1.1 Motivation

The emission of nitrogen oxides (NO_x) from automobile exhaust was recognised as a major source of air-pollution in the early 1950s (*1*). NO_x consists primarily of nitric oxide (NO) and nitrogen dioxide (NO_2) which are produced in all combustion processes by the oxidation of atmospheric nitrogen and fuel-bound nitrogen. NO_2 is linked to causing bronchitis, pneumonia, susceptibility to viral infection and alterations to immune system (*2, 3*). It also contributes to acid rain, urban smog and ozone (*2*). NO_2 is produced from the oxidation of NO, a reaction which proceeds rapidly in sunlight especially in the presence of hydrocarbons (*4*). Therefore, NO is the key starting point in the chain of events leading to various health and environmental concerns described earlier. Thus, if NO is prevented from entering the atmosphere, most of the downstream effects of NO_x pollution can be eliminated. Although NO is produced by lightening and volcanic activity, its main source is the combustion of fossil fuels especially in automobiles and industrial combustors. As early as 1952, two major components of the automobile exhaust, namely, the hydrocarbons (HC) and NO_x were identified as the main contributors to the problem of photochemical smog formation in urban centres (*1*). Because of the smog problem, the U.S. automobile manufacturers began studying the problem of automobile emission in 1953, and in 1957 recognized that the use of an oxidation catalytic converter was a viable approach for reducing HC emissions (*1*).

Automobile catalytic converters were introduced in the U.S. in 1974 to lower the emission of carbon monoxide (CO) and HC (*5*). The NO_x standard of 2 g/mile could be met by using exhaust gas recirculation which leads to the formation of less NO_x in the engine (*6*). Since 1981, more complex control systems have been used in the U.S. in order to satisfy the stricter 1 g/mile emission requirement for NO_x. Increasingly stringent regulations on NO_x have fuelled the search for better catalysts since then. Literally thousands of catalysts have been tested in the laboratories around the world and many have been patented. Presently, all of the automobile converter catalysts contain noble metals, such as platinum, rhodium and palladium. This type of catalyst is called a three-way-catalyst because it simultaneously promotes the conversion of three common pollutants namely, CO, HC and NO_x. NO is selectively reduced by CO in the presence of excess oxygen. The selectivity towards the NO+CO reaction is attributed to the presence of rhodium catalyst in the converter (*6*). At a typical exhaust gas temperature of 770 K, only rhodium is somewhat favourably selective towards the NO+CO reaction. At a lower temperature of 570 K, both platinum and rhodium are equally selective for the NO+CO reaction (*7*). To obtain maximum conversion efficiencies for the three pollutants, the air-to-fuel ratio is controlled using a "closed-loop" feed-back control system (*5*). A large number of reactions occur in the automobile catalytic converter under the actual operating conditions involving HC, CO, NO_x, oxygen (O_2), water and other intermediates. However, the reactions between CO, NO and/or O_2 have been studied extensively to understand the role of the catalyst for simultaneous oxidation (of CO by O_2) and reduction (of NO by CO).

The reduction of NO by CO over noble metal catalysts has been the subject of several studies in the last two decades because of its importance in automobile catalytic converters. These studies were carried out on both single crystals and supported catalysts containing either platinum or rhodium. Several studies revealed very complex phenomena occurring for the platinum-catalyzed NO+CO reaction. The reaction has been shown to exhibit self-sustained oscillations, both on crystalline platinum (*8-12*) as well as on supported platinum catalysts (*13*). In addition, the reaction has also been shown to exhibit reaction rate multiplicity on crystalline platinum surfaces (*10-12, 14*). Temperature programmed reaction studies (*15, 18*) have revealed the "explosive" nature of the reaction from the rapid evolution of carbon dioxide and nitrogen products in an extremely narrow temperature range. The mechanisms underlying these complex phenomena cannot be explained by simple Langmuir-Hinshelwood kinetics. While the exact mechanism by which NO is reduced by CO on platinum catalysts has not been completely determined, several studies (*19-25*) have reported the formation of nitrous oxide (N_2O) as an intermediate in the overall NO+CO reaction, particularly at temperatures below 580 K. At a typical operating temperature of 770 K in an automobile catalytic converter, the overall NO+CO reaction proceeds according to Eq. (1.1).

$$2NO + 2CO \rightarrow 2CO_2 + N_2 \tag{1.1}$$

The formation of N_2O at lower temperature, and its subsequent reduction by CO, can be described by the reactions according to Eqs. (1.2) and (1.3), respectively (*24*).

$$2NO + CO \rightarrow CO_2 + N_2O \tag{1.2}$$

$$N_2O + CO \rightarrow CO_2 + N_2 \tag{1.3}$$

Therefore, the N_2O+CO reaction according to Eq. (1.3) is considered to be an important subset of the overall NO+CO reaction. Despite its importance in the overall NO+CO reaction, the reaction of N_2O with CO on platinum catalyst has rarely been the main focus of an investigation (*26, 27*). Therefore, this study was undertaken to understand the role of the N_2O formation and other complex phenomena that occur for the platinum catalyzed NO+CO reaction.

1.2 Objective

The main objective of this study is to investigate the platinum catalyzed NO+CO reaction in order to gain an insight into the complex behaviour of the reaction reported in previous studies and to understand the formation of N_2O at low temperatures. Most of the previous work was carried out at high temperatures, where N_2O was not observed or was found in insignificant amounts. As such, the platinum catalyzed N_2O+CO reaction has not previously been thoroughly studied. Therefore, an additional objective of the study is to gain a thorough understanding of the N_2O+CO reaction as a sub-reaction of the overall NO+CO reaction. Finally, it is intended to explain the observed experimental behavior by appropriate kinetic models.

1.3 Methodology

A step-wise approach has been used in this study. The N_2O+CO reaction has been investigated as a first step in the study of the overall NO+CO reaction. The experiments were performed using an external recycle reactor containing a 0.5 wt% Pt/Al_2O_3 catalyst. All of the experiments were carried out at temperatures below 580 K because of the observations from other studies that N_2O formation is significant in the NO+CO reaction at these temperatures. Both reactions, namely, the N_2O+CO reaction and the NO+CO reaction, have been investigated using experimental steady-state and transient behavior. The steady-state experiments are concerned with examining isothermal multiplicity behavior, while the transients are generated using feed composition cycling. The steady-state bifurcation behaviour of the reaction can be used for a sensitive discrimination among several rival mechanisms as shown by Graham and Lynch (*28*) in an earlier study of the platinum-catalyzed CO oxidation. In a later study, Graham and Lynch (*29*) used the technique of variable-phase feed composition cycling to study the transient behaviour of the CO+O_2 reaction and developed a mechanism which consistently described the steady-state bifurcation and the reaction-rate resonance during feed cycling. Because of the apparent similarity between the CO+O_2 reaction and the CO+N_2O and CO+NO reactions, the same techniques using steady-state bifurcation and forced composition cycling are employed for this study.

1.4 Outline

This thesis consists of six chapters. This introductory chapter is followed by Chapter 2 which describes the steady-state behaviour of the N_2O+CO reaction. The steady-state multiplicity behaviour of the N_2O+CO reaction has been used to discriminate among four different mechanisms. In Chapter 2, it is shown that only a model based on a CO self-exclusion (from Pt surface) effect can describe the observed steady-state multiplicity behaviour. In Chapter 3, the transient behaviour of the N_2O+CO reaction during the forced feed cycling has been described. The effect of the cycle frequency and the phase angle between the NO and CO feed cycles on the resonant behaviour of the reaction has been discussed. A kinetic model, described in Chapter 3, provides a consistent explanation for the steady-state multiplicity and the resonance during feed cycling. The fourth chapter describes the steady-state multiplicity behaviour of the NO+CO reaction. The effect of temperature and feed composition on the multiplicity behaviour and the selectivity of the NO+CO reaction towards N_2O formation has been discussed. The steady-state multiplicity and the N_2O selectivity has been described by a kinetic model based on a seven-step reaction mechanism. It is also shown that the N_2O+CO reaction occurs to a substantial extent in the overall NO+CO reaction. In Chapter 5, the transient behaviour of the NO+CO reaction during feed composition cycling has been described. The effect of the feed composition, cycling frequency and the phase angle between the CO and NO feed cycles on the resonance behaviour of the reaction has been discussed. Finally, Chapter 6 summarizes the conclusions of this study and provides some recommendations about future work.

1.5 References

1. Briggs, W.S. in "Applied Industrial Catalysis" (B.E. Leach, Ed.), Vol. 3, p. 241-270 Academic Press Inc. 1984.
2. Chiron, M. in "Catalysis and Automotive Pollution Control: Proceedings of the First International Symposium, Brussels, Sept. 1986" (A. Crucq and A. Frennet, Eds.), p. 1-10, Elsevier Science Publishers, B.V., Amsterdam, 1987.
3. Armor, J.N. in "Environmental Catalysis" (J. N. Armor, Ed.) ACS Symposium Series 552, p. 1-6, American Chemical Society, Washington DC 1994.
4. Impens, R. in "Catalysis and Automotive Pollution Control: Proceedings of the First International Symposium, Brussels, Sept. 1986", (A. Crucq and A. Frennet, Eds.), p. 11-24, Elsevier Science Publishers B.V., Amsterdam 1987.

5. Taylor, K.C. in "Catalysis Science and Technology" (J.R. Anderson and M. Boudart, Eds.), Vol. 5, p. 119-170, Springer-Verlag, Berlin 1984.

6. Taylor, K.C. in "Catalysis and Automotive Pollution Control: Proceedings of the First International Symposium, Brussels, Sept. 1986", (A. Crucq and A. Frennet, Eds.), p. 97-116, Elsevier Science Publishers B.V., Amsterdam 1987.

7. Hahn, T. and Lintz, H.G., *Appl. Surf. Sci.* **40**, 59-63 (1989).

8. Adlhoch, W. and Lintz, H.G., *Z. Phys. Chemie Neue Folge* **103**, 207-211 (1976).

9. Adlhoch, W., Lintz, H.G. and Weisker, J., *Surf. Sci.* **103**, 576-585 (1981).

10. Schwartz, S.B. and Schmidt, L.D., *Surf. Sci.* **183**, L269-L278 (1987)

11. Schwartz, S.B. and Schmidt, L.D., *Surf. Sci.* **206**, 169-186 (1988).

12. Fink, Th., Dath, J.P., Imbihl, R. and Ertl, G., *J. Chem. Phys.* **95**, 2109-2126 (1991).

13. Schüth, F. and Wicke, E. in "Instationary Processes and Dynamic Experimental Methods in Catalysis, Electrochemistry and Corrosion" (G. Sandstede and G. Kreysa, Eds.), Dechema Monogr., Vol. 120, p. 429-441 (1989).

14. Bolten, H., Hahn, T., LeRoux, J. and Lintz, H.G., *Surf. Sci.* **160**, L529-L532 (1985).

15. Lesley, M.W. and Schmidt, L.D., *Surf. Sci.* **155**, 215-240 (1985).

16. Lesley, M.W. and Schmidt, L.D., *Chem. Phys. Lett.* **102**, 459-463 (1983).

17. Fink, Th., Dath, J.P., Bassett, M.R., Imbihl, R. and Ertl, G., *Vacuum* **41**, 301-303 (1990).

18. Fink, Th., Dath, J.P., Bassett, M.R., Imbihl, R. and Ertl, G., *Surf. Sci.* **245**, 96-110 (1991).

19. Lambert, R.M. and Comrie, C.M., *Surf. Sci.* **46**, 61-80 (1974).

20. Lorimer, D. and Bell, A.T., *J. Catal.* **59**, 223-238 (1979).

21. Kudo, A., Steinberg, M., Bard, A.J., Campion, A., Fox, M.A., Mallouk, T.E., Webber, S.E. and White, J.M. **125**, 566-587 (1990).

22. Solymosi, F., Völgyesi, L. and Sárkány, J., *J. Catal.* **54**, 336-344 (1978).

23. Adlhoch, W. and Lintz, H.G., *Surf. Sci.* **78**, 58-68 (1978).

24. Shelef, M. and Otto, K., *J. Catal.* **10**, 408-412 (1968).

25. Muraki, H. and Fujitani, Y., *Ind. Eng. Chem. Prod. Res. Dev.* **25**, 414-419 (1986).

26. Adlhoch, W., Kohler, R. and Lintz, H.G., *Z. Phys. Chemie. Neue Folge* **120**, 111-118 (1980).

27. Lintz, H.G., *Surf. Sci.* **108**, L486-L489 (1981).

28. Graham, W.R.C. and Lynch, D.T., *AIChE J.* **33**, 792-800 (1987).

29. Graham, W.R.C. and Lynch, D.T., *AIChE J.* **36**, 1796-1806 (1990).

2. N_2O REDUCTION BY CO: STEADY-STATE BEHAVIOR[*]

2.1 Introduction

The reduction reactions of various nitrogen oxides by carbon monoxide over noble metal catalysts have been studied extensively because of their importance in automobile catalytic converters. At a typical exhaust gas temperature of 770 K, while nitric oxide (NO) is present in significant amounts, nitrous oxide (N_2O) is not commonly observed. Therefore, the reduction of NO by CO over noble metal catalysts has been the main focus of several studies. It has been shown that the reduction reaction of NO by CO can exhibit complex behavior such as steady-state multiplicity (*1,2*) and self-sustained oscillations (*2-8*). A catalyst surface reconstruction process for Pt(100) has been suggested (*5-7*) as possibly being responsible for some of the observed complex behavior. While the exact mechanism by which NO is reduced by CO over the supported noble metal catalysts has not been completely determined, several studies (*9-18*) have reported the formation of N_2O as an intermediate in the overall NO+CO reaction, particularly at temperatures below 580 K. Thus, an understanding of the detailed mechanism of the N_2O+CO reaction is necessary in order to understand the complex behavior of the overall NO+CO reaction over supported noble metal catalysts.

Despite the frequent observation of N_2O formation and reaction during the reduction of NO by CO, the reaction of N_2O with CO on noble metal catalysts has only rarely been the primary focus of an investigation (*17, 19-21*). Adlhoch *et al.*(*19*) found that the rate of the N_2O+CO reaction over polycrystalline platinum is two orders of magnitude lower than the rate of the NO+CO reaction, and that N_2O decomposition is the rate limiting step. Lintz (*20*) compared the reaction probabilities of the NO+CO, N_2O+CO and O_2+CO reactions over polycrystalline platinum and proposed an elementary reaction sequence for the N_2O+CO reaction. McCabe and Wong (*17*) investigated the kinetics of the N_2O+CO reaction over a supported rhodium catalyst and proposed a mechanism for the reaction. They also reported that the N_2O+CO reaction rate is several orders of magnitude lower than the rates of the NO+CO and O_2+CO reactions. Cho (*21*) presented a kinetic analysis showing that the rate of the N_2O+CO reaction, as an intermediate reaction in the NO+CO reaction system, can be two to three orders of magnitude higher than the rate of the isolated N_2O+CO reaction.

---

[*] A version of this chapter has been published - Sadhankar, R.R., Ye, J. and Lynch, D.T., *Journal of Catalysis,* **146**, 511 - 522 (1994)

It is possible that the lack of a single rate-controlling step for all conditions is responsible for several different mechanisms having been proposed for the reduction reaction of N_2O by CO. Alternatively, the fact that a derived rate expression is consistent with the experimental data provides only a necessary but not a sufficient condition that a model is based upon the correct reaction mechanism. Very good agreement is often possible solely because rate functions of the Langmuir-Hinshelwood type are very adept at fitting data. An additional interesting observation is that, despite the similarity of the N_2O+CO and O_2+CO reaction systems, there are as yet no reports in the literature of multiplicity behavior for the N_2O+CO reaction on noble metal catalysts.

In an earlier study, Graham and Lynch (*22*), used the steady-state multiplicity behavior of the O_2+CO reaction over supported platinum catalyst to discriminate among several kinetic models. In this study, a similar discrimination among several kinetic models will be performed by using the experimental bifurcation behavior for the reduction of N_2O by CO over a supported platinum catalyst. The steady-state multiplicity for this reaction has been observed over the temperature range of 460-520 K. Four kinetic models are examined and it is shown that only a model based on carbon monoxide self-exclusion from the platinum catalyst is able to describe all of the observed behavior. The proposed mechanism consists of several elementary steps, namely, the reversible adsorption of CO, the irreversible dissociative adsorption of N_2O to form adsorbed atomic oxygen and gaseous N_2, and the reaction of adsorbed carbon monoxide and atomic oxygen to form gaseous CO_2. A kinetic model based on this reaction mechanism and incorporating the CO self-exclusion effect is able to describe the reaction rate multiplicity with an explicit rate expression.

2.2 Experimental Equipment and Materials

The recycle reactor system used in this study has been previously used by Lynch and Wanke (*23*). The subsequent modifications to the feed metering and controlling system were done by Graham and Lynch (*22, 24*). Further modifications to the system for the purpose of this study, include computer automation and replacement of the infrared spectrophotometer by dedicated gas analyzers. The experimental equipment can be grouped into three major parts, a recycle reactor system, feed system and gas analyzers.

The recycle reactor system is shown in Figure 2.1. The recycle reactor vessel is constructed from a 2.5 cm diameter stainless steel pipe, with a total free volume of 47 cm^3. The reactor contained 20 g of Englehard catalyst containing 0.5 wt% platinum supported on γ-Al_2O_3 in the form of pellets. The cylindrical pellets were approximately 3 mm by 3 mm in size, with the Pt deposited in a thin layer on the exterior.portion of the pellets. The catalyst bed was diluted with 60 g of 3 mm diameter glass beads. As a result of some of the modifications to the recycle tubing, the effective free volume of the recycle system including the reactor (without the catalyst and the glass beads), metal bellows compressor and the associated tubing was determined to be 215 cm^3 from frequency response measurements similar to those described by Lynch and Walters (*25*).

The reactor was placed in a fluidized sand bath equipped with a resistance heater, controlled by a Barber-Coleman model 520 solid-state controller. The reactor

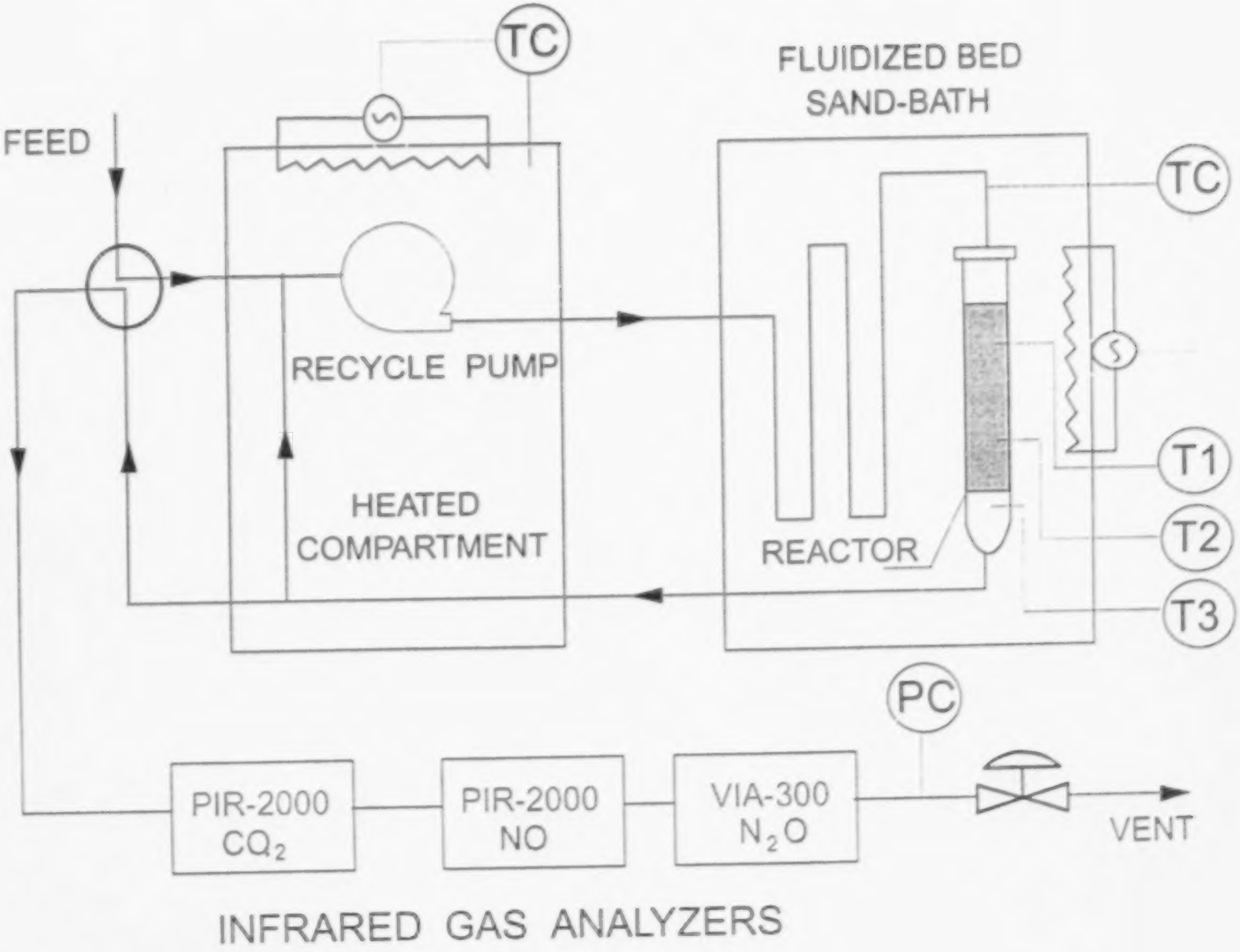
FEED
TC
RECYCLE PUMP
HEATED
COMPARTMENT
FLUIDIZED BED
SAND-BATH
TC
REACTOR
T1
T2
T3
PC
PIR-2000
CQ$_2$
PIR-2000
NO
VIA-300
N$_2$O
VENT
INFRARED GAS ANALYZERS

Figure 2.1 Recycle Reactor System Schematic.

temperatures were monitored by four type J thermocouples, two of which were inserted into the catalyst bed, one was inserted below the catalyst bed and one was inserted into the inlet tubing at the top of the reactor. The inlet temperature was used to control the heat input to the sand bath. The inlet consisted of approximately 1 m of 6.4 mm diameter stainless-steel tubing immersed in the sand bath. The reactor operated essentially isothermally with a maximum recorded temperature difference of 2 K across the catalyst bed. The temperature controller was able to maintain the reactor temperature within ±1 K. A Metal Bellows Corporation model MB-118 HT compressor driven by a 1 hp variable speed motor was used for gas recirculation. The motor speed could be manually set in the range of 300-2000 rpm. At the normal operating speed of 1400 rpm, the recycle flow from the pump was measured to be 500 cm^3/s. The reactor pressure was always maintained at 103 kPa and the temperatures used in this study were 461, 480, 499 and 520 K. Thus, for a feed flow of 185 cm^3(STP)/min, a recycle ratio of 85 to 98 was achieved at the reactor operating conditions. From frequency response measurements, the mixing in the reactor was found to approximate closely that of an ideal CSTR.

The recycle compressor and the recycle tubing were housed in an insulated box equipped with a resistance heater and a recirculating fan for preheating of the feed gas. The temperature in the preheat compartment was maintained at 150 °C, and was limited by the softening temperature of the teflon seals of the bellows compressor. The exit stream from the reactor was routed to gas analyzers. The reactor pressure was maintained at 103 kPa by means of a Moore Instrument Co. model 40-100 pressure regulator, located downstream of the gas analyzers. The reactor pressure was measured by a Hiese model 7108 B digital absolute pressure gauge.

The feed gas system is shown schematically in Figure 2.2. The feed composition and the flow rates were controlled by three Matheson model 8250 mass flow controllers. The mass flow controllers for CO and N_2O had a span of 100 cm^3 (STP)/min and the controller for the total flow to the reactor has a span of 500 cm^3/min. Flow rates between 15% and 85% of the span could be accurately set on these mass flow controllers. An

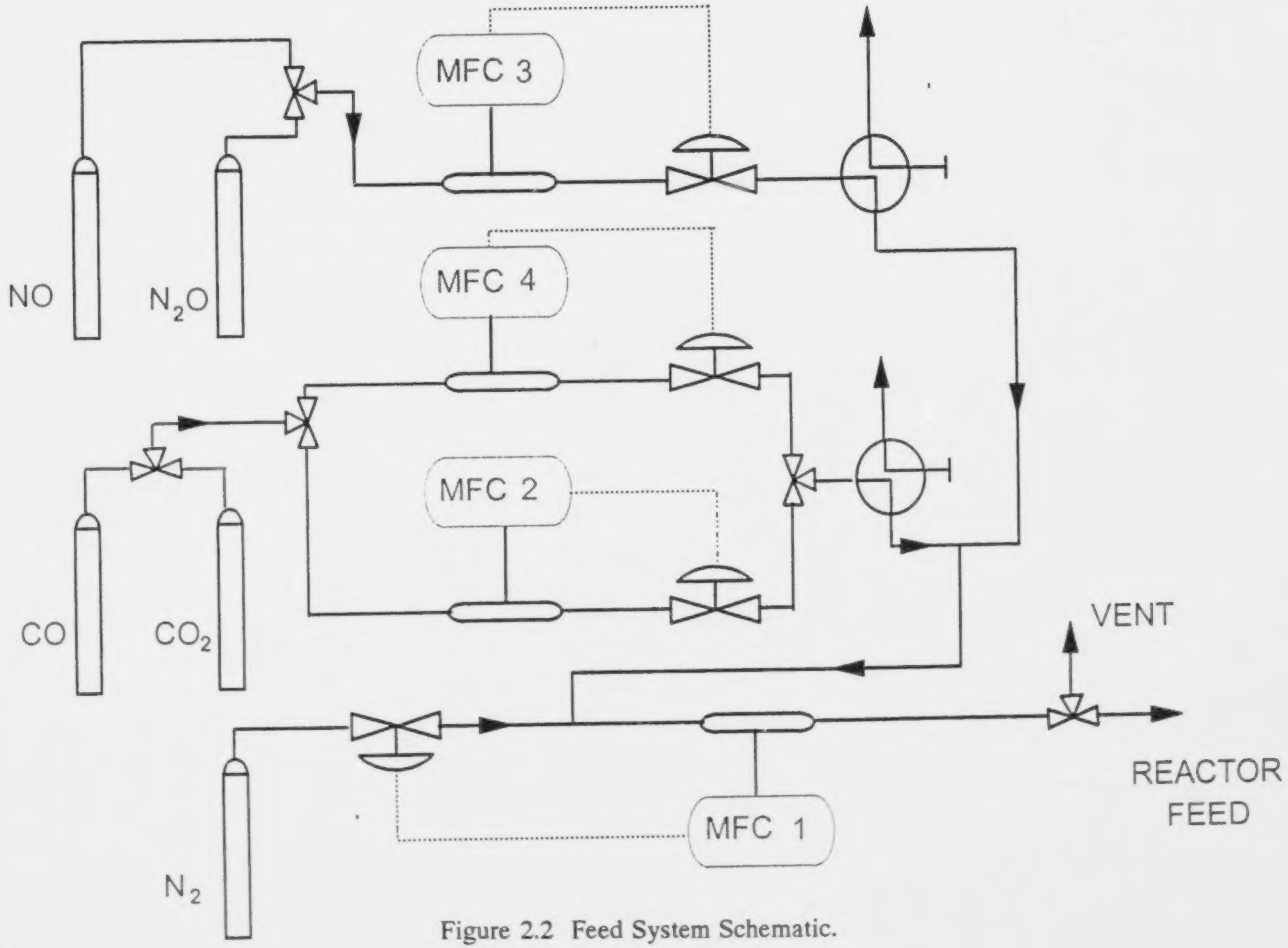
MFC 3
MFC 4
MFC 2
MFC 1
NO
N_2O
CO
CO_2
N_2
VENT
REACTOR
FEED

Figure 2.2 Feed System Schematic.

additional mass flow controller, Matheson model 8259, with a range of 0-30 cm^3(STP)/min was installed in parallel with the CO mass flow controller and it was used for metering small flows of CO. The flow controllers were calibrated using a bubble column. The calibration charts for the mass flow controllers are shown in Appendix A. An air-actuated four-way valve, Whitey model 131 DA, was located downstream of each of the CO and N_2O mass flow controllers. The flow controllers and the valves were interfaced to an IBM-compatible microcomputer using Optomux digital/analogue conversion equipment. This equipment was also used for monitoring reactor temperatures, individual and total flow rates and the on-line gas analyzers. The gases used for this study were purchased from Linde and included gas mixtures of 2%, 5% or 10% CO in N_2; 2% or 10% N_2O in N_2 and prepurified N_2. Feed compositions were in the ranges of 0-2% N_2O and 0-2% CO, with nitrogen for the balance of the feed.

The effluent stream from the reactor was routed through two infrared type gas analyzers connected in series. Horiba infrared gas analyzers PIR-2000 and VIA-300 were used for measuring CO_2 and N_2O respectively. The analyzers were calibrated at the beginning of each experiment, using N_2 for zero calibration and a gas mixture (0.982% CO_2 in N_2, 2% CO_2 in N_2, or 2% N_2O in N_2) for the span calibration.

2.3 Results

The experiments were concerned with examining the reaction rate dependence on concentration, and the steady-state rate multiplicity behavior, in the temperature range of 460-520 K. Matsuura and Kato (*26*) have shown that steady-state rate multiplicity occurs for heterogeneous catalytic reactions in an isothermal CSTR when the reactant concentration in the feed is such that the rate curve intersects the CSTR mass balance line at three points on a rate versus reactant concentration plot. At least one of the three states is always unstable when multiplicity occurs. This type of feed concentration multiplicity can occur even in the absence of intrinsic rate multiplicity which can be represented by hysteresis in the rate versus reactor concentration curve. Eigenberger (*27*) has shown that intrinsic rate multiplicity can be caused by the competing chemisorption of two species upon the same active sites of a catalyst and that the rate expression has to be implicit to possess multiple solutions. The experiments described herein were aimed at studying multiplicity as described by Matsuura and Kato (*26*) rather than intrinsic rate multiplicity as described by Eigenberger (*27*). Emphasis was particularly placed on determination of the reactor feed composition at which bifurcation in steady-state CO conversion occurs. The term "bifurcation point" will be used to refer to the CO feed concentration at which the CO conversion abruptly changes from a low to a high value, or from a high to a low value.

In the first group of experiments, the reactor temperature, the total feed flow rate to the reactor and the N_2O concentration in the feed were held constant while varying the CO feed concentration during each experimental run. Sets of measurements were made at each of three different temperatures, 461, 480 and 499 K, respectively, and, at each temperature, experiments were carried out using three different N_2O concentrations, 0.4%, 0.7% and 1.2%, respectively. The results of these nine sets of experimental data are summarized in Fig. 2.3 and tabulated in Appendix B.

At the beginning of each experiment, the CO feed concentration was set to be much less than the N_2O feed concentration. The attainment of steady-state was determined by monitoring the CO_2 and N_2O concentrations in the reactor effluent stream. The CO feed concentration was then increased in steps, allowing a minimum of 3 hours at every step to reach steady-state conditions. It was observed that, while the CO conversion was 100% at low CO feed concentrations, increasing the CO concentration beyond a certain limit (high-to-low conversion bifurcation point) caused the CO conversion to drop from nearly 100% to a very low value. For example, for the right-most curve in Fig. 2.3(a) (499 K, 1.2% N_2O), the high-to-low conversion bifurcation occurred for a feed containing between 1.055% and 1.082% CO. Each experiment was then repeated starting with a feed CO concentration which was much in excess of the feed N_2O concentration (low conversion region). Stepwise decrease of the %CO in the feed

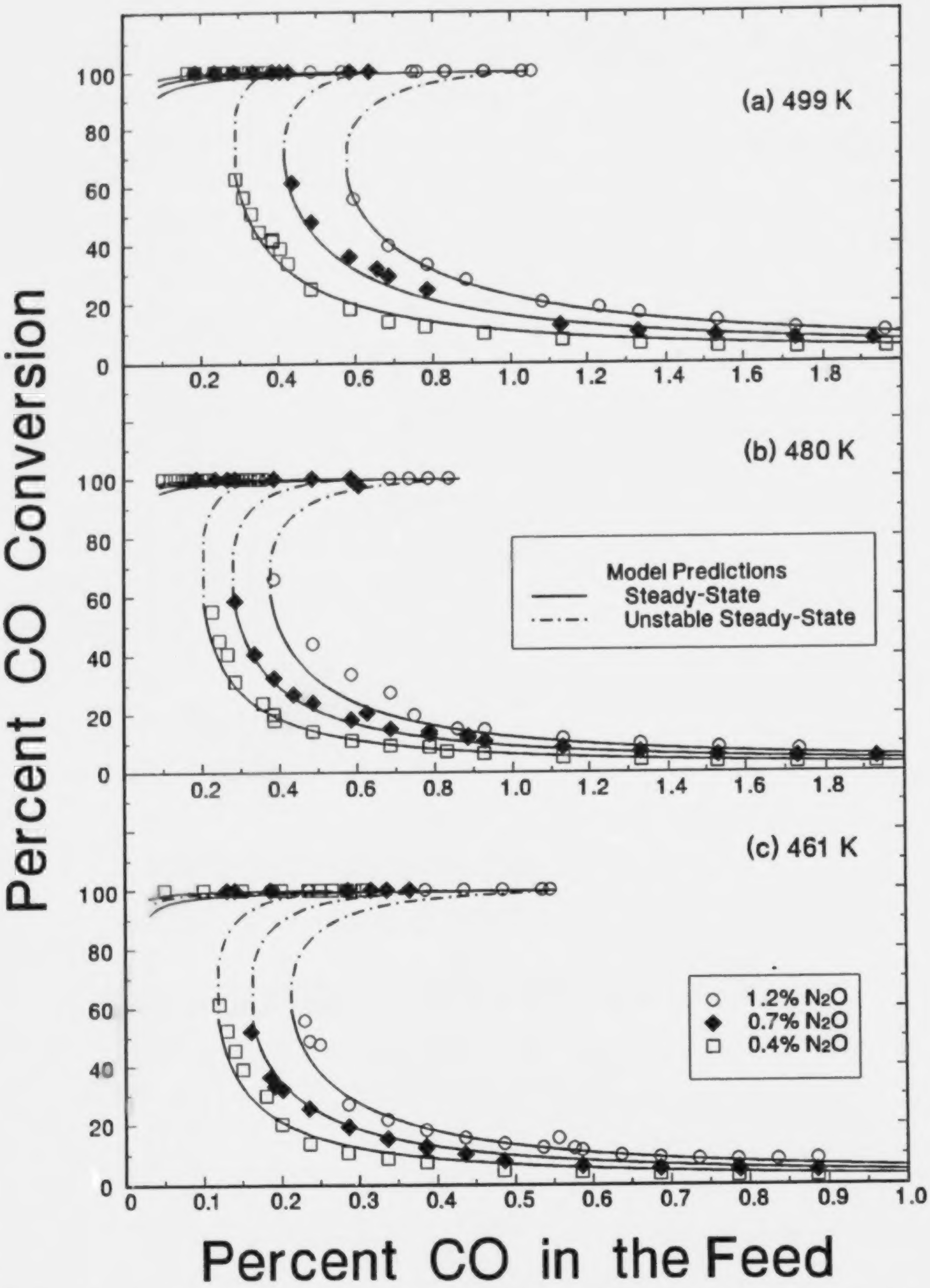

Figure 2.3 Multiplicity Behavior During the Reduction of N_2O by CO at 461-499 K.

caused the conversion to increase gradually (from nearly 10% at 1.96% CO to nearly 55% at 0.596% CO as shown by the open circles in Fig. 2.3(a). Further decrease in CO feed concentration, below the low-to-high conversion bifurcation point, caused the CO conversion to increase to 100%. In Fig. 2.3(a), the low-to-high conversion bifurcation occurred at a feed CO composition of between 0.586% and 0.596% for the experiment with 1.2% N_2O in the feed. The bifurcation points were bracketed by repeating the experiments with small step sizes in CO feed concentration, until reproducible steady-states were achieved. Operating periods of longer than 3 hours were often necessary in order to bracket a bifurcation point.

An additional three sets of experiments were carried out at 520 K by reversing the roles of CO and N_2O. For the experiments at 520 K, the N_2O concentration in the feed was varied while holding the %CO in the feed constant for each of the experimental runs. The results of three runs, with feed CO of 0.676%, 0.915% and 1.166%, respectively, are summarized in Fig. 2.4. Although Fig. 2.4 has a totally different appearance when compared to Fig. 2.3, the multiplicity behavior shown in both of the figures is similar. As can be seen from Fig. 2.4, almost 100% CO conversion was obtained for experiments with N_2O in large excess relative to CO. Decreasing the N_2O concentration below the composition corresponding to the high-to-low conversion bifurcation point caused the CO conversion to drop from 100% to a much lower value. A low CO conversion was obtained in the experiments which were started with excess CO in the feed. Increasing the N_2O in the feed led to a gradual increase in the CO conversion. Near the low-to-high conversion bifurcation point, the CO conversion increased rapidly to 100%.

The experimental locations of the bifurcation points are shown by paired sets of symbols in Fig. 2.5. The pair of an empty symbol and a dark empty symbol brackets a low-to-high conversion bifurcation point and the pair of a dark empty symbol and a filled symbol brackets a high-to-low conversion bifurcation point. The bifurcation points at 499 K are not shown in Fig. 2.5 for reasons of clarity. The low-to-high conversion bifurcation points at 499 K almost coincide with the high-to-low conversion bifurcation points at 461

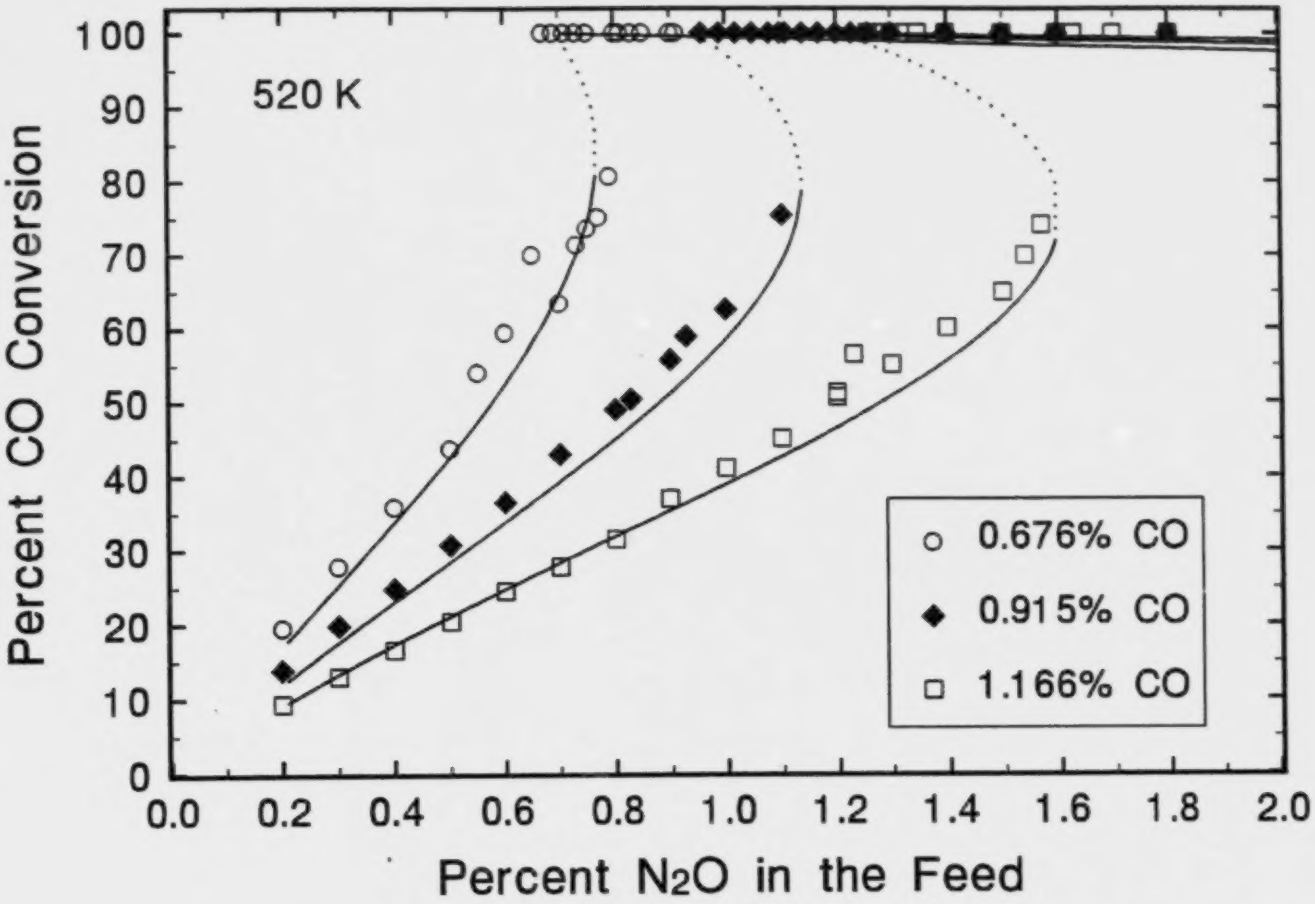

Figure 2.4 Multiplicity Behavior During the Reduction of N_2O by CO at 520 K.
(——— , steady-state and ··········, unstable steady-state predicted by Mechanism 4)

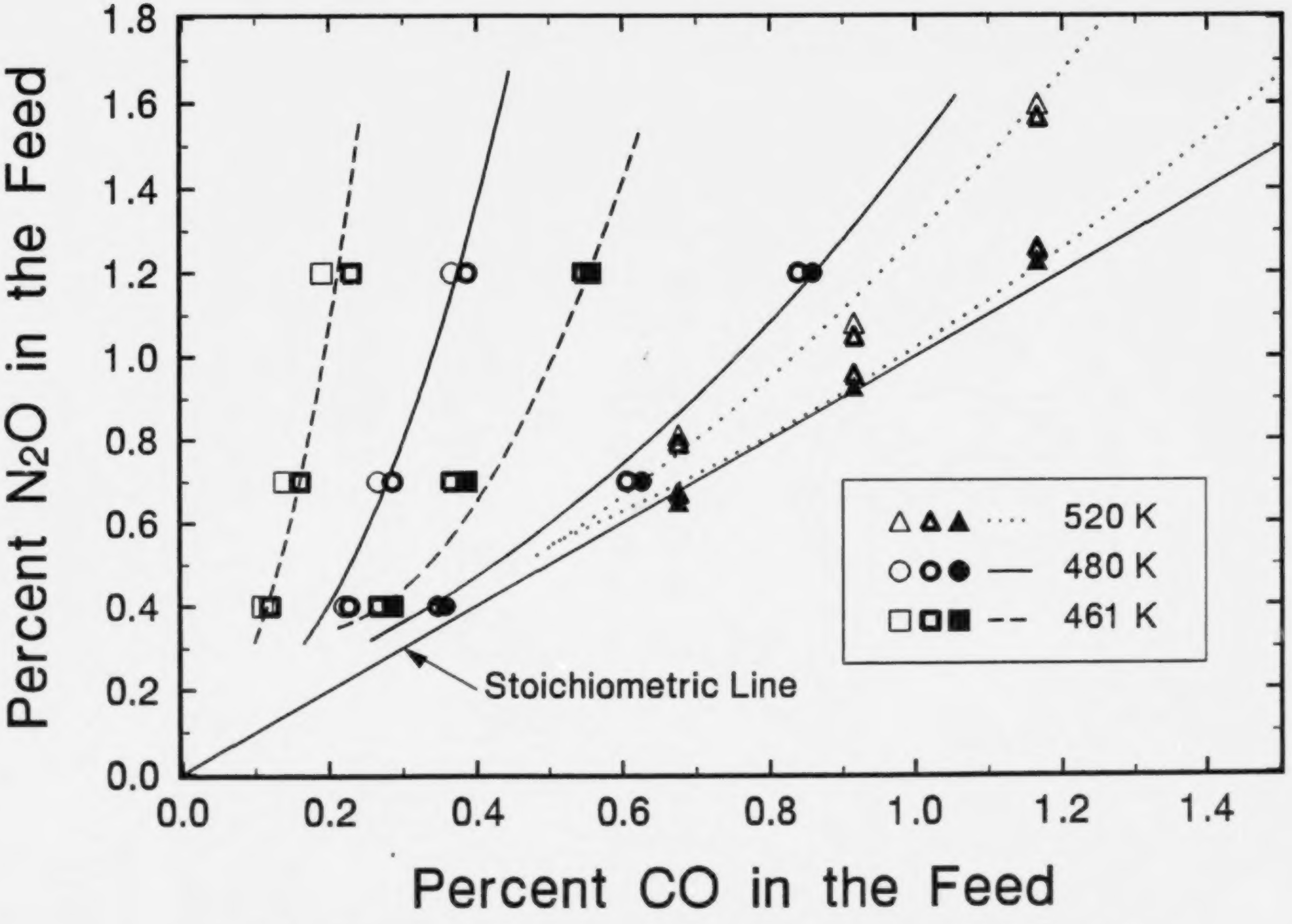

Figure 2.5 Dependence of Bifurcation Points on Temperature and Feed Composition.
(——— , ----------, ·········· predictions from Mechanism 4)

K. The high-to-low conversion bifurcation points at 499 K lie between the two 520 K bifurcation boundaries. The multiplicity region lies within the two bifurcation boundaries. In the region to the left of the low-to-high conversion bifurcation boundary, CO conversion is almost 100%. The low conversion region lies to the right of the high-to-low conversion bifurcation boundary. It can be seen from Fig. 2.5 that the bifurcation point locations shift in the direction of higher %CO with increasing temperature and increasing %N_2O in the feed.

It is generally agreed that during N_2O reduction by CO, an adsorbed oxygen species is formed through N_2O decomposition. In addition to reaction with CO, it is possible that an oxygen desorption reaction could also be involved as a process for removal of surface oxygen. Therefore, a sensitive oxygen analyzer (Customs Sensors and Technology model 8205 - lowest range 0-2 ppm O_2) was employed to measure reactor oxygen content with a feed consisting of 1.5% N_2O in N_2 at 499 K. No change in oxygen content between the feed and effluent streams could be detected, therefore, oxygen desorption does not occur in the temperature range under consideration. In another experiment with a feed containing 2% CO in N_2, no CO_2 could be detected in the reactor effluent, therefore, reaction between two adsorbed CO molecules to form CO_2 and surface carbon does not occur at the temperatures used in this study.

To ensure that the experimental measurements represent the intrinsic kinetics of the reaction, it is necessary to determine to what extent, if any, the experimental observations have been affected by internal and external mass transfer limitations. The absence of inter-particle mass transfer effects was verified experimentally by varying the recycle flow delivered by the compressor. No effect on CO conversion was observed for a wide range of recycle flow rates. In addition, the ratio of the surface CO concentration to bulk CO concentration, calculated from a mass transfer coefficient correlation (*28*), was predicted to be approximately 0.995 for the experiments, which further confirms the absence of the inter-particle mass transfer resistance. The intra-particle diffusional effects were expected to be negligible because the catalyst was an egg-shell type catalyst in which all of the platinum was deposited in the outer 10% (or less) of the volume of the pellets. Moreover, the per-pass conversion in the reactor was always less than 1%.

Intra-particle diffusional effects were also assessed by determining the value of a Thiele modulus of the form:

$$\phi_S = \frac{r_P^2(-r_{CO})}{D_{eff}C_S} \tag{2.1}$$

Satterfield (*28*) suggests that, for an isothermal system consisting of an irreversible reaction of a single reactant, whose kinetics can be represented by a power-law relationship, intrinsic kinetics are observed if $\Phi_S < 6$ for a zeroth-order reaction or $\Phi_S < 1$ for a first-order reaction. In addition Smith *et al.* (*29*) have shown that for a negative-order reaction, $\Phi_S < 10$ is sufficient for intrinsic kinetics to be measured. For the experimental data in the low-conversion regions of Figs 2.3 and 2.4 (negative-order kinetics with respect to CO), the calculated values of Φ_S vary from a low of 0.01 (at 461 K for 0.4% N_2O and 0.67% CO in the feed) to a high of 1.6 (at 520 K with 0.8% N_2O and 0.67% CO in the feed). Therefore, it can be said that the measurements in the low-conversion region are not affected by internal diffusion limitations. Unfortunately, the same can not be stated conclusively for the high-conversion (positive-order kinetics with almost 100% CO conversion) because it was not possible to determine the very low reactor concentrations reliably with the gas analysis equipment employed in this study. Thus, because of the possibility of diffusional effects on the high-conversion data, emphasis has been placed in the following on using the low-conversion data for discrimination among the various mechanisms and estimation of the model parameters. The high-conversion data has only been used to the extent that, when estimating parameters, an attempt has always been made to have model experimental agreement regarding the locations of the high-to-low conversion bifurcation points.

2.4 Models of Reaction Mechanism

The overall reaction in which CO is oxidized by N_2O involves elementary steps consisting of adsorption, desorption and surface reaction. In the temperature range of interest (<600 K), CO adsorbs reversibly on platinum (*30*). The adsorption and/or decomposition of N_2O on platinum and other noble metal catalysts have been studied by several authors. Lintz and Riekert (*31*) compared the reaction probabilities of N_2O decomposition from several studies and they concluded that the observations regarding the N_2O+CO system were quite reproducible. Alnot *et al.* (*32*) reported the dissociative adsorption of N_2O on a recrystallized platinum ribbon with the release of molecular N_2 in the temperature range 300-500 K. Takoudis and Schmidt (*33*) studied the kinetics of N_2O decomposition on polycrystalline Pt in the temperature range of 673-1473 K and proposed a Langmuir-Hinshelwood rate expression. In their derivation, the rate limiting step was assumed to be the decomposition of adsorbed N_2O, while adsorption-desorption equilibrium was assumed for both N_2O and O_2. They also concluded that the surface coverage of adsorbed N_2O is equal to unity at low temperature and proportional to the partial pressure of N_2O at high temperatures. However, in a later study, Schmidt *et al.* (*34*) reported that N_2O does not appear to chemisorb on platinum in UHV experiments in the temperature range of 700-1600 K.

The surface reaction between adsorbed CO and adsorbed oxygen is believed to be the main reaction for the production of CO_2 (*17, 21*) when CO is oxidized by N_2O. However, an Eley-Rideal type reaction between gas-phase CO and oxygen has also been suggested (*20*) as a route for the production of CO_2 in the overall N_2O+CO reaction.

A main consideration in proposing a reaction mechanism is that it should be able to describe the experimental multiplicity behavior. In this study, four mechanisms have been examined in an attempt to describe the experimental bifurcation and reaction rate behavior of the N_2O+CO reaction.

2.4.1 Mechanism 1

The first mechanism used to describe the rate multiplicity was a classical Langmuir-Hinshelwood type model consisting of the following elementary steps.

$$CO(g) + M \rightleftharpoons M\text{-}CO \tag{2.2}$$

$$N_2O(g) + M \rightarrow N_2(g) + M\text{-}O \tag{2.3}$$

$$M\text{-}CO + M\text{-}O \rightarrow CO_2(g) + 2M \tag{2.4}$$

At steady-state, the mass balance equations for the adsorbed species can be written as follows, where all parameters are defined in the **Notation** section:

$$k_1L[CO](1-\theta_{CO}-\theta_O) - k_{-1}L\theta_{CO} - k_3L^2\theta_O\theta_{CO} = 0 \tag{2.5}$$

$$k_2L[N_2O](1-\theta_{CO}-\theta_O) - k_3L^2\theta_O\theta_{CO} = 0 \tag{2.6}$$

Equations (2.5) and (2.6) can be solved to express the fractional surface coverage of CO and oxygen in terms of the CO and N_2O gas-phase concentrations as given by Equations (2.7) and (2.8), respectively:

$$\theta_{CO} = \frac{K_1[CO] - (K_{21} + K_{23})[N_2O]}{1 + K_1[CO] - K_{21}[N_2O]} \tag{2.7}$$

$$\theta_O = \frac{K_{23}[N_2O]}{K_1[CO] - K_{21}[N_2O]} \tag{2.8}$$

The specific rate of CO_2 formation is given by:

$$r_{CO_2} = K_{LH}\theta_O\theta_{CO} \tag{2.9}$$

The reactor is assumed to be an ideal CSTR, and therefore, the gas-phase species mass balances are given by the following two equations:

$$Q([CO]_o - [CO]) = WK_{LH}\theta_O\theta_{CO} \tag{2.10}$$

$$Q([CO]_o - [CO]) = Q([N_2O]_o - [N_2O]) \tag{2.11}$$

Equations (2.7), (2.8), (2.10) and (2.11) can be used to relate the percentage CO conversion to the reactant compositions in the reactor. Because the experimental CO conversion is known as a function of reactant concentrations, it is possible to estimate the values of the kinetic parameters so as to obtain agreement between the model and the data. An initial estimate of the parameters was obtained by forcing the model predictions to match the low-to-high conversion bifurcation point locations. The experimental data for near 100% CO conversion were not used for the initial parameter estimation, because it was not possible to determine the very low reactor concentrations reliably with the gas analysis equipment employed in this study when the CO conversion approached 100%. The final parameter values were selected to minimize the sum of squared errors in the predicted bifurcation points.

In Fig. 2.6, the CO conversion predictions from Mechanism 1 are compared with the experimental data (represented by the solid circles) at 499 K with 1.2% N_2O in the feed. The parameter values used for Fig. 2.6 are listed in Table 2.1. To generate a continuous curve, Equations (2.7),(2.8),(2.10) and (2.11) were reduced to a single, cubic equation in $[N_2O]$ by successive substitution. The roots of the cubic equation for $[N_2O]$ were then determined by the 'roots' function of MATLAB (*35*) with different values of %CO in the feed. MATLAB programs for calculation of CO conversion by various mechanisms are listed in Appendix C. The $[N_2O]$ equation has three physically

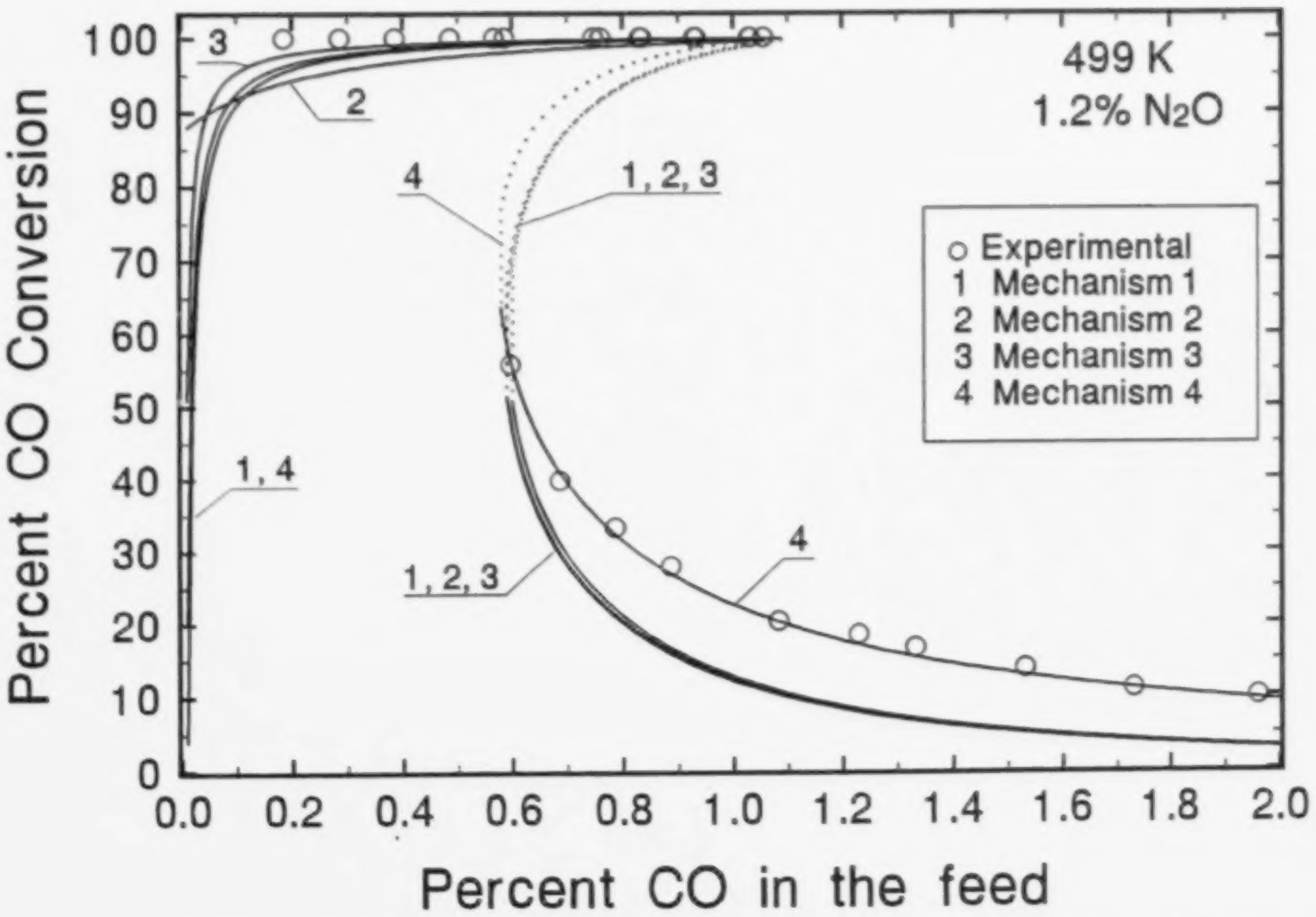

Figure 2.6 Comparison of Predictions from Mechanisms 1 to 4 to Experimental Bifurcation Points and CO Conversions.

reasonable roots in the region of multiplicity. The dotted lines in Fig. 2.6 indicate that the steady state is unstable; in the multiplicity region two of the steady states are stable and one is unstable. It can be seen from Fig. 2.6 that the predictions from Mechanism 1 match the experimental bifurcation points. However, the predicted CO conversions are somewhat less than the experimental values in the region of low CO concentrations in the feed (<0.3%CO) and very markedly less than the experimental values in the region of high CO concentrations in the feed (0.6%-2%). An attempt was made to adjust the parameter values to obtain better agreement between the experiments and the predictions, however, it was not possible to find a single set of parameter values that could describe both the experimental CO conversions as well as the bifurcation point locations.

Table 2.1

Parameter Values at 499 K for Mechanism 1 to 4

	Mechanism			
Parameter	1	2	3	4
K_1	1000	2115	605	1200
K_{21}	$1.9\text{x}10^{-2}$	$4.5\text{x}10^{-2}$		$1.7\text{x}10^{-2}$
K_{23}	8	39.4		8
K_{31}			$1.45\text{x}10^{-3}$	
K_{43}		4.9		
K_5			4.8	
K_{63}			2.4	
K_{65}			0.15	
K_{LH}	$1.721\text{x}10^{-6}$	$3.891\text{x}10^{-7}$	$1.721\text{x}10^{-6}$	$1.371\text{x}10^{-6}$
N_{CO}				1.025

It is possible to increase the CO conversion on the high conversion branch (the region of low %CO in the feed) either by increasing the CO adsorption-desorption constant, K_1, or by reducing the values of the parameters K_{21} or K_{23}. However, adjusting the parameters in this fashion leads to an increasing discrepancy between the predicted and the experimental locations of the high-to-low conversion bifurcation points. It is seen in Fig. 2.6 that the predicted CO conversion decreases rapidly as the CO in the feed is reduced below approximately 0.2%. This occurs because N_2O decomposition is increasingly favoured over CO adsorption as the feed %CO is reduced while holding the %N_2O constant. Thus, the oxygen surface coverage increases rapidly and inhibits CO adsorption. As the oxygen surface coverage approaches unity, the CO fractional surface coverage, and consequently the CO conversion, decreases to zero. This is at odds with the experimental data in which the CO conversion was observed to be constant at close to 100% as the feed %CO was decreased. It should be noted, however, that reliable experimental measurements were not possible for very low values of the %CO in the feed because of the previously noted analyzer limitations. The problem of oxygen saturating the surface would not occur if oxygen desorption occurs to any significant extent. However, this explanation is not applicable because, as already mentioned, the possibility of oxygen desorption was examined experimentally and ruled out.

The model predictions for the low conversion branch (high feed %CO) could be improved only slightly by increasing K_{LH} or by reducing K_1, but this can only be achieved at the expense of an increasing discrepancy in the prediction of the low-to-high conversion bifurcation point location. Specifically, both the bifurcation points shift in the direction of higher feed %CO for an increase in K_{LH} or for a decrease in K_1 or K_{23}. Both bifurcation points are relatively insensitive to changes in the value of K_{21} by as much as ±75%. The number of significant digits shown in Table 2.1 (and in subsequent tables of parameter values) does not imply that the parameters have been determined to this degree of precision. This number of significant digits is given so that others can reproduce the calculations. Changing any individual parameter can result in significant changes in the predictions but simultaneous changes to several parameters can result in equivalent predictions being produced.

From the preceding it is seen that the standard Langmuir-Hinshelwood type model has serious deficiencies. Although, this mechanism can describe the multiplicity behavior, it is not possible for any single set of parameter values to produce complete agreement with all of the experimental behavior (bifurcation point locations and reaction rate dependence on composition).

2.4.2 Mechanism 2

Lintz (*20*) proposed a mechanism for the N_2O+CO reaction over polycrystalline Pt which, in addition to the three steps of Mechanism 1, also included an Eley-Rideal (ER) reaction between gas-phase CO and adsorbed oxygen.

$$CO(g) \ + \ M\text{-}O \ \rightarrow \ CO_2(g) \ + \ M \qquad (2.12)$$

Thus, Mechanism 2 consists of the four reaction steps (2.2)-(2.4) and (2.12). The steady-state balance for the adsorbed CO is identical to Eq. (2.5), and the balance for the adsorbed oxygen is given by:

$$k_2L[N_2O](1 - \theta_{CO} - \theta_O) - k_3L^2\theta_O\theta_{CO} - k_4L[CO]\theta_O = 0 \qquad (2.13)$$

The rate of CO_2 formation is given by:

$$r_{CO_2} = K_{LH}\theta_O(\theta_{CO} + K_{43}[CO]) \qquad (2.14)$$

Equations (2.5) and (2.13) cannot be solved explicitly for the fractional surface coverage of CO and oxygen in that quadratic equations are obtained for θ_{CO} and θ_O. Therefore, Eqs. (2.5), (2.10), (2.11) and (2.13) were reduced to a single tenth-order polynomial in $[N_2O]$ and solved by using the MATLAB 'roots' function. The $[N_2O]$ polynomial has three physically reasonable roots in the region of multiplicity and a single physically reasonable root elsewhere. As can be seen from Fig. 2.6, Mechanism 2 predicts near

100% conversion of CO at low %CO in the feed. The model parameter, K_{43}, which is the ratio of the reaction rate constants for the ER and the surface reactions, has a value of 4.9. However, in an extensive review of CO oxidation on noble metal catalysts, Engel and Ertl (*30*) concluded that for CO oxidation over Pt catalysts there is a lack of evidence for the ER reaction proceeding to any significant degree. Thus, in order to predict high CO conversion in the low %CO feed region, it is necessary to have a very large value for the ER rate constant, relative to the LH rate constant, which is inconsistent with earlier studies. In addition, as seen in Fig. 2.6, the use of the ER reaction does not produce any improvement in the prediction of the low conversion branch, relative to Mechanism 1. Hence, the inclusion of an ER step cannot be used to eliminate the model-experimental discrepancies noted in Mechanism 1.

2.4.3 Mechanism 3

In the earlier two models, it has been assumed that N_2O adsorbs dissociatively on a platinum surface. However, as suggested by Takoudis and Schmidt (*33*), N_2O decomposition on platinum could occur via an adsorbed N_2O species as follows:

$$N_2O(g) + M \rightleftharpoons M\text{-}N_2O \tag{2.15}$$

$$M\text{-}N_2O \rightarrow N_2(g) + M\text{-}O \tag{2.16}$$

Mechanism 3 consists of four steps, namely reactions (2.2), (2.4), (2.15) and (2.16). McCabe and Wong (*17*) used a similar mechanism to describe N_2O reduction by CO on an alumina-supported rhodium catalyst in the temperature range of 550 to 700 K. They assumed that weakly adsorbed N_2O serves as a precursor to dissociative adsorption. The steady-state balances for the three adsorbed species yield the following equations:

$$k_1L[CO](1 - \theta_{CO} - \theta_O - \theta_{N_2O}) - k_{-1}L\theta_{CO} - k_3L^2\theta_O\theta_{CO} = 0 \quad (2.17)$$

$$k_5L[N_2O](1 - \theta_{CO} - \theta_O - \theta_{N_2O}) - k_{-5}L\theta_{N_2O} - k_6L\theta_{N_2O} = 0 \quad (2.18)$$

$$k_6L\theta_{N_2O} - k_3L^2\theta_O\theta_{CO} = 0 \quad (2.19)$$

Equations (2.17)-(2.19) can be rearranged to produce explicit expressions for the fractional surface coverage of CO, oxygen and N_2O, namely:

$$\theta_{CO} = \frac{K_1(1 + K_{65})[CO] - K_5K_{63}(1 + K_{31})[N_2O]}{(1 + K_{65})(K_1[CO] + 1) + K_5(1 - K_{31}K_{63})[N_2O]} \quad (2.20)$$

$$\theta_O = \frac{K_5K_{63}[N_2O]}{(1 + K_{65})K_1[CO] - K_5K_{31}K_{63}[N_2O]} \quad (2.21)$$

$$\theta_{N_2O} = \frac{\theta_{CO}\theta_O}{K_{63}} \quad (2.22)$$

The rate of CO_2 formation is given by Eq. (2.9). Unfortunately, as shown in Fig. 2.6, the CO conversion predictions from Mechanism 3 are very similar to those from Mechanism 1. This was found to occur for all sets of parameter values examined provided that model-experimental agreement concerning the location of the bifurcation points was required. Thus, the existence of an adsorbed N_2O surface species cannot resolve the model-experimental discrepancies noted in Mechanism 1.

2.4.4 Mechanism 4

As shown in the preceding, for feed CO in the range of 0.6%-2%, all three of the models predict CO conversions which are much less than the experimental observations.

Therefore it can be concluded that the classical Langmuir-Hinshelwood-Hougen-Watson (LHHW) type mechanisms which were examined cannot describe the overall reaction behavior. In a study of the O_2+CO reaction, Graham and Lynch (*22*) encountered similar problems with the classical LHHW mechanisms. They found that, in order to obtain model-experimental agreement, it was necessary to invoke a CO self-exclusion effect, which proposes that an adsorbed CO molecule excludes other CO molecules from an area equivalent to N_{CO} surface Pt atoms, where N_{CO} is slightly greater than unity. The experimental evidence for this effect is provided by the studies of Freel (*36*), Dorling and Moss (*37*) and Yao *et al.* (*38*) who have shown that the fractional saturation coverage of the adsorbed CO on small particle size (<5nm) supported platinum is less than unity. Based on these studies, the CO self-exclusion factor, N_{CO}, has a value in the range of 1.0 to 1.25 corresponding to a CO fractional saturation coverage of 0.8 to 1.0 on a highly dispersed catalyst.

The CO self-exclusion effect does not add any additional steps to a reaction mechanism, instead it modifies the mathematical form of the rate expression for CO adsorption. Graham and Lynch (*22*) showed that the rate of CO adsorption with the CO self-exclusion effect is given by:

$$r_{CO,ads} = k_1 L[CO](1 - \theta_{CO} - \theta_O)\frac{(1 - N_{CO}\theta_{CO})}{(1 - \theta_{CO})} \qquad (2.23)$$

In a classical Langmuir-Hinshelwood model (e.g. Mechanism 1) N_{CO}=1 which results in Eq. (2.23) becoming identical to the CO-adsorption term used in Eq. (2.5). Mechanism 4 consists of the same elementary steps as Mechanism 1, except that the CO self-exclusion effect has been added. For reactions (2.2) to (2.4) the steady-state balance for adsorbed oxygen is given by Eq. (2.6). However, due to the CO self-exclusion effect, the steady-state balance for adsorbed CO is modified to become:

$$k_1L[CO](1 - \theta_{CO} - \theta_O)\frac{(1 - N_{CO}\theta_{CO})}{(1 - \theta_{CO})} - k_{-1}L\theta_{CO} - k_3L^2\theta_{CO}\theta_O = 0 \qquad (2.24)$$

Equations (2.6) and (2.24) can be solved explicitly for θ_{CO} and θ_O yielding:

$$\theta_{CO} = \frac{K_1[CO] - (K_{21} + K_{23})[N_2O]}{1 + N_{CO}K_1[CO] - K_{21}[N_2O]} \qquad (2.25)$$

$$\theta_O = \frac{K_{23}[N_2O](1 + (N_{CO} - 1)K_1[CO] + K_{23}[N_2O])}{(K_1[CO] - K_{21}[N_2O]) + K_{23}[N_2O](N_{CO}K_1[CO] - K_{21}[N_2O])} \qquad (2.26)$$

It is seen that Eqs. (2.25) and (2.26) reduce to Eqs. (2.7) and (2.8), respectively, for a value of N_{CO} equal to unity. The rate of formation of CO_2 is given by Eq. (2.9). It can be seen from Fig. 2.6 that the predictions from Mechanism 4 are markedly improved relative to the first three mechanisms. The CO conversion predictions for the low-conversion branch exactly match the experimental results while maintaining agreement with the location of the bifurcation points, something which was not possible for the first three mechanisms. Of course, the CO self-exclusion effect does not significantly affect the conversion predictions in the high-conversion region because in this region the CO fractional surface coverage is very low.

A further test for Mechanism 4 is to determine if the predictive ability of the model is not limited to just the data in Fig. 2.6, but instead can be used over a wide range of experimental conditions. As shown in Figs. 2.3 and 2.4, for a constant value of the CO self-exclusion factor, N_{CO}=1.025, the conversion predictions of Mechanism 4 are in excellent agreement with the twelve sets of experimental data which span wide ranges of temperature and feed compositions. In addition, as shown in Fig. 2.5, Mechanism 4 is also able to describe the composition and temperature dependence of the bifurcation boundaries.

As given in Table 2.2, different sets of values of the rate parameters (K_1, K_{21}, K_{23}, K_{LH}) are, of course, needed for each of the four different temperatures used in the experiments. However, from Fig. 2.7 it is seen that an Arrhenius-type temperature dependency holds for each of the four rate parameters. It should be noted that, because several of the rate parameters are ratios of rate constants, it is possible to have both positive and negative slopes. Thus, except for K_{LH}, the values of E/R given in Table 2.2 are grouped terms which are not true activation energies. Assuming that CO adsorption is non-activated, the activation energy for CO desorption, E_{-1}, is calculated from E_1/R to be 41.0 kJ/mol. Similarly, the activation energy of the surface reaction between adsorbed CO and oxygen species, E_3, is calculated from E_{LH}/R to be 74.5 kJ/mol. The activation energy for the N_2O dissociation reaction, E_2, can be calculated from either the sum of E_{23}/R and E_{LH}/R or by subtracting E_1/R from E_{21}/R. The former approach yields a value of 91.2 kJ/mol while the latter gives a value of 92.7 kJ/mol. It is seen that both approaches give similar results, with the average value of E_2 being 92 kJ/mol.

Table 2.2

Temperature Dependence of Parameters for Mechanism 4

Parameter	461 K	480 K	499 K	520 K	E/R
K_1	2550	1725	1200	750	-4,931
K_{21}	0.8	1.35	2.2	3.7	6,215
K_{23}	5.4	6.6	8.0	8.8	2,029
K_{LH}	1.652×10^{-7}	3.579×10^{-7}	6.538×10^{-7}	15.5×10^{-7}	8,951
N_{CO}	1.025	1.025	1.025	1.025	

The above values of activation energies obtained from estimating the parameters

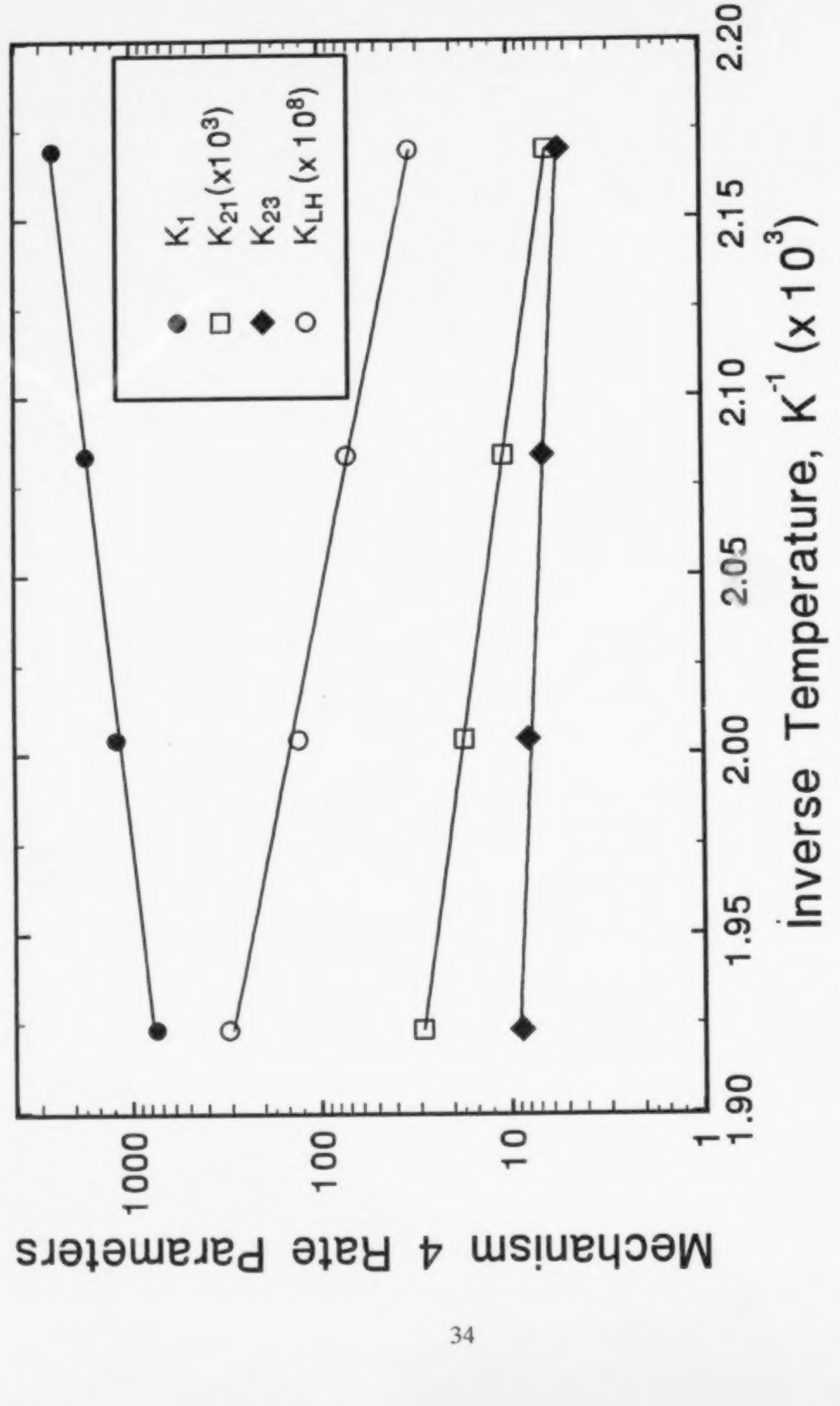

Figure 2.7 Arrhenius-Type Plot of Parameters for Mechanism 4.

for Mechanism 4 can be compared with the values obtained from other studies. Mechanism 4 predicts that the CO fractional surface coverage is close to its saturation value of $1/N_{CO}$ in the region of high %CO in the feed (the low conversion region) and drops sharply to a very low value ($\theta_{CO} < 0.1$) when the feed %CO is decreased below the low-to-high bifurcation point (the high conversion region). The apparently low value (41 kJ/mol) of the CO desorption activation energy, E_{-1}, which is needed to describe the experimental data can be attributed to the existence of a CO saturated surface when the CO conversion is low. Ertl *et al.* (*39*), using a combination of TPD, LEED and work function measurements, reported that the activation energy of CO on Pt(111) declined with CO surface coverage. They reported that the activation energy of adsorption decreases linearly from 138 kJ/mol at $\theta_{CO} \approx 0$ to 113 kJ/mol at $\theta_{CO} = 0.5$, at which point a sharp decrease to 92 kJ/mol occurred, followed by a rapid decrease in E_{-1} for $\theta_{CO} > 0.6$. They derived an isosteric heat of adsorption of approximately 54 kJ/mol at $\theta_{CO} = 0.7$ from LEED data. Seebauer *et al.* (*40*) also reported a similar coverage dependence for the heat of adsorption of CO on Pt(111) using laser induced thermal desorption measurements. They found that the heat of adsorption of 134 kJ/mol at low coverage declined rapidly with surface coverage to a low value of 42 kJ/mol at near saturation coverage of $\theta_{CO} >$ 0.6. The pre-exponential factor of CO desorption was also reported to have a low value of $3\text{x}10^7$ for a CO saturated surface. The value of E_{-1} of 41.0 kJ/mol used in this study to describe the experimental data is thus seen to be close to the values of 54 kJ/mol and 42 kJ/mol reported by Ertl *et al.* (*39*) and Seebauer *et al.* (*40*), respectively, for CO saturated Pt(111) surface.

In an extensive review of CO oxidation over platinum, Engel and Ertl (*30*) reported that the value of the activation energy of the LH reaction between adsorbed CO and the adsorbed oxygen, E_3, has been found from several studies to be in the range of 33 to 96 kJ/mol, although they contend that a value of 33 kJ/mol may not be justified. Several studies (*22, 24, 41-43*) have used values of 40 to 80 kJ/mol for E_3 to describe CO oxidation on platinum. The value of E_3=74.5 kJ/mol used in this study falls in the range of values from these other studies. Although the value of the activation energy for gaseous N_2O dissociation on Pt, E_2, is not readily available from prior experimental studies reported in the literature, values of 146 kJ/mol (*33*) and 75 kJ/mol (*17*) have been used in modelling studies for the activation energy of dissociation of adsorbed N_2O as compared with a value of E_2=92 kJ/mol used in this study.

As shown in Figs. 2.3 to 2.6, Mechanism 4 can provide an excellent description of the experimental observations. However, some caution must still be exercised because it is found that several quite dissimilar sets of values can all produce similar descriptions of the data. This difficulty has previously been noticed by Graham and Lynch (*22*) and can be resolved by using both dynamic and steady-state data when estimating parameter values. Thus, while it was not possible to change an individual parameter value from that given in Table 2.2 without producing an increased model-experimental discrepancy, it nevertheless is possible to maintain excellent model-experimental agreement by making simultaneous adjustments to several (or all) of the parameter values. This is shown in Table 2.3 where three alternative sets of parameter values (Cases I to III) are given which produce very similar (essentially identical) model predictions compared to the base case parameters. As can be seen from Table 2.3, the low values of CO desorption energy, E_{-1}, and pre-exponential factor, k_{-1}^o, are consistent with the model prediction of the surface being saturated with CO in the low CO conversion region. The model predictions for the high conversion region (with low %CO in the feed) show that the fractional coverage is less than 0.4.

To examine further the effect of the coverage dependence of the CO desorption activation on the model predictions, a step change in the CO adsorption and desorption rate constants was incorporated in the model. With this modification the CO conversion was calculated using the parameters listed in Table 2.2 while decreasing the feed %CO, and a step change in the values of E_{-1}, k_{-1}^o and S_{CO} to 134 kJ/mol, 10^{15} s^{-1} and 0.6, respectively was made at the low-to-high bifurcation point. The predictions from the modified model are shown in Fig 2.8. As can be seen from Fig. 2.8, the CO conversions in the high conversion region are in excellent agreement with the experimental data.

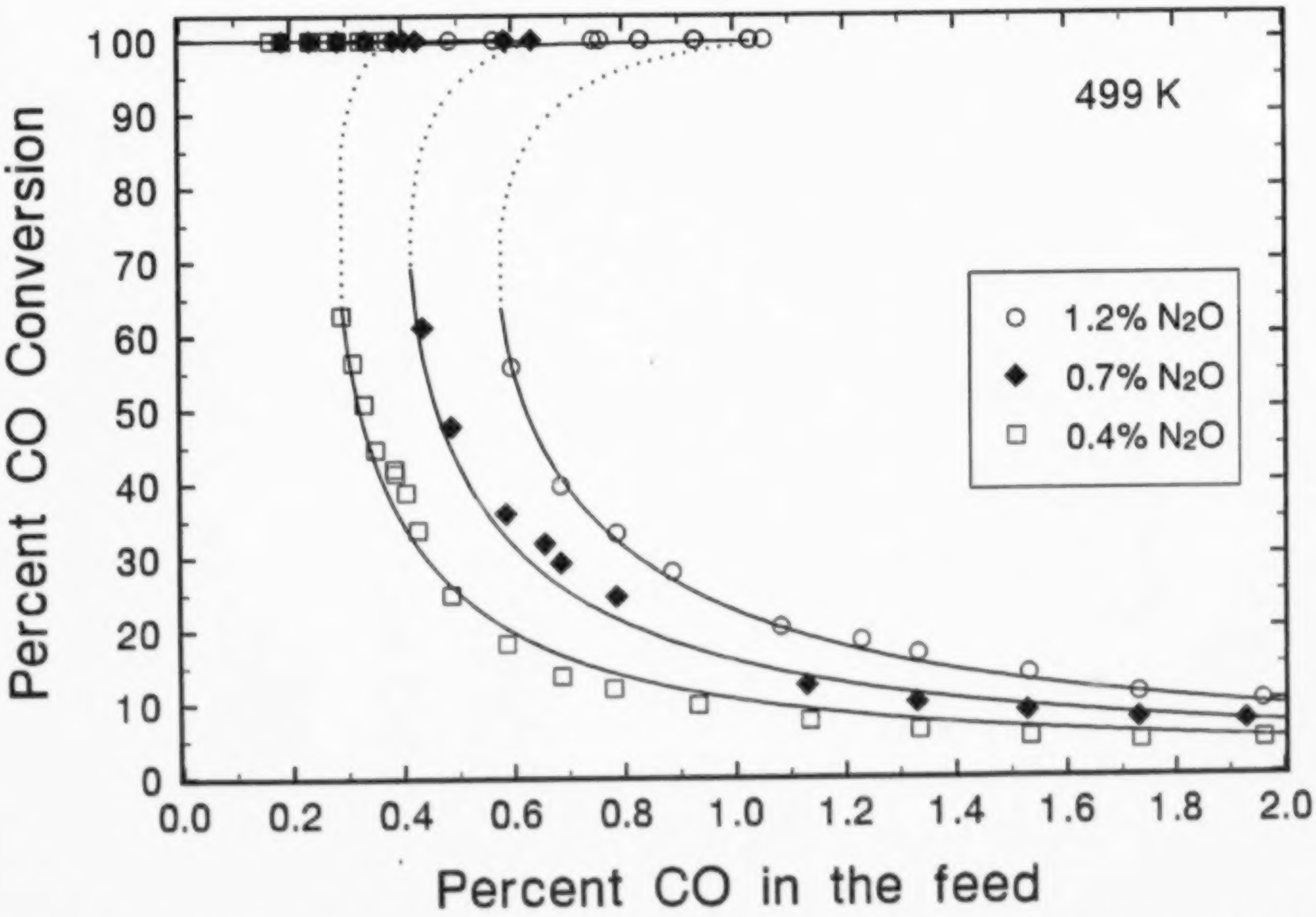

Figure 2.8 Predictions from Mechanism 4 at 499 K with Coverage Dependent Adsorption and Desorption Rate Constants.

However, because the parameters K_1 and K_{23} are coverage dependent, the rate expression is not explicit in terms of gas phase concentrations of CO and N_2O.

Table 2.3

Sets of Kinetic Parameters for Mechanism 4 which Give Similar Predictions

Parameter	Base Case	Case I	Case II	Case III
K_1 (499 K)	1200	900	1100	960
K_{21} (499 K)	0.0173	0.012	0.0123	0.0123
K_{23} (499 K)	8	7.85	4	8
K_{LH} (499 K)	$1.308\text{x}10^{-6}$	$1.3\text{x}10^{-6}$	$1.0\text{x}10^{-6}$	$1.27\text{x}10^{-6}$
N_{CO}	1.025	1.02	1.0275	1.025
E_{-1}	41.0	49.8	39.7	51.0
E_2	92.0	79.1	85.8	78.7
E_3	74.5	65.7	75.3	65.7
k_{-1}^o	$1.305\text{x}10^6$	$1.513\text{x}10^7$	$8.16\text{x}10^5$	$1.847\text{x}10^7$
k_2^o	$4.902\text{x}10^9$	$2.013\text{x}10^8$	$4.669\text{x}10^8$	$1.857\text{x}10^8$
k_3^o	$4.684\text{x}10^{11}$	$5.185\text{x}10^{10}$	$4.381\text{x}10^{11}$	$5.093\text{x}10^{10}$
S_{CO}	0.01	0.01	0.01	0.01

The rate of CO_2 formation is given by Eq. (2.9), where the fractional surface coverage for CO and oxygen are given by Eqs. (2.25) and (2.26), respectively. The rate expressions can be simplified in the unique low-conversion and the unique high-conversion regions. In the unique low-conversion region of Fig. 2.6, the numerical predictions indicate that the fractional surface coverage of CO is close to its saturation value which is equal to the inverse of N_{CO}. The same conclusion can be drawn from Eq. (2.25) by considering that in the unique low-conversion (high feed %CO) region, K_1[CO] is orders of magnitude greater than $K_{21}[N_2O]$ and $K_{23}[N_2O]$ and therefore Eq. (2.25) can be simplified as follows:

$$\theta_{CO} = \frac{1}{N_{CO}} \tag{2.27}$$

Similarly Eq. (2.26) can be simplified as follows:

$$\theta_{O} = \frac{K_{23}[N_2O](1 + (N_{CO} - 1)K_1[CO] + K_{23}[N_2O])}{K_1[CO](1 + K_{23}N_{CO}[N_2O])} \tag{2.28}$$

Therefore the rate of reaction for the unique low-conversion steady-state can be determined by the following equation:

$$r_{CO_2} = \frac{K_{LH}K_{23}[N_2O](1 + (N_{CO} - 1)K_1[CO] + K_{23}[N_2O])}{N_{CO}K_1[CO](1 + K_{23}N_{CO}[N_2O])} \tag{2.29}$$

In the unique high-conversion region, the numerical predictions from Mechanism 4 show that the surface is essentially covered with oxygen. Therefore, the CO self-exclusion effect does not affect the predictions in the unique high-conversion region. This can readily be seen from Fig. 2.6, where the CO conversion predictions by Mechanism 4 are very similar to those from Mechanism 1 for low feed %CO. Therefore, the rate function for the unique high-conversion region can be simplified by assuming a value of unity for the CO self-exclusion factor N_{CO}=1. The rate expression, Eq.(2.9), combined with Eqs. (2.25) and (2.26) with $N_{CO}=1$, yield:

$$r_{CO_2} = \frac{K_{LH}K_{23}[N_2O](K_1[CO] + (K_{21} + K_{23})[N_2O])}{(K_1[CO] - K_{21}[N_2O])(1 + K_1[CO] - K_{21}[N_2O])} \tag{2.30}$$

Equation (2.30), essentially, predicts the rate of CO_2 formation by Mechanism 1, where CO self-exclusion effect was not considered. The rate predictions from Eqs. (2.29) and (2.30) are compared with the experimental data at 499 K with 1.2% N_2O in the feed in

Fig. 2.9. It can be seen from Fig. 2.9 that Eqs. (29) and (30) describe the rate behavior in the unique low-conversion and the unique high-conversion region, respectively and they also describe the rate behavior for a part of the multiplicity region.

Notwithstanding the concern with respect to uniqueness of the values of the model parameters, of the four mechanisms examined herein, Mechanism 4 incorporating the CO self-exclusion effect is the only kinetic model that predicts CO conversions for the low-conversion steady-states which are as high as the values obtained experimentally. However, as seen in Fig. 2.3, in the region of high CO conversion a slight discrepancy is apparent between the model and the experimental data, particularly for very low values of %CO in the feed. As shown in Fig. 2.8, it is possible to predict CO conversions near 100% for low %CO in the feed by incorporating coverage dependent CO adsorption and desorption rate constants. It is also possible to predict CO conversions near 100% for low %CO in the feed by incorporating an oxygen self-exclusion effect in the model. Herz and Marin (*44*) have proposed the existence of such an effect in an attempt to describe the steady-state oxidation of CO by O_2 on supported platinum catalysts. In their model, the oxygen self-exclusion effect was very large, with oxygen being excluded from up to one-half of the surface (N_O=2). Lynch (*45*) used a similar oxygen self-exclusion effect to describe CO oxidation on a Pt catalyst during forced composition cycling. Incorporation of this effect into Mechanism 4 (or Mechanism 1) would modify the balance equation for surface oxygen as follows:

$$k_2 L[N_2O](1 - \theta_{CO} - \theta_O)\frac{(1 - N_O\theta_O)}{(1 - \theta_O)} - k_3 L^2\theta_O\theta_{CO} = 0 \qquad (2.31)$$

However, if the oxygen self-exclusion effect is incorporated in Mechanism 4, it is not possible to obtain an explicit rate expression in terms of CO and N_2O concentrations. Therefore, the effect of oxygen self-exclusion was tested on Mechanism 1. From the solution of Eqs. (2.5), (2.10), (2.11) and (2.31) it is found that CO conversions of near 100% can be obtained for feed CO of less than 0.2% by using a very small value of

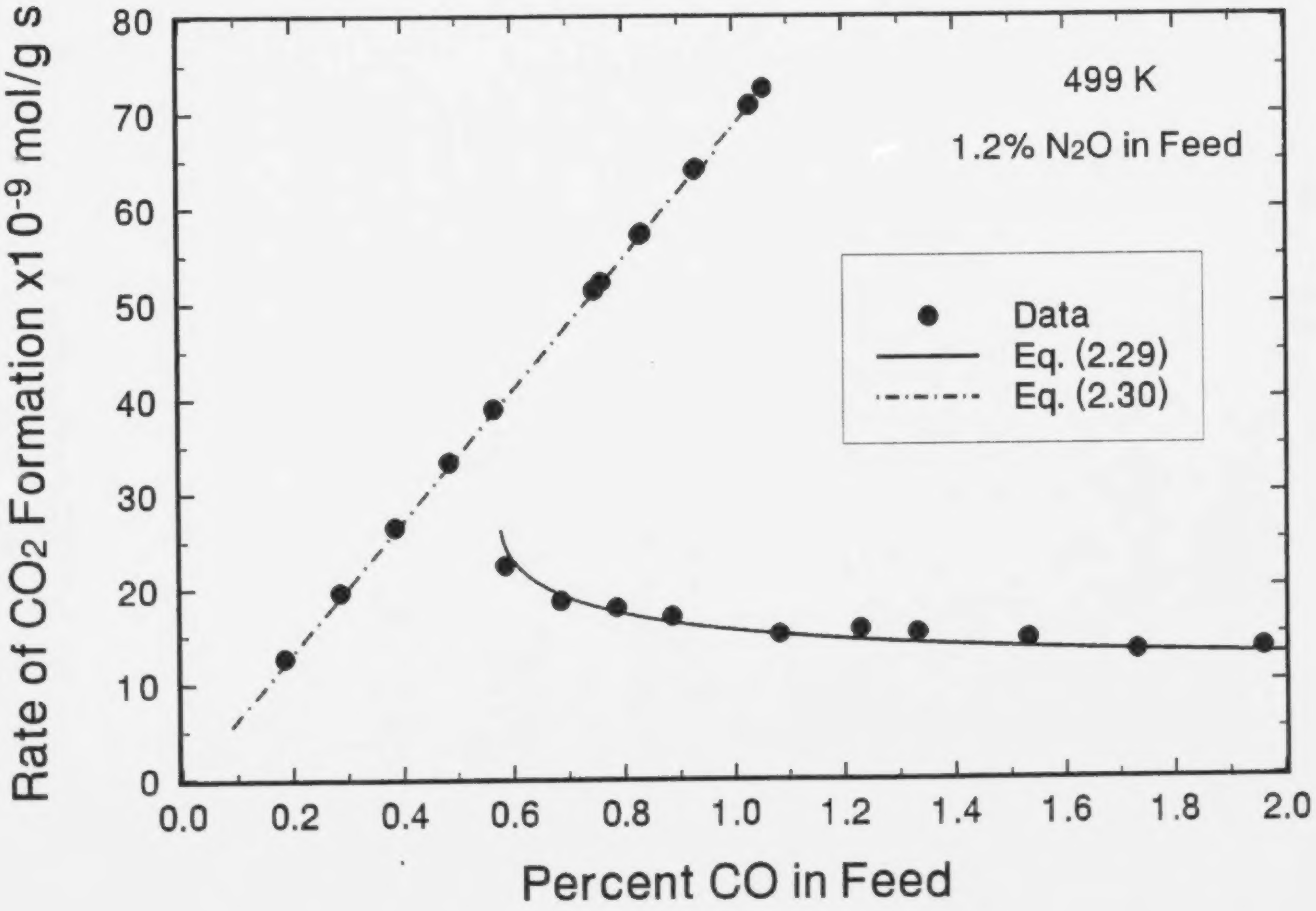

Figure 2.9 Reaction Rates in the Unique Steady-State Regions.

N_O=1.008 for the oxygen self-exclusion factor.

2.5 Conclusions

The N_2O+CO reaction over an alumina-supported platinum catalyst exhibits steady-state multiplicity in the temperature range of 461-520 K. To our knowledge, this is the first report of steady-state multiplicity for the N_2O+CO reaction. The effects of temperature and feed composition on the bifurcation boundaries have been determined. The bifurcation points shift in the direction of increasing feed %CO with increasing temperature and increasing %N_2O in the feed.

All of the four kinetic models examined in this study were able to predict the existence of reaction rate multiplicity. However, for high values of %CO in the feed, only a model based on a CO self-exclusion effect could quantitatively describe both the bifurcation point locations as well as predict CO conversions which were in agreement with the experimental observations. The same conclusion has previously been reached by Graham and Lynch (*22*) from an examination of several possible mechanisms for the O_2+CO reaction on a supported platinum catalyst. The proposed mechanism consists of several elementary steps, namely, the reversible adsorption of CO, the irreversible dissociative adsorption of N_2O to form gaseous N_2 and adsorbed atomic oxygen, and the surface reaction between adsorbed CO and adsorbed atomic oxygen to form gaseous CO_2. The CO self-exclusion effect allows N_2O to adsorb on a CO saturated surface and, therefore, the predicted CO conversions for high %CO in the feed are as high as the experimental values. Complete model-experimental agreement in the high-conversion region required either incorporation of a coverage dependent CO desorption activation energy or the use of an oxygen self-exclusion effect.

2.6 Notation

a	total Pt surface area of supported catalyst, 9.4 m^2

$[CO]$	reactor CO concentration, mol/m^3
$[CO]_o$	feed CO concentration, mol/m^3
C_S	gas-phase concentration of CO at catalyst particle surface, mol/cm^3
D_{eff}	effective diffusion coefficient for CO into an alumina pellet with a BET surface area of 109 m^2/g and an average pore size of 3 nm, $2.3\text{x}10^{-3}$ cm^2/s at 499 K
E_{LH}/R	slope of Arrhenius-type curve for model parameter K_{LH}, K
E_1/R	slope of Arrhenius-type curve for model parameter K_1, K
E_{-1}	activation energy for CO desorption, kJ/mol
E_2	activation energy for N_2O dissociation, kJ/mol
E_3	activation energy for surface reaction, kJ/mol
E_{21}/R	slope of Arrhenius-type curve for model parameter K_{21}, K
E_{23}/R	slope Arrhenius-type curve for model parameter K_{23}, K
k_1	CO adsorption rate constant, $6.87 S_{CO}\sqrt{T}/L$ m^3/mol·s
k_{-1}	CO desorption rate constant, $k^o_{-1}\exp(-E_{-1}/RT)$, s^{-1}
k^o_{-1}	CO desorption pre-exponential factor, s^{-1}
k_2	N_2O dissociation rate constant, $k^o_2\exp(-E_2/RT)$, m^3/mol·s
k^o_2	N_2O dissociation pre-exponential factor, m^3/s·mol
k_3	surface reaction rate constant, $k^o_3\exp(-E_3/RT)$, m^2/mol·s
k_4	Eley-Rideal reaction rate constant, m^3/mol·s
k_5	N_2O adsorption rate constant, m^3/mol·s
k_{-5}	N_2O desorption rate constant, s^{-1}
k_6	N_2O-M dissociation rate constant, s^{-1}
K_1	ratio of CO adsorption to desorption rate constants, (k_1/k_{-1}), m^3/mol
K_{21}	ratio of N_2O decomposition to CO desorption rate constants, (k_2/k_{-1}), m^3/mol
K_{23}	ratio of N_2O decomposition to surface reaction rate constants, (k_2/k_3L), m^3/mol
K_{31}	ratio of surface reaction to CO desorption rate constants, (k_3L/k_{-1})

K_{43}	ratio of Eley-Rideal to surface reaction rate constants, (k_4/k_3L), m^3/mol
K_5	ratio of N_2O adsorption to desorption rate constants, (k_5/k_{-5}), m^3/mol
K_{63}	ratio of N_2O-M decomposition to surface reaction rate constants, (k_6/k_3L), m^3/mol
K_{65}	ratio of N_2O-M decomposition to N_2O desorption rate constants, (k_6/k_{-5})
K_{LH}	surface reaction rate parameter, (ak_3L^2/W), mol/g·s
L	adsorption capacity of platinum surface, $2x10^{-5}$ mol/m^2
M	vacant site on platinum surface
$M\text{-}CO$	adsorbed CO species on catalyst surface
$M\text{-}N_2O$	adsorbed N_2O species on catalyst surface
$M\text{-}O$	adsorbed oxygen species on catalyst surface
N_{CO}	CO self-exclusion factor
N_O	oxygen self-exclusion factor
$[N_2O]$	reactor N_2O concentration, mol/m^3
$[N_2O]_o$	feed N_2O concentration, mol/m^3
Q	total feed flow rate to the reactor at reactor conditions, $1.11x10^{-8}T$, m^3/s
$-r_{CO}$	observed reaction rate based on catalyst volume, $mol/s{\cdot}cm^3$
$-r_{CO,ads}$	rate of CO adsorption, $mol/m^2{\cdot}s$
r_{CO_2}	rate of CO_2 formation, mol/g·s
r_p	radius of catalyst particle, (3xvolume/surface area), 0.15 cm
S_{CO}	CO sticking probability on platinum catalyst surface
T	reactor temperature, K
W	mass of catalyst, 20 g

Greek Letters

θ_{CO}	fractional CO surface coverage
θ_{N_2O}	fractional N_2O surface coverage
θ_O	fractional oxygen surface coverage

ϕ_S Thiele modulus

2.7 References

1. Bolten, H., Hahn, T., LeRoux, J. and Lintz, H.G., *Surf. Sci.* **160**, L529-L532 (1985).
2. Schwartz, S.B. and Schmidt, L.D., *Surf. Sci.* **206**, 169-186 (1988).
3. Adlhoch, W. and Lintz, H.G., *Z. Phys. Chem., Neue Folge* **103**, 207-211 (1976).
4. Adlhoch, W., Lintz, H.G. and Weisker, T., *Surf. Sci.* **103**, 576-585 (1981).
5. Lesley, M.W. and Schmidt, L.D., *Surf. Sci.* **155**, 215-240 (1985).
6. Schwartz, S.B. and Schmidt, L.D., *Surf. Sci.* **183**, L269-L277 (1987).
7. Schüth, F. and Wicke, E., in "Instationary Processes and Dynamic Experimental Methods in Catalysis, Electrochemistry and Corrosion", (G. Sandstede and G. Kreysa, Eds.), Dechema Monogr. Vol. 120, p. 429-441 (1989).
8. Imbhil, R., Fink, Th. and Krisher, K., *J. Chem. Phys.* **96**, 6236-6248 (1992).
9. Shelef, M. and Otto, K., *J. Catal.* **10**, 408-412 (1968).
10. Lambert, R.M. and Comrie, C.M., *Surf. Sci.* **46**, 61-80 (1974).
11. Adlhoch, W. and Lintz, H.G., *Surf. Sci.* **78**, 58-68 (1978).
12. Lorimer, D. and Bell, A.T., *J. Catal.* **59**, 223-238 (1979).
13. Hecker, W.C. and Bell, A.T., *J. Catal.* **84**, 200-215 (1983).
14. Klein, R.L., Schwartz, S. and Schmidt, L.D., *J. Phys. Chem.* **89**, 4908-4914 (1985).
15. Lim, K.J., Löffler, D.G. and Boudart, M., *J. Catal.* **100**, 158-168 (1986).
16. Cho, B.K., Shanks, B.H. and Bailey, J.E., *J. Catal.* **115**, 486-499 (1989).
17. McCabe, R.W. and Wong, C., *J. Catal.* **121**, 422-431 (1990).

18. Kudo, A., Steinberg, M., Bard, A.J., Campion, A., Fox, M.A., Mallouk, T.E., Webber, S.E. and White, J.M., *J. Catal.* **125**, 565-567 (1990).

19. Adlhoch, W., Kohler, R. and Lintz, H.G., *Z. Phys. Chem., Neue Folge* **120**, 111-118 (1980).

20. Lintz, H.G., *Surf. Sci.* **108**, L486-L489 (1981).

21. Cho, B.K., *J. Catal.* **138**, 255-266 (1992).

22. Graham, W.R.C. and Lynch, D.T., *AIChE J.* **33**, 792-800 (1987).

23. Lynch, D.T. and Wanke, S.E., *J. Catal.* **88**, 333-344 (1984).

24. Graham, W.R.C. and Lynch, D.T., *AIChE J.* **36**, 1796-1806 (1990).

25. Lynch, D.T. and Walters, N.P., *Chem. Eng. Sci.* **45**, 1089-1096 (1990).

26. Matsuura, T. and Kato, M., *Chem. Eng. Sci.* **22**, 171-184 (1967).

27. Eigenberger, G., *Chem. Eng. Sci.* **33**, 1255-1261 (1978).

28. Satterfield, C.N., "Heterogeneous Catalysis in Practice", p. 349, McGraw-Hill, New York (1980).

29. Smith, T.G., Zahradnik, J and Carberry, J.J., *Chem. Eng. Sci.* **30**, 763-767 (1975).

30. Engel, T. and Ertl, G., *Adv. in Catal.* **28**, 1-78 (1979).

31. Lintz, H.G. and Riekert, L., *J. Catal.* **88**, 244-245 (1984).

32. Alnot, M., Cassuto, A., Fussy, J. and Pentenero, A., *Jpn. J. Appl. Phys.*, Suppl. 2, Part 2, 79-84 (1974).

33. Takoudis, C.G. and Schmidt, L.D., *J. Catal.* **80**, 274-279 (1983).

34. Schmidt, L.D., Hansenberg, D., Schwartz, S. and Papapolymerou, G.A., in "Catalyst Characterization Science - Surface and Solid State Chemistry", ACS Symposium

Series 288, (M.L. Deviney and J.L. Gland, Eds.), p. 177-184 (1985).

35. The Math Works Inc., "The Student Edition of MATLAB - for MS-DOS Personal Computers", p. 394, Prentice-Hall, Engelwood Cliff, NJ (1992).

36. Freel, J., *J. Catal.* **25**, 149-160 (1972).

37. Dorling, T.A. and Moss, R.L., *J. Catal.* **7**, 378-385, (1967).

38. Yao, H.C., Sieg, M. and Plummer, H.K., *J. Catal.* **59**, 365-374 (1979).

39. Ertl, G., Neumann, M. and Streit, K.M, *Surf. Sci.* **64**, 393-410 (1977).

40. Seebauer, E.G., Kong, A.C.F. and Schmidt, L.D., *Surf. Sci.* **176**, 134-156 (1986).

41. Lynch, D.T., Emig, G. and Wanke, S.E., *J. Catal.* **97**, 456-468 (1986).

42. Kurtanjek, Ź. and Froment, G.F., *Chem. Eng. Sci.* **40**, 3189-3201 (1991).

43. Sales, B.C., Turner, J.E. and Maple, M.B., *Surf. Sci.* **114**, 381-394 (1982).

44. Herz, R.K. and Marin, S.P., *J. Catal.* **65**, 281-296 (1980).

45. Lynch, D.T., *Can. J. Chem. Eng.* **62**, 691-698 (1984).

3. N_2O REDUCTION BY CO:
FORCED COMPOSITION CYCLING [**]

3.1 Introduction

The reduction of nitrous oxide (N_2O) by carbon monoxide (CO) over noble metal catalysts is an important reaction during the reduction of nitric oxide by carbon monoxide in automobile catalytic converters (*1-3*). In an earlier study (*4*), described in Chapter 2, the steady-state multiplicity behavior of the N_2O+CO reaction over an alumina-supported Pt catalyst was used in discriminating among several rival mechanisms. Four kinetic models were examined and it was found that only a model based on CO self-exclusion from the platinum catalyst was able to describe all of the observed behavior. However, several dissimilar sets of values of kinetic parameters produced similar model predictions, which were all in excellent agreement with the experimental data. To resolve such questions concerning kinetic models, a variety of transient response techniques have been employed. Kobayashi (*5*) used step changes in the feed concentration of CO and N_2O to study the N_2O+CO reaction over a silver catalyst. From the transient response curves of CO_2 and N_2 it was possible to distinguish between the three Hougen-Watson type kinetic models which gave similar predictions for the steady-state experiments.

Graham and Lynch (*6*) used the experimental bifurcation behavior of the CO+O_2 reaction over a supported Pt catalyst to discriminate among several rival mechanisms. However, the proposed kinetic model based on a CO self-exclusion effect could not describe the complex reaction dynamics such as chaos and self-sustained oscillations. In a subsequent study (*7*), based on a transient response technique involving periodic cycling of the feed composition, a kinetic model was proposed that could describe all of the observed complex behavior of the CO+O_2 reaction including steady-state multiplicity, self-sustained oscillations and rate-enhancement during feed composition cycling.

[**] An version of this chapter has been published - Sadhankar, R.R. and Lynch, D.T., *Journal of Catalysis* **149**, 278-291 (1994).

In an extensive review of the periodic operation of catalytic reactors, Bailey (*8*) showed that the cyclic operation of catalytic reactors can lead to large improvements in reaction rate, selectivity, or both. In addition, periodic operation can be used to gain insight into the underlying reaction mechanism. The technique of square-wave cycling has been used to study both the oxidation of CO over noble metal catalysts (7, 9-17) as well as the NO+CO reaction (*1, 3*). Several of these studies (*9-12*) reported significant increases in the time-average reaction rate of the CO+O_2 reaction which could not be described by a Langmuir-Hinshelwood type reaction mechanism. Lynch (*13, 14*) used the forced composition cycling technique to explain the resonant behavior of the CO oxidation reaction over a supported Pt catalyst. Other studies (*16, 17*) have used the forced cycling technique combined with infrared spectroscopy to study the underlying mechanism of CO oxidation over supported noble metal catalysts. Cho *et al.* (*1*) studied the reduction of NO by CO over a supported Rh catalyst during symmetric and asymmetric feed cycling experiments. They reported the formation of N_2O as an important step during the CO+NO reaction. Muraki and Fujitani (*3*) studied the effect of cycle period on N_2O selectivity for the NO+CO reaction over a supported Pt catalyst using cycled feeds. Graham and Lynch (*7*) used the technique of variable phase cycling of the feed composition to study the reaction dynamics of CO oxidation over an alumina supported Pt catalyst. They observed that variation of the phase angle between the oxygen and the CO feed cycles led to an increase in time-average conversion over and above that which occurs for the out-of-phase feed cycling. The phase angle between the two feed cycles was thus identified as an important parameter in maximizing the conversion.

The technique of variable phasing of inputs during forced composition cycling was used in this study of the N_2O+CO reaction. It is found that a time-average CO conversion as high as five times the steady-state conversion can be achieved using variable-phase, forced feed cycling. The model described in Chapter 2 is found to be incapable of describing all of the observed dynamic data. This model is further improved by incorporating an additional feature, namely the adsorbate induced Pt surface-phase transition (*7, 18*) which leads to a consistent explanation of the observed dynamic behavior as well as the steady-state multiplicity behavior described in Chapter 2.

3. 2 Methods

The experiments were carried out using a recycle reactor system containing 20 g of 0.5 wt% Pt/Al_2O_3 catalyst supplied by Engelhard. The experimental equipment and the catalyst have been previously described in Chapter 2. From an earlier investigation (*7*) on a batch of a similar catalyst, the specific surface areas of the platinum catalyst and the alumina support were estimated to be 0.47 m^2/g and 104.6 m^2/g, respectively, with the CO_2 adsorption capacity of the alumina support, L_s, assumed to be 1.2×10^{-6} mol/m^2. The reactor pressure, temperature and the total feed flow to the reactor were always maintained at 103 kPa, 499 K and 185 cm^3(STP)/min., respectively. The recycle ratio at the reactor operating conditions was estimated to be 90 from the measurement of the recycle pump flow. Under these conditions, as discussed previously in Chapter 2, it has been found that the mixing in the recycle reactor closely approximates that of an ideal CSTR.

The gases used in this study were purchased from Linde and included gas mixtures of 4.99% or 10% CO in N_2, 10.01% N_2O in N_2 and prepurified N_2. The feed compositions were in the ranges of 0-2.4% N_2O and 0-2.4% CO, with nitrogen for the balance of the feed.

Four-way valves, located downstream of the mass flow controllers on the feed lines for CO and N_2O (Fig. 2.2), were used to generate square-wave composition cycles as described by Graham and Lynch (*7, 15*). The time-averaged feed composition was maintained at 1.2% N_2O and 1.2% CO for all of the experiments in this study. This was achieved by setting the desired flow-rates of CO and N_2O through the mass flow controllers and sequentially switching the downstream four-way valves between the 'vent' position and the 'feed' position for each half cycle as shown in Fig. 3.1. The square-wave cycling of the CO and N_2O feed compositions did not affect the total feed flow rate to the recycle reactor, which was always maintained at 185 cm^3 (STP)/min. by regulating the flow of make-up nitrogen. Therefore, the recycle ratio was always maintained at approximately 90 (ideal CSTR behavior), during the feed composition cycling.

At the start of every experiment, following purging of the reactor with nitrogen, N_2O was always introduced into the reactor before CO was admitted, and therefore, the N_2O feed cycle has a 'phase lead' over the CO feed cycle. The N_2O phase lead is expressed in terms of degrees considering a complete feed cycle to contain 360 degrees, as shown in Fig. 3.1, where feed cycling with N_2O phase leads of 90, 180 and 270 degrees are illustrated. The valve switching sequence and the cycle times could be controlled independently by digital signals from a microcomputer. Therefore, it was possible to achieve any cycle time and N_2O phase lead with the experimental equipment. The frequency of cycling is defined as the inverse of the cycle period. The cycling frequencies used in this study were in the range of 0.1 to 20 mHz.

A comparison of the steady-state operation with the cyclic operation (with feed composition cycling) of the reactor is presented on a phase-plane diagram in Fig. 3.2. As explained previously in Chapter 2, the multiplicity region lies in between the two bifurcation boundaries represented by the paired circle symbols. The region of unique high conversion steady-state lies to the left of the multiplicity region and the unique low-conversion steady-state occurs in the region to the right of the multiplicity region. For the steady-state operation (with non-cycled feed), the feed composition will always be stoichiometric with 1.2% N_2O and 1.2% CO, as shown by a diamond symbol in Fig. 3.2. As can be seen from Fig. 3.2, the steady-state operation leads to low-conversion. When the valves are cycled such that the N_2O phase lead is $0°$ or $360°$ (in-phase cycling), the

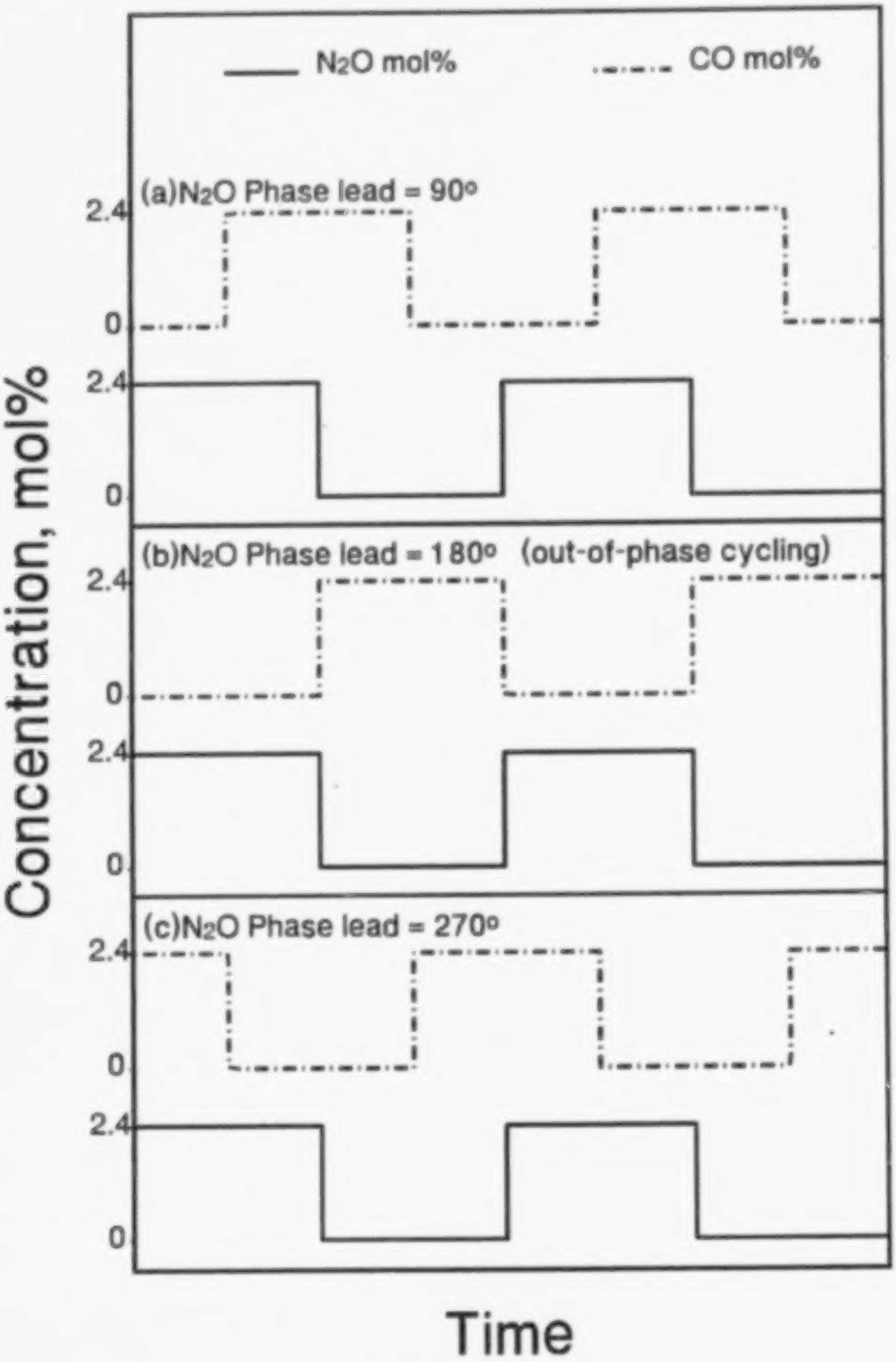

Figure 3.1 Feed Cycling Strategies

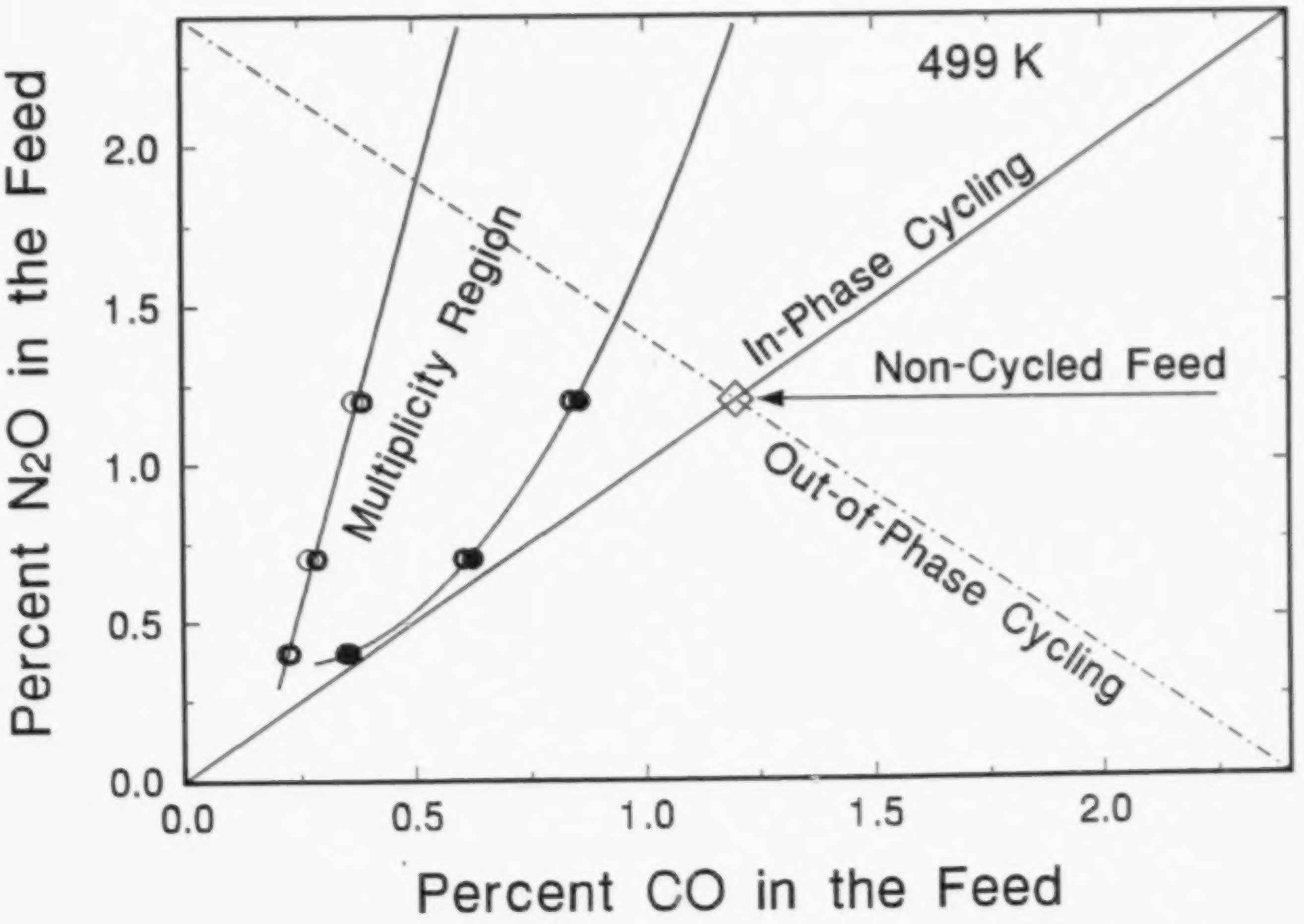

Figure 3.2 Comparison of Steady-State and Cyclic Operations

feed composition varies between (0% N_2O, 0% CO) and (2.4% N_2O, 2.4% CO) corresponding to the two end points of the solid-line diagonal. The gas-phase composition in the reactor, for in-phase cycling, is likely to be in the lower right triangle (to the right of the solid line diagonal). Therefore, the time-average conversion for the in-phase cycling will be low, as can be readily seen from Fig. 3.2. However, for the out-of-phase cycling (N_2O phase lead of 180°), the feed composition varies between the two points on the dashed-line diagonal, namely, (2.4% N_2O, 0% CO) and (0% N_2O and 2.4% CO). Therefore, the gas-phase composition in the reactor will be in the region to the left of the dashed-line diagonal, which also includes a part of the high-conversion region. Therefore, the time-average conversion during out-of-phase feed cycling will be higher than the steady-state conversion. Out of the three modes of reactor operation examined in Fig. 3.2, only the out-of-phase cycling leads to improvement in CO conversion. The effect of other values of the N_2O phase leads as well as the cycling frequencies can not be readily seen from Fig. 3.2 and these are discussed later in the chapter with respect to the experimental results.

The reactor CO_2 and N_2O concentrations were measured by Horiba infrared gas analyzers model PIR-2000 and VIA-300, respectively. The analyzers were calibrated at the beginning of each experiment using a gas mixture (2.04% CO_2 in N_2 and 2% N_2O in N_2), for the span calibration and N_2 for the zero calibration. The attainment of cycle invariance (steady-state cycling) was determined by monitoring the reactor CO_2 and N_2O responses. In general, 10 to 30 cycles were used for each experiment. A total of 306 experiments were carried out with different combinations of the cycling frequencies and the N_2O phase lead.

3.3 Results

Experiments involving feed composition cycling were carried out under isothermal conditions (499 K) with a constant total flow to the reactor so that the results could be directly compared with the results of the steady-state experiments from the earlier study

(*4*). The steady-state CO conversion at 499 K is summarized in Fig. 3.3, as a function of the feed composition. The arrows in Fig. 3.3(a) indicate the bifurcation from high-to-low and low-to-high conversion steady-states during the step-wise increase or decrease of the feed CO, respectively, when the feed N_2O is held constant at 1.2%. It can be seen from Fig. 3.3(a) that a feed composition of 1.2% CO and 1.2% N_2O is in the unique low-conversion region to the right of the multiplicity region. The steady-state CO conversion under these conditions was 20%.

In the first set of experiments, the CO and N_2O feed cycles were out-of-phase with each other, with an N_2O phase lead of 180 degrees. Therefore, the feed concentration alternated between 0% CO and 2.4% N_2O for the first half-cycle to 2.4% CO and 0% N_2O for the second half-cycle. The CO_2 response and the time-average CO conversions were determined for the out-of-phase cycling over a frequency range of 0.7 to 20 mHz. In the second part of the study, the effect of N_2O phase leads of 90 degrees and 270 degrees, respectively, on the time-average CO conversion was studied over a frequency range of 0.1 to 20 mHz. In the third part of the study, the experiments were carried out at a fixed cycling frequency and the effect of N_2O phase lead on the time-average CO conversion was studied. The experiments were repeated for five different cycling frequencies.

3.3.1 Out-of-phase cycling

The dynamic CO_2 response during out-of-phase cycling is shown by the dashed lines in Fig 3.4. At a low cycling frequency of 0.77 mHz (Fig. 3.4(a)), the CO_2 concentration increased slowly after the N_2O was switched on. At the beginning of the N_2O half-cycle, the catalyst surface is saturated with adsorbed CO from the previous CO half-cycle and gas-phase CO concentration is very close to 2.4%. Due to the lack of empty sites for N_2O dissociation, the surface reaction does not proceed to any appreciable extent. This observation is also consistent with the experimental finding that a unique low conversion steady-state was obtained for high feed CO concentrations (Fig.

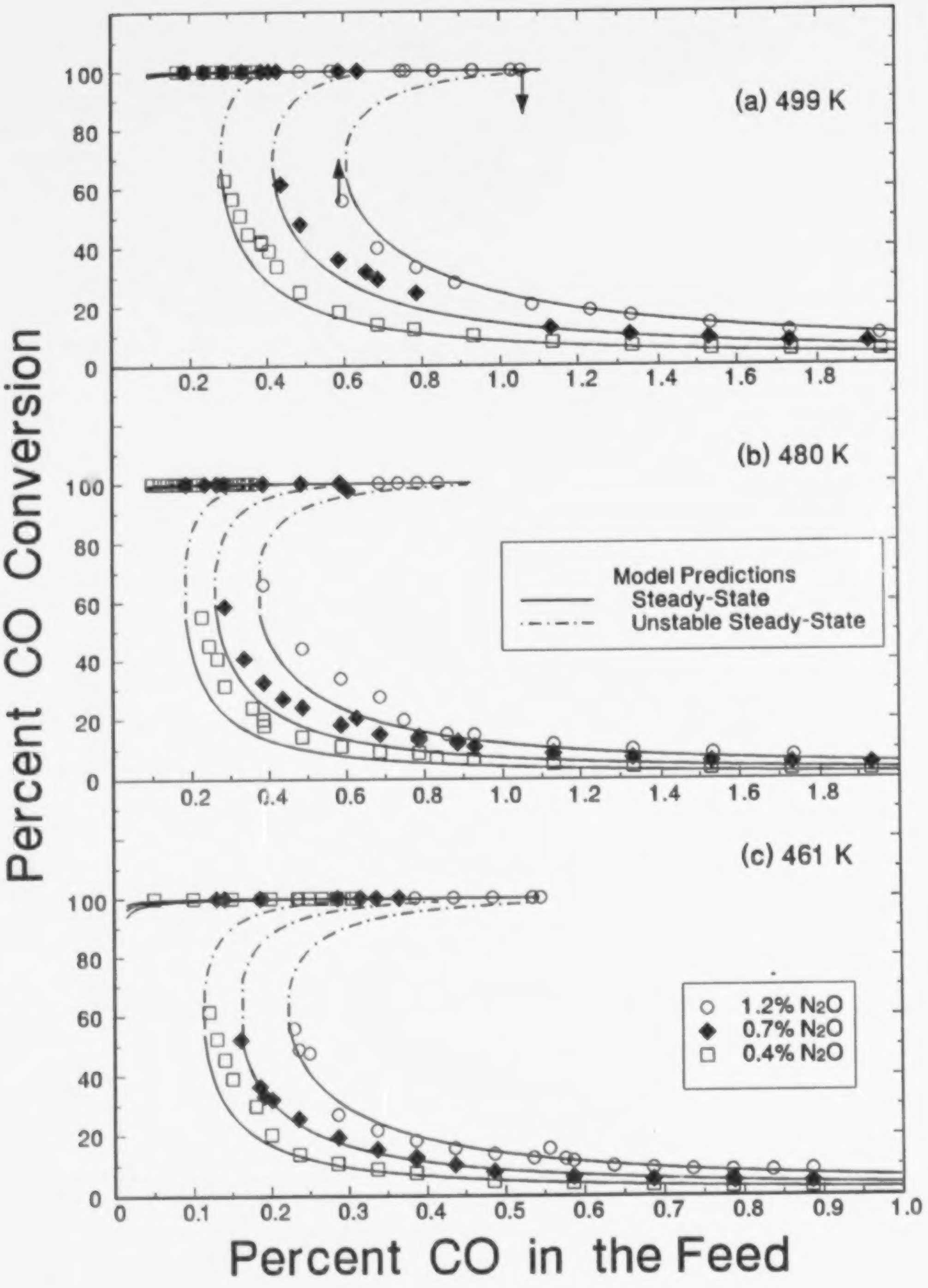

Figure 3.3 Multiplicity Behavior During the Reduction of N_2O by CO at 461 - 520 K and Predictions of Pt Surface-Phase Transition Model

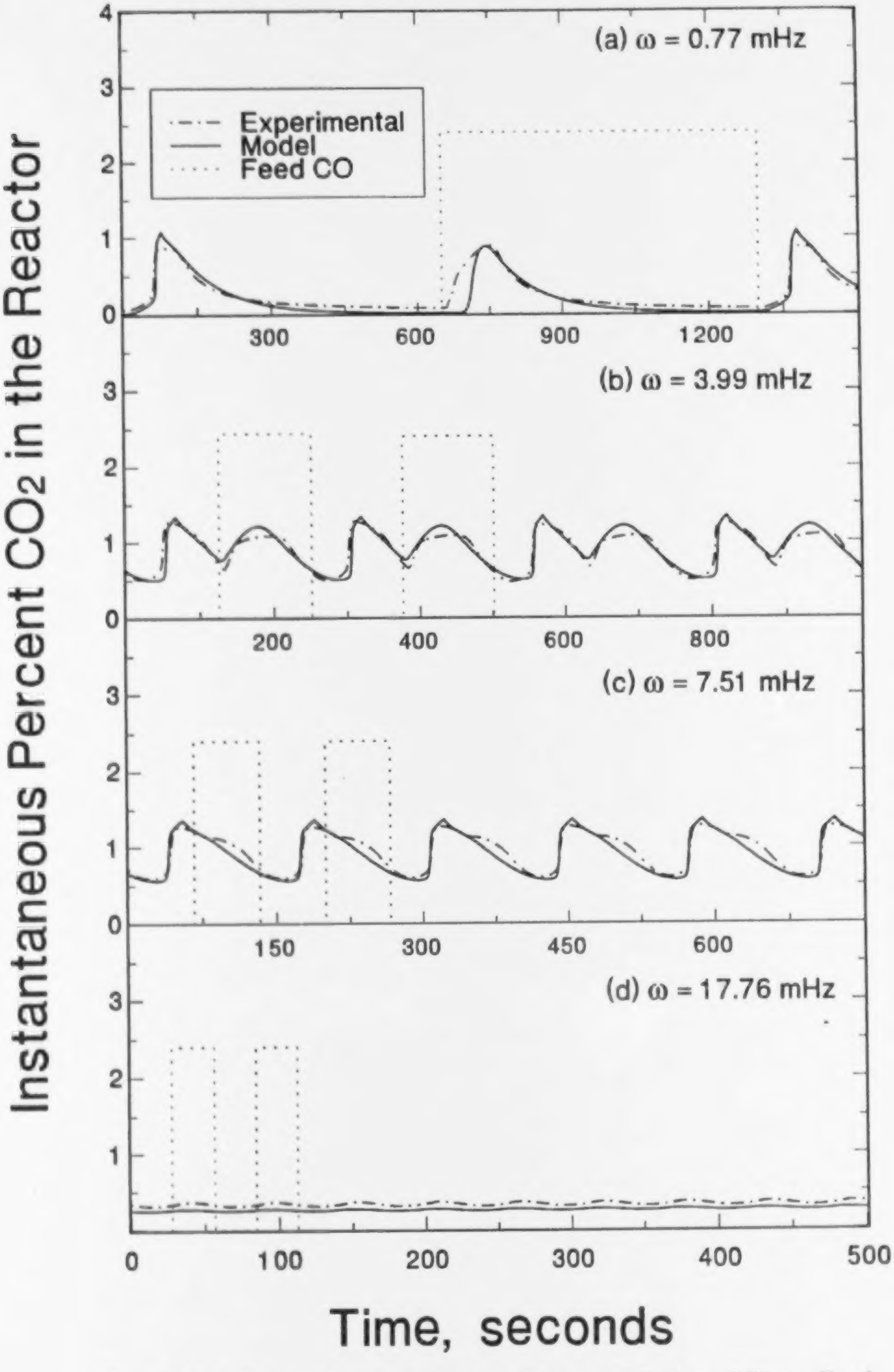

Figure 3.4 Dynamic CO_2 Response During 180° Out-of-Phase Feed Composition Cycling

3.3). As the gas-phase CO is depleted via transport out of the reactor, more active sites become available on the catalyst surface for N_2O dissociative adsorption. When sufficient active surface sites are available for N_2O dissociation, the CO_2 concentration rises rapidly and reaches a peak value. The reactor CO_2 concentration then decreases as the gas-phase CO is depleted and the adsorbed CO is removed by reaction. The catalyst surface then becomes covered with adsorbed oxygen by the end of the N_2O half-cycle.

When CO is switched on, and N_2O is switched off, the CO_2 concentration increases rapidly. The CO entering the reactor readily reacts with the adsorbed oxygen. After the gas-phase N_2O is completely depleted, the CO_2 concentration drops almost exponentially as the CO cleans the catalyst surface of the remaining adsorbed oxygen. The surface then becomes saturated with adsorbed CO by the end of the CO half-cycle. Typically, two peaks in CO_2 concentration, one in each half-cycle, were observed for frequencies lower than 5 mHz. The CO_2 response at the cycling frequency of 3.99 mHz is shown in Fig. 3.4(b). A comparison of Figs 3.4(a) and (b) shows that the time-average CO_2 concentration is higher at a frequency of 3.99 mHz as compared with that which is obtained at a frequency of 0.77 mHz. The CO_2 concentration does not fall to zero during the long cycles (Fig. 3.4(a)) because of the CO_2 desorption from the alumina support.

As the frequency is increased above 5 mHz, the two peaks in CO_2 concentration per feed cycle began to merge resulting in a single maximum per cycle as shown in Fig. 3.4(c) for a cycling frequency of 7.51 mHz. The magnitude of the CO_2 response to the feed cycling decreased as the frequency was further increased until as can be seen in Fig 3.4(d), at a cycling frequency of 17.76 mHz, the time-average CO_2 concentration was approximately equal to the steady-state value.

The time-average CO conversions for the out-of-phase cycling experiments were calculated from the CO_2 response curves and are given in Fig. 3.5. It is seen that the CO conversion increased almost linearly with increasing frequency up to 4 mHz. This can

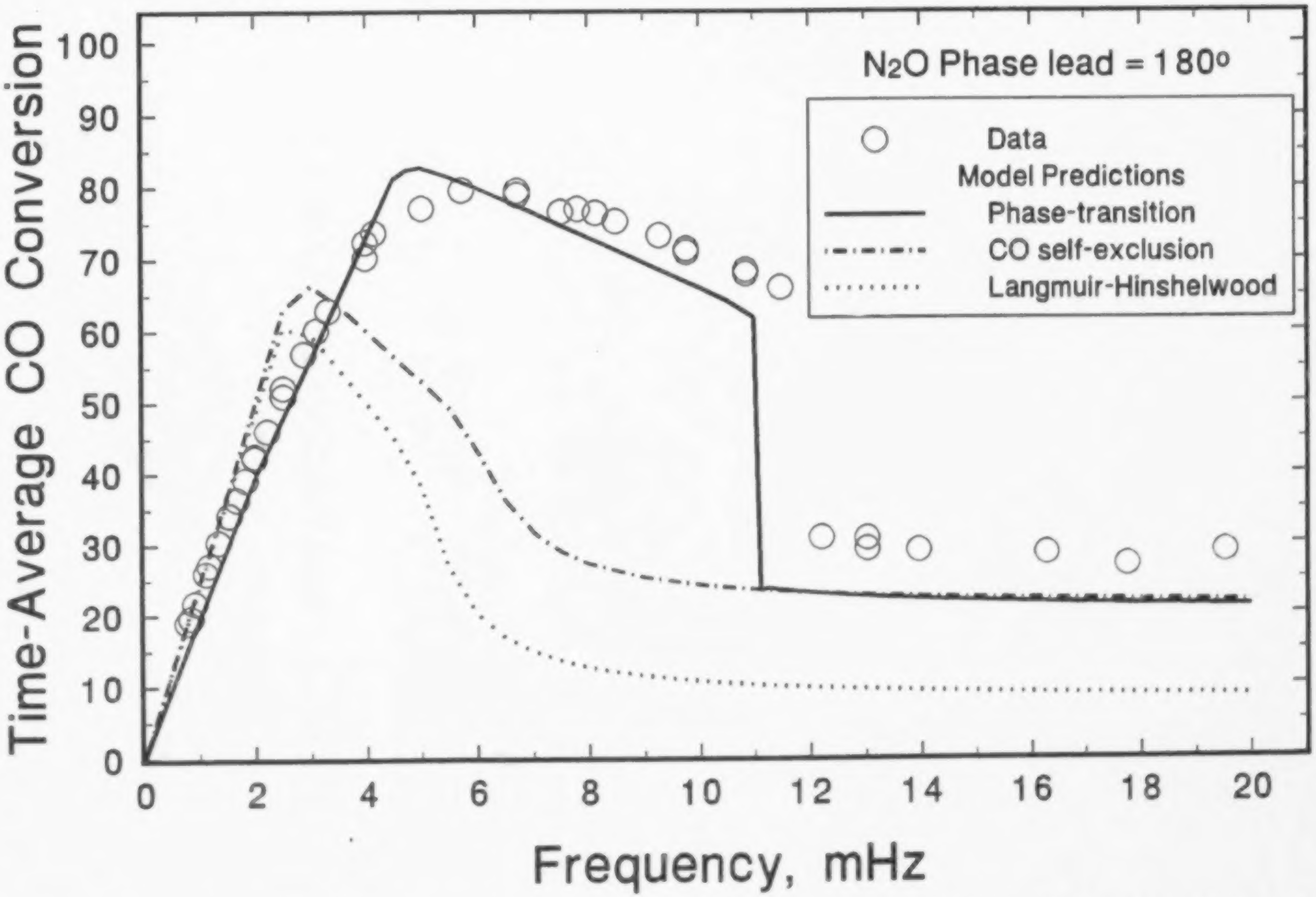

Figure 3.5 Comparison of Model Predictions to Experimental Data of Time-average Conversion for Out-of-Phase Cycling.

be explained in a manner similar to that which was used to explain the CO conversion for the CO+O_2 reaction during out-of-phase cycling by Graham and Lynch (7). At low frequencies, two peaks of CO_2 concentration per cycle (Fig. 3.4(a)) were observed and the areas under the curve for each half-cycle were approximately equal. The CO_2 production in each half-cycle can be estimated by considering the surface reaction of a monolayer of adsorbed species (CO or oxygen) plus complete reaction of one reactor volume of gas-phase species (CO or N_2O). The total CO_2 production per cycle is almost constant for all of the low frequencies. Because the CO feed per cycle is equal, CO conversion is therefore, linearly proportional to the frequency of cycling. Thus, the time-average CO conversion at low frequencies can be estimated by:

$$f_{TA}=\frac{(2a_m L_m+2V[N_2O]_o)}{Q_o[CO]_o}\,100\omega \qquad (3.1)$$

A comparison of the prediction of time-average CO conversion from equation (3.1) with the experimental data is presented in Fig. 3.6 for frequencies up to 2.5 mHz. As can be seen from Fig. 3.6, the predictions match the experimental results for frequencies lower than 1.25 mHz. However, the predicted conversion from equation (3.1) is higher than the experimental values for frequencies above 2.5 mHz due to the incomplete saturation of the surface at the higher frequencies.

As can be seen from Fig. 3.5, the highest CO conversion of 79.5% was obtained at a frequency of 6.7 mHz, and it is approximately four times the steady-state conversion. As the frequency exceeded approximately 12 mHz, the time-average CO conversion abruptly dropped to a low value of 28%. At high frequencies, the gas phase CO and N_2O concentrations are always in the region of feed compositions which give low conversion steady-states (Fig. 3.3). The gas-phase CO concentration does not decrease significantly even by the end of the N_2O half-cycle, and therefore the catalyst surface is always highly covered with adsorbed CO during high frequency feed cycling which leads to a low time-average CO conversion. The critical frequency at which a transition in the

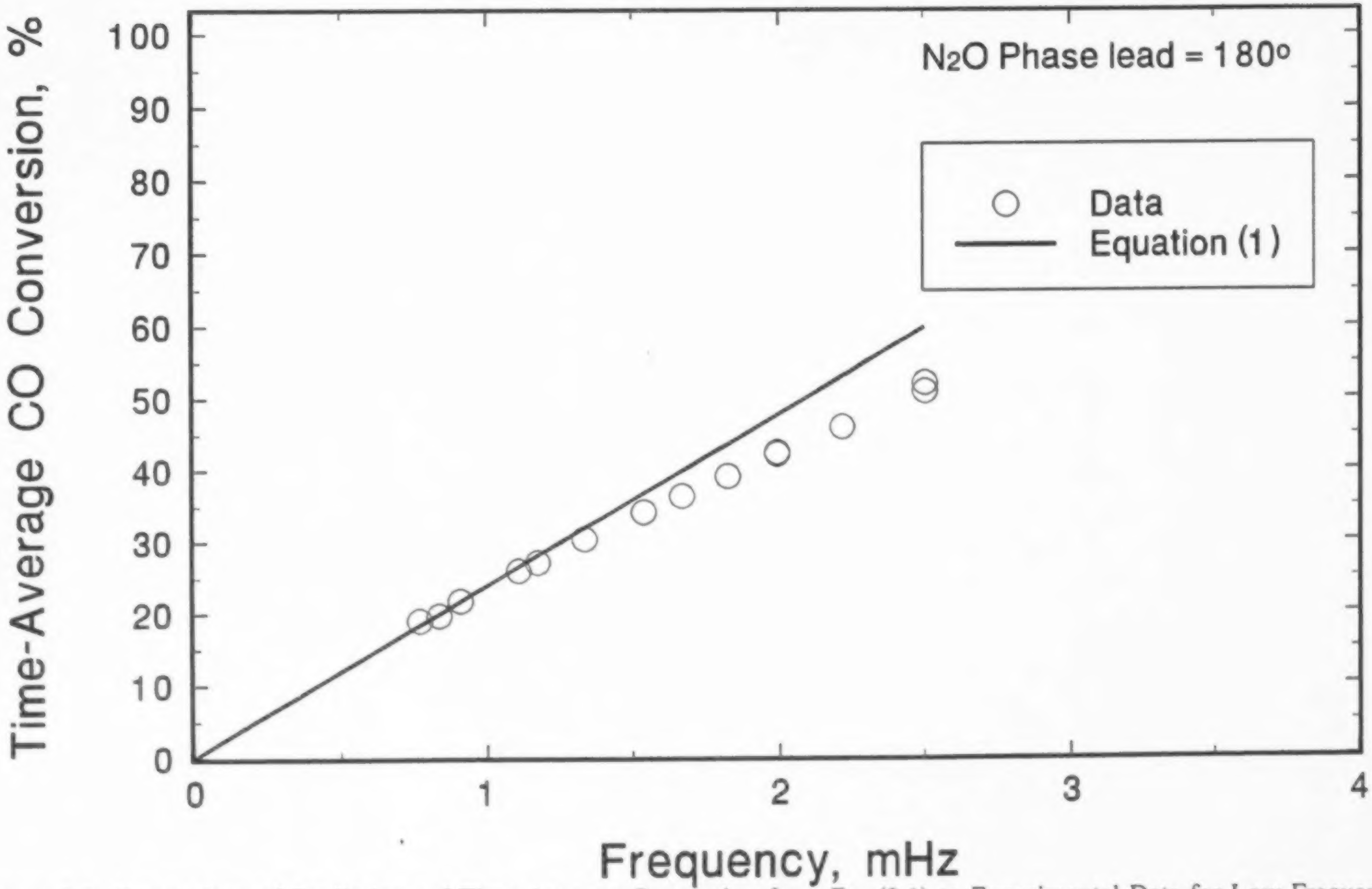

Figure 3.6 Comparison of Predictions of Time-Average Conversion from Eq. (3.1) to Experimental Data for Low Frequency Out-of-Phase Cycling.

time-average CO conversion occurs from a high value to a low value can be estimated from the steady-state bifurcation behavior of the reaction, as demonstrated elsewhere (7). The critical frequency for these out-of-phase cycling experiments lies between 11.5 and 12.2 mHz.

3.3.2 N_2O Phase leads of 90° and 270°

In the second part of the study, the experiments were carried out with N_2O phase leads of 90° and 270°, respectively, over a cycling frequency range of 0.1 to 20 mHz. The N_2O phase lead of 270° is equivalent to a CO phase lead of 90°. The time-average CO conversions are summarized in Fig. 3.7. For frequencies lower than 8 mHz, the time-average CO conversions for feed cycling with 90° N_2O phase lead were generally higher than those observed for 270° N_2O phase lead.

For the 90° N_2O phase lead cycling, the time-average CO conversion rose rapidly with increasing frequency up to 0.25 mHz. For frequencies between 0.25 and 3 mHz, the time-average CO conversion was approximately proportional to the cycling frequency. The highest time-average conversion of 93% was obtained at a frequency of 4.5 mHz, although a value of approximately 90% was found over the entire frequency range of 4 to 6.5 mHz within the accuracy of measurement. At a critical frequency of 8 mHz, the time-average CO conversion dropped abruptly from 88% to 25%.

For feed cycling with an N_2O phase lead of 270°, a linear relationship between the cycling frequency and the time-average CO conversion was observed over the frequency range of 0.2 to 2 mHz. The highest conversion of 52% was obtained at a frequency of 3.33 mHz for the feed cycling with 270° N_2O phase lead. In the critical frequency range, the conversion dropped from 36% at 8.33 mHz to 25% at 9.1 mHz. A comparison of Fig. 3.5 and Fig. 3.7 shows that the highest CO conversion for an N_2O phase lead of 180° lies between the highest CO conversions obtained for 90° (93%) and 270° (52%) N_2O phase leads, respectively.

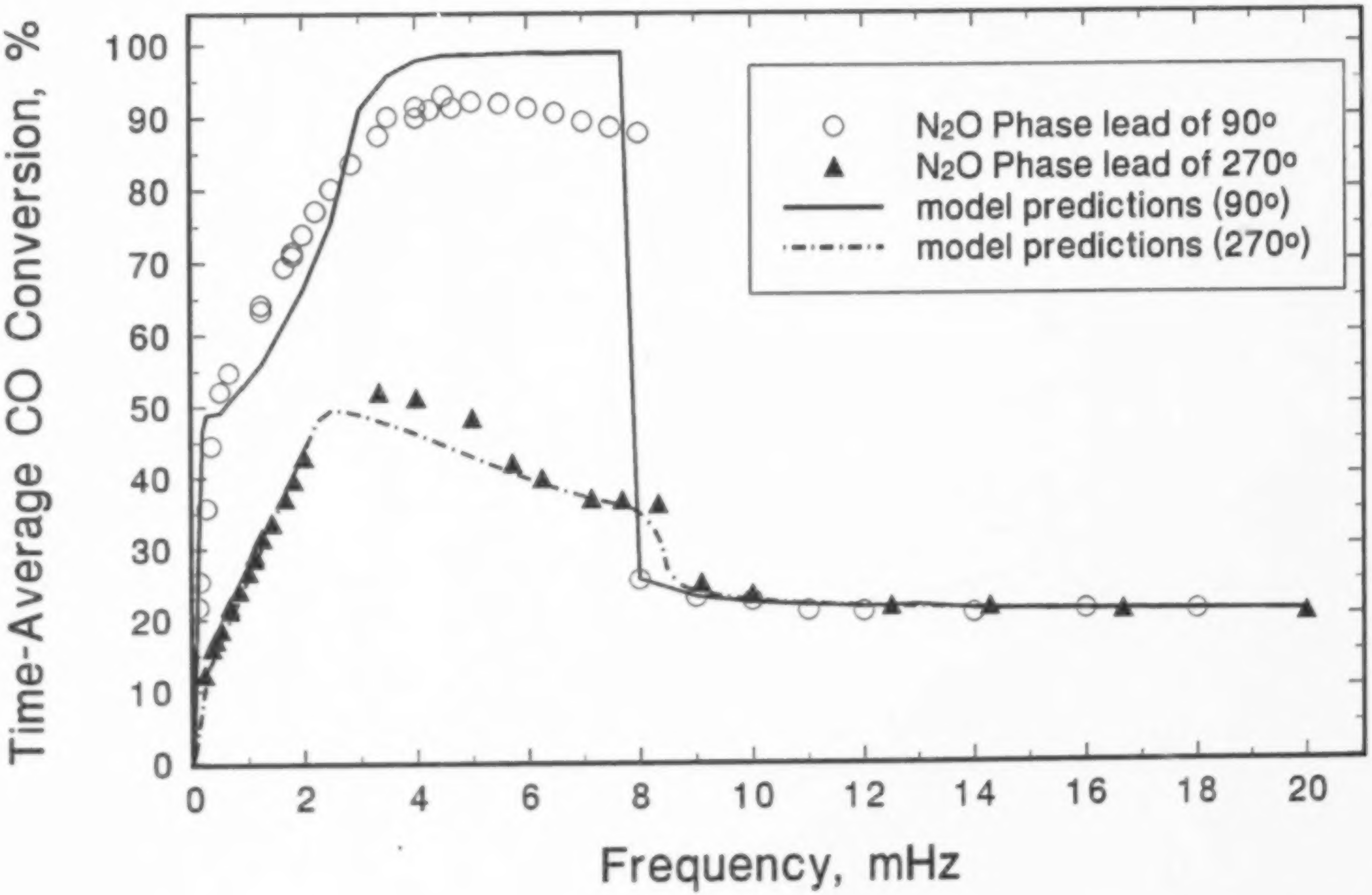

Figure 3.7 Effect of Cycling Frequency on Time-Average CO Conversion for N_2O Phase Leads of 90° and 270°.

The CO_2 response curves at a frequency of 1.25 mHz are shown by the dashed lines in Fig. 3.8 for feed cycling with N_2O phase leads of 90° and 270°, respectively. An examination of these CO_2 response curves in Fig. 3.8 provides an explanation for high CO conversions obtained for 90° N_2O phase lead cycling. A comparison of Figs. 3.8(a) and (b) shows that both the cycles can be divided into four quadrants, each with feed containing only CO, both CO and N_2O, only N_2O, and no CO or N_2O (blank feed), respectively, although the sequence of these quadrants is different for Figures 3.8(a) and 3.8(b). For 90° N_2O phase lead cycling, the feed containing only N_2O in the first quadrant removes the residual adsorbed CO from the previous blank-feed cycle and therefore the CO_2 production in the first quadrant is limited. The surface is saturated with oxygen by the end of the first quadrant. In the second quadrant of the cycle, the feed CO readily adsorbs on the surface saturated with adsorbed oxygen and a high reaction rate is obtained. Almost 50% of the total CO_2 production occurs in the second quadrant of the cycle. In the third quadrant, the feed containing only CO reacts with the residual N_2O from the previous quadrant. The reaction rate decreases as the N_2O is depleted. By the end of the third quadrant, the surface is again saturated with adsorbed CO. In the fourth quadrant, the CO_2 desorbs from the alumina support. Some of the adsorbed CO also desorbs in the fourth quadrant due to the very low partial pressure of CO in the reactor. Therefore, the CO_2 production in the first quadrant is limited due to the residual adsorbed CO.

When the feed is cycled with an N_2O phase lead of 270°, the first quadrant of the cycle has a feed containing both CO and N_2O. However, the CO_2 production is very small. This is because the catalyst surface is saturated with adsorbed CO from the previous (fourth) quadrant with CO-only feed. Therefore, for a sufficiently long cycle, the CO conversion in this quadrant will be equal to the steady-state conversion of 20%. In the second quadrant, when CO is switched off (feed containing only N_2O), the gas-phase N_2O does not readily dissociate on the CO-saturated catalyst surface. As the adsorbed CO gradually reacts, sufficient active sites become available for N_2O dissociation and the reaction rate increases rapidly as evident by a sharp CO_2 peak in this

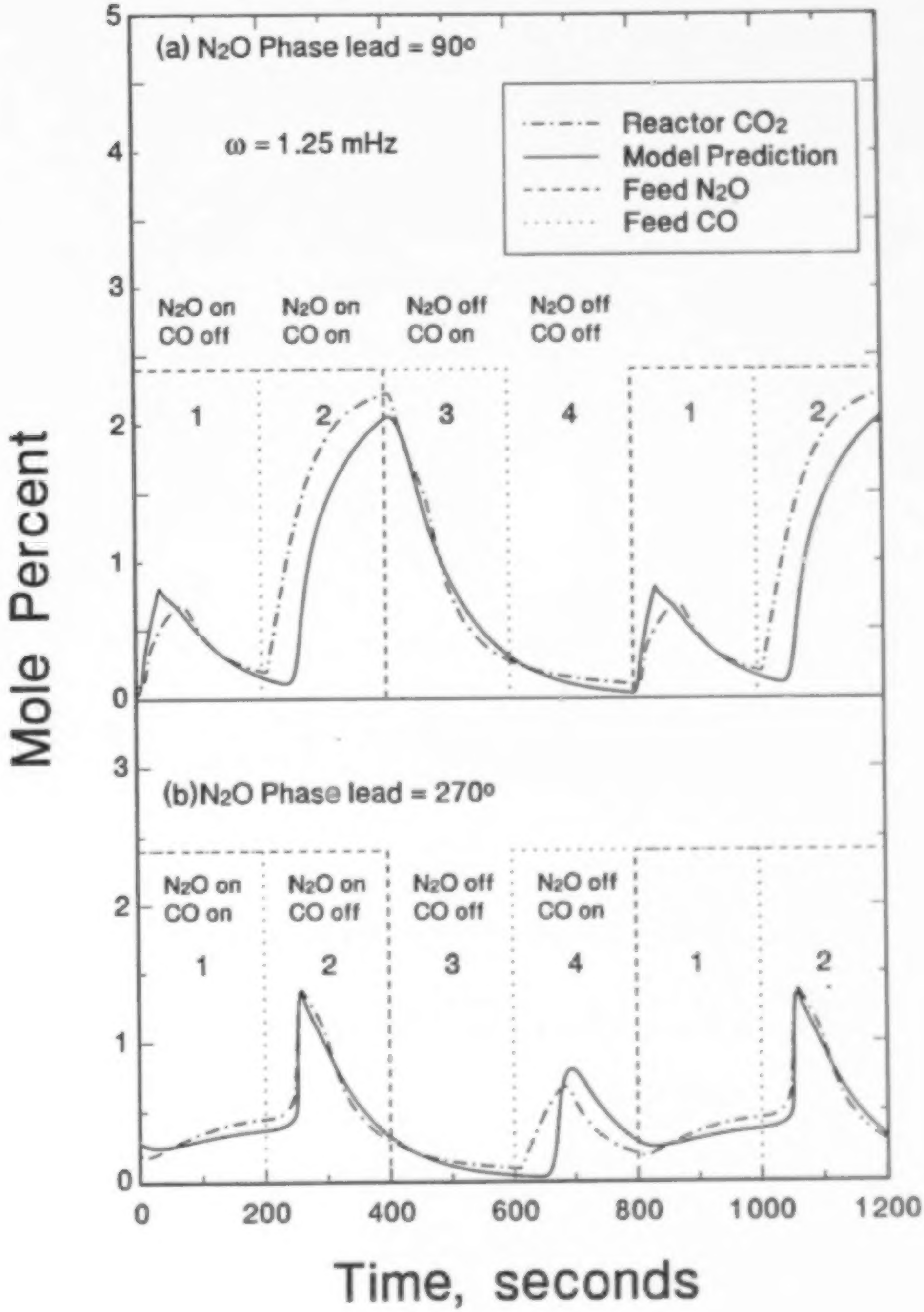

Figure 3.8 Dynamic CO_2 Response for 90° and 270° N_2O Phase-Lead.

quadrant. The catalyst surface is covered by adsorbed oxygen by the end of the second quadrant. In the third quadrant, the feed does not contain either CO or N_2O and therefore the CO_2 production is mainly due to desorption from the alumina support. In the fourth quadrant, the feed contains only CO which reacts with the residual adsorbed oxygen from the previous quadrant. The CO_2 production is limited by the amount of residual adsorbed oxygen at the beginning of the fourth quadrant.

The main difference between Figs 3.8(a) and (b) is the CO_2 production in the over-lap quadrant of the cycle with feed containing both CO and N_2O. The catalyst surface is saturated with adsorbed oxygen at the beginning of the over-lap quadrant for an N_2O phase lead of 90° and a high reaction rate is obtained. On the other hand, the catalyst surface is saturated with adsorbed CO at the beginning of the over-lap quadrant for an N_2O phase lead of 270° and this leads to a low reaction rate. A very similar phenomenon was observed at several other frequencies over the range of 0 to 7.7 mHz. It can therefore be generalized that, for frequencies lower than the critical frequency, the time-average CO conversion will be higher for N_2O phase leads of less than 180°, as compared with that which is obtained with N_2O phase leads of greater than 180°.

3.3.3 Variable Phasing of Inputs

In the earlier experiments, the effect of cycling frequency on the time-average CO conversion was studied for three values of N_2O phase lead of 90°, 180°, and 270°, respectively. To determine the effect of phase-angle on the time-average conversion, the experiments were carried out by varying the N_2O phase lead between 0° and 360° while holding the cycling frequency constant. The results of the experiments carried out at five different frequencies are summarized in Fig. 3.9.

At a low frequency of 2 mHz (Fig. 3.9(a)), the time-average CO conversion increased rapidly with increasing N_2O phase lead between 10° and 40°. The highest CO conversion of 93.5% was obtained at 40° phase lead. The time-average CO conversion

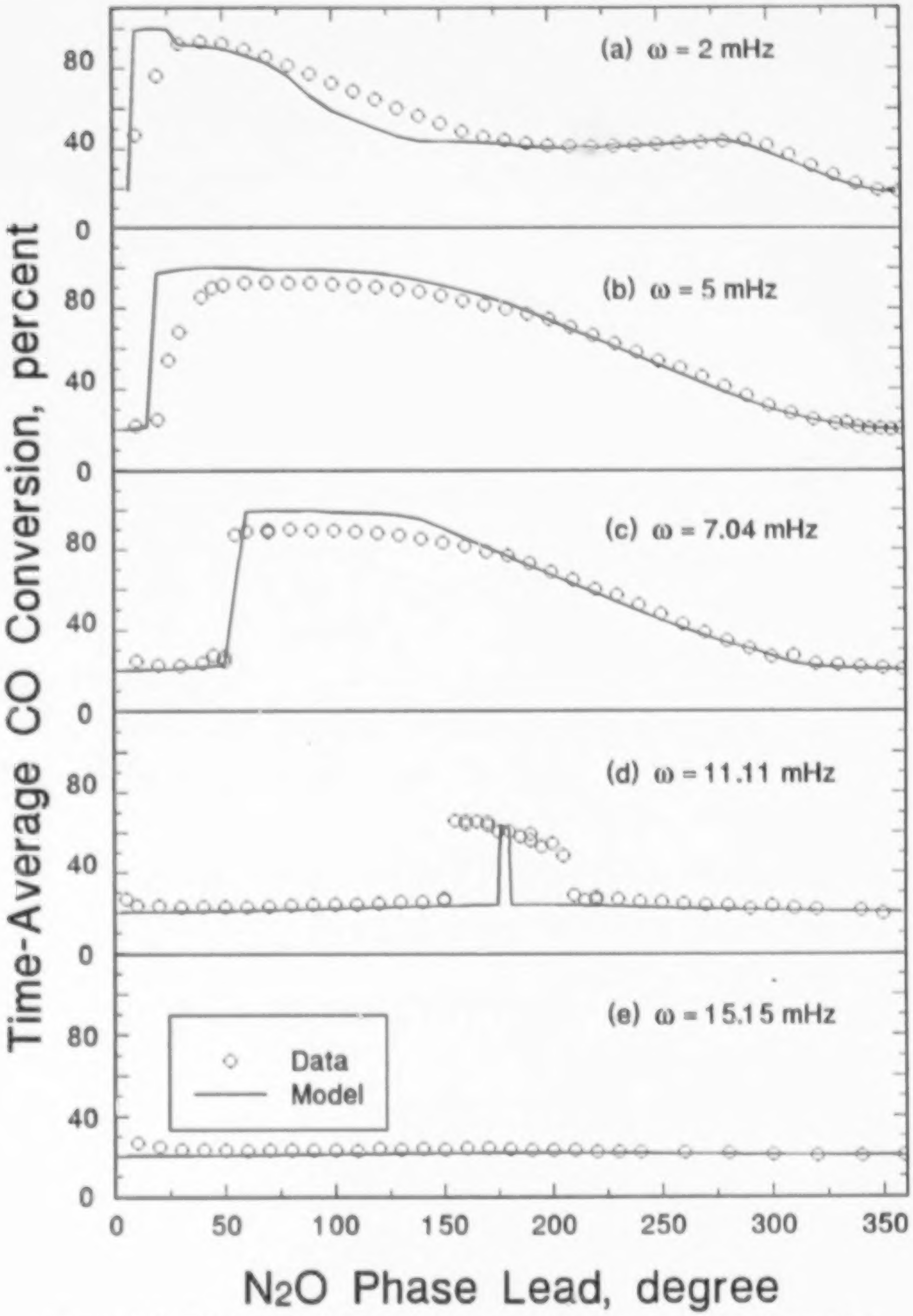

Figure 3.9 Effect of N_2O Phase-Lead on the Time-Average CO Conversion During Cycling.

then decreased with increasing N_2O phase leads between 50° and 180°. The time-average conversion was approximately constant at 42% over the range of phase-leads between 180° and 300°. The conversions in the range of phase-leads between 180° and 300° can also be estimated by equation (3.1) without significant error, as demonstrated for the out-of-phase cycling in Fig. 3.5. The time-average conversions decreased sharply as the phase-lead was increased above 310°. The experimental observations of Fig. 3.9(a) also support the earlier generalization that relatively high time-average conversions are obtained for N_2O phase leads of less than 180°.

For feed cycling at 5 mHz, as shown in Fig. 3.9(b), the time-average CO conversion was approximately equal to its steady-state value of 20% at small phase-leads of 10° to 20°, and then rose sharply as the phase-lead was increased to 45°. A high time-average conversion of between 80 and 92.5% was attained over a wide range of phase-leads of 50° to 180°. An increase in phase lead above 180° caused the time-average conversion to drop gradually and eventually reached its steady-state value for phase-leads of 320° to 360°. A very similar behavior was also observed at a cycling frequency of 7.04 mHz (Fig. 3.9(c)) except that the span of phase-leads over which high conversions were obtained was narrower than that encountered at 5 mHz. The other significant difference between Figs 3.9(b) and (c) is that the size of the regions of near-steady-state conversion increased as the frequency increased. As the frequency was increased further to 11.11 mHz (Fig. 3.9(d)), the rate enhancement was obtained only for a narrow range of phase-leads (155° to 205°). For a high frequency of 15.15 mHz, the time-average conversion was approximately equal to its steady-state value for all phase-leads as shown in Fig. 3.9(e).

The CO_2 response curves for a cycling frequency of 5 mHz, at five different N_2O phase leads are shown by dashed lines in Fig. 3.10. For phase-leads of 10° and 330°, there is a significant overlap of CO and N_2O feed cycles, so that the gas-phase composition in the reactor is always in the low-conversion region (Fig. 3.3(a)) characterized by a catalyst surface saturated with adsorbed CO. Therefore, the low

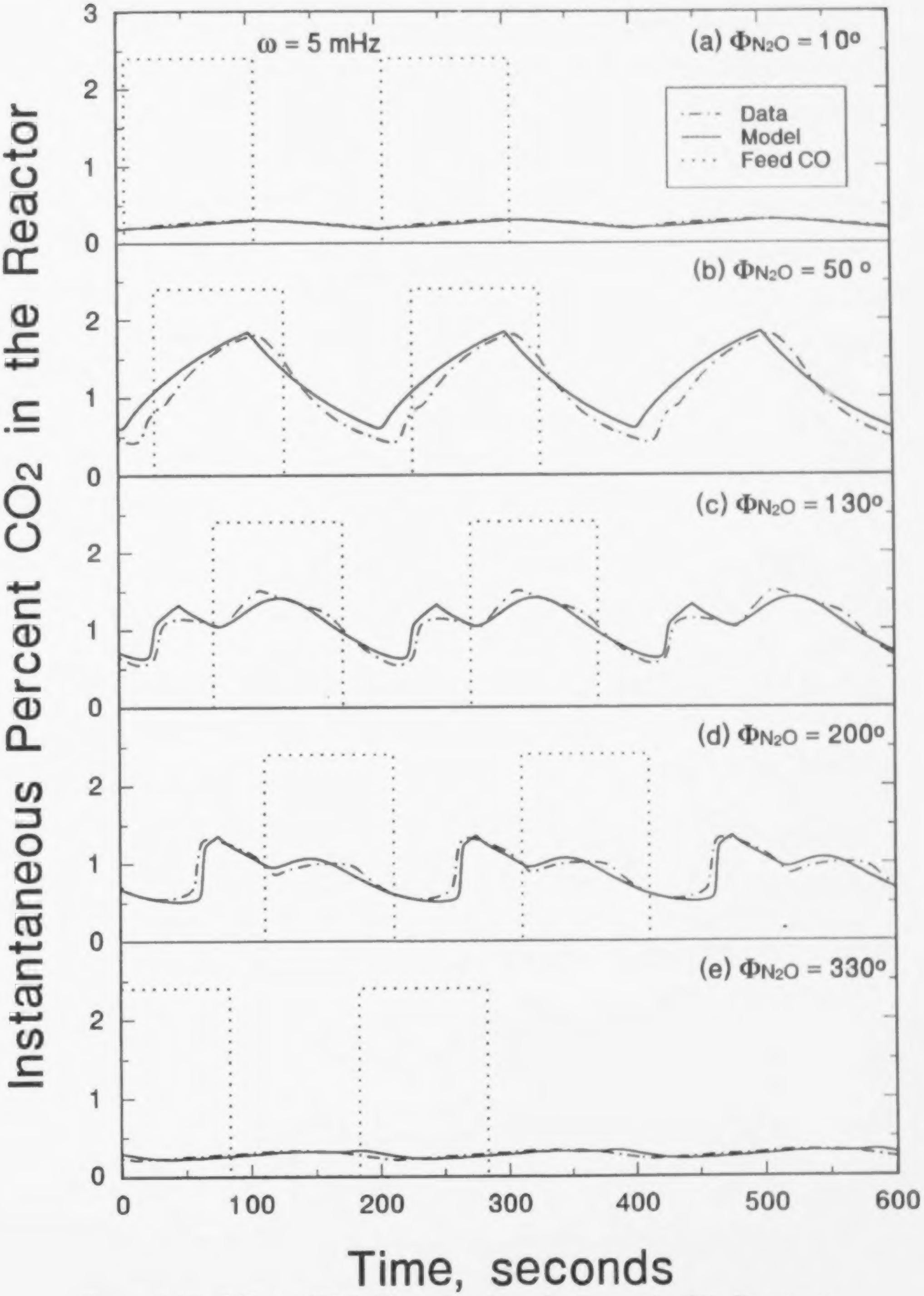

Figure 3.10 Effect of N_2O Phase-Lead on the Dynamic CO_2 Response.

reaction rates result in relatively flat CO_2 curves, as shown in Figs 3.10(a) and (e). For phase-leads of 50° and 130°, sufficient time is available for reacting away most of the adsorbed CO and the catalyst surface is saturated by adsorbed oxygen before the CO and N_2O feed cycles overlap. Therefore, high reaction rates are obtained in the region of CO and N_2O overlap, as characterized by the large peaks of CO_2 in Figs 3.10(b) and (c). A comparison of Figs 3.10(c) and (d) shows that the major CO_2 peak occurs in the CO-N_2O overlap part of the cycle for 130° phase lead and in the N_2O-only part of the cycle for 200° phase-lead. The differences between Figs 3.10(c) and (d) are very similar to the differences in Figs 3.8(a) and (b), for which an explanation was given earlier.

From these experiments it is apparent that the maximum time-average conversion can be obtained for an appropriate combination of N_2O phase lead (less than 180°) and cycling frequency. In this study the highest time-average CO conversion of 93.5% was attained at a frequency of 2 mHz with an N_2O phase-lead of 40°. In general, a certain overlap of the CO and N_2O cycles gives a time-average conversion which is higher than the highest conversion obtained for the out-of-phase cycling, particularly for the intermediate frequency range of 2 to 7 mHz. These observations are consistent with the findings of Graham and Lynch for the $CO+O_2$ reaction (7).

3.4 Mathematical model

A mathematical model for the reaction processes must be able to describe the dynamic behavior of the reaction and the rate enhancements observed in this study as well as the steady-state multiplicity discussed in Chapter 2. As a starting point, the steady-state model which was earlier used to describe the multiplicity behavior was re-cast in a dynamic form to determine if description of the reaction dynamics was possible.

3.4.1 CO Self-exclusion Model

In Chapter 2, the steady-state multiplicity of the N_2O+CO reaction over an alumina supported Pt catalyst was described by a model incorporating carbon monoxide self-exclusion from the platinum surface. The proposed reaction mechanism consisted of the following three elementary steps.

$$CO(g) + M \rightleftharpoons M\text{–}CO \tag{3.2}$$

$$N_2O(g) + M \rightarrow N_2(g) + M\text{–}O \tag{3.3}$$

$$M\text{–}CO + M\text{–}O \rightarrow CO_2(g) + 2M \tag{3.4}$$

It was shown that the CO self-exclusion effect could describe the experimental low-conversion steady-state results. The CO self-exclusion effect requires that an adsorbed CO molecule exclude other CO molecules from an area equivalent in size to N_{CO} surface Pt atoms, where N_{CO} is slightly greater than unity.

The reactor used in this study can be modelled as an isothermal CSTR due to the high recycle ratio that was employed. As previously shown in Chapter 2, the internal diffusion and external mass transfer resistances are negligible under the experimental conditions used in this study. Thus, mass balances on the gas-phase and surface species produce the following six dimensionless ordinary differential equations, where all symbols are defined in the **Notation** section.

$$\frac{dX}{d\tau} = X_o - Q_n X - K_1 X(1 - \theta_{CO} - \theta_O)\frac{(1 - N_{CO}\theta_{CO})}{(1 - \theta_{CO})} + K_{-1}\theta_{CO} \tag{3.5}$$

$$\frac{dY}{d\tau} = Y_o - Q_n Y - K_2 Y(1 - \theta_{CO} - \theta_O) \tag{3.6}$$

$$\frac{dZ}{d\tau} = Z_o - Q_n Z + K_3\theta_{CO}\theta_O - K_4 Z(1 - \xi_{CO_2}) + K_{-4}\xi_{CO_2} \tag{3.7}$$

$$\frac{d\theta_{CO}}{d\tau} = \alpha_m[K_1X(1 - \theta_{CO} - \theta_O)\frac{(1 - N_{CO}\theta_{CO})}{(1 - \theta_{CO})} - K_{-1}\theta_{CO} - K_3\theta_{CO}\theta_O] \tag{3.8}$$

$$\frac{d\theta_O}{d\tau} = \alpha_m[\frac{F_{N_2O}}{F_{CO}}K_2Y(1 - \theta_{CO} - \theta_O) - K_3\theta_{CO}\theta_O] \tag{3.9}$$

$$\frac{d\xi_{CO_2}}{d\tau} = \alpha_s[K_4Z(1 - \xi_{CO_2}) - K_{-4}\xi_{CO_2}] \tag{3.10}$$

where

$$\begin{aligned} Q_n = {} & 1 - F_{CO}[K_1X(1 - \theta_{CO} - \theta_O)\frac{(1 - N_{CO}\theta_{CO})}{(1 - \theta_{CO})} \\ & -K_{-1}\theta_{CO} - K_3\theta_{CO}\theta_O + K_4Z(1 - \xi_{CO_2}) - K_{-4}\xi_{CO_2}] \end{aligned} \tag{3.11}$$

Equations (3.5) to (3.10) can be used to describe the steady-state behavior by setting the time-derivatives in the equations to zero and solving the resulting algebraic equations. For steady-state operation, $X_o=1$, $Y_o=1$, and $Q_n=1$, and in addition $Z_o=0$ for all conditions because CO_2 was not present in the feed. The values of the kinetic parameters, K_1, K_{-1}, K_2 and K_3 must be selected so as to describe all of the time-average CO conversions during cycling experiments as well as the steady-state multiplicity data from the earlier experimental study (*4*). The time-average CO conversion is not affected by the adsorption and desorption of CO_2 on the alumina support. Therefore, in initial attempts at determining appropriate values of the kinetic parameters, the values of the CO_2 adsorption and desorption rate constants, K_4 and K_{-4} were set equal to zero while calculating time-average CO conversions. Further simplification of the model was made by setting Q_n equal to unity because of the low values of the gas-phase concentrations used in this study. The set of five differential equations (3.5)-(3.9) was integrated over several cycles, using a variable step-size fourth-order Runge-Kutta-Fehelberg method to calculate the time average CO conversion during feed composition cycling.

Integration was always performed using the initial conditions $X=Y=Z=\theta_{CO}=\theta_O=0$. During composition cycling, the dimensionless feed concentrations of CO and N_2O, X_o and Y_o, respectively, have values of either 2 or 0, as given by the following conditions for the nth cycle:

for all values of ϕ_{N_2O}

$$Y_o = 2, \qquad (n-1)\tau_c \le \tau < (n-\frac{1}{2})\tau_c \tag{3.12}$$

$$Y_o = 0, \qquad (n-\frac{1}{2})\tau_c \le \tau < n\tau_c \tag{3.13}$$

for $0^\circ \le \phi_{N_2O} < 180^\circ$

$$X_o = 0 \qquad (n-1)\tau_c \le \tau < (n-1+\frac{\phi_{N_2O}}{360})\tau_c \tag{3.14}$$

$$X_o = 2 \qquad (n-1+\frac{\phi_{N_2O}}{360})\tau_c \le \tau < (n-\frac{1}{2}+\frac{\phi_{N_2O}}{360})\tau_c \tag{3.15}$$

$$X_o = 0 \qquad (n-\frac{1}{2}+\frac{\phi_{N_2O}}{360})\tau_c \le \tau < n\tau_c \tag{3.16}$$

for $180^\circ \le \phi_{N_2O} < 360^\circ$

$$X_o = 2 \qquad (n-1)\tau_c \le \tau < (n-\frac{3}{2}+\frac{\phi_{N_2O}}{360})\tau_c \tag{3.17}$$

$$X_o = 0 \qquad (n-\frac{3}{2}+\frac{\phi_{N_2O}}{360})\tau_c \le \tau < (n-1+\frac{\phi_{N_2O}}{360})\tau_c \tag{3.18}$$

$$X_o = 2 \qquad (n-1+\frac{\phi_{N_2O}}{360})\tau_c \le \tau < n\tau_c \tag{3.19}$$

The attainment of cycle invariance was determined according to the procedures described by Lynch (*13*). When several sequential integrations were performed, *i.e.*, ω varied, ϕ_{N_2O} varied, etc., the initial conditions for successive integrations were based on the final state of the immediately preceding converged cycle.

The initial estimates of the kinetic parameters were obtained from the values used to describe the steady-state multiplicity behavior (*4*). It was found that the model predictions for time-average CO conversion for the feed cycling were considerably lower than the experimental data. The model predictions for time-average CO conversions for feed cycling could be improved by increasing the values of rate parameters K_2 and K_3.

However, increasing the values of K_2 and K_3 necessitated the change of other parameters in order to maintain agreement with the steady-state data. In particular, it was necessary to reduce the value of the CO self exclusion factor, N_{CO}, in order to be able to describe the experimental low-conversion steady-state data and the low-to-high conversion bifurcation points for high values of K_2 and K_3. However, the large values of K_2 and K_3 also resulted in significant model-experimental discrepancies in the values of feed CO% at which high-to-low conversion bifurcation occurs for steady-state experiments. While maintaining a complete model-experimental agreement for the steady-state data, it was possible to vary the values of K_2 and K_3 only marginally when attempting to improve the predictions of the time-average CO conversions during feed cycling. Over large regions of parameter space, the values of the CO adsorption and desorption rate parameters, K_1 and K_{-1}, did not have any significant effect on model predictions as long as the ratio of K_1 to K_{-1} was maintained constant. The main effect of lower values of K_1 and K_{-1} was a reduction in the number of integration steps needed for solving the differential equations. Therefore, in order to prevent the computational requirements from becoming unmanageable, relatively low values of K_1 and K_{-1} (while holding the ratio constant) were always used. A low value of K_1 implies a correspondingly low value of the CO sticking probability, S_{CO}. Therefore, the values of K_1, K_{-1} and S_{CO} used in this study are lower than the values used in Chapter 2 as can be seen from Table 3.1. It is possible to increase arbitrarily the value of S_{CO} by one or more orders of magnitude (with a corresponding increase in k_{-1}° to keep K_1/K_{-1} constant) without significantly affecting the predictions from the model.

The predictions of the time-average CO conversion for out-of-phase feed cycling from the CO self-exclusion model are shown by the dashed line in Fig. 3.5, where it can be seen that the model predictions approximately match the experimental data at frequencies below 3 mHz and at high frequencies above 11 mHz. In order to describe as much of the dynamic data as possible while maintaining a near complete agreement with the steady-state data from Chapter 2, it was also necessary to use different values of the other rate parameters, namely, K_2, K_3 and N_{CO}, as shown in Table 3.1. As discussed earlier, the time-average conversion for the low frequencies can be estimated reasonably accurately by equation (3.1) and therefore, is relatively insensitive to the reaction mechanism model. However, the model predictions are consistently lower than the experimental data for the intermediate frequency range of 3 to 11 mHz. The effect of CO self-exclusion is illustrated by setting N_{CO} equal to unity as shown by the dotted line in Fig. 3.5. As can be seen from Fig 3.5, the time-average CO conversions predicted from a Langmuir-Hinshelwood type model (N_{CO}=1) are consistently lower than those predicted by the CO self-exclusion model, particularly for frequencies higher than 11 mHz. This observation is consistent with the earlier study (*4*) where only the CO self-exclusion effect could account for the experimentally observed CO conversions for the unique low-conversion steady-state. Therefore, CO self-exclusion was considered as an integral part of the further model development. In order to describe the high values of time-average conversion during feed cycling experiments, as well as the steady-state multiplicity, it was necessary to use a surface phase transformation model similar to that described by Lynch *et al.* (*7,18*).

Table 3.1

Model Parameters at 499 K

Parameter	CO Self-Exclusion Model	Surface-Phase Transition Model	Chapter 2 Mechanism 4
K_1	28,000	28,000	2,604,422
K_{-1} (1% CO feed)	100	15.75 (ψ_2 = 1)	7,395
K_2	18	23.6	37.8
K_3 (1% CO feed)	20	20 (ψ_3 = 1)	15.46
S_{CO}	1.076×10^{-4}	1.076×10^{-4}	1×10^{-2}
L_m	2×10^{-5}	1.42×10^{-5}	2×10^{-5}
N_{CO}	1.018	1.0015	1.025

3.4.2 Surface-Phase Transformation Model

It has been shown that a clean Pt(100) surface undergoes a reconstruction from a (1x1) structure to a quasi-hexagonal order corresponding to a complicated (5x20) LEED pattern (*19*) which appears to be the thermodynamically favoured structure (*20*). Numerous studies (*21-26*) have shown that the reconstruction [(5x20) LEED pattern] exhibited by the clean Pt(100) surface is removed by the adsorbate-induced interaction of CO, O_2, H_2 or NO. Thiel *et al. (27)* observed that the nucleation of (1x1) patches occurs on the reconstructed (hex) surface of Pt(100) even at a very low CO surface coverage and proceeds until the entire surface has been converted to the (1x1) phase at θ_{CO}=0.5. On the other hand, during CO desorption, the hex-phase does not return until the fractional CO surface coverage is decreased below 0.3. The reconstructed surface (hex phase) is less active as compared to the unreconstructed (1x1) surface. The oxygen sticking probability is low for the surface in hex-phase (*26*), but is at least two orders of magnitude larger for the (1x1) surface (*28*). A similar observation is reported by Bonzel *et al.* (*29*) for NO adsorption on Pt(100). They observed no adsorption of NO on reconstructed hex-surface at temperatures higher than 380 K. On the other hand, the unreconstructed (1x1) surfaces were able to adsorb NO molecularly up to temperatures of 410 K.

The phenomenon of the adsorbate-induced reversible surface-phase transition for the clean Pt(100) surface, and resulting reaction rate enhancements have been used to describe the kinetic oscillations of the CO+O_2 reaction (*30*) and the NO+CO reaction (*31, 32*) under high vacuum conditions on well characterized catalyst surfaces. However, to describe the rate oscillations of CO oxidation on supported Pt catalyst and Pt foils at near atmospheric pressure, various other mechanisms have been proposed. For example, a process of slow oxidation and reduction of the catalyst surface (*33, 34*) has been used to model the rate oscillations of CO oxidation on Pt at atmospheric pressure. It has also been suggested (*35*) that the formation of platinum oxide is catalyzed by silicon impurities on the supported catalyst. Other studies (*36, 37*) proposed that a process of slow activation/deactivation of the catalyst surface due to diffusion of carbon to the surface may be responsible for observed oscillations of CO oxidation on Pt foil at atmospheric pressure. A kinetic model based on the variation of the catalyst surface temperature (*38*) has also been suggested to describe the self-sustained oscillations of CO oxidation on silica-supported Pt pellets at atmospheric pressure. Nevertheless, the Pt(100) surface transformation phenomenon has been successfully used (*18*) to describe the self-sustained oscillations of CO oxidation on alumina-supported Pt catalyst at atmospheric pressure. A similar mechanism has also been suggested (*39*) for oscillations of NO+CO reaction on polycrystalline Pt-Al_2O_3 catalyst in FTIR spectroscopic investigations. Schwartz and Schmidt (*31*) suggested that the adsorbate induced 1x1↔hex surface-phase transition may be operative on supported Pt catalysts because in many reactive gases all crystallographic orientations tend to facet into predominantly (100) crystal planes. Wang *et al.* (*40*) have shown that supported platinum crystallites form predominantly (100) crystal planes when grown in hydrogen. These studies lend support to the model based on Pt(100) surface-phase transition to describe the rate oscillations on supported Pt catalyst. Graham and Lynch (*7*) used the surface-phase transformation effect to describe the complex behavior, including steady-state multiplicity and reaction rate enhancement during feed cycling, of the CO+O_2 reaction on an alumina-supported Pt catalyst at atmospheric pressure. Because of the apparent similarity of the CO+N_2O and CO+O_2 reaction systems, the same surface-phase transformation phenomenon has been used in this study to describe reaction rate enhancement for the CO+N_2O reaction during feed cycling.

As shown by Graham and Lynch (*7*), the use of the surface-phase transformation model requires that the rate constants for oxygen adsorption and surface reaction with CO depend on the CO surface coverage in a very nonlinear fashion. A graphical representation of the reversible surface-phase transition due to CO adsorption is shown in Fig. 3.11 for the N_2O+CO reaction. It is assumed that the catalyst surface is in phase-1 at low CO surface coverage. Phase-1 is a low activity phase similar to the reconstructed quasi-hexagonal phase of Pt(100). The catalyst surface remains in phase-1 until the fractional CO surface coverage reaches a high critical value of 0.95, when the entire surface is instantaneously transformed into phase-2. Phase-2 is a high activity phase

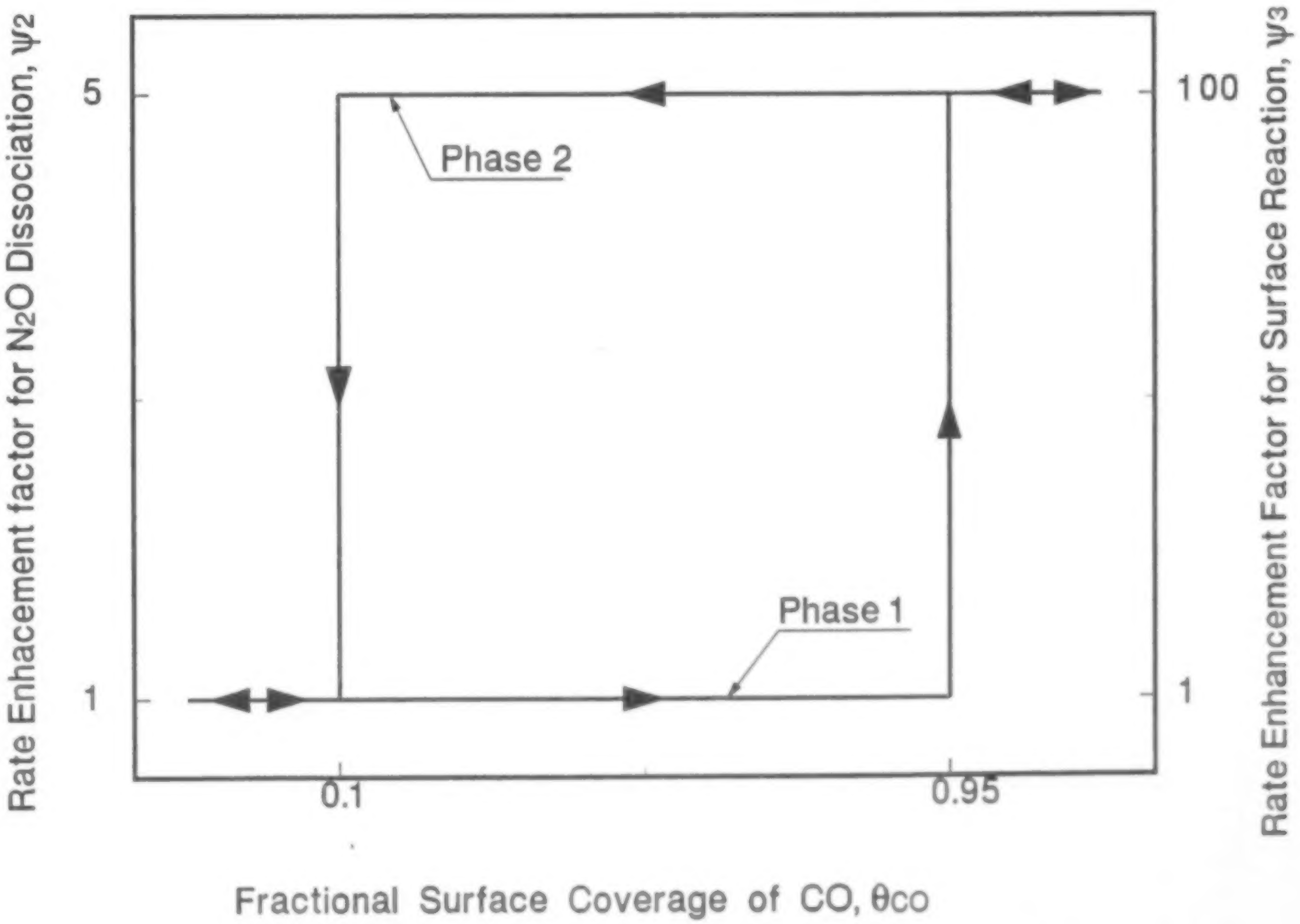

Figure 3.11 Reaction Rate Enhancement due to CO-Adsorbate Dependent Pt Surface-Phase Transition.

similar to the unreconstructed (1x1) phase of Pt(100). In phase-2, the N_2O dissociation rate constant, k_2, and the surface reaction rate constant, k_3, have high values relative to phase-1. The surface remains in phase-2 until the fractional CO surface coverage falls to a low critical value of 0.1, when the entire surface is instantaneously transformed back to phase-1. Mathematical formulation of this effect results in k_2 and k_3 being given by:

$$k_2 = \psi_2 k_2^o \exp(-E_2/RT) \qquad (3.20)$$

$$k_3 = \psi_3 k_3^o \exp(-E_3/RT) \qquad (3.21)$$

where ψ_2 and ψ_3 are the enhancement factors which are greater than unity (5 and 100, respectively) when the surface is in the (1x1) phase (high CO coverage). For the reconstructed (5x20) phase (low CO coverage), $\psi_2=1$ and $\psi_3=1$ always holds. For intermediate coverage between $\theta_{CO}=0.1$ and $\theta_{CO}=0.95$, the values of ψ_2 and ψ_3 depend on the prior state of the surface as shown in Fig. 3.10.

Graham and Lynch (*7*) used the same value of 250 for the enhancement factors for the (1x1) phase for both the surface reaction rate constant and the oxygen sticking probability. In this study a lower value of $\psi_2(=5)$ as compared to $\psi_3(=100)$ was sufficient to describe the high time-average CO conversions obtained during the feed cycling experiments. It would therefore appear that the rate enhancement for N_2O dissociation due to hex↔(1x1) surface transition is much smaller than the increase of approximately two orders of magnitude for the oxygen sticking probability. This can be attributed to the differences in the adsorption mechanisms of O_2 and N_2O. In a study of comparative adsorption of O_2 and N_2O on recrystallized platinum ribbons using thermal desorption and mass spectrometry, Alnot *et al.* (*41*) noted that oxygen adsorption at 300 K leads to three binding states while N_2O adsorption fills only the most energetic one. The sticking coefficient for O_2 dissociative adsorption at 500 K was found to be 0.16 as compared to 0.0068 for N_2O dissociative adsorption. They attributed the differences between O_2 and N_2O dissociative adsorption to steric factors. Daniel *et al.* (*42*) noted that for a clean Rh(100) surface, the saturation coverage of oxygen is twice as large for O_2 as N_2O. McCabe and Wong (*2*) attributed the lower rate of the CO+N_2O reaction compared to CO+O_2 and CO+NO reactions under the conditions characterized by high CO surface-coverage to the lower rate of dissociative adsorption of N_2O as compared to the rate of dissociative O_2 and NO adsorption on alumina-supported Rh catalyst.

The time-average CO conversions were calculated by integrating equations (3.5)-(3.9). In the initial attempts at determining suitable model parameters, the values of K_1, K_{-1}, K_2, K_3 and N_{CO} were chosen so that the model predictions matched the experimental CO conversions both for out-of-phase feed cycling (Fig. 3.5) and for the steady-state experiments at 499 K (Fig. 3.3(a)). The model parameters were then further adjusted so as to describe not only the experimental data for all of the forced composition cycling experiments (Figs 3.5, 3.7 and 3.9) but also the steady-state data from the earlier study (Figs. 3.3(b), 3.3(c) and 3.12). All integrations were carried out over several cycles until the CO conversion per cycle based on CO, N_2O and CO_2 matched within 0.2% of each other and did not change more than 0.2% for two consecutive cycles. The percent change in the fractional oxygen surface coverage was used as a criterion as given by equation (3.22).

$$\left|\frac{\theta_O(n\tau_c) - \theta_O((n-1)\tau_c)}{\theta_O((n-1)\tau_c)}\right| \le 10^{-3} \qquad n = 1,2,3....... \qquad (3.22)$$

The model predictions for time-average CO conversions for out-of-phase cycling are shown by the solid line in Fig. 3.5. The initial slope of the conversion-frequency curve is strongly dependent on the ratio of the bulk volume to catalyst surface capacitances (α_m) as demonstrated by Lynch (*14*). Therefore, the value of the catalyst adsorption capacity, L_m, was adjusted down from 2×10^{-5} to 1.42×10^{-5} mol/m^2, to match the predictions with the experimental data for the frequencies lower than 3 mHz. The other kinetic parameter values are listed in Table 3.1.

As can be seen from Table 3.1, different values of the parameters K_{-1}, K_2, K_3 and N_{CO} were used for the two models. The parameter values for the CO self-exclusion model were selected so as to describe all of the steady-state multiplicity data presented in Chapter 2 and to the extent possible, the time-average CO conversions obtained in this study. However, as shown in Fig. 3.5, this model fails to describe the high values of time-average CO conversions obtained during out-of-phase feed composition cycling. Any attempt to force the model predictions to match the out-of-phase feed cycling data led to significant model-experimental discrepancies for the steady-state multiplicity data.

The model parameters for the surface-phase transformation model have been chosen so as to describe both the dynamic and the steady-state experimental data. A comparatively low value of N_{CO}=1.0015 was necessary for the surface-phase transformation model because of the high enhancement (100 times) of the surface reaction rate for phase-2. Nevertheless the CO self-exclusion effect was still required in the model in order to describe the unique low conversion steady-state data. As shown in Fig. 3.5, the model predicts that above a critical frequency of 11 mHz no improvement in the time-average conversion can be obtained. This prediction is consistent with the experimental results which indicate a critical frequency in the range of 11.5 and 12.2 mHz. The time-average conversion predicted by the model is less than the experimental data by approximately 5% for frequencies greater than 7 mHz. However, the surface-phase transformation model is clearly superior to the CO self-exclusion model for describing the rate enhancement obtained during out-of-phase cycling in the intermediate frequency range of 2.5 to 11 mHz.

The surface-phase transformation model was also able to describe the steady-state multiplicity behavior presented in Chapter 2 as shown in Fig. 3.3. The steady-state behavior at 520 K could also be predicted by the model as shown in Fig 3.12. The high and low bifurcation boundaries predicted by the model closely match the experimental

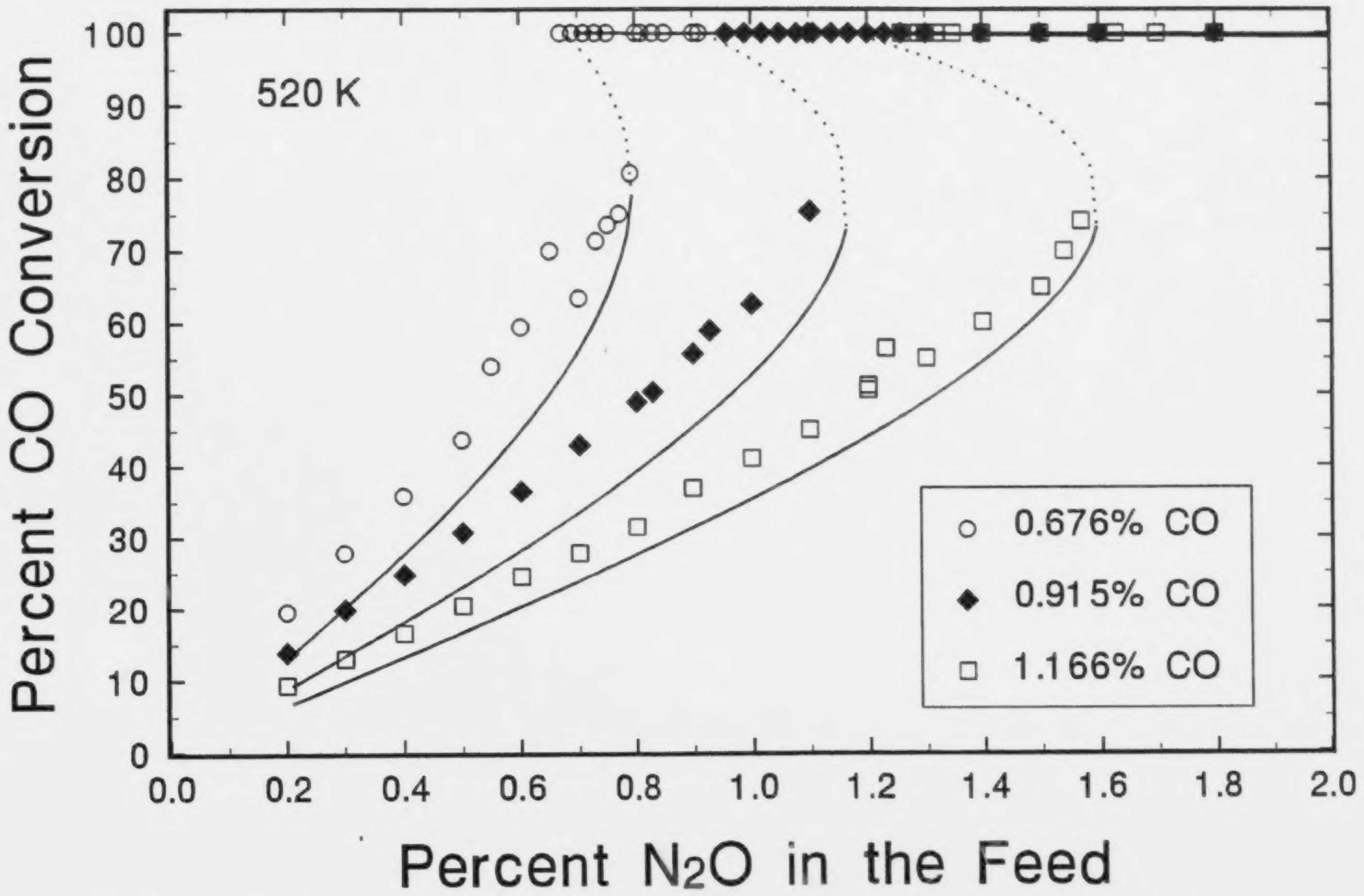

Figure 3.12 Experimental-Model Comparison of the Steady-State Multiplicity Behavior at 520 K.
([———] steady-state and [··········] unstable steady-state predictions)

bifurcation points as shown in Fig 3.13. The kinetic parameters used to describe the steady-state data at four different temperatures are tabulated in Table 3.2. These parameters follow an Arrhenius type temperature dependency as shown in Fig. 3.14.

Table 3.2

Parameter Values for Surface-Phase Transition Model

Parameter	461 K	480 K	499 K	520 K
K_1	26,913	27,482	28,000	28,583
K_{-1} ($\psi_2=1$) (1% CO feed)	5.25	9.1	15.75	24.5
K_2	7	12.5	23.6	54
K_3 ($\psi_3=1$) (1% CO feed)	2.8	7.2	20	53

The activation energies and the pre-exponential factors found from the Arrhenius plots of Fig. 3.14 are listed in Table 3.3, where the values from Chapter 2 are also listed for comparison. It can be seen from Table 3.3 that the activation energies used in this study are within 30% of the values used in Chapter 2 to describe the steady-state behavior, where an extensive comparison with other experimental studies was made.

To predict the dynamic CO_2 response of the model, the effect of CO_2 adsorption-desorption on the alumina support was accounted for through the use of values of K_4 and K_{-4} given in the **Notation** section. The model predictions for the dynamic CO_2 response for the out-of-phase cycling are shown by the solid lines in Fig. 3.4. It can be seen that excellent model-experimental agreement is achieved with only a slight mismatch occurring in a few locations. The time-average conversion calculated from the model for the out-of-phase cycling is shown by the solid curve in Fig. 3.5. It is seen that the model can describe the high time-average conversions in the intermediate frequency range,

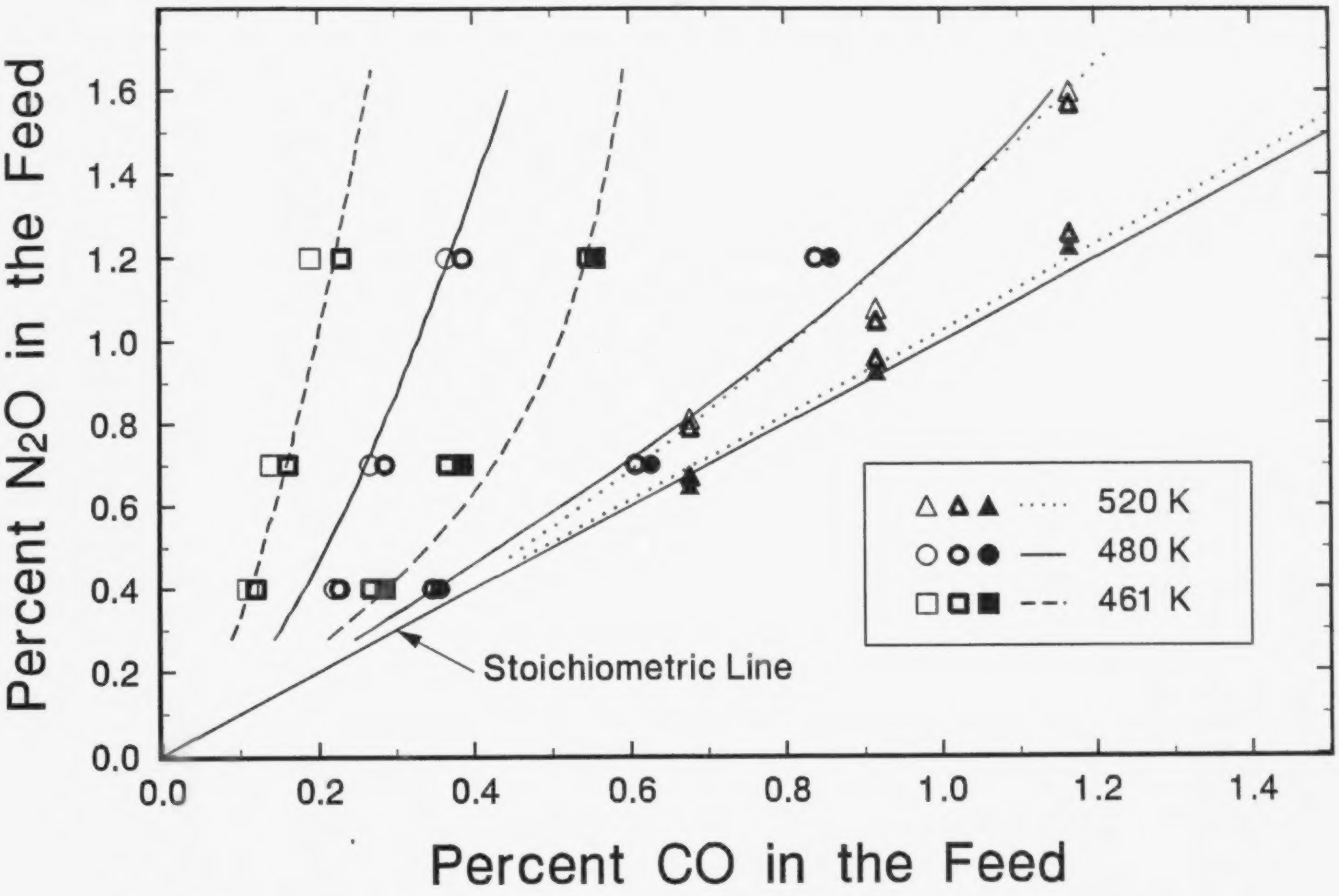

Figure 3.13 Experimental-Model Comparison of the Steady-State Bifurcation Boundaries (———— , ---------, ·············, model predictions)

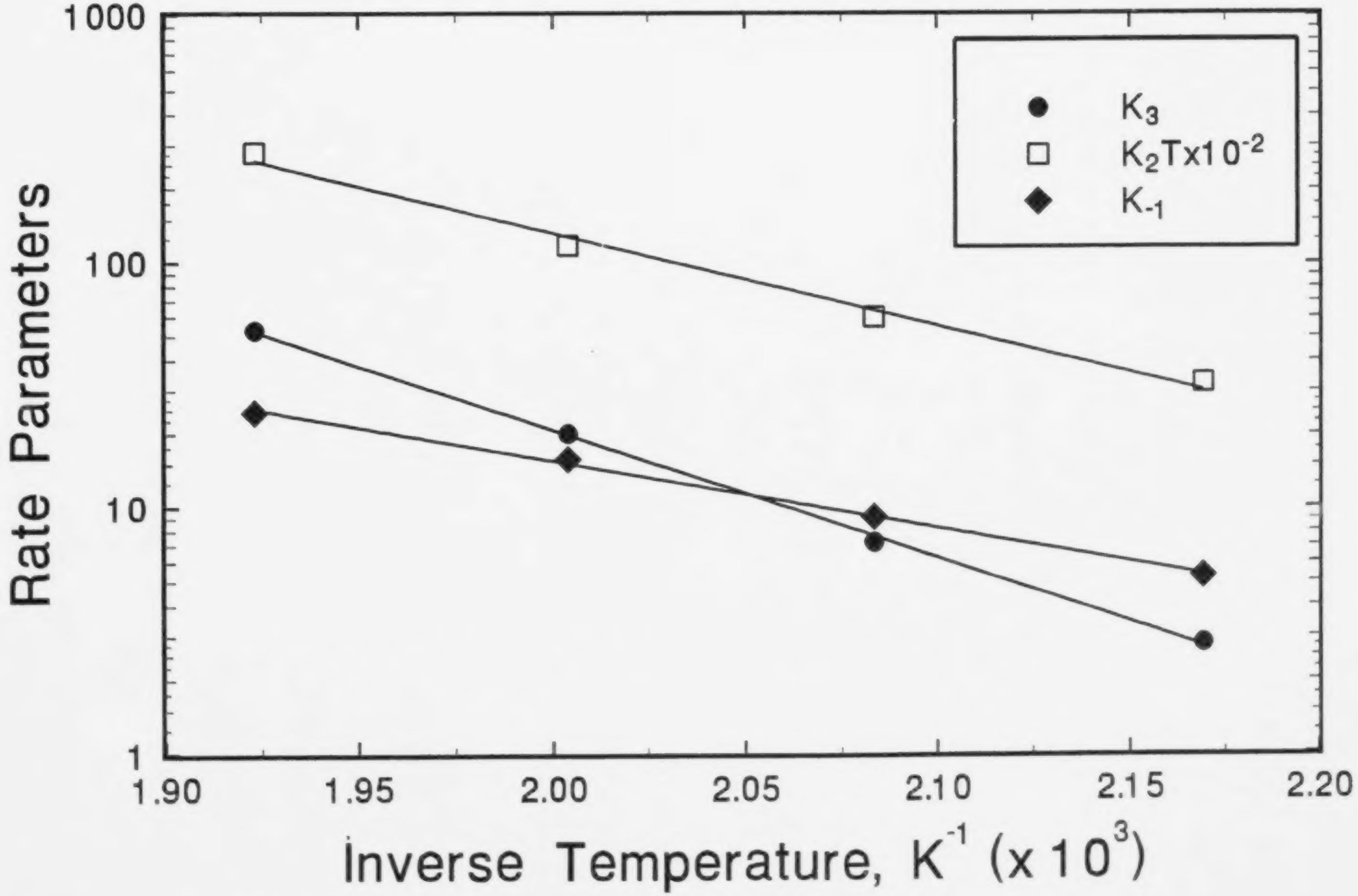

Figure 3.14 Arrhenius-type Plot of the Pt Surface-Phase Transition Model Parameters.

something that was not possible to achieve with the other two models examined earlier.

Table 3.3

Comparison of Kinetic Parameters

Parameter	CO Self-Exclusion Model	Surface-Phase Transition Model	Chapter 2 Mechanism 4
k_{-1}^o	$6.314\text{x}10^3$	$6.298\text{x}10^4$	$1.305\text{x}10^6$
k_2^o	$4.841\text{x}10^8$	$4.062\text{x}10^8$	$4.902\text{x}10^9$
k_3^o	$5.321\text{x}10^{11}$	$5.235\text{x}10^{14}$	$4.684\text{x}10^{11}$
E_1	36.8	52.8	41.0
E_2	85.8	72.8	92.0
E_3	74.3	100.0	74.5

The time-average conversions calculated from the model for 90° and 270° phase leads are shown in Fig. 3.7. The model predicts near 100% conversion for 90° phase lead in the frequency range of 4 and 7.8 mHz, which is approximately 10% higher than the experimental data. Otherwise, the model describes all of the other features of the conversion-frequency curve including the initial slope, the high conversions at intermediate frequencies and the critical frequencies which closely match the experimental results. Figure 3.8 shows close model-experimental agreement for the dynamic CO_2 response at a frequency of 1.25 mHz.

It can be seen from Fig. 3.9 that the model can almost quantitatively describe the effect of N_2O phase lead on the time-average conversion. The model predicts near 100% time-average conversion for a range of N_2O phase leads at frequencies of 2, 5 and 7.04 mHz as shown in Figs. 3.9(a), (b) and (c), respectively. In Fig. 3.9(d), the model predictions are shown for a frequency of 11 mHz and these are qualitatively very similar to the experimental results at 11.11 mHz frequency, although the conversion improvements are predicted only for a narrow range (176° to 180°) of phase leads. The model predicts no improvement in CO conversions for frequencies higher than 11 mHz. Figure 3.9 shows that the model predictions for the dynamic CO_2 response closely match the experimental results for the five frequencies.

The model predictions of near 100% time-average conversions, as shown in Figs. 3.7 and 3.9 suggests that a true global maximum in time-average conversion exists in the range of the frequencies and the phase-leads corresponding to near 100% conversion predictions. The maximum time-average conversion can be predicted by optimizing the objective function, f_{TA}, in equation (3.23).

$$f_{TA} = \frac{100}{\tau_c}\int_0^{\tau_c} Z(\tau)d\tau \tag{3.23}$$

The constraints for the optimization are given by the ordinary differential equations (3.5) to (3.10). Zolotarskii *et al.* (*43*) presented an analysis of a similar optimal periodic-control problem and observed that the optimal performance is attained when the two input cycles overlap to a certain extent, which is consistent with this study.

3.5 Conclusions

The kinetic behavior of the N_2O+CO reaction over an alumina-supported Pt catalyst has been examined using forced feed-composition cycling experiments. The composition cycling strategies involved variation of the phase-angle between the two square-wave cycles of CO and N_2O, respectively, in a manner similar to that used by Graham and Lynch (7) for CO+O_2 reaction. The time-average CO conversions during the cycling experiments were significantly higher than the steady-state conversion of 20% at 499 K. The maximum time-average conversion for the experiments with N_2O phase leads of less than 180° were higher than the maximum conversion obtained during the out-of-phase cycling. In this study, the maximum conversion of 93.5% was obtained at a cycling frequency of 2 mHz at an N_2O phase lead of 40°. The reaction rate enhancements were generally observed in the intermediate frequency range (ω<11 mHz), for an intermediate value of N_2O phase lead. At cycling frequencies higher than 11 mHz, as well as for phase leads closer to 0° and 360°, the time-average conversion was very close to its steady-state value. These observations are similar to those made for the $CO+O_2$ reaction (7).

A kinetic model incorporating the two main features, namely, the adsorbate induced 1x1↔hex surface-phase transformation of Pt and the CO self-exclusion effect, has been proposed to describe the dynamic behavior including the high time-average conversion and the dynamic CO_2 response during cycling. The model is based on a reaction mechanism consisting of three elementary steps, namely, the reversible adsorption of CO, the irreversible dissociative adsorption of N_2O to form adsorbed oxygen and gaseous N_2, and the reaction of adsorbed carbon monoxide and adsorbed atomic oxygen to produce gaseous CO_2. For a particular set of values of the kinetic parameters, the model could quantitatively describe the dynamic behavior during feed composition cycling, as well as the experimental steady-state multiplicity behavior of the reaction at several temperatures. Thus, this relatively simple model adequately describes a large amount of steady-state and dynamic data.

3.6 Notation

a_m	total Pt surface area of supported catalyst, 9.4 m^2
a_s	total surface area of the support, 2092 m^2
[CO]	reactor CO concentration, mol/m^3
$[CO]_o$	time-average feed CO concentration, $F_{CO}P/RT$, mol/m^3
$[CO_2]$	reactor CO_2 concentration, mol/m^3
E_{-1}	activation energy for CO desorption, kJ/mol
E_2	activation energy for N_2O dissociation, kJ/mol

E_3	activation energy for surface reaction, kJ/mol
E_{-4}	activation energy for CO_2 desorption from the support, 83.1 kJ/mol
F_{CO}	time-average mole fraction CO in feed
F_{N_2O}	time-average mole fraction N_2O in feed
f_{TA}	time-average CO conversion, %
k_1	CO adsorption rate constant, $6.87 S_{CO} T^{0.5}/L_m$, $m^3/mol \cdot s$
k_{-1}	CO desorption rate constant, $k_{-1}^o \exp(-E_1/RT)$, s^{-1}
k_{-1}^o	CO desorption pre-exponential factor, s^{-1}
k_2	N_2O dissociation rate constant, $\psi_2 k_2^o \exp(-E_2/RT)$, $m^3/mol \cdot s$
k_2^o	N_2O dissociation pre-exponential factor, $m^3/mol \cdot s$
k_3	surface reaction rate constant, $\psi_3 k_3^o \exp(-E_3/RT)$, $m^2/mol \cdot s$
k_3^o	surface reaction pre-exponential factor, $m^2/mol \cdot s$
k_{-4}	CO_2 desorption rate constant, $k_{-4}^o \exp(-E_{-4}/RT)$, s^{-1}
k_{-4}^o	CO_2 desorption pre-exponential factor, 3.83×10^9 s^{-1}
K_1	dimensionless CO adsorption rate constant, $a_m L_m k_1/Q_o$
K_{-1}	dimensionless CO desorption rate constant, $a_m L_m k_{-1}/Q_o[CO]_o$
K_2	dimensionless N_2O dissociation rate constant, $a_m L_m k_2/Q_o$
K_3	dimensionless surface reaction rate constant, $a_m L_m^2 k_3/Q_o[CO]_o$
K_4	dimensionless CO_2 adsorption rate constant, $5.48 S_{CO_2} a_s T^{0.5}/Q_o$
K_{-4}	dimensionless CO_2 desorption rate constant, $a_s L_s k_{-4}/Q_o[CO]_o$
M-CO	adsorbed CO species on catalyst surface
M-O	adsorbed oxygen species on catalyst surface
L_m	adsorption capacity of platinum surface, mol/m^2
L_s	CO_2 adsorption capacity of the support, 1.2×10^{-6}, mol/m^2
n	number of cycles
N_{CO}	CO self-exclusion factor
$[N_2O]$	reactor N_2O concentration, mol/m^3
$[N_2O]_o$	time-average feed N_2O concentration, mol/m^3
P	reactor pressure, 1.03×10^5 Pa

Q_o	feed volumetric flow rate at the reactor operating conditions, $1.11\text{x}10^{-8}T$, m^3/s
Q_n	ratio of exit to feed volumetric flow rates
R	gas constant, 8.314 $m^3 \cdot Pa/mol \cdot K$
S_{CO}	CO sticking probability on catalyst
S_{CO_2}	CO_2 sticking probability on alumina support, $8.3\text{x}10^{-9}$
t	time, s
T	reactor temperature, 499 K for cycling experiments
V	effective free volume of the reactor, $2.15\text{x}10^{-4}$ m^3
X	dimensionless reactor CO concentration, $[CO]/[CO]_o$
X_o	instantaneous dimensionless feed CO concentration (0 or 2 in this study)
Y	dimensionless reactor N_2O concentration, $[N_2O]/[N_2O]_o$
Y_o	instantaneous dimensionless feed N_2O concentration (0 or 2 in this study)
Z	dimensionless reactor CO_2 concentration, $[CO_2]/[CO]_o$
Z_o	instantaneous dimensionless feed CO_2 concentration (0 in this study)

Greek Letters

α_m	ratio of bulk volume to metal surface capacitances, $[CO]_o V/a_m L_m$ (0.48 in this study)
α_s	ratio of bulk volume to support surface capacitances, $[CO]_o V/a_s L_s$ (0.024 in this study)
θ_{CO}	fractional CO surface coverage on platinum surface
θ_O	fractional oxygen surface coverage of platinum surface
ξ_{CO_2}	fractional CO_2 surface coverage on the support surface
τ	dimensionless time based on the reactor residence time, $Q_o t/V$
τ_c	dimensionless cycle period, $Q_o/V\omega$
ϕ_{N_2O}	N_2O phase lead, degrees
ψ_2	enhancement factor for N_2O dissociation, 1 for (5x20) phase and 5 for

	(1x1) phase
ψ_3	enhancement factor for surface reaction, 1 for (5x20) phase and 100 for (1x1) phase
ω	frequency of cycling, $Q_o/V\tau_c$, Hz

3.7 References

1. Cho, B.K., Shanks, B.H. and Bailey, J.E., *J. Catal.* **115**, 486-499 (1989).
2. McCabe, R.W. and Wong, C., *J. Catal.* **121**, 422-431 (1990).
3. Muraki, H. and Fujitani, Y., *Ind. Eng. Chem. Prod. Res. Dev.* **25**, 414-419 (1986).
4. Sadhankar, R., Ye, J. and Lynch, D.T., *J. Catal.* **146**, 511-522 (1994).
5. Kobayashi, M., in "Chemical Reaction Engineering - Boston", ACS Symposium Series 176, (J. Wei and C. Georgakis, Eds.), p. 213-223, ACS, Washington, 1981.
6. Graham, W.R.C. and Lynch, D.T., *AIChE J.* **33**, 792-800 (1987).
7. Graham, W.R.C. and Lynch, D.T., *AIChE J.* **36**, 1796-1806 (1990).
8. Bailey, J.E. in "Chemical Reactor Theory: A Review", (L. Lapidus and N.R. Amundson, Eds.), p. 758-813, Prentice-Hall, Engelwood Cliffs, NJ, 1977.
9. Cutlip, M.B., *AIChE J.* **25**, 502-508 (1979).
10. Cutlip, M.B., Hawkins, C.J., Mukesh, D., Morton, W. and Kenney, C.N., *Chem. Eng. Commun.* **22**, 329-344 (1983).
11. Zhou, X., Barshad, Y. and Gulari, E., *Chem. Eng. Sci.* **41**, 1277-1284 (1986).
12. Cho, B.K., *Ind. Eng. Chem. Fumdam.* **22**, 410-420 (1983).
13. Lynch, D.T., *Can. J. Chem. Eng.* **61**, 183-188 (1983).
14. Lynch, D.T., *Can. J. Chem. Eng.* **62**, 691-698 (1984).
15. Graham, W.R.C. and Lynch, D.T. in "Catalysis 1987 - Proceedings of the Tenth North American Meeting of the Catalysis Society (San Diego 1987)", (J.M. Ward, Ed.), *Stud. Surface Sci. and Catal.* **38**, 693-703 (1988).
16. Vaporciyan, G., Annapragada, A. and Gulari, E., *Chem. Eng. Sci.* **43**, 2957-2966 (1988).

17. Prairie, M.R., Cho, B.K., Oh, S.H., Shinouskis, E.J. and Bailey, J.E., *Ind. Eng. Chem. Res.* **27**, 1396-1407 (1988).

18. Lynch, D.T., Emig, G. and Wanke, S.E., *J. Catal.* **97**, 456-468 (1986).

19. Heilmann, P., Heinz, K. and Müller, K., *Surf. Sci.* **83**, 487-497 (1979).

20. McCarroll, J.J., *Surf. Sci.* **53**, 297-316 (1975).

21. Helms, C.R., Bonzel, H.P. and Kelemen, S., *J. Chem. Phys.* **65**, 1773-1782 (1976).

22. Bonzel, H.P. and Pirug, G., *Surf. Sci.* **62**, 45-66 (1977).

23. Norton, P.R., Davies, J.A., Creber, D.K., Sitter, C.W. and Jackman, T.E., *Surf. Sci.* **108**, 205-224 (1981).

24. Behm, R.J., Thiel, P.A., Norton, P.R. and Ertl, G., *J. Chem. Phys.* **78**, 7437-7447 (1983).

25. Gardner, P., Tüshaus, M., Martin, R. and Bradshaw, A.M., *Surf. Sci.* **240**, 112-124 (1990).

26. Barteau, M.A., Ko, E.I. and Madix, R.J., *Surf. Sci.* **102**, 99-117 (1981).

27. Thiel, P.A., Behm, R.J., Norton, P.R. and Ertl, G., *J. Chem. Phys.* **78**, 7448-7458 (1983).

28. Pirug, G., Brodén, G. and Bonzel, H.P. in "Proceedings of the Seventh International Vacuum Congress and the Third International Conference on Solid Surfaces (Vienna 1977)", (R. Dobrozemsky, F. Rüdenauer, F.P. Viehböck and A. Berth, Eds), p. 907-910, International Union for Vacuum Science Technique and Application, 1977.

29. Bonzel, H.P., Brodén, G. and Pirug, G., *J. Catal.* **53**, 96-105 (1978).

30. Ertl, G., Norton, P.R. and Rüstig, J., *Phys. Rev. Lett.* **49**, 177-180 (1982).

31. Schwartz, S.B. and Schmidt, L.D., *Surf. Sci.* **183**, L269-L277 (1987).

32. Schwartz, S.B. and Schmidt, L.D., *Surf. Sci.* **206**, 169-186 (1988).

33. Sales, B.C., Turner, J.E. and Maple, M.B., *Surf. Sci.* **114**, 381-394 (1982).

34. Kurtanjek, Ž. and Froment, G.F., *Chem. Eng. Sci.* **40**, 3189-3201 (1991).

35. Yeates, R.C., Turner, J.E., Gellman, A.J. and Somorjai, G.A., *Surf. Sci.* **149**, 175-190 (1985).

36. Burrows, V.A., Sundaresan, S., Chabal, Y.J. and Christman, S.B., *Surf. Sci.* **180**, 110-135 (1987).

37. Collins, N.A., Sundaresan, S. and Chabal, Y.J., *Surf. Sci.* **180**, 136-152 (1987).

38. Dagonnier, R., Dumont, M. and Nuyts, J., *J. Catal.* **66**, 130-146 (1980).

39. Schüth, F. and Wicke, E. in "Instationary Processes and Dynamic Experimental Methods in Catalysis, Electrochemistry and Corrosion", (G. Sandstede and G. Kreysa, Eds.), Dechema Monogr. Vol. 120, p. 429-441, Dechema, Frankfurt-am-Main, 1989.

40. Wang, T., Lee, C. and Schmidt, L.D., *Surf. Sci.* **163**, 181-197 (1985).

41. Alnot, M., Cassuto, A., Fusy, J. and Pentenero, A., *Jpn. J. Appl. Phys. Suppl.*, **2**(2), 79-84 (1974).

42. Daniel, W.M., Kim, Y., Peebles, H.C. and White, J.M., *Surf. Sci.* **111**, 189-204 (1981).

43. Zolotarskii, I.A., Bogdashev, S.M. and Matros, Yu. Sh., *React. Kinet. Catal. Lett.* **37**, 43-48 (1988).

4. NO REDUCTION BY CO: STEADY-STATE BEHAVIOR[*]

4.1 Introduction

Increasingly stringent regulations on NO_x emission from automobile exhaust have led to several studies on the reduction of nitric oxide (NO) over noble metal catalysts in the last two decades. In automobile catalytic converters NO is selectively reduced by CO in the presence of excess oxygen over supported catalysts containing noble metals such as platinum, palladium and rhodium (*1*). Several studies have focused on the partition of CO in the automobile exhaust between the reduction reaction with NO and the oxidation reaction with oxygen (*2-7*). At a typical exhaust gas temperature of 800 K, only rhodium is somewhat favourably selective for the NO+CO reaction under net reducing conditions, although at the lower temperature of 570 K, both platinum and rhodium are equally selective for the NO+CO reaction (*4*). Even in the absence of oxygen, the reaction between NO and CO has been shown to exhibit very complex behavior. Several studies have reported self-sustained rate oscillations for the NO+CO reaction, both on crystalline platinum (*8-12*) as well as on supported platinum catalysts (*13*). In addition, the reaction has also been shown to exhibit reaction rate multiplicity on crystalline platinum surfaces (*10-12, 14*). Temperature programmed reaction studies (*15-18*) have revealed the "explosive" nature of the reaction from the rapid evolution of the CO_2 and N_2 products in an extremely narrow temperature range. The mechanism underlying these complex phenomena cannot be explained by simple Langmuir-Hinshelwood kinetics. Several mechanisms based on Pt(100) surface phase transition (1x1 ↔ hex) and autocatalysis have been proposed (*11, 12, 15-19*) to explain the multiplicity, rate-oscillations and "surfaceexplosions" for the NO+CO reaction. The additional difficulty in understanding the reaction mechanism arises from the fact that nitrous oxide (N_2O) has been observed as a reaction by-product in the overall NO+CO reaction on platinum, particularly at temperatures below 580 K (*20-27*).

---

[*] A version of this chapter has been submitted for publication - Sadhankar, R.R. and Lynch, D.T., *Journal of Catalysis* (submitted November 1994).

At a typical operating temperature of 800 K in an automobile catalytic converter, the overall NO+CO reaction is represented by Eq. (4.1)

$$2CO + 2NO \rightarrow 2CO_2 + N_2 \tag{4.1}$$

The formation of N_2O at lower temperatures can be represented by the overall reaction according to Eq. (4.2).

$$CO + 2NO \rightarrow CO_2 + N_2O \tag{4.2}$$

It has been suggested (*28*) that the N_2O formed by the above reaction is subsequently reduced by CO according to the overall reaction as given by Eq. (4.3).

$$CO + N_2O \rightarrow CO_2 + N_2 \tag{4.3}$$

The CO+N_2O reaction (Eq. (4.3)) is thus considered as an important subset of the overall NO+CO reaction. Some of the recent studies (*29-31*) have investigated the N_2O+CO reaction on a rhodium catalyst in order to gain further understanding of the overall NO+CO reaction. From these studies it has been found that Eq. (4.1) which represents the overall NO+CO reaction at high temperatures (800 K) is in fact a combination of the two reactions represented by Eqs (4.2) and (4.3), respectively. It can be easily seen that only two of the three reactions (either 4.1 and 4.2 or 4.2 and 4.3) can describe the material balance even if all the three reactions are independent. Therefore, at low temperatures, where a significant amount of N_2O is formed as a reaction product, the overall reaction can be represented by any two of the three reactions discussed above. Generally, the first two reactions, shown by Eqs. (4.1) and (4.2), respectively, have been used (*22, 25, 27*) to describe the NO+CO reaction at low temperatures. It has also been suggested (*26, 31*) that the NO+CO reaction can be exclusively represented by the later two reactions (Eqs. (4.2) and (4.3)) over the entire temperature range, suggesting that N_2 is exclusively formed by the decomposition of N_2O rather than via desorption following recombination of two adsorbed nitrogen atoms.

Because of its importance in the NO+CO reaction, the N_2O+CO reaction over supported platinum catalyst has been studied previously using both steady-state and transient techniques as described in Chapters 2 and 3 (*32, 33*), respectively. In Chapter 2, it has been shown that the steady-state multiplicity behavior of the N_2O+CO reaction could be used to discriminate among several rival mechanisms. Therefore, steady-state bifurcation information could also be useful in the study of the NO+CO reaction. In this study, it was found that the NO+CO reaction exhibits steady-state multiplicity in the temperature range of 465-520 K. A significant amount of N_2O was also observed, particularly for the high-conversion steady-states obtained for the feed containing excess NO. The kinetic model developed previously in Chapter 2 to describe the steady-state multiplicity of the N_2O+CO reaction was considered as an integral part of the kinetic model for the NO+CO reaction. A reaction mechanism consisting of seven elementary steps has been proposed to describe the experimental data.

4.2 Methods

The experiments were carried out using a recycle reactor containing 20 g of 0.5 wt% Pt/γ-Al_2O_3 catalyst supplied by Engelhard. The equipment was. the same as previously described in Chapter 2 except that the recycle pump was replaced by a Metal Bellows Corporation model MB-158 pump driven by a 0.1 hp motor operating at a speed of 1725 rpm. This recycle pump delivered a recycle flow of 600 cm^3/s as against 500 cm^3/s for the previously used pump, model MB-118 HT. Unlike the model MB-118 HT, which was installed in a heated compartment, the pump model MB-158 was mounted on a base-plate at ambient temperature. The recycle tubing connecting the recycle pump and the reactor was externally insulated to maintain near isothermal condition in the recycle loop. An additional infrared gas analyzer, Horiba PIR-2000 was used for the continuous measurement of NO concentration in the reactor effluent.

The catalyst used in this study was taken from the same batch of catalyst that was used previously for the study of the N_2O+CO reaction described in Chapters 2 and 3. The gas mixtures were purchased from Linde and included mixtures of 1.99%, 2.02% or 4.97% CO in N_2 and 2.04%, 5.09% or 5.13% NO in N_2. Pre-purified N_2 was used to make-up the total flow to the reactor, which was always maintained at 185 cm^3(STP)/min. The span calibration of the gas analyzers for CO_2, N_2O and NO, was performed at the beginning of each experiment using gas mixtures of 0.982% CO_2 in N_2, 2% N_2O in N_2 and 2.04% NO in N_2, respectively. The zero-calibration of these gas analyzers was performed using pre-purified nitrogen. Following the calibration of the gas analyzers, the catalyst was pre-treated before the start of each experiment. It has been reported (*34*) that two different steady-states are obtained for the NO+CO reaction depending on the pretreatment of Pt/Al_2O_3 catalyst either in reducing or oxidizing environments, respectively. Therefore, the catalyst was always pre-treated in an oxidizing environment for 2 hours. It has also been reported (*35*) that heating a $Pt/\gamma\text{-}Al_2O_3$ catalyst in NO causes sintering of the Pt particles. A significant amount of sintering was reported even for a dilute (0.1%) NO gas mixture at temperatures as low as 200 °C. Therefore, a gas mixture of 2% N_2O in N_2 was used for the catalyst pretreatment.

The reactor pressure was always maintained at 103 kPa. The experiments were carried out under isothermal conditions at four different temperatures of 465, 485, 505 and 520 K, respectively. At these operating conditions, the recycle ratio was calculated to be in the range of 103 to 116. As discussed previously in Chapter 2, the recycle reactor system closely resembles an ideal CSTR under these conditions. As with the N_2O+CO reaction study described in Chapter 2, the experiments were aimed at studying the changes in isothermal steady-state multiplicity behavior with respect to the direction of variation in feed composition. This is in contrast to the earlier reports (*10-12*) in which the changes in the rate multiplicity with respect to the direction of variation in temperature at a fixed feed composition have been studied. The methods used were the same as those described previously for the N_2O+CO reaction system in Chapter 2. At each of the three temperatures, namely, 465, 485 and 505 K, the steady-state measurements were made following step-wise increases or decreases in the feed CO concentration while holding the NO concentration in the feed constant. At each of these three temperatures, the experiments were performed using three different values of the feed NO concentration, namely, 0.45%, 0.7% and 1.2%. This results in nine sets of experimental data for the steady-state bifurcation measurements. The steady-state measurements were made after four hours following a step change in the feed CO concentration. In the last set of experiments carried out at 520 K, the feed CO concentration was held constant while the feed NO concentration was varied in a stepwise fashion. Four different sets of experiments were carried out at 520 K using feed CO concentrations of 0.235%, 0.31%, 0.435% and 0.685%, respectively. Thus, in total 13 sets of experiments, each comprised of two sub-sets of experiments corresponding to the step-wise increase and the step-wise decrease, respectively, of the concentration of the variable component (NO or CO) in the feed, were carried out in the temperature range of 465-520 K.

4.3 Results

The experimental data including the feed flows, reactor temperatures and the gas analyzer readings were recorded by the computer at an interval of one minute during the course of each experiment. The attainment of steady-state was determined by analyzing the stored data. If the percent variation in the CO_2 and N_2O concentrations for the ten-minute interval immediately following four hours after a change in feed composition was less than 0.5%, then the reactor was considered to be operating at a steady-state. It was observed that a steady-state was not always reached in four hours, particularly when the feed composition was such that a bifurcation occurred from a high-conversion to a low-conversion steady-state or vice-versa. The experimental data on steady-state conversions has been tabulated in Appendix F. The experimental results are discussed below in terms of NO conversion, CO conversion and N_2O selectivity.

4.3.1 NO Conversion

NO conversion can be easily calculated from the measured values of the feed flows and the NO concentration in the reactor. It can also be estimated from the measured concentrations of CO_2, N_2O and NO in the reactor. If the overall reaction is represented by any two of the three reactions given by Eqs. (4.1)-(4.3), and if the volume change due to reaction is neglected, then the gas-phase mass balance yields the following equation.

$$[NO]_o = [NO] + [N_2O] + [CO_2] \tag{4.4}$$

It was found that the NO conversion calculated by these two methods matched closely, especially for the high-conversion data. The NO conversions reported in this study are the average values of the NO conversions calculated by the above two methods.

The NO conversions for the experiments carried out in the temperature range of 465-505 K are summarized in Fig. 4.1. The high-conversion branches in Fig. 4.1 correspond to the experiments which were started with approximately 0.1% CO in the feed. It can be seen from Fig. 4.1 that the NO conversion increased with the step-wise increase in the feed CO concentration on the high-conversion branch. The increase in feed %CO beyond a certain limit (high-to-low conversion bifurcation point) caused the NO conversion to drop from a high value to a low value. The high-to-low conversion bifurcation points shifted in the direction of higher feed %CO with both increasing feed %NO and increasing temperature. It can also be seen from Fig. 4.1 that the NO conversion on the high-conversion branch decreased with an increase in the feed %NO. For example, at 505 K, with approximately 0.3% CO in the feed, the NO conversions were 90% for 0.45% NO, 65% for 0.7% NO and 40% for 1.2% NO, respectively. This is due to CO being the limiting reactant for these feed conditions. In actual fact, the rate of disappearance of NO increases while the NO conversion decreases. This is caused by an increasing rate of production of N_2O at high feed concentrations of NO. It is also apparent from Fig. 4.1 that the NO conversions on the high-conversion branch are not affected significantly by temperature except for a noticeable shift in the high-to-low

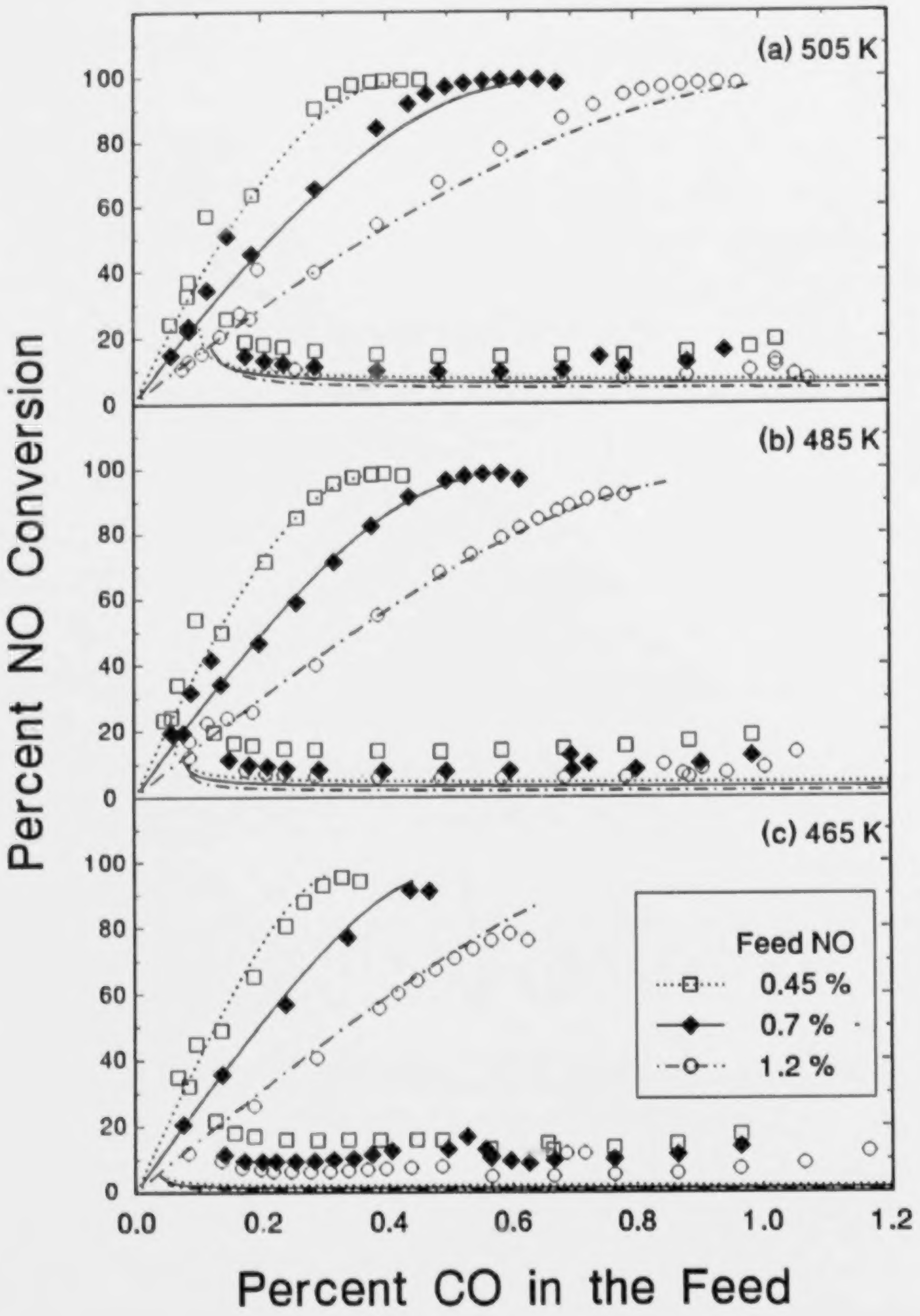

Figure 4.1 NO conversion multiplicity for the NO+CO reaction at 465-505 K. (··················, ——————, — · — · — · predictions of Eqs [4.19-24])

conversion bifurcation points towards higher feed %CO.

The low-conversion branches of Fig 4.1 correspond to the experiments which were started with nearly 1.2% CO in the feed. The step-wise decrease in feed %CO did not significantly affect the NO conversion. It can be seen from Fig. 4.1 that NO conversion increases with the decrease in feed NO% and this behavior is similar to that observed on the high-conversion branch. It can also be seen that the low-conversion branches were relatively insensitive to the changes in temperature.

The low-to-high conversion bifurcation occurred when the feed CO% was decreased to a value at which there was an abrupt increase in CO conversion to near 100%. This was accompanied by a relatively small increase in NO conversion. The low-to-high conversion bifurcation points shifted slightly in the direction of higher feed %CO with an increase in feed %NO and an increase in temperature, an observation which is consistent with that for the high-to-low bifurcation points. All of the nine low-to-high conversion bifurcation points shown in Fig. 4.1 occurred in the range of feed CO between 0.09% and 0.2%.

The NO conversions obtained for the experiments carried out at 520 K, in which the roles of CO and NO in the feed were reversed, are summarized in Fig. 4.2. The high conversion branches correspond to the experiments which were started with approximately 2.5% NO in the feed following which the %NO in the feed was decreased in a step-wise fashion. It can be seen that the NO conversion on the high-rate branch increases with an increase in feed %CO or a decrease in the feed %NO. The high-to-low conversion bifurcation points shift in the direction of increasing feed %NO with an increase in %CO in the feed. The low-conversion branches of Fig. 4.2 correspond to the experiments which were started with approximately 0.2% NO in the feed. The NO conversion on the low-conversion branch was near 10% over most of the range of concentrations examined with only a slight decrease in NO conversion with increasing feed %CO seen in Fig. 4.2. The low-to-high conversion bifurcation for the feed containing 0.235% CO occurred when

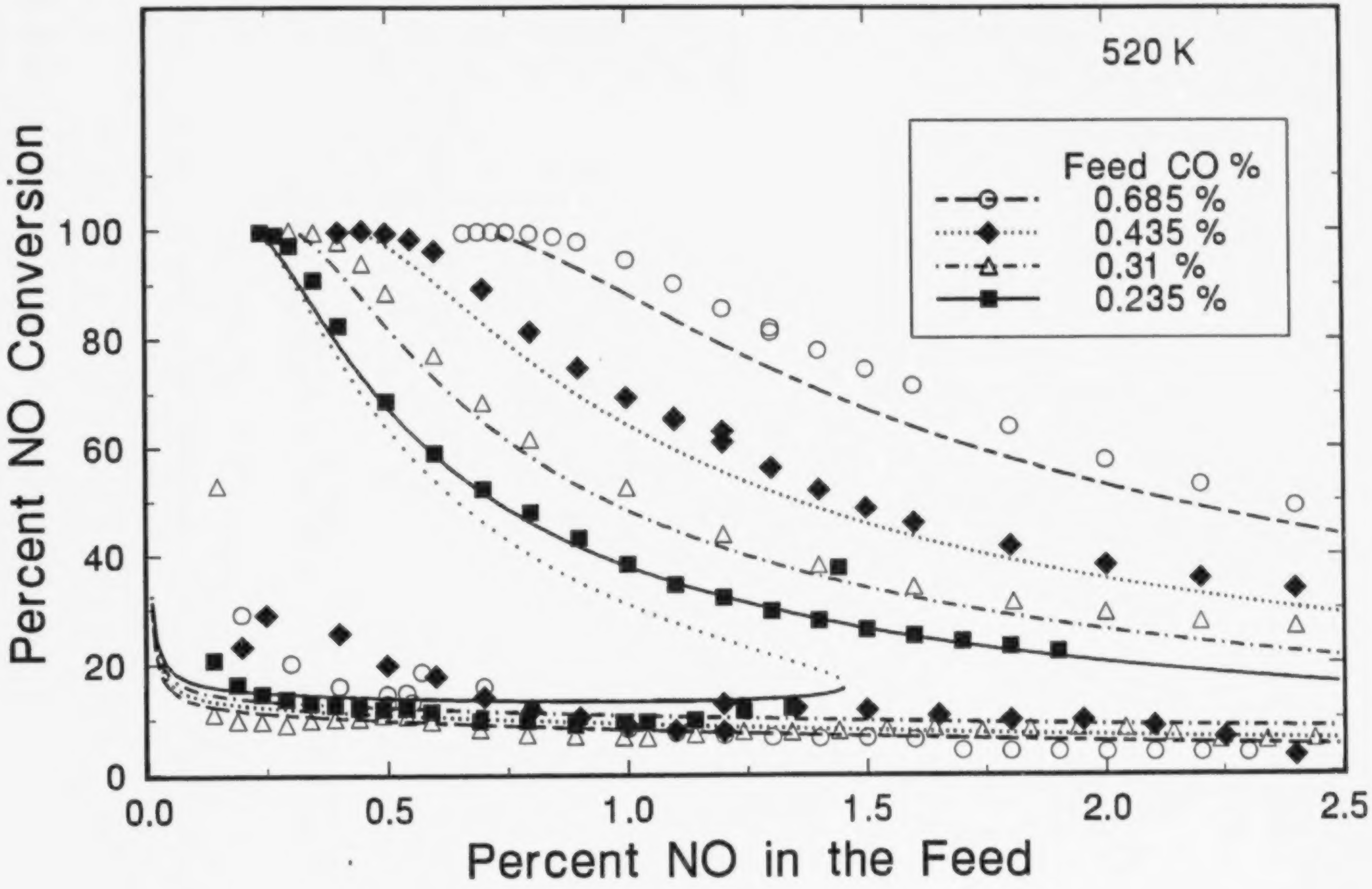

Figure 4.2 NO conversion multiplicity for the NO+CO reaction at 520 K.(— — — — —, ·················, —————, — · — · — predictions of Eqs [4.19-24], · · · · · · · · unstable steady-state predictions of Eqs [4.19-24])

the feed NO was increased from 1.34% to 1.44%. The low-to-high bifurcation points for the other three experiments carried out with feed CO of 0.31%, 0.435% and 0.685%, respectively, were not obtained even when the feed NO was increased to 2.5%. Because of the limitations on the flow meter, NO gas-analyzer (maximum range 0-2.5%) and the maximum NO concentrations in the gas mixtures, the low-to-high bifurcation points were not determined for feeds containing more than 0.235% CO.

4.3.2 CO Conversion

The CO conversions are summarized in Figs 4.3 and 4.4 for the experiments carried out at 465-505 K and at 520 K, respectively. The CO conversions on the high-conversion branch were always near 100% as can be seen from Figs 4.3 and 4.4. As described in the preceding section, for a particular feed NO%, the NO conversion on the high-conversion branches of Fig. 4.1 is limited by the near complete conversion of CO.

On the low-conversion branch of Fig. 4.3, the CO conversion increases gradually with a decrease in feed %CO and then abruptly increases to 100% at the bifurcation point. Therefore, the CO conversion, instead of NO conversion, was used as the criterion to bracket the low-to-high conversion bifurcation points. It can be seen from Fig. 4.3(c) that the three low-to-high bifurcation points at 465 K occurred within a narrower range of feed %CO, as compared with the three bifurcation points at 505 K (Fig.4.3(a)). The low-conversion branches of Fig. 4.4 show that the CO conversion decreases with an increase in feed %CO, which confirms the inhibiting effect of CO on the reaction. These results are very similar to those found for the N_2O+CO reaction described in Chapter 2. A comparison of CO conversion at 520 K with the results in Chapter 2 (Fig. 2.4) indicates that the NO+CO reaction is more strongly inhibited by CO than the N_2O+CO reaction in the low-conversion steady-state region. This could be due to the N_2O and NO decomposition reaction requiring different number of catalytic sites. Therefore, the rate of CO_2 formation for the NO+CO reaction is lower than that for the N_2O+CO reaction in the low-conversion steady-state region. However, for the high-conversion steady-states,

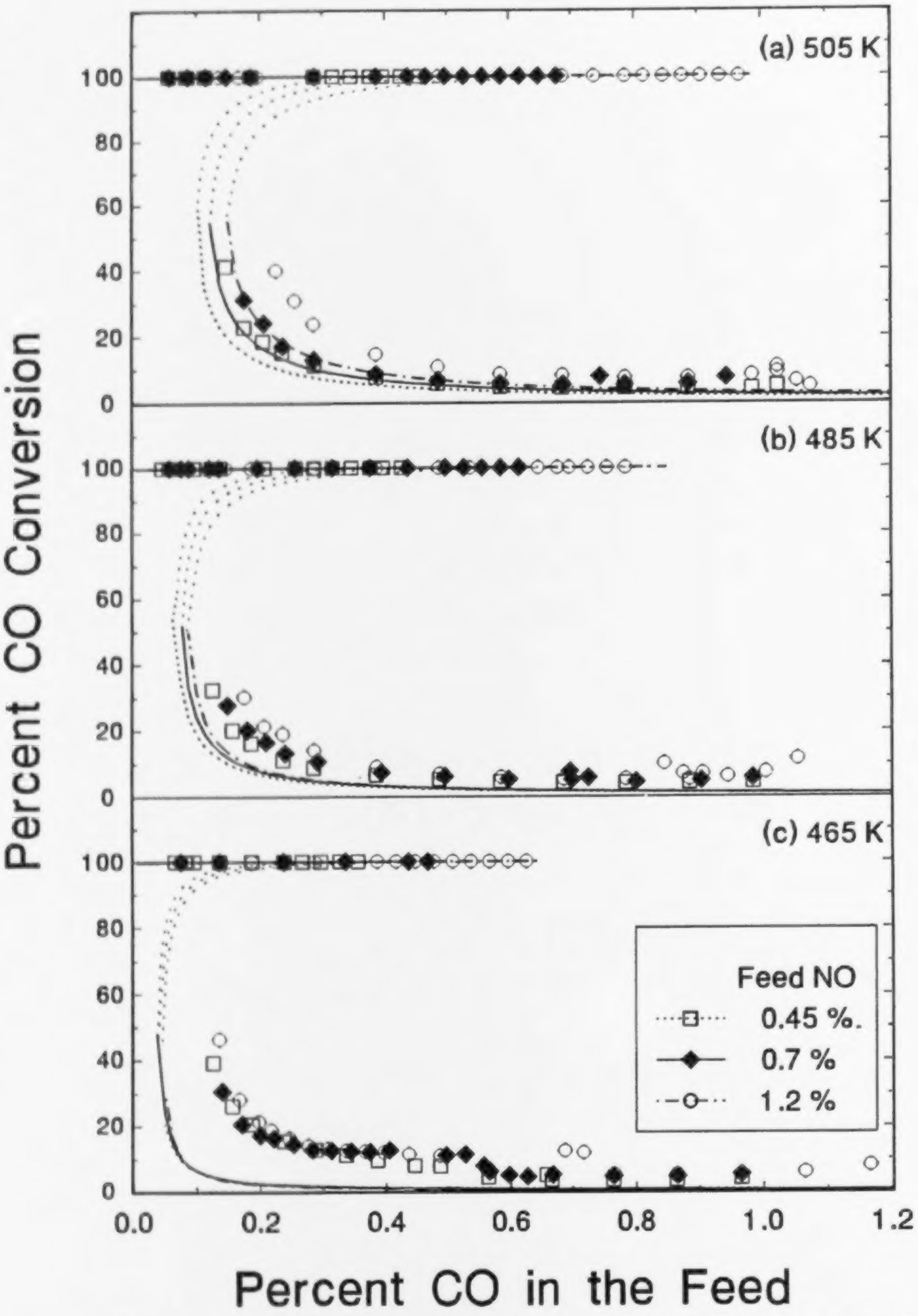

Figure 4.3 CO conversion multiplicity for the NO+CO reaction at 465-505 K. (··················, ——————, — · — · — · predictions of Eqs[4.19-24], · · · · · · · · unstable steady-state predictions of Eqs [4.19-24])

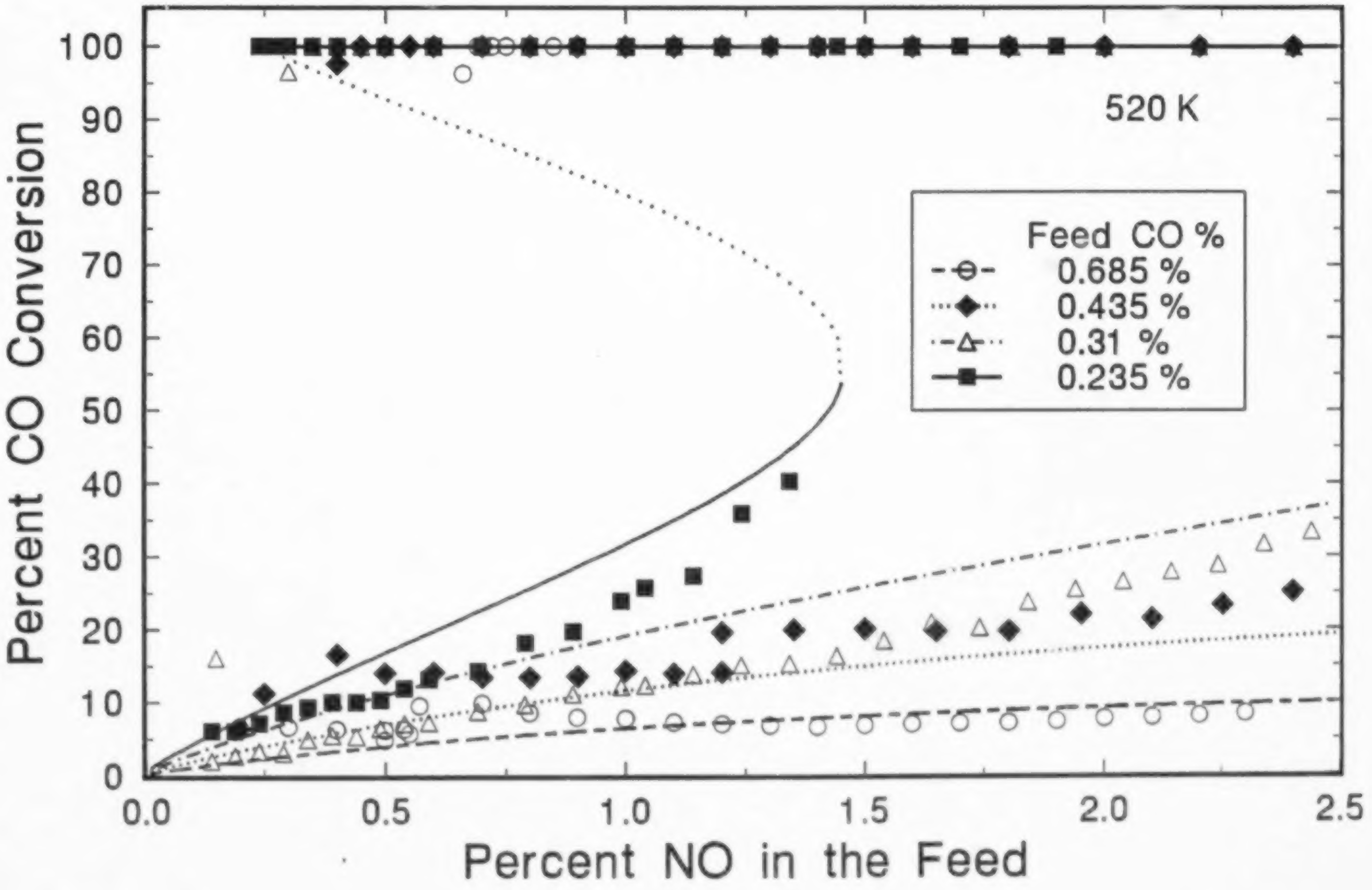

Figure 4.4 CO conversion multiplicity for the NO+CO reaction at 520 K. (— — — — —, ·················, ————————, — · — · — · predictions of Eqs [4.19-24], · · · · · · · · unstable steady-state predictions of Eqs [4.19-24])

the rate of CO_2 formation is limited by near complete conversion of CO and is therefore approximately equal for both of the reactions.

4.3.3 N_2O Selectivity

The reactor N_2O formation is summarized in Figs 4.5 and 4.6 for the experiments carried out at 465-505 K and 520 K, respectively. As can be seen from Fig. 4.5, on the high-conversion branch, N_2O in the reactor increases with an increase in feed %CO and reaches a maximum, after which it decreases with further increases in feed %CO. The maxima in the N_2O curves shift in the direction of increasing feed %CO with an increase in feed NO%. Higher feed NO% also led to higher N_2O% in the reactor.

On the low-conversion branch of Fig. 4.5, the N_2O% in the reactor was very low and N_2O measurement was limited by the range of the gas analyzer (lowest range 0-0.5%). Although, a slight trend of increasing %N_2O with increasing %NO in the feed is apparent from Fig. 4.5(a), there is not a marked dependence of %N_2O on the feed %CO or the temperature for the low-conversion branch.

From Fig. 4.6, it can be seen that, on the high-conversion branch at 520 K, the %N_2O in the reactor decreases gradually with a decrease in %NO in the feed, and then decreases rapidly near the bifurcation point. The reactor N_2O is strongly dependent on feed CO and increases with feed CO%. On the low-conversion branch of Fig. 4.6, the N_2O% decreases slightly with an increase in feed %CO. These observations are consistent with those seen in Fig. 4.5.

The N_2O selectivity is defined as a fraction of the total NO converted to N_2O,

$$Y_{N_2O} = \frac{2[N_2O]}{[NO]_o - [NO]} \qquad (4.5)$$

The N_2O selectivity on the high-rate branch as a function of the ratio of NO to CO in the

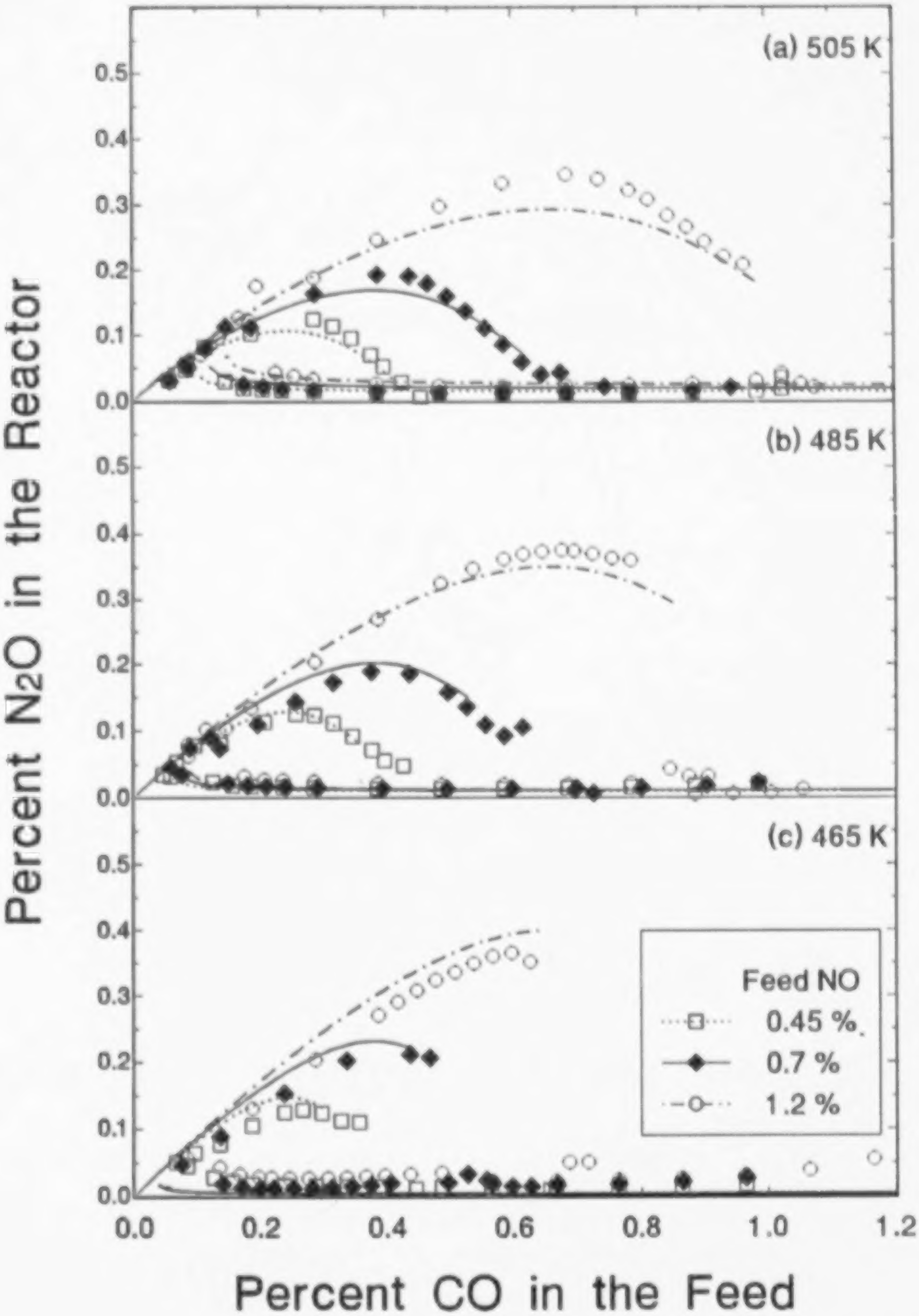

Figure 4.5 Multiplicity of the rate of N_2O formation for the NO+CO reaction at 465 -505 K. (··················, ————, —·—·—· predictions of Eqs [4.19-24])

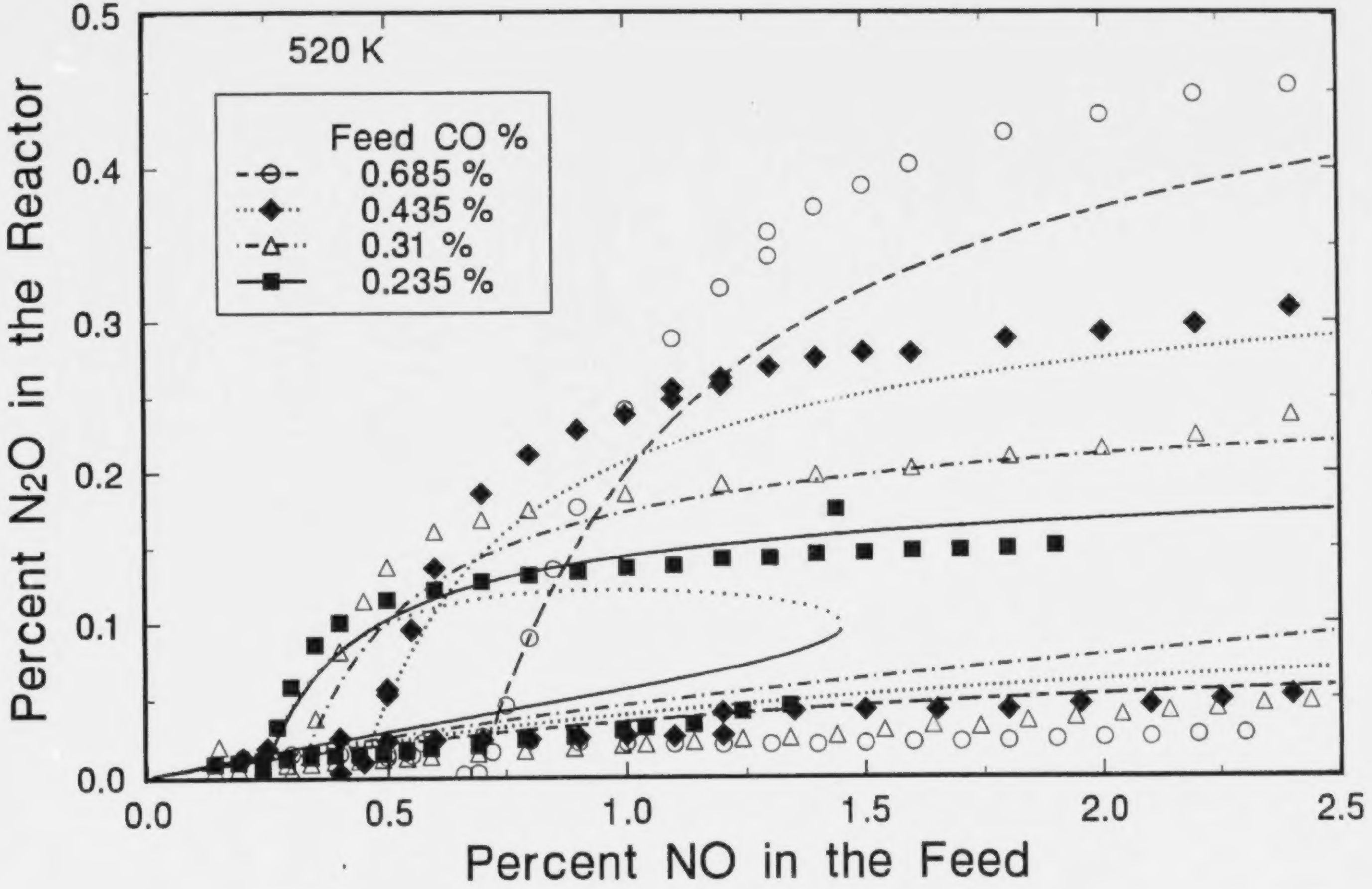

Figure 4.6 Multiplicity of the rate of N_2O formation for the NO+CO reaction at 520 K. (— — — — —, ··················, —————, — · — · — · predictions of Eqs [4.19-24], · · · · · · · · unstable steady-state predictions of Eqs [4.19-24]))

feed is shown in Figs 4.7 and 4.8. Near the bifurcation point, the N_2O selectivity increases strongly with an increase in $[NO]_o/[CO]_o$ as can be seen from Figs 4.7 and 4.8, following which it reaches a plateau. The lowest N_2O selectivity occurs at the high-to-low conversion bifurcation point where the NO conversion is the highest. From Figs 4.7 and 4.8 it appears that the N_2O selectivity on the high-conversion branch is not significantly affected by the temperature in the range of 465-520 K.

4.4 Discussion

4.4.1 Reaction Mechanism

Various mechanisms have been proposed to describe the NO+CO reaction on noble metal catalysts depending upon the experimental conditions used in the studies. For example, the reaction steps for the formation and subsequent dissociation of N_2O were not included in the reaction mechanism used to describe the data when N_2O was not observed or when it was found in insignificant amounts (*12, 18, 24, 36-40*). A mechanism consisting of seven reaction steps given by Eqs. (4.6)-(4.12) is used in this study to describe the observed steady-state multiplicity and the N_2O selectivity

$$CO_{(g)} + M \rightleftharpoons M\text{-}CO \qquad (4.6)$$

$$NO_{(g)} + M \rightleftharpoons M\text{-}NO \qquad (4.7)$$

$$M\text{-}NO + M \rightarrow M\text{-}N + M\text{-}O \qquad (4.8)$$

$$M\text{-}N + M\text{-}N \rightarrow N_{2(g)} + 2M \qquad (4.9)$$

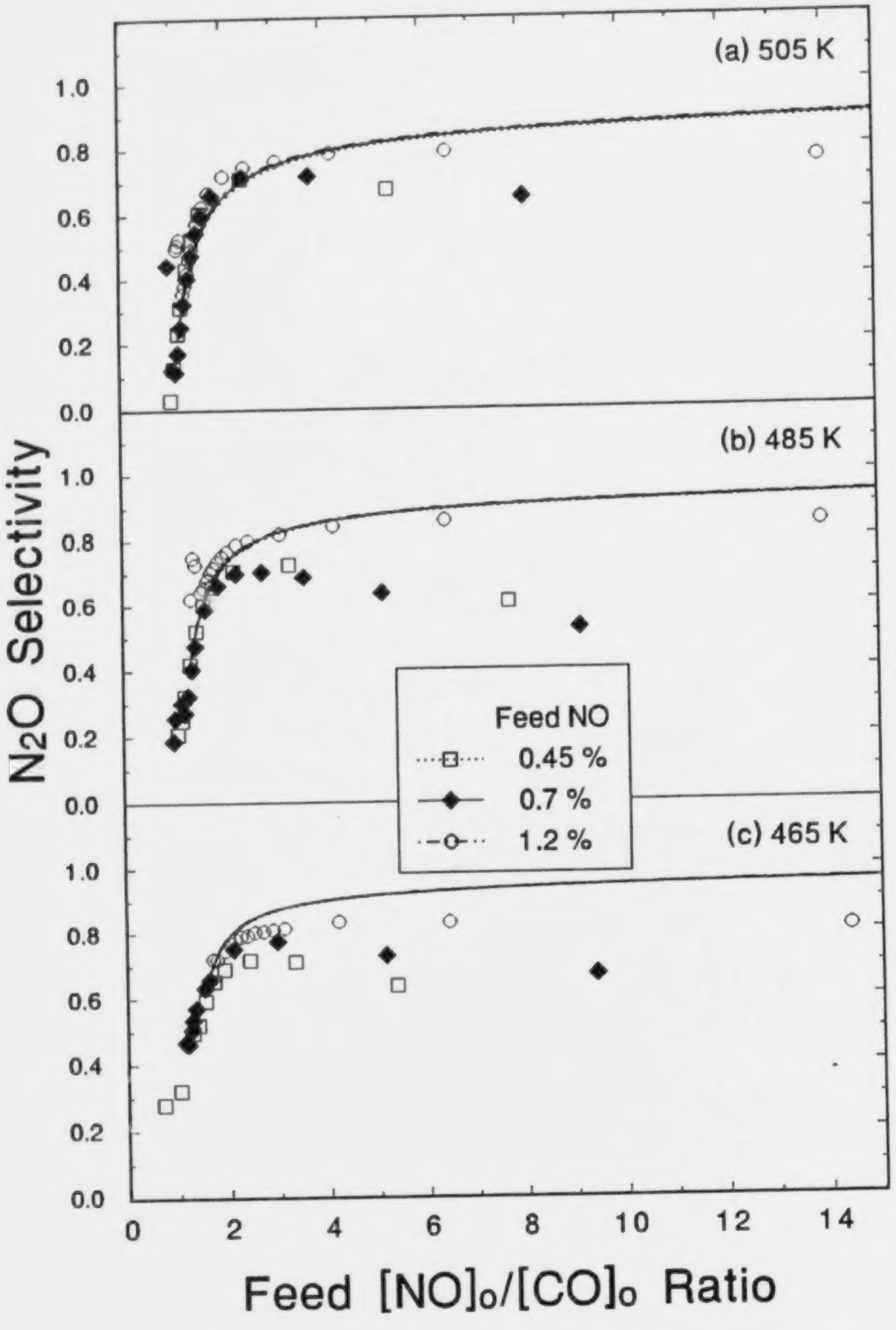

Figure 4.7 N_2O selectivity for the NO+CO reaction at 465-505 K (high-rate branch only). (··················, ——————, — · — · — · predictions of Eqs [4.19-24])

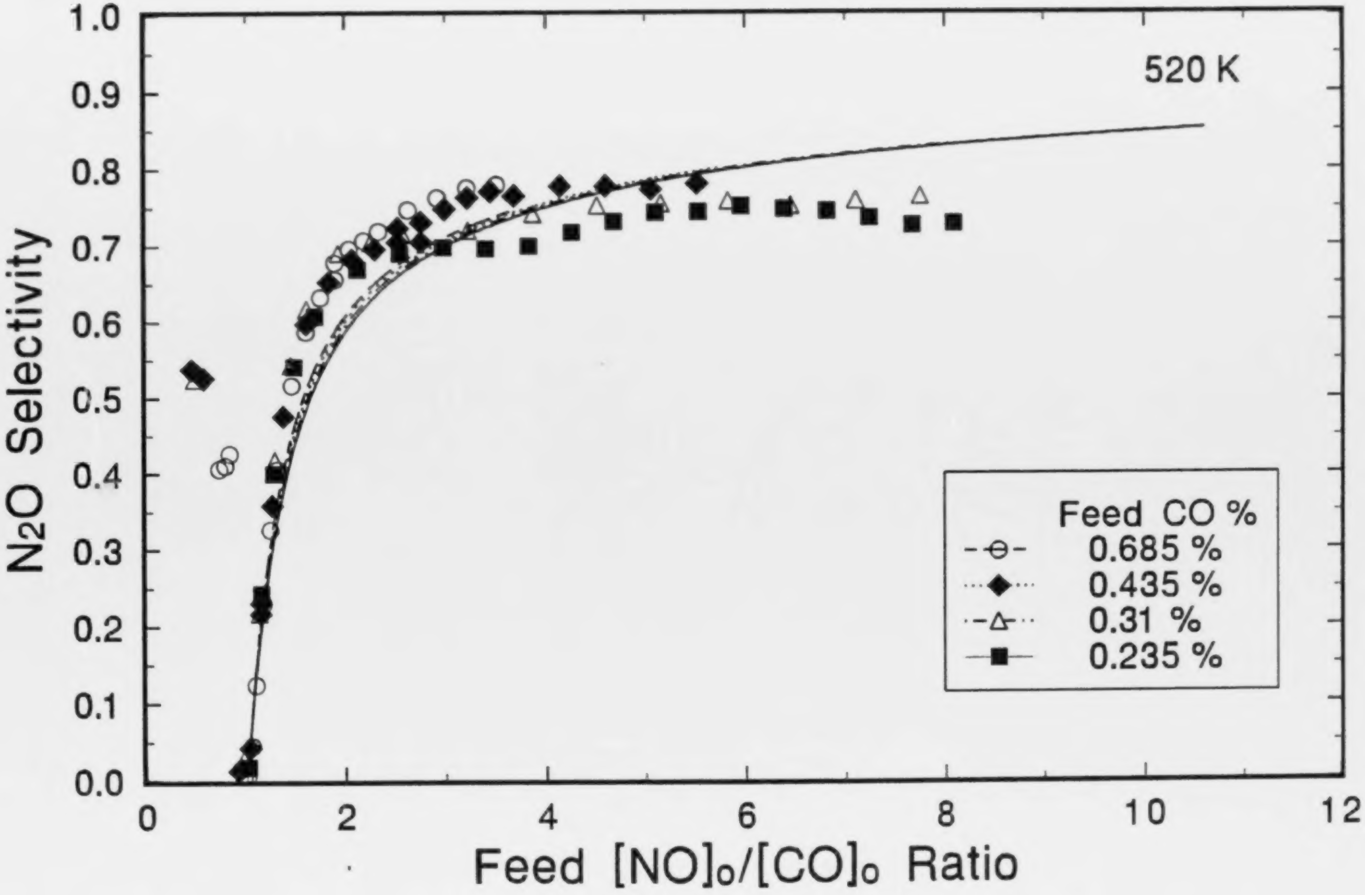

Figure 4.8 N_2O selectivity of NO+CO reaction at 520 K (high-rate branch only).
(— — — — —, ··················, ——————, — · — · — · predictions of Eqs [4.19-24])

$$M\text{-}NO + M\text{-}N \rightarrow N_2O_{(g)} + 2M \qquad (4.10)$$

$$N_2O_{(g)} + M \rightarrow N_{2(g)} + M\text{-}O \qquad (4.11)$$

$$M\text{-}CO + M\text{-}O \rightarrow CO_{2(g)} + 2M \qquad (4.12)$$

The reaction steps involving the reversible chemisorption of CO (Reaction (4.6)), the dissociative adsorption of N_2O (Reaction (4.11)), and the surface reaction for the formation of CO_2 (Reaction (4.12)) are identical to those used previously to describe the N_2O+CO reaction under identical conditions in Chapter 2. The reversible adsorption of NO, the subsequent dissociation of NO and desorption of gaseous N_2 are represented by reaction steps (4.7)-(4.9). The adsorption of NO on platinum has been extensively studied. These studies show that NO adsorbs molecularly on Pt(100) at temperatures lower than 343 K causing (hex ↔ 1x1) phase transition (*41, 42*) and the adsorbed NO layer dissociates into gaseous nitrogen and adsorbed oxygen at temperatures between 450 and 500 K (*18, 42, 43*). Similar observations of dissociative adsorption of NO at temperatures of 454-500 K have been reported for polycrystalline Pt (*44*) and supported platinum catalysts (*45, 46*), although NO does not seem to dissociate on a Pt(111) surface (*47, 48*). The three reactions steps (4.7)-(4.9) have been used by others to describe NO decomposition on Pt (*48, 49*) and the NO+CO reaction on noble metal catalysts (*18, 21, 28, 31, 50, 51*).

The formation of nitrous oxide according to reaction step (4.10) has been suggested by Pirug and Bonzel (*44*) in a study of NO decomposition on polycrystalline Pt and has been used to describe the NO+CO reaction on noble metal catalysts (*20, 21, 51-54*). The desorption of adsorbed oxygen is known to occur at temperatures above 700 K (*18, 45*). Therefore, the oxygen desorption reaction is not included in the proposed mechanism.

Alternative routes for N_2 and N_2O formation during the NO+CO reaction have been suggested in other studies. Chin and Bell (*55*) observed two peaks of N_2 in the TPD spectra of adsorbed NO on a rhodium catalyst. They attributed the high temperature peak to N_2 desorption according to reaction step (4.9) and the low temperature peak to a reaction between adsorbed nitrogen and adsorbed NO as given by reaction step (4.13).

$$M\text{-}N + M\text{-}NO \rightarrow N_{2(g)} + M\text{-}O + M \qquad (4.13)$$

The N_2 formation step, reaction (4.13), has been used alone or together with reaction step (4.9) to describe the NO+CO reaction on noble metal catalysts (*38, 51-54*). Lintz and co-workers (*6, 36, 56*) described the N_2 formation in the overall NO+CO reaction over polycrystalline noble metal catalysts of Pt, Pd and Rh by the following reaction.

$$M\text{-}NO + M\text{-}NO \rightarrow N_{2(g)} + M\text{-}O + M\text{-}O \qquad (4.14)$$

However, based on TPD spectra of adsorbed NO on Pt(100), Fink *et al.* (*12, 18, 37, 50*) assumed the desorption of nitrogen to occur via reaction step (4.9) in their extensive mathematical modelling studies of NO+CO reaction on Pt(100).

The formation of N_2O by decomposition of an NO dimer, according to reaction step (4.15) has been suggested to describe the NO+CO reaction over supported Pt catalysts at 300 K (*22*). However, it is not known if such a reaction occurs to any significant extent at the temperatures used in this study.

$$M\text{-}NO + M\text{-}NO \rightarrow M\text{-}(NO)_2 + M \rightarrow N_2O_{(g)} + O\text{-}M + M \qquad (4.15)$$

Klein *et al.* (*24*) suggested a bimolecular reaction according to Eq. (4.16) to describe the steady-state reaction kinetics of the NO+CO reaction over polycrystalline Pt over a wide range of temperatures, pressures and reactant partial pressures.

$$M\text{-}NO + M\text{-}CO \rightarrow CO_{2(g)} + M\text{-}N + M \qquad (4.16)$$

The bimolecular reaction step (4.16) was also identified as a rate limiting step in the NO+CO reaction on polycrystalline Pt (*39, 40, 57*). However, Lambert and Comrie (*20*) and Fink *et al.* (16) did not find any evidence of such a bimolecular reaction in their study of NO+CO reaction on single crystal Pt catalysts.

Apart from the various reaction steps discussed above, isocyanate species have been observed during infrared studies of the NO+CO reaction on supported noble metal catalysts (*21, 23, 53, 58-61*). The surface isocyanate species (Rh-NCO) have been found on supported Rh catalysts (*53, 59*) and therefore an additional reaction of isocyanate formation according to Eq. (4.17) was proposed (*53*) in the description of the NO+CO reaction.

$$M\text{-}N + CO_{(g)} \rightleftharpoons M\text{-}NCO \qquad (4.17)$$

However, it has been reported (*53*) that the Rh-NCO species is very unstable and the isocyanate groups move from the rhodium microcrystallites and spill over on to the silica support to form a more stable Si-NCO species, particularly under the conditions where the partial pressure of NO is lower than that of CO. Brown and Gonzales (*58*) did not observe isocyanate formation on silica supported Pt at 300 K. However, Solymosi *et al.* (*23*) observed stable isocyanate formation on silica-supported Pt at 573 K. They also found that the stability of the isocyanate complexes is sensitive to the support. The isocyanate species were found to be more stable for silica-supported Pt than for alumina-supported Pt. It has been suggested that the isocyanate formed on Pt surfaces can migrate to the alumina support (*23, 62*). It has been proposed (*21*) that the loss of catalyst activity under reducing condition is associated with a change in the electronic properties of the supported Pt crystallites, caused by the accumulation of large concentrations of isocyanate groups on the support in the areas adjacent to the crystallites. Lorimer and Bell (*21*) did not account for the formation of NCO groups while describing the NO+CO reaction over Pt/SiO_2 catalyst at 573 K, because only a fraction of NO consumed was associated with the formation of isocyanate. Chang and Hegedus (*60*) reported that a large fraction of the catalyst surface is covered by isocyanate species, which did not appear to participate in the NO+CO reaction over Pt/Al_2O_3 at a temperature of 723 K. In this study the isocyanate formation reactions have not been included in the reaction mechanism because of the uncertainty of the exact role that the isocyanates play in the NO+CO reaction over a supported Pt catalyst.

4.4.2 Mathematical Model

The proposed mechanism described by reaction steps (4.6)-(4.12) includes three reactions, namely, elementary steps (4.6), (4.11) and (4.12), respectively, which were used previously to describe the steady-state multiplicity of the N_2O+CO reaction in Chapter 2. Therefore, the kinetic model developed in Chapter 2 for the N_2O+CO reaction was considered as an integral part of the model development for the NO+CO reaction. As with the N_2O+CO reaction, it was necessary to include the CO self-exclusion effect in the model, particularly to describe the data for the low-conversion steady states. As described earlier in Chapter 2, the CO self-exclusion effect allows NO to adsorb on a Pt surface saturated with CO. The CO self-exclusion effect was incorporated into the model for the NO+CO reaction by modifying the rate expression for CO adsorption according to Eq. (4.18) which is identical to Eq. (2.23) which is used in Chapter 2 for the N_2O+CO reaction.

$$r_{CO,\,ads} = k_6 L[CO]\theta_V \frac{(1-N_{CO}\theta_{CO})}{(1-\theta_{CO})} \tag{4.18}$$

All parameters used in the equations are defined in the **Notation** section. The experimental conditions of temperature, feed composition and conversions, used in this study are similar to those used previously for the N_2O+CO reaction steady-state experiments (*32*), where it was shown that the internal and external mass transfer effects were negligible. Therefore, it has been assumed that the experimental results obtained in this study represent the intrinsic kinetics of the reaction. The recycle reactor has been assumed to be an ideal CSTR and the volume changes due to reaction have been neglected. Based on the preceding assumptions, the mass balance equations for the adsorbed CO, atomic oxygen, NO and atomic nitrogen species are given by Eqs (4.19)-(4.22), respectively.

$$k_6 L[CO]\theta_V \frac{(1-N_{CO}\theta_{CO})}{(1-\theta_{CO})} - k_{-6}L\theta_{CO} - k_{12}L^2\theta_O\theta_{CO} = 0 \qquad (4.19)$$

$$k_8 L^2\theta_{NO}\theta_V + k_{11}L[N_2O]\theta_V - k_{12}L^2\theta_O\theta_{CO} = 0 \qquad (4.20)$$

$$k_7 L[NO]\theta_V - k_{-7}L\theta_{NO} - k_8 L^2\theta_{NO}\theta_V - k_{10}L^2\theta_{NO}\theta_N = 0 \qquad (4.21)$$

$$k_8 L^2\theta_{NO}\theta_V - k_9 L^2\theta_N^2 - k_{10}L^2\theta_{NO}\theta_N = 0 \qquad (4.22)$$

The mass balance equations for the gas-phase NO, N_2O and CO_2 species are given by Equations (4.23), (4.24) and (4.25), respectively.

$$Q[NO]_o - Q[NO] = ak_7 L[NO]\theta_V - k_{-7}L\theta_{NO} \qquad (4.23)$$

$$Q[N_2O] = ak_{10}L^2\theta_{NO}\theta_N - ak_{11}L[N_2O]\vartheta_V \qquad (4.24)$$

$$Q[CO_2] = Q[CO]_o - Q[CO] = ak_{12}L^2\theta_{CO}\theta_O \qquad (4.25)$$

The fractional concentration of vacant surface sites, θ_V, is given by:

$$\theta_V = 1 - \theta_{CO} - \theta_O - \theta_{NO} - \theta_N \qquad (4.26)$$

If the overall reaction is represented by the two reactions according to Eqs (4.1) and (4.2), then the steady-state gas-phase mass balance leads to:

$$Q([NO]_o - [NO]) = Q([CO]_o - [CO]) + Q[N_2O] \qquad (4.27)$$

Equation (4.27) is also valid if the overall reaction is described by the two reactions according to Eqs. (4.2) and (4.3). Equation (4.4), used earlier to describe the calculation of NO conversion, can be easily derived from Eq. (4.27). For steady-state calculations, it is sufficient to solve a set of six equations, namely Eqs. (4.19)-(4.24), after expressing θ_V and [CO] in terms of θ_{CO}, θ_O, θ_{NO}, θ_N, [NO] and [N_2O] through the use of Eqs. (4.26) and (4.27). Equations (4.19)-(4.24) were solved by the Newton-Raphson method using MATLAB programs listed in Appendix G. The values of the ten parameters, namely, k_6, k_{-6}, k_7, k_{-7}, k_8, k_9, k_{10}, k_{11}, k_{12} and N_{CO} are of course required to solve the equations. The parameter values were obtained by an iterative approach. Because of large relative uncertainty in the data for the low-conversion branch, only the data for the high conversion branch was used to obtain initial estimates of the parameter values at each temperature. The parameter values were then adjusted to describe the data on both the high-conversion and the low conversion branches while reducing the sum of squared error in the prediction of the bifurcation points. The effect of individual parameters on the model prediction was studied by individually increasing the value of each parameter by at least 5 times the original value, except for N_{CO} which was increased by 10%. The effects of increasing the individual parameter values on the model predictions for the low-conversion and high-conversion steady-states are listed in Table 4.1.

Table 4.1

Effect of Increasing the Value of a Parameter on the Model Predictions

Parameter	High-Conversion Branch			Low-Conversion Branch		
	NO Conv.	%N_2O	High-to-Low Bifurcation pt.	NO Conv.	%N_2O	Low-to-High Bifurcation pt.
k_6	-	-	-	↓	↓	↓
k_{-6}	-	-	-	↑	↑	↑
k_7	↑	↑	↓	↑	↑	↑
k_{-7}	↓	↓	↓	↓	↓	↓
k_8	↓	↓	↓	↑	↑	↑
k_9	↓	↓	↑	-	-	-
k_{10}	↑	↑	↑	-	-	↑
k_{11}	↓	↓	↑	-	-	-
k_{12}	-	-	↑	-	-	-
N_{CO}	-	-	-	↑	↑	↑

The upward-pointing arrows (↑) in Table 4.1 indicate an increase while the downward pointing arrows (↓) indicate a decrease in the predicted values. In Table 4.1 the dashes indicate that the effect of the change in a particular parameter value was insignificant. As can be seen from Table 4.1, the parameters k_6, k_{-6} and N_{CO} affected the model predictions only on the low-conversion branch while the parameters k_9, k_{11} and k_{12} affected the predictions only on the high-conversion branch. The remaining parameters, namely, k_7, k_{-7}, k_8 and k_{10} have an influence on the model predictions both for the low-conversion and the high-conversion steady-states. The effect of decreasing the individual parameter values was exactly opposite of that shown in Table 4.1.

In determining the parameter values at the four different temperatures used in this study, the parameters were forced to follow an Arrhenius-type temperature relationship. A constant value of 1.05 was used for the CO self-exclusion factor, N_{CO}, irrespective of temperature. The values of the rate constants used in this study are not the true optimum values because similar model predictions are possible with other sets of dissimilar rate constants. A similar observation was made earlier in the modelling study of the N_2O+CO reaction multiplicity behavior in Chapter 2.

The model predictions for NO conversion are shown by the curves in Figs. 4.1 and 4.2. As can be seen from Fig. 4.1, the predicted NO conversions are in good agreement with the experimental data for the high-conversion steady-states. However, the model predictions in the low-conversion region are consistently lower than the experimental values. The model-experimental discrepancy was the largest at the lowest temperature of 465 K used in this study. The model predictions at 520 K are in good agreement with the experimental data for both the high-conversion and the low-conversion regions, as can be seen from Fig. 4.2. The model also predicts an unstable steady-state as shown by the dotted curve connecting the two bifurcation points on Fig. 4.2. The unstable steady-state predictions are not shown in Fig. 4.1 for reasons of clarity.

It can be seen from the curves in Fig. 4.3 that the model-experimental comparison for CO conversion is very similar to that for NO conversion. The CO conversions on the low-conversion branch and the low-to-high bifurcation points predicted by the model are consistently lower than the experimental values. However, the model qualitatively predicts the effect of feed NO on the low-to-high bifurcation point locations with all three low-to-high bifurcation points clustered together in a narrow range of feed %CO at 465 K while at 505 K, the three bifurcation points are clearly separated.

The model predictions for N_2O% in the reactor are shown by the curves in Figs. 4.5 and 4.6. In general, good model-experiment agreement can be found for the high conversion branches of Figs. 4.5 and 4.6. The model also predicts the maxima in the N_2O

curves. On the low-conversion branches, the model predicts that the feed NO has negligible effect on reactor N_2O% at 465 K and a more pronounced effect at 520 K. For clarity, the unstable steady-state predictions of the model are not shown in Fig. 4.5.

It was not possible to match the model predictions with the experimental data on the low conversion branch while following an Arrhenius-type temperature dependency of the rate constants and trying to match the bifurcation points and the high-conversion data. The incorporation of the CO self-exclusion effect in the model improved the predictions for the low-to-high conversion bifurcation points. A higher value of the CO self-exclusion factor, N_{CO}, will of course improve the predictions at 465 K but will result in an increased model-experimental discrepancy at 520 K. Therefore a compromise value of N_{CO}=1.05 was used. It is possible to obtain very good model-experimental agreement using different values of rate constants for the high-conversion and low-conversion branches. For example, by using two different values of the activation energy for NO desorption (E_{-7}) alone, it was possible to obtain an overall good model-experimental agreement. It may also be possible to use the concept of adsorbate-induced surface-phase-transition, as described earlier in Chapter 3 for the N_2O+CO reaction, to obtain a better model-experimental agreement. Because of a high degree of uncertainty for the low-conversion data, any model assumption made to fit the entire experimental data, will have to be validated by additional data, particularly from transient experiments. Nevertheless the simple model proposed here describes the majority of the experimental data in this study.

The rate constants used in the model followed an Arrhenius-type of temperature dependency as can be seen from Fig. 4.9. The activation energies and the pre-exponential factors found from the Arrhenius curves in Fig. 4.9 are listed in Table 4.2. The units of the pre-exponential factors listed in Table 4.2 can be found in the **Notation** section.

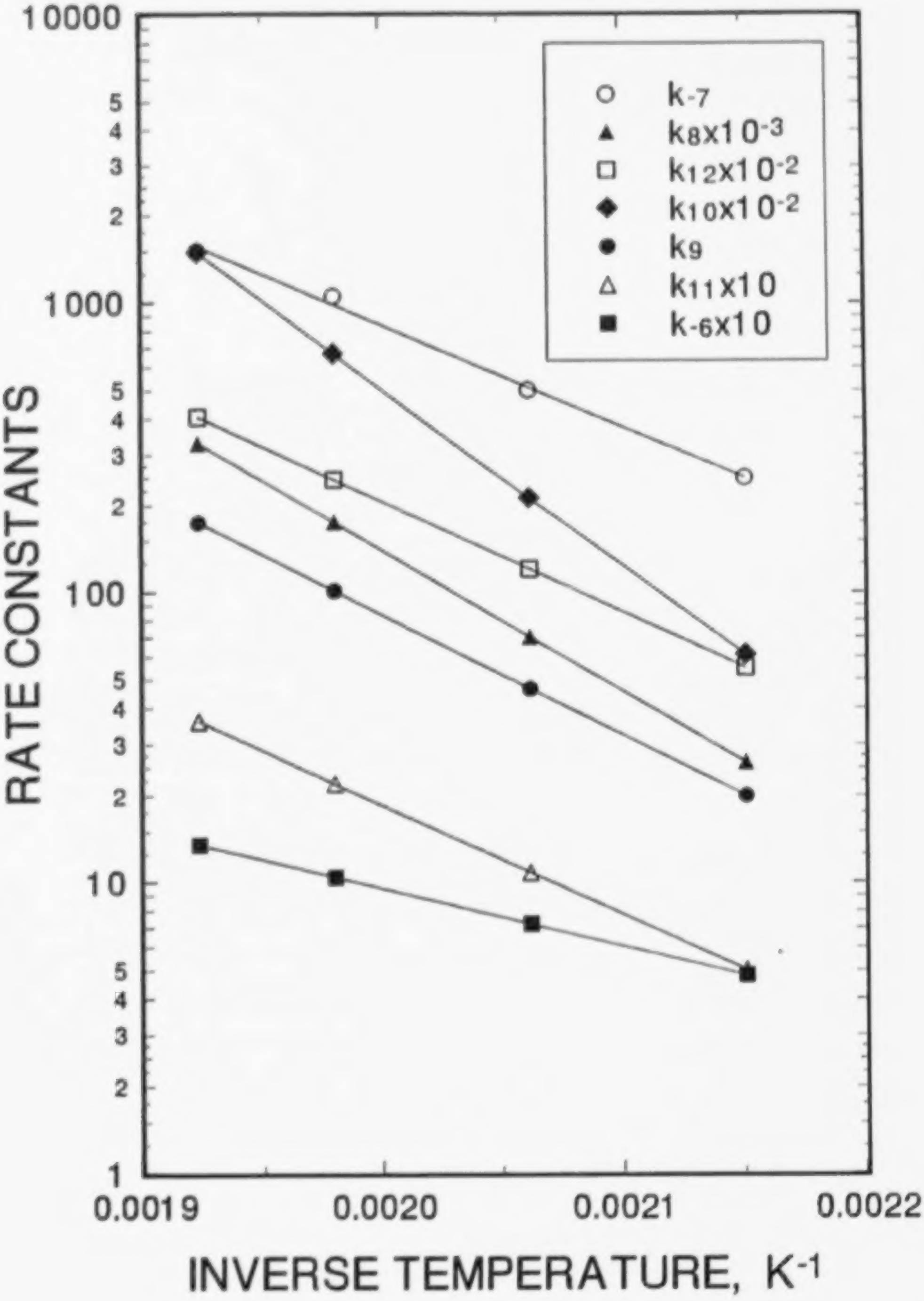

Figure 4.9 Arrhenius Plot of Rate Constants

Table 4.2

Kinetic Parameters

Rate Constant	Activation Energy E_i, kJ/mol	Pre-exponential factor, k_i^o
k_{-6}	37.78	8,440
k_{-7}	66.82	8.051×10^{9}
k_{8}	116.81	8.072×10^{17}
k_{9}	79.06	1.522×10^{10}
k_{10}	92.93	7.156×10^{13}
k_{11}	72.20	6.447×10^{7}
k_{12}	73.14	9.050×10^{11}

The values of the activation energies listed in Table 4.2 are in the range of the values used in other studies. As found earlier in Chapters 2 and 3 for the N_2O+CO reaction system, a low value of the activation energy for CO desorption, E_{-6} (37.8 kJ/mol), was again necessary to describe the low-conversion branch. A similar observation of a low value of E_{-6} for high CO surface coverage has been made in a study of the NO+CO reaction on platinum foils (*40*). The values of the activation energies for the N_2O dissociation reaction (Reaction step (4.11)), E_{11}, and surface reaction (Reaction step (4.12)), E_{12},are comparable to the values used for the N_2O+CO reaction in Chapters 2 and 3. The activation energy for NO desorption, E_{-7} (66.8 kJ/mol), is slightly lower than the values obtained from the literature, namely, 85-105 kJ/mol on Pt(111) (*20, 43, 47*), 150 kJ/mol on Pt(100) (*43*) and 138 kJ/mol on polycrystalline platinum (*20*). However, it has been observed that the presence of co-adsorbed CO lowers the NO desorption temperature by as much as 100 K (*48*) on Pt(111) which indicates that the co-adsorption of CO lowers the activation energy for NO desorption. Therefore, a low value of the NO desorption activation energy used in this study could possibly be due to the interaction of adsorbed CO. The value of the activation energy for NO dissociation, E_8 (116.8 kJ/mol) closely matches the value of 117 kJ/mol found by Pirug and Bonzel (*44*) in their flash-desorption studies of NO on polycrystalline platinum. The value of the activation energy for the N_2O formation reaction, E_{10}, is not readily available in the literature. However, a value of 77.4 kJ/mol for E_{10} has been used previously (*55*) for modelling of the NO+CO reaction over Rh/SiO_2 catalyst as against a value of 92.9 kJ/mol used in this study. Finally, the activation energy for nitrogen desorption, E_9, compares favourably with the values reported in the literature, namely, 88 kJ/mol on carbon supported Pt (*49*) and 105±12.5 kJ/mol for crystalline Pt (*63*).

4.4.3 N_2O selectivity

The model predictions for the N_2O selectivity on the high-rate branch of steady states are shown in Figs 4.7 and 4.8. It can be seen that the model adequately describes the experimental data for the high-conversion steady states. The model also predicts that the feed NO% does not significantly affect the N_2O selectivity at a particular temperature and $[NO]_o/[CO]_o$ ratio, as can be seen by the significant overlapping of the three model curves corresponding to the three different values of the feed NO% in Fig. 4.7. The lowest N_2O selectivity is predicted to occur at the high-to-low bifurcation point where NO conversion is the highest. A similar relationship between N_2O selectivity and $[NO]_o/[CO]_o$ ratio was observed by Muraki *et al.* (*54*) in their study of the NO+CO reaction on Pd/Al_2O_3 catalyst. The experimental results for the high-conversion steady-states in Figs 4.7 and 4.8 show an insignificant effect of temperature on the N_2O selectivity although the model predicts a small decrease in selectivity with temperature. A similar observation regarding an insignificant influence of temperature on N_2O selectivity for the NO+CO reaction on Rh(111) catalyst has been made in the temperature range of 525-675 K (*51*). However, a decrease in N_2O selectivity with an increase in temperature for a stoichiometric feed mixture has also been reported from composition cycling experiments (*27, 28*).

It was found that the model predictions on the high-rate branch are not affected significantly by deleting the nitrogen desorption step (Reaction step (4.9)) from the reaction mechanism. This is because the rate constant k_9 is at least two orders of magnitude smaller than the rate constant k_{10} as can be seen from the values given in Table 4.2. Therefore, from the θ_N balance, Eq. (4.22), the rate of the NO dissociation reaction (Reaction step (4.8)) must be approximately equal to the rate of the N_2O formation reaction (Reaction step (4.10)). This suggests that, at least for the high-rate branch, the entire reaction process can be represented by the two reactions given by Eqs. (4.2) and (4.3). Cho (*31*) also reached a similar conclusion after a mechanistic analysis of the NO+CO reaction system. Shelef and Otto (*26*) observed that the N_2O concentration passed through a peak as the reactor temperature was increased when a feed containing a stoichiometric excess of NO was reduced by CO over supported Pt catalyst. They suggested that the observed N_2O peak can be explained by considering that the reaction proceeds according to two consecutive processes given by Eqs. (4.2) and (4.3) over the whole temperature range.

An analysis of the experimental data of N_2O formation in Fig. 4.5 shows that the reactor N_2O for the high-conversion branch can be approximately related to the feed composition by the following two equations.

$$[N_2O] = \frac{[CO]_o}{2} \qquad for\ [CO]_o \leq \frac{2}{3}[NO]_o \qquad (4.28)$$

$$[N_2O] = [NO]_o - [CO]_o \qquad for\ [CO]_o > \frac{2}{3}[NO]_o \qquad (4.29)$$

The maximum in N_2O curves in Fig. 4.5 occur at the point of intersection of two lines defined by Eqs (4.28) and (4.29) at which the feed composition ratio of $[NO]_o/[CO]_o$ equals 1.5. Therefore, the N_2O formation for the high conversion branch can be approximately described by a single quadratic equation (4.30) which has two roots defined by Eqs. (4.28) and (4.29).

$$2[N_2O]^2 + B[N_2O] + C = 0 \qquad (4.30)$$

where

$$B = [CO]_o - 2[NO]_o \qquad (4.31)$$

and

$$C = [CO]_o([NO]_o - [CO]_o) \qquad (4.32)$$

The reactor N_2O concentration calculated by Eq. (4.30) is compared with the experimental data at 485 K and 520 K in Fig. 4.10 as a function of the feed composition. It can be seen from Fig. 4.10 that Eq. (4.30) which was based on the data at 465-505 K also approximately describes the data at 520 K. It is also apparent from Fig. 4.10 that the rate of N_2O formation decreases rapidly and linearly with a decrease in the $[NO]_o/[CO]_o$ ratio below 1.5. However, for $[NO]_o/[CO]_o>1.5$, the rate of N_2O formation may increase or decrease with a decrease in the composition ratio depending on whether the feed CO is increased or the feed NO is decreased. From the above results it can be easily shown that the highest N_2O selectivity of 0.667 occurs in the high-conversion steady-state region for the feed composition ratio of $[NO]_o/[CO]_o\geq 1.5$, and that the N_2O selectivity gradually decreases as the feed composition ratio of $[NO]_o/[CO]_o$ is gradually reduced to a value corresponding to the high-to-low conversion bifurcation.

It was earlier shown that the overall reaction can be assumed to proceed according to two consecutive reactions of N_2O formation and subsequent disappearance according to Eqs. (4.2) and (4.3), respectively. Therefore, from the preceding analysis it is possible to draw certain conclusions for the high-conversion steady-state region where CO conversion is approximately 100%. For the feed composition with $[NO]_o/[CO]_o\geq 1.5$, it can be easily seen from Eqs. (4.27) and (4.29) that the NO conversion is also 100% along

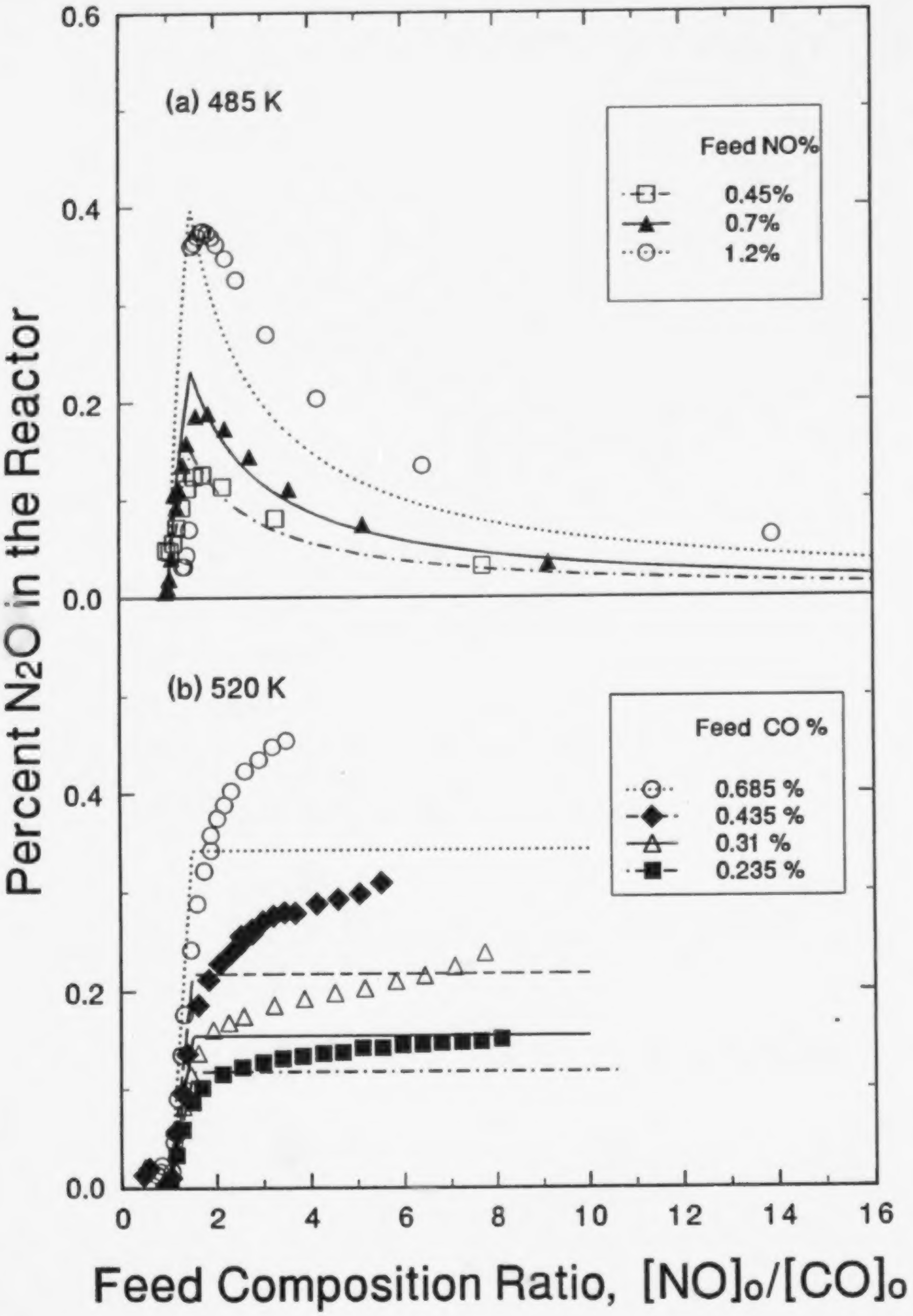

Figure 4.10 Reactor N_2O concentration for the high-conversion steady-state of NO+CO reaction. (— — — — —, ………………, ————————, — · — · — · predictions of Eq. [4.30])

with CO conversion of 100%. Secondly, for the feed composition with $[NO]_o/[CO]_o=1.5$, it can be shown from Eqs. (4.28) and (4.29) that 75% of the total CO reacts via reaction of Eq. (4.2) to form N_2O. The extent of CO conversion by reaction (4.2) gradually decreases from 75% as the ratio $[NO]_o/[CO]_o$ is gradually decreased below 1.5 until the high-to-low conversion bifurcation point is reached. Therefore, the extent of CO conversion by NO+CO reaction according to Eq. (4.2) varies between 50% and 75% of the total CO conversion in the high-conversion steady-state. These results show that the N_2O+CO reaction according to Eq. (4.3) occurs to a significant extent and is therefore an important sub-reaction of the overall NO+CO reaction.

4.5 Conclusions

Although reaction rate multiplicity for the NO+CO reaction with respect to variation in temperature has been reported in the literature (*10-12*), this study shows that the NO+CO reaction also exhibits isothermal steady-state multiplicity with respect to variation in feed composition in the temperature range 465-520 K. As with the N_2O+CO reaction described earlier in Chapter 2, a high-conversion steady state is obtained when the initial feed contains NO in excess of CO (net oxidizing feed). For an initial feed containing CO in excess of NO (net reducing feed), low steady-state conversions were obtained. N_2O was formed as a reaction product in all of the experiments although significantly larger amounts of N_2O are observed for the high-conversion steady-states. An interesting observation for the high conversion steady states was that the reactor N_2O-concentration increased with an increase in the feed CO up to a certain maximum and then gradually decreased with further increases in the feed CO. In the region of low-conversion steady states, the NO+CO reaction is more strongly inhibited by CO than the N_2O+CO reaction.

A kinetic model based on a reaction mechanism consisting of seven reaction steps qualitatively describes the observed reaction behavior and also quantitatively predicts most of the experimental results. The CO self-exclusion effect was incorporated in the model to describe the low-to-high conversion bifurcation behavior in a manner similar to that used previously for the N_2O+CO reaction in Chapter 2. A simplified analysis of the data suggests that the rate of N_2O formation decreases rapidly as the ratio of NO to CO concentrations in the feed drops below a critical value of approximately 1.5. It is also shown that the overall reaction process can be adequately described by two consecutive reactions, namely, the reduction of NO by CO to form N_2O according to Eq. (4.2) and subsequent reduction of N_2O by CO according to Eq. (4.3). The N_2O selectivity was found to be a strong function of the ratio of NO to CO in the feed. The N_2O selectivity was the lowest for a feed composition near the high-to-low conversion bifurcation point where the NO conversion was a maximum. The effect of temperature on N_2O selectivity was negligible in the temperature range 465-520 K. The major effect of temperature on the reaction behavior was a shift of the high-to-low conversion bifurcation points towards a higher ratio of CO to NO concentrations in the feed. Multiplicity occurred for a wider range of feed compositions for the NO+CO reaction as compared with that for the N_2O+CO reaction studied earlier (*32*).

4.6 Notation

a	total Pt surface area of supported catalyst, 9.4 m^2
E_i	activation energy for the ith forward reaction
E_{-i}	activation energy for the ith reverse reaction
k_i^o	pre-exponential factor for the rate constant, k_i, units same as k_i
k_{-i}^o	pre-exponential factor for the rate constant k_{-i}, units same as k_i
k_6	CO adsorption rate constant, $6.87 S_{CO} T^{0.5}/L$, $m^3/mol \cdot s$
k_{-6}	CO desorption rate constant, $k_{-6}^o \exp(-E_{-6}/RT)$, s^{-1}
k_7	NO adsorption rate constant, $6.64 S_{NO} T^{0.5}/L$, $m^3/mol \cdot s$
k_{-7}	NO desorption rate constant, $k_{-7}^o \exp(-E_{-7}/RT)$, s^{-1}
k_8	NO-M dissociation rate constant, $k_8^o \exp(-E_8/RT)$, $m^2/mol \cdot s$
k_9	nitrogen desorption rate constant, $k_9^o \exp(-E_9/RT)$, $m^2/mol \cdot s$
k_{10}	N_2O formation rate constant, $k_{10}^o \exp(-E_{10}/RT)$, $m^2/mol \cdot s$
k_{11}	N_2O dissociation rate constant, $k_{11}^o \exp(-E_{11}/RT)$, $m^3/mol \cdot s$

k_{12}	CO_2 formation rate constant, $k_{12}^{o}\exp(-E_{12}/RT)$, m^2/mol·s
L	adsorption capacity of platinum surface, 2×10^{-5} mol/m^2
M	vacant site on platinum surface
M-X	adsorbed species X (X= CO, NO, nitrogen or oxygen) on platinum catalyst surface
N_{CO}	CO self-exclusion factor, 1.05 in this study
Q	total feed flow rate to the reactor at reactor conditions, $1.11\times10^{-8}T$ m^3/s
$r_{CO,\,ads}$	rate of CO adsorption, mol/m^2·s
R	gas constant, 8.314 J/mol·K
S_{CO}	CO sticking probability on platinum, 0.01
S_{NO}	NO sticking probability on platinum, 0.01
T	reactor temperature, K
Y_{N_2O}	N_2O selectivity
[X]	concentration of gas phase species X (X=CO, NO, N_2, N_2O or CO_2) in the reactor, mol/m^3
$[X]_o$	concentration of gas phase species X (X=CO, NO, N_2, N_2O or CO_2) in the feed, mol/m^3
$X_{(g)}$	gas phase species X (X=CO, NO, N_2, N_2O or CO_2)

Greek Letters

θ_{CO}	fractional CO surface coverage
θ_N	fractional nitrogen surface coverage
θ_{NO}	fractional NO surface coverage
θ_O	fractional oxygen surface coverage
θ_V	fraction of vacant sites on the surface

4.7 References

1 Taylor, K.C. in "Catalysis Science and Technology, Vol. 5", (Anderson, J.R. and Boudart, M., eds.), p. 119-170, Springer-Verlag, Berlin, 1984.

2. Tauster, S.J. and Murrell, L.L., *J. Catal.* **53**, 260-265 (1978).

3. Taylor, K.C. and Schlatter, J.C., *J. Catal.* **63**, 53-71 (1980).

4 Hahn, T. and Lintz, H.G., *Appl. Surf. Sci.* **40**, 59-63 (1989).

5 Hahn, T. and Lintz, H.G., *Surf. Sci.* **211**, 1030-1037 (1989).

6 Carballo, L.M., Hahn, T. and Lintz, H.G., *Surf. Sci.* **40**, 53-58 (1989).

7 Oh, S.E. and Carpenter, J.E., *J. Catal.* **101**, 114-122 (1986).

8 Adlhoch, W. and Lintz, H.G., *Z. Phys. Chemie Neue Folge* **103**, 207-211 (1976).

9 Adlhoch, W., Lintz, H.G. and Weisker, T., *Surf. Sci.* **103**, 576-585 (1981).

10 Schwartz, S.B. and Schmidt, L.D., *Surf. Sci.* **183**, L269-L278 (1987).

11 Schwartz, S.B. and Schmidt, L.D., *Surf. Sci.* **206**, 169-186 (1988).

12 Fink, Th., Dath, J.P., Imbihl, R. and Ertl, G., *J. Chem. Phys.* **95**, 2109-2126 (1991).

13 Schüth, F. and Wicke, E. in "Instationary Processes and Dynamic Experimental Methods in Catalysis, Electrochemistry and Corrosion", (G. Sandstede and G. Kreysa, Eds.), Dechema Monogr. Vol. 120, p. 429-441 (1989).

14 Bolten, H., Hahn, T., LeRoux, J. and Lintz, H.G., *Surf. Sci.* **160**, L529-L532 (1985).

15 Lesley, M.W. and Schmidt, L.D., *Surf. Sci.* **155**, 215-240 (1985).

16 Lesley, M.W. and Schmidt, L.D., *Chem. Phys. Lett.* **102**, 459-463 (1983).

17 Fink, Th., Dath, J.P., Bassett, M.R., Imbihl, R. and Ertl, G., *Vacuum* **41**, 301-303 (1990).

18 Fink, Th., Dath, J.P., Bassett, M.R., Imbihl, R. and Ertl, G., *Surf. Sci.* **245**, 96-110 (1991).

19 Banholzer, W.F. and Masel, R.I., *Surf. Sci.* **137**, 339-360 (1984).

20 Lambert, R.M. and Comrie, C.M., *Surf. Sci.* **46**, 61-80 (1974).

21 Lorimer, D. and Bell, A.T., *J. Catal.* **59**, 223-238 (1979).

22 Kudo, A., Steinberg, M., Bard, A.J., Campion, A., Fox, M.A., Mallouk, T.E., Webber, S.E. and White, J.M., *J. Catal.* **125**, 566-567 (1990).

23 Solymosi, F., Völgyesi, L. and Sárkány, J., *J. Catal.* **54**, 336-344 (1978).

24 Klein, R.L., Schwartz, S. and Schmidt, L.D., *J. Phys. Chem.* **89**, 4908-4914 (1985).

25 Adlhoch, W. and Lintz, H.G., *Surf. Sci.* **78**, 58-68 (1978).

26 Shelef, M. and Otto, K., *J. Catal.* **10**, 408-412 (1968).

27 Muraki, H. and Fujitani, Y., *Ind. Eng. Chem. Prod. Res. Dev.* **25**, 414-419 (1986).

28 Cho, B.K., Shanks, B.H. and Bailey, J.E., *J. Catal.* **115**, 486-499 (1989).

29 McCabe, R.W. and Wong, C., *J. Catal.* **121**, 422-431 (1990).

30 Belton, D.N. and Schmieg, S.J., *J. Catal.* **138**, 70-78 (1992).

31 Cho, B.K, *J. Catal.* **138**, 255-266 (1992).

32 Sadhankar, R.R., Ye, J. and Lynch, D.T., *J. Catal.* **146**, 511-522 (1994).

33 Sadhankar, R.R. and Lynch, D.T., *J. Catal.* **149,** 278-291 (1994).

34 Taylor, K.C., Sinkevitch, R.M. and Klimisch, R.L., *J. Catal.* **35**, 34-43 (1974).

35 Lööf, P., Stenbom, B., Norden, H. and Kasemo, B., *J. Catal.* **144**, 60-76 (1993).

36 Adlhoch, W. and Lintz, H.G., *Surf. Sci.* **78**, 69-78 (1978).

37 Dath, J.P., Fink, Th., Imbihl, R. and Ertl, G., *J. Phys. Chem.* **96**, 1582-1589 (1992).

38 Oh, S.E., Fisher, G.B., Carpenter, J.E. and Goodman, D.W., *J. Catal.* **100**, 360-376 (1986).

39 Banse, B.A., Wickham, D.T. and Koel, B.E., *J. Catal.* **119**, 238-248 (1989).

40 Scharpf, E.W. and Benziger, J.B., *J. Catal.* **136**, 342-360 (1992).

41 Gardner, P., Tüshaus, M., Martin, R. and Bradshaw, A.M., *Surf. Sci.* **240**, 112-124 (1990).

42 Bonzel, H.P. and Pirug, G., *Surf. Sci.* **62**, 45-60 (1977).

43 Gorte, R.J., Schmidt, L.D. and Gland, J.L., *Surf. Sci.* **109**, 367-380 (1981).

44 Pirug, G. and Bonzel, H.P., *J. Catal.* **50**, 64-76 (1977).

45 Lööf, P., Kasemo, B., Andersson, S. and Frestad, A., *J. Catal.* **130**, 181-191 (1991).

46 Morrow, B.A., Chevrier, J.P. and Moran, L.E., *J. Catal.* **91**, 208-215 (1985).

47 Mizuno, M., Kasai, H. and Okiji, A., *Surf. Sci.* **242**, 464-469 (1991).

48 Gorte, R.J. and Schmidt, L.D., *Surf. Sci.* **111**, 260-278 (1981).

49 Lim, K.J., Löffler, D.G. and Boudart, M.J., *J. Catal.* **100**, 158-166 (1986).

50 Imbihl, R., Fink, Th. and Krischer, K., *J. Chem. Phys.* **96**, 6236-6248 (1992).

51 Belton, D.N. and Schmieg, S.J., *J. Catal.* **144**, 9-15 (1993).

52 Hecker, W.C. and Bell A.T., *J. Catal.* **84**, 200-215 (1983).

53 Hecker, W.C. and Bell, A.T., *J. Catal.* **85**, 389-397 (1984).

54 Muraki, H., Shinjoh, H. and Fujitani, Y., *Ind. Eng. Chem. Prod. Res. Dev.* **25**, 419-424 (1986).

55 Chin, A.A. and Bell, A.T., *J. Phys. Chem.* **87**, 3700-3706 (1983).

56 Lintz, H.G., *Surf. Sci.* **108**, L486-L489 (1981).

57 Schmidt, L.D., Hasenberg, D., Schwartz, S. and Papapolymerou, G.A. in "Catalyst Characterization Science, Surface and Solid State Chemistry" (M.L. Deviney and J.L. Gland, Eds.) ACS Symposium Series 288, p. 177-184, ACS Washington D.C. (1985).

58 Brown, M.F. and Gonzalez, R.D., *J. Catal.* **44**, 477-487 (1976).

59 Arai, H. and Tominaga, H., *J. Catal.* **43**, 131-142 (1976).

60 Chang, C.C. and Hegedus, L.L., *J. Catal.* **57**, 361-377 (1979).

61 Dictor, R., *J. Catal.* **109**, 89-99 (1988).

62 Hegedus, L.L., Chang, C.C., McEwen, D.J. and Sloan, E.M., *Ind. Eng. Chem. Fundam.* **19**, 367-373 (1980).

63 Schwaha, K. and Bechtold, E., *Surf. Sci.* **66**, 383-393 (1977).

5. NO REDUCTION BY CO:
FORCED COMPOSITION CYCLING[**]

5.1 Introduction

The three-way catalyst currently used in automobile catalytic converters simultaneously promotes the conversion of three common pollutants in the exhaust gas, namely CO, NO_x and unburnt hydrocarbons. To obtain maximum conversion efficiencies for the three pollutants, the air-to-fuel ratio is controlled close to the stoichiometric composition using a "closed-loop" feed-back control system. The control signal oscillations inherent in the closed-loop system produce oscillations in the exhaust composition, at a typical frequency of one per second (*1*). Therefore, the reactions between NO, CO (*2, 3*) and oxygen (*4*) have been studied under cycled feed-stream conditions in order to understand the reactions occurring in automobile catalytic converters.

The steady-state kinetics of NO reduction by CO was investigated in an earlier study, described in Chapter 4. It was observed that the NO+CO reaction exhibits isothermal steady-state multiplicity in the temperature range of 465-520 K. The steady-state multiplicity behavior of the NO+CO reaction makes it an ideal candidate for further investigation using the technique of forced composition cycling because of the possibility of reaction rate enhancement. In earlier studies of the N_2O+CO reaction (*5, 6*), described in Chapters 2 and 3, the steady-state multiplicity behavior and corresponding reaction rate enhancement during forced feed composition cycling were observed. The forced composition cycling experiments also provided further insight into the mechanism of the N_2O+CO reaction and led to an improvement of the kinetic model which was developed earlier to describe the steady-state multiplicity behavior.

[**] An abstract of this chapter has been accepted for oral presentation - Sadhankar, R.R. and Lynch, D.T., 2nd International Conference on Unsteady State Processes in Catalysis, St. Louis, Missouri, USA, Sept. 1995. (Manuscript will be published following a peer review in the *Canadian Journal of Chemical Engineering*)

Muraki and Fujitani (*2*) compared the activities and N_2O selectivity of the NO+CO reaction using cycled feed and non-cycled feed in the temperature range of 470-770 K. They observed that the maximum improvement in the activity was obtained for the supported Pt catalyst, which also showed the highest selectivity for N_2O formation among all of the supported noble metal catalysts during the feed cycling experiments. In a subsequent study, Muraki *et al.* (*7*) used the transient responses of the cycled feed streams to study the mechanism of the NO+CO reaction over a Pd/Al_2O_3 catalyst. Hegedus *et al.* (*4*) studied the response of the surface concentrations on a Pt/Al_2O_3 catalyst by periodically switching the stoichiometry of the feed stream containing NO, CO and O_2 between net reducing and net oxidizing. They observed that the surface concentration of isocyanate and CO responded sensitively to the frequency of the feed-stream concentration oscillations. They also found that the surface was free of isocyanates at high frequency cycling. Cho *et al.* (*3*) observed that the formation of N_2O is an important intermediate step for the NO+CO reaction over a Rh/Al_2O_3 catalyst using symmetric and asymmetric feed cycling experiments. In a later study, Cho (*8*) used a cycling scheme involving alternating NO and N_2O flows to the reactor in the presence of a constant CO flow to study the mechanistic importance of the N_2O+CO reaction in the overall NO+CO reaction.

In this study, the NO+CO reaction has been investigated using the technique of variable-phase feed composition cycling, similar to that used earlier to study the N_2O+CO reaction (*6*) described in Chapter 3. The experiments were carried out at 485 K to gain further insight into the role of N_2O formation in the overall NO+CO reaction.

5.2 Methods

The experiments were carried out using a recycle reactor system containing 20 g of 0.5 wt.% Pt/γ-Al_2O_3 catalyst. The experimental equipment and the catalyst have been described earlier in Chapter 3. The gas mixtures were purchased from Linde and included mixtures of 2.02% or 5.94% CO in N_2 and 2.04%, 5.09% or 7.89% NO in N_2. For the calibration of the Horiba gas analyzers for CO_2, NO and N_2O, gas mixtures containing 0.982% CO_2 in N_2, 2.04% NO in N_2 and 2% N_2O in N_2, respectively, were used. The zero calibration of the gas analyzers was performed using pre-purified nitrogen. The pre-purified nitrogen was also used to maintain a constant total feed flow of 185 cm^3 (STP)/min to the reactor during the cycling of NO and CO feed flows. All the experiments were carried out at 485 K. The reactor pressure was always maintained at 103 kPa. Under these operating conditions, the recycle ratio was estimated to be 110. Because of the high recycle ratio, the recycle reactor system closely resembles an ideal CSTR. As shown earlier for the N_2O+CO reaction in Chapter 2, the mass transfer resistances under these operating conditions are negligible. Therefore, the experimental measurements can be considered to be representative of the intrinsic kinetics.

The feed composition cycles were generated using the four-way valves located on the CO and NO feed lines (Fig. 2.2) in a manner similar to that used for the N_2O+CO reaction study described in Chapter 3. The variable-phase feed cycling strategies were similar to those illustrated in Fig. 3.1 for the N_2O+CO reaction. The time-average feed composition during the cycling experiments was always stoichiometric with equal moles of NO and CO. The gas analyzers were calibrated at the beginning of each experiment. Following the calibration of the gas analyzers, the catalyst was treated for 2 hours in an oxidizing environment with a 2% N_2O in N_2 gas mixture consistent with the steady-state experiments described in Chapter 4. The cycling frequencies used in this study were in the range of 0.5 mHz to 20 mHz. For each of the experiments, the feed flow, gas-phase concentrations at the reactor exit and the reactor temperatures were continuously logged by a microcomputer. Cycle invariance was determined by analyzing the CO_2 and NO response curves. The time-average conversions for all of the experiments are tabulated in Appendix H.

5.3 Results and Discussions

5.3.1 Out-of-Phase Cycling

The first set of experiments were carried out by alternately switching the NO and CO four-way valves, so that the NO feed cycle had a phase lead of 180° over the CO feed cycle. In the earlier study described in Chapter 4, the results of the steady-state experiments at 485 K described in Fig. 4.1(b) show that the stoichiometric feed composition always gave a low-conversion steady-state. To compare the results with the steady-state experiments, the out-of-phase cycling experiments were also carried out using three different time-average feed compositions with 0.45 mol%, 0.7 mol% and 1.2 mol% of each of NO and CO, respectively. For each of the three feed compositions, the experiment was started by out-of-phase cycling of the feed composition at a frequency of 0.5 mHz, following the pre-treatment of the catalyst in an oxidizing environment as described earlier. The cycling frequency was then increased in steps of 0.5 mHz, allowing 2.5 hours at every step to reach cycle-invariance (steady-state cycling). The CO_2 and NO response curves showed that 2.5 hours duration was sufficient to reach cycle invariance. The time-average conversions of CO and NO were calculated by the time integration of the CO_2 and NO response curves, respectively. The NO conversion to N_2O was calculated in a similar manner from the N_2O response curves. The experimental results of the time-average conversions are summarized in Fig. 5.1.

It can be seen from Fig. 5.1(a) that the CO conversion increased with the increase in cycling frequency and reached a maximum. The initial linear portions of the three curves can be described by an equation similar to equation (3.1) which was used earlier to describe the N_2O+CO reaction. Based on the regression analysis of the CO conversion data at low frequencies, equation (5.1) adequately describes the data at low frequencies

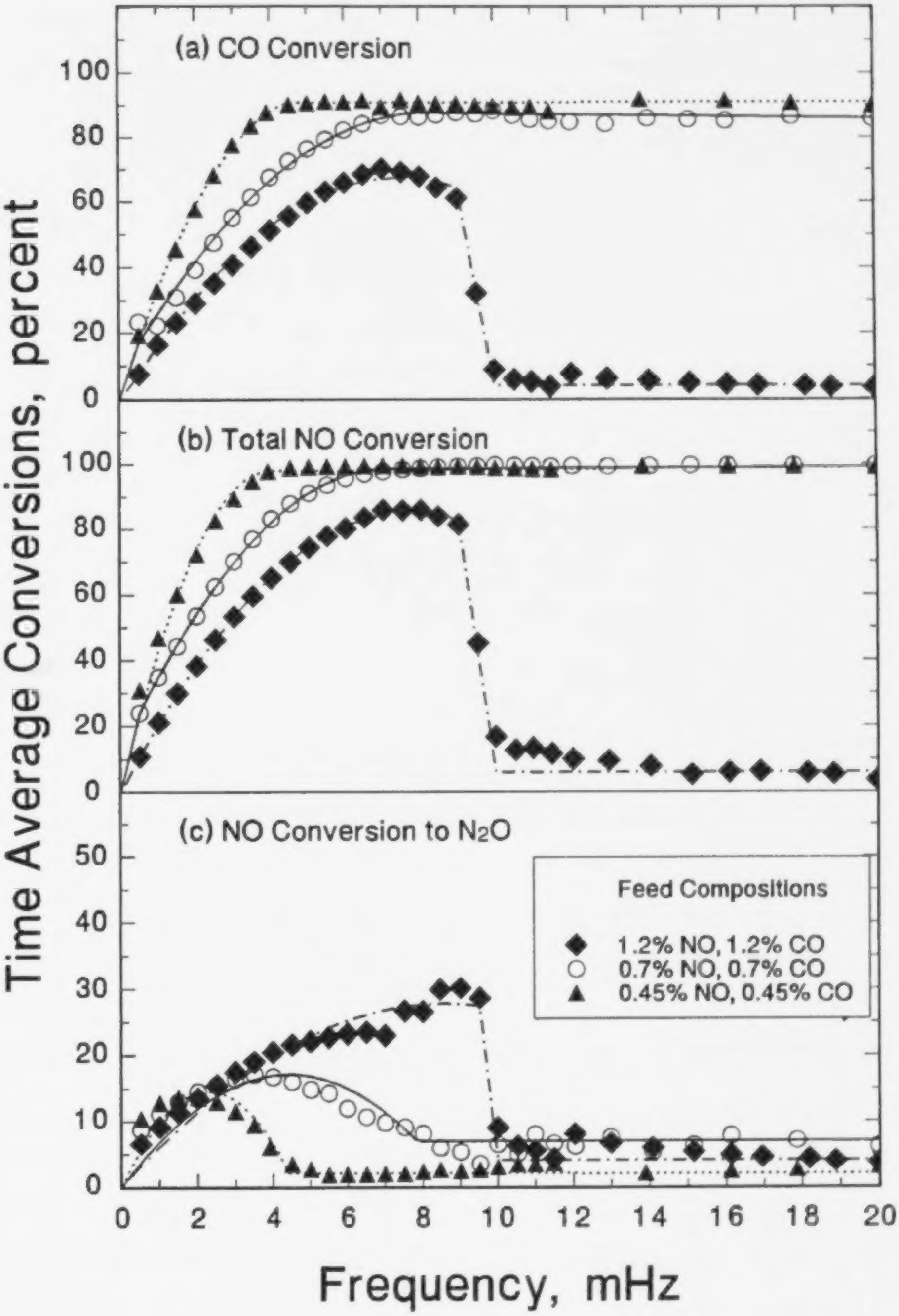

Figure 5.1 Time-Average Conversions for Out-of-Phase Feed Cycling

as shown in Fig. 5.2.

$$f_{co} = \frac{0.22 a_m L_m + 2.4 V[NO]_o}{Q_o[CO]_o} 100\omega \qquad (5.1)$$

Equation (5.1) also shows that the CO conversion varies inversely with the feed CO concentration at a particular frequency. This provides an explanation for the observation from Fig. 5.1(a) that the CO conversion was higher for the feed containing low concentrations of NO and CO, particularly for the region of low frequencies. The value of the first constant (0.22) in equation (5.1) is much smaller than 2 used in the theoretically derived equation (3.1). This discrepancy may be due to the assumption that two complete monolayers are involved in the reaction whereas only a fraction of the monolayer may actually be involved in the reaction. Secondly, the adsorption capacity of the catalyst surface, L_m, may be lower for NO and CO adsorption as compared to the value of 1.42×10^{-5} mol/m^2 used in equation (5.1). A similar observation has been made earlier for the O_2+CO reaction by Graham and Lynch (*9*).

The maximum CO conversion occurred at a lower frequency for the feed containing lower concentrations of NO and CO as can be seen from Fig. 5.1(a). This particular observation is discussed in further detail later in this chapter. The other important observation from Fig. 5.1(a) is that the CO conversion for the feed containing 1.2% NO and 1.2% CO abruptly dropped to a low value at a critical frequency of 9.5 mHz. This observation is similar to that made earlier for the N_2O+CO reaction as shown in Fig. 3.4. The low CO conversion obtained for cycling frequencies higher than 9.5 mHz was approximately equal to the steady-state CO conversion of 2%. The cycling at high frequencies causes the gas-phase CO and NO concentrations in the reactor to be always nearly stoichiometric and therefore the conversions are approximately equal to that obtained for the low-conversion steady-state (Fig. 4.1(b)). However, as can be seen from Fig. 5.1(a), the CO conversion was consistently high at high frequencies for the feeds with lower reactant concentrations, namely 0.45% and 0.7% of each of NO and CO,

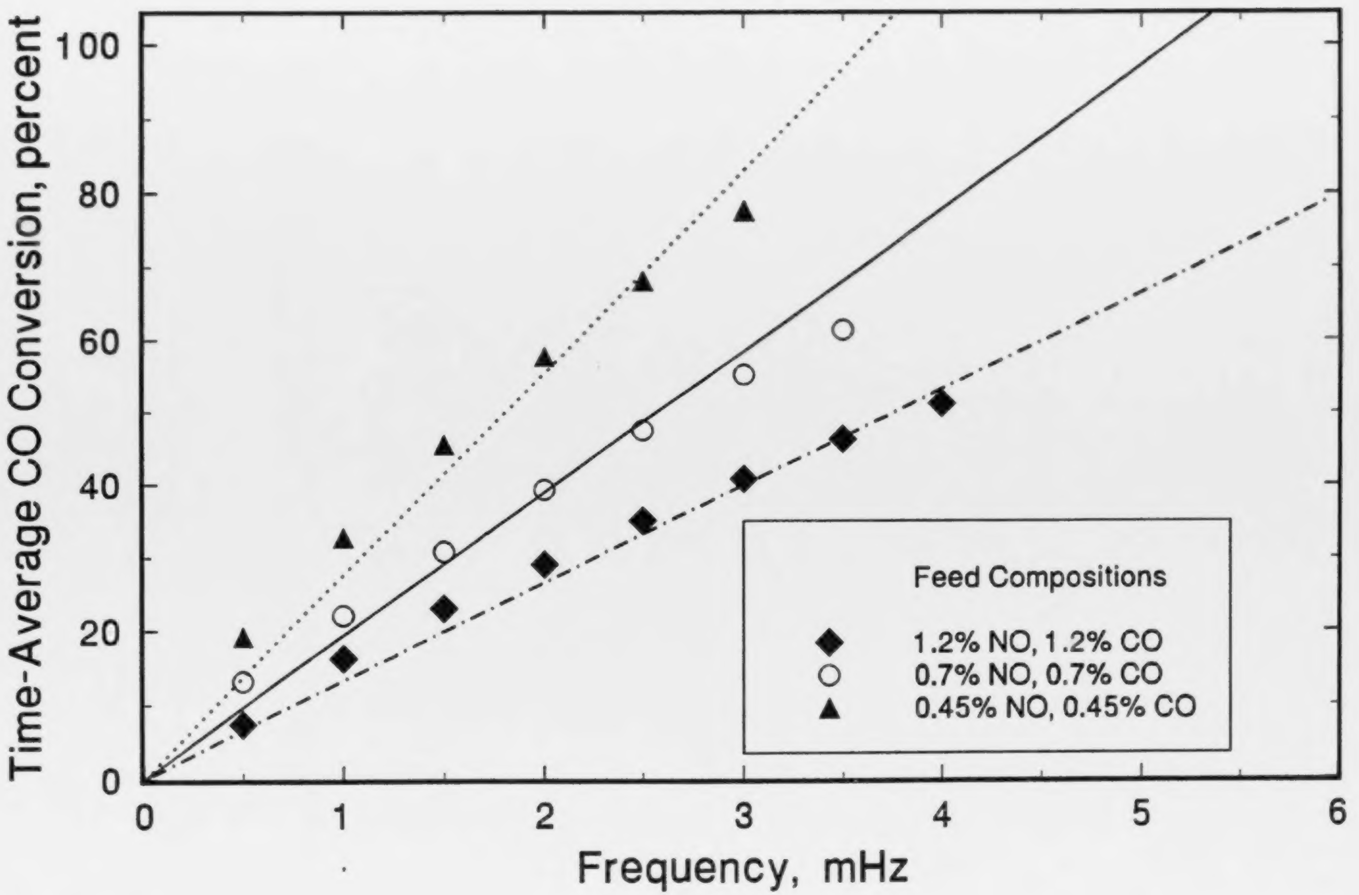

Figure 5.2 Comparison of Predictions from Eq. (5.1) (shown by lines) to Experimental Data at Low Frequencies.

respectively. These results were surprising, because the earlier studies of the N_2O+CO (Chapter 3) and O_2+CO (*9, 10*) reactions, showed that the time-average CO conversion for out-of-phase feed cycling dropped abruptly to a low value as the frequency was increased beyond a critical frequency.

In order to find a possible explanation for the results shown in Fig. 5.1(a), the results from the earlier steady-state experiments were re-examined critically. An examination of the steady-state bifurcation diagram of the NO+CO reaction in Fig. 4.1(b) shows that for the feed containing 0.45% and 0.7% NO, respectively, the high-to-low conversion bifurcation occurs when the feed composition approaches stoichiometric proportions. However, the same results show that the high-to-low conversion bifurcation for the feed containing 1.2% NO occurs for a feed CO concentration which is much lower than the stoichiometric value of 1.2%. Therefore, it is possible to obtain high time-average CO conversion during forced composition cycling with low feed concentrations as long as the gas-phase composition in the reactor remains slightly oxidizing (NO in excess of CO). This further raises a question as to how many cycles are needed in order to achieve convergence to a low time-average conversion cycle-invariant state for forced composition cycling at high frequency with low feed concentrations.

The NO conversion curves shown in Fig. 5.1(b) follow trends very similar to that for the CO conversion curves shown in Fig. 5.1(a), except that the NO conversion was always higher than the CO conversion. However, it was not possible to describe the NO conversion data at low frequencies by a linear relationship similar to equation (5.1). This non-linearity in NO conversion-frequency relationship becomes apparent from the examination of the N_2O formation data in Fig. 5.1(c). As expected from the earlier steady-state experiments at 485 K (Fig. 4.3(b)), significant amounts of N_2O were observed in the reactor as shown in Fig. 5.1(c). In Chapter 4, the overall NO+CO reaction in the temperature range of 465-520 K was described by the following three reactions.

$$2CO + 2NO \rightarrow 2CO_2 + N_2 \qquad (5.2)$$

$$CO + 2NO \rightarrow CO_2 + N_2O \qquad (5.3)$$

$$CO + N_2O \rightarrow CO_2 + N_2 \qquad (5.4)$$

Under steady-state conditions, the NO and CO conversions were related by equation (4.27), based on the above reactions. A similar equation can be used for the cycle-invariant state to relate the time-average conversions, assuming that the volume change due to the reaction is negligible and the time-average feed composition is always stoichiometric. The relationship between the total NO conversion, f_{NO}, CO conversion, f_{CO}, and NO conversion to N_2O, f_{N_2O}, for the cycle-invariant state can be approximately described by equation (5.5).

$$f_{NO} = f_{CO} + \frac{f_{N_2O}}{2} \qquad (5.5)$$

It can be seen from Fig. 5.1 that the NO conversion is always greater than the CO conversion, although the difference between the NO and CO conversions is not exactly accounted for by the NO conversion to N_2O according to Eq. (5.5), possibly due to the errors in measurement. Cho *et al.* (*3*) observed that the NO and CO conversions and the N_2O formation during the feed cycling of NO and CO over a supported Rh catalyst followed a relationship similar to Eq. (5.5). A non-linear relationship between the NO conversion to N_2O and the cycling frequency is obvious from Fig. 5.1(c). Although the total NO conversion increased monotonically with increasing frequency, the NO conversion to N_2O initially increased with increasing frequency, reached a maximum and then decreased with a further increase in frequency, particularly for the feeds with lower reactant concentrations (0.45% and 0.7%). However for the feed containing 1.2% NO and 1.2% CO, the NO conversion to N_2O increased monotonically with increasing frequency and decreased abruptly to a low value at a critical frequency of 9.5 mHz. The NO conversion to N_2O was a minimum when the NO conversion was a maximum for the feeds containing the lower reactant concentrations of 0.45% and 0.7%, respectively. This observation is consistent with the finding in Chapter 4 that the N_2O selectivity is a minimum at the highest NO conversion, although the conclusions in Chapter 4 were based on experiments with varying feed composition. In Chapter 4, the steady-state N_2O selectivity for the low-rate steady-states averaged 0.7. However, the results in Fig. 5.1 show that the N_2O selectivity depends strongly on the cycling frequency. This observation is consistent with a review by Bailey (*11*) where the periodic operation of catalytic reactors was found to alter the selectivity of the reaction.

To understand the effect of the feed composition on the transient behavior of the reaction, further experiments were carried out to study the transient response using non-cycled feed streams. For these experiments, the catalyst was pre-treated in an oxidizing environment as described earlier following which the feed composition was set at the specified values. As can be seen from the CO_2 response curves in Fig. 5.3(a), the feed composition has a major influence on the instantaneous CO conversion. The instantaneous CO conversions remained high for a longer period of time for the feed containing lower concentrations of NO and CO. It can also be seen from Fig. 5.3(a) that the steady-state for the N_2O+CO reaction is reached faster than that for the NO+CO reaction. Fig. 5.3 shows that, although the CO_2 mol% remained almost constant for the initial part of the reaction, the N_2O mol% gradually increased and reached a maximum just when CO_2 mol% started to decrease and the NO mol% started to increase. The N_2O% then gradually decreased as the CO and NO conversions also gradually decreased to the steady-state values. This shows that N_2O formation is favoured on an initially oxidized surface at low CO and NO conversions. This result is consistent with the observations from the steady-state experiments (Chapter 4) where N_2O selectivity was found to be strongly and inversely dependent on NO conversion for the high-rate steady-states. It was also observed that the catalyst pretreatment has a major influence on the transient response. For the catalyst pre-treated with 2% CO for 2 hours, the instantaneous CO and NO conversions were consistently low and the steady-state was reached within

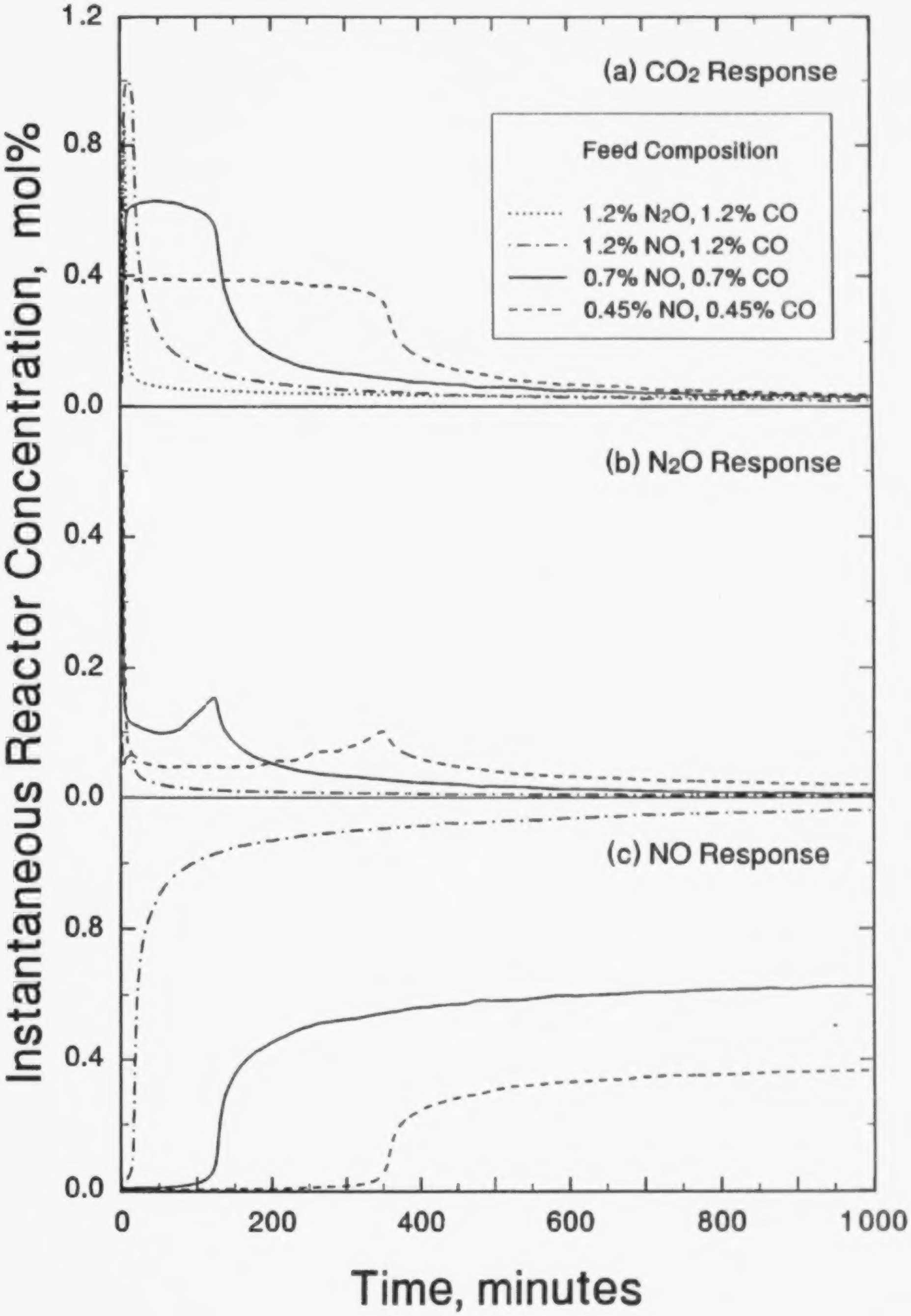

Figure 5.3 Transient Response of Reactor Concentrations for Non-Cycled Feed

2 hours. The long periods of time required to reach the steady-states for the feed containing low concentrations of NO and CO in these experiments may also be necessary to achieve the convergence during cycling experiments. The results of the CO and NO conversion obtained from the steady-state experiments (Fig. 5.3) are compared with the maximum conversions obtained during the out-of-phase cycling experiments (Fig. 5.1) in Table 5.1. The comparison in Table 5.1 shows that it is possible to obtain a time-average conversion which is several times higher than the steady-state conversion, using the forced composition cycling technique as has been observed in earlier studies of the N_2O+CO reaction (Chapter 3) and the O_2+CO reaction (*9, 10*).

Table 5.1

Conversions during steady-state and out-of-phase cycling experiments

Feed Composition		Steady-State Conversions		Maximum Conversion with out-of-phase cycling	
CO	NO	CO	NO	CO	NO
0.45	0.45	7.8	11.8	91.6	99.5
0.7	0.7	4.2	5.1	88.4	99.7
1.2	1.2	1.9	3.8	70.25	85.7

The next step was to see if the long-term transients observed for the non-cycled feeds containing low reactant concentrations could also be observed with the feed cycling. Therefore, further experiments were carried out by out-of-phase cycling of the feeds with three different compositions at a frequency of 10 mHz for extended periods and the results are summarized in Fig. 5.4. The data points in Fig. 5.4 represent the time-average CO conversion for a particular cycle. It can be seen from Fig. 5.4 that the time-average CO conversion remained almost constant at 90% for the feed containing 0.45% NO and

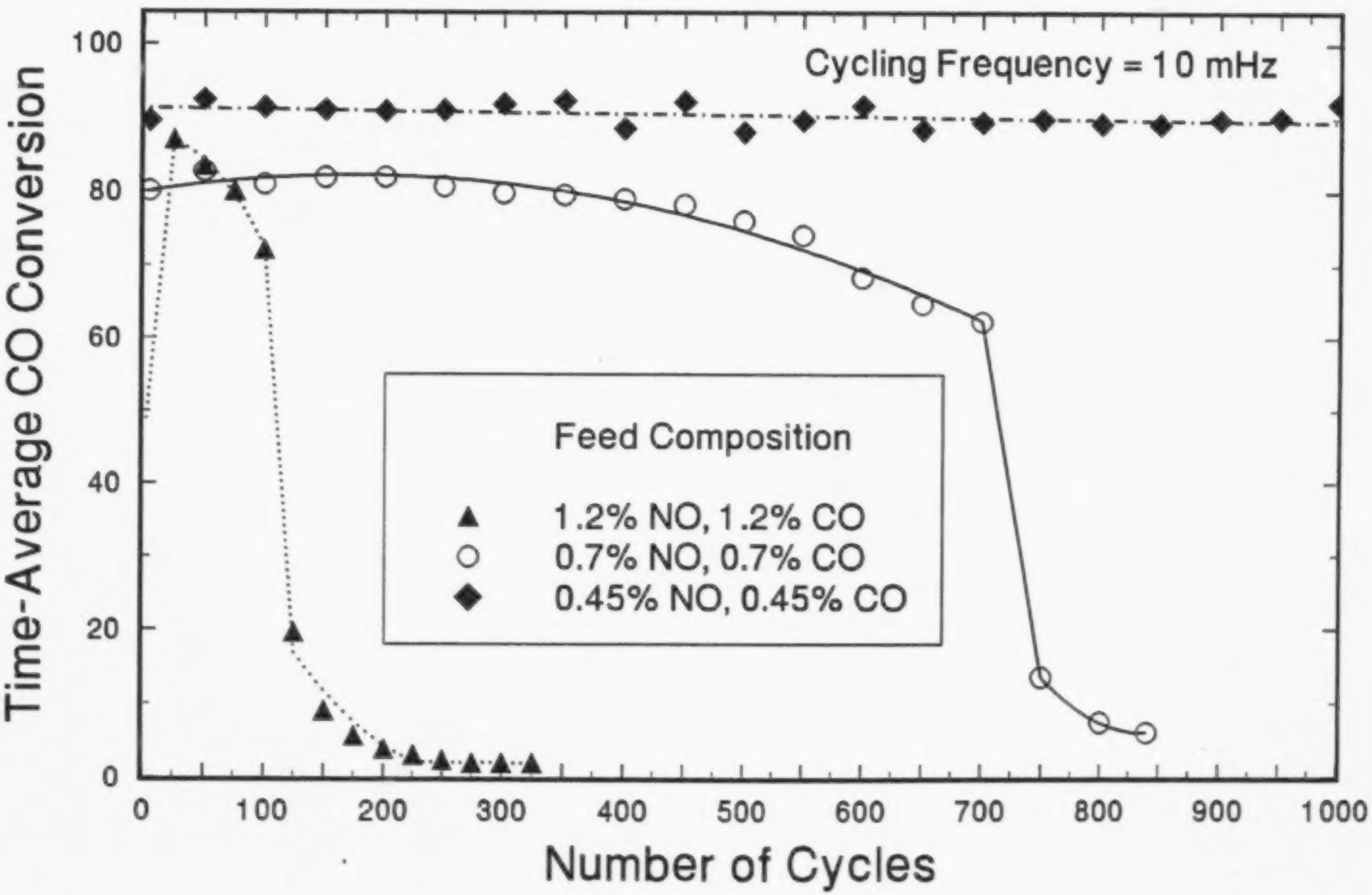

Figure 5.4 Effect of Feed Composition on Number of Cycles Required to Reach Cycle-Invariance.

0.45% CO even after 1000 cycles (28 hours). The CO conversion for the feed containing 0.7% NO and 0.7% CO dropped to a low value only after 700 cycles (19.5 hours) but the convergence was not achieved even after 850 cycles. For the feed containing 1.2% NO and 1.2% CO, the convergence was achieved after 225 cycles. The reaction behavior during cycling (Fig. 5.4) is very similar to that observed earlier for the non-cycled feed streams (Fig. 5.3) except that the time required for convergence during cycling is longer than that for the non-cycled feed. In another similar experiment (out-of-phase cycling at 10 mHz), with a feed containing 0.45% NO and 0.45% CO, the CO conversion was consistently high at approximately 90% for 1780 cycles (49.5 hours), after which the experiment was abandoned. Therefore, it is not known if the time-average CO conversion for the feed containing 0.45% NO and 0.45% CO will ever drop to a low value for extended periods of cycling at 10 mHz.

A comparison of the reaction behavior for the feed cycling (Fig. 5.4) and for non-cycled feed (Fig. 5.3) shows that the time required to reach the steady-state or the cycle-invariant state, respectively, depends strongly and inversely on the reactant concentrations in the feed. Generally, the time required to reach a cycle-invariant state at high frequencies (cycle period $\approx \tau_a$), appears to be longer than the time required to reach a steady-state (with non-cycled feed) for equivalent feed composition. Therefore, the transient behavior using non-cycled feed, can to an extent, help in designing the experiments with feed cycling. For example, from the transient CO_2 response curves in Fig. 5.3(a), one could conclude that a relatively smaller number of cycles would be required to achieve cycle-invariance for the N_2O+CO reaction as compared with the NO+CO reaction.

In earlier experiments (Fig. 5.1), the cycle invariance was determined by analyzing the CO_2 and NO response curves after 2.5 hours of cycling. The CO conversion per cycle did not change by more than 1% for 10 consecutive cycles. However, the results in Fig. 5.4, show that such a criterion for cycle invariance may lead to wrong conclusions. A possible explanation for the slow cycle convergence for the feeds containing low reactant concentrations can be found from the modelling studies of Lynch (*12*) for the O_2+CO reaction as follows. The two characteristic time constants of the reactor are defined as τ_v, the reactor volume space time given by equation (5.6) and τ_a, the space time based on the surface capacity of the catalyst given by equation (5.7)

$$\tau_v = \frac{V}{Q_o} \tag{5.6}$$

$$\tau_a = \frac{a_m L_m}{Q_o [CO]_o} \tag{5.7}$$

The ratio of the two characteristic times, α_m, given by equation (5.8) is also the ratio of the gas-phase to surface capacitances for CO.

$$\alpha_m = \frac{\tau_v}{\tau_a} = \frac{V[CO]_o}{a_m L_m} \tag{5.8}$$

For the reactor system used in this study, τ_v is 39 s and τ_a is calculated to be 81 s, 137 s and 216 s for the feed CO concentrations of 1.2%, 0.7% and 0.45%, respectively. The actual values of τ_a may be lower than the values calculated above, because the surface capacity for CO may be lower than $a_m L_m$, as seen earlier while discussing equation (5.1). Although the cycle period of 100 s (Fig. 5.4) is larger than the reactor space time τ_v, it is lower than τ_a for the feeds containing 0.45% and 0.7% of each of CO and NO, respectively. Therefore, the surface concentrations of the adsorbed species change relatively slowly and a large number of cycles are required before a cycle-invariant state is obtained. In another modelling study of the O_2+CO reaction, Lynch (*13*) showed that the maximum time-average conversion during out-of-phase feed cycling occurs for a cycle period which is close to the dominant characteristic time of the system. In earlier experimental studies of the CO+O_2 reaction (*9, 10*) and the N_2O+CO reaction (Chapter 3), the maximum CO conversion was obtained for the cycle periods which were approximately of the same magnitude, or larger than, the dominant characteristic time of the system. Therefore, the observation in Fig. 5.1(a) that the maximum conversion occurs at a lower frequency (larger cycle period) for the feed containing lower reactant concentrations (larger τ_a), is consistent with the earlier studies.

Because of the large number of cycles required to reach a cycle-invariant state, further experiments were limited to the time-average feed composition of 1.2% NO and 1.2% CO. The out-of-phase cycling experiments were repeated for the frequencies above 5 mHz to verify the earlier results where the conversions abruptly dropped to a low value at a critical frequency of 9.5 mHz. The cycling was carried out for at least 9 hours at every frequency following the catalyst pre-treatment in oxidizing atmosphere. It was found that the time-average conversions abruptly dropped to a low value for the cycling frequency of 6 mHz (cycle period of 167 s) instead of 9.5 mHz (cycle period of 105 s) found in the earlier experiments (Fig. 5.1). It is interesting to note that the cycle period of 167 s is more than twice the calculated characteristic time, τ_a, of 81 s. The CO_2 response curves at the cycling frequency of 6 mHz are shown in Fig. 5.5. A continuous CO_2 response curve is shown in Fig. 5.5(a) and an expanded view in three different time windows is shown in Fig. 5.5(b). As can be seen from Fig. 5.5(b), the convergence to cycle invariance is very slow. The CO_2 response curves for the ten consecutive cycles between the 50th and 60th cycles (2.3 to 2.8 hours of cycling) gives a false impression of cycle invariance according to the criterion used in the earlier experiments. The time-average conversions from these experiments along with the results at low frequencies from the earlier experiments are summarized in Fig. 5.6.

5.3.2 Variable Phase Cycling

In the earlier experiments, the NO phase lead was always held constant at 180° while varying the cycling frequency. The next set of experiments were carried out by varying the NO phase lead while holding the cycling frequency constant. The time-average conversions at three different frequencies are summarized in Fig. 5.7. Because

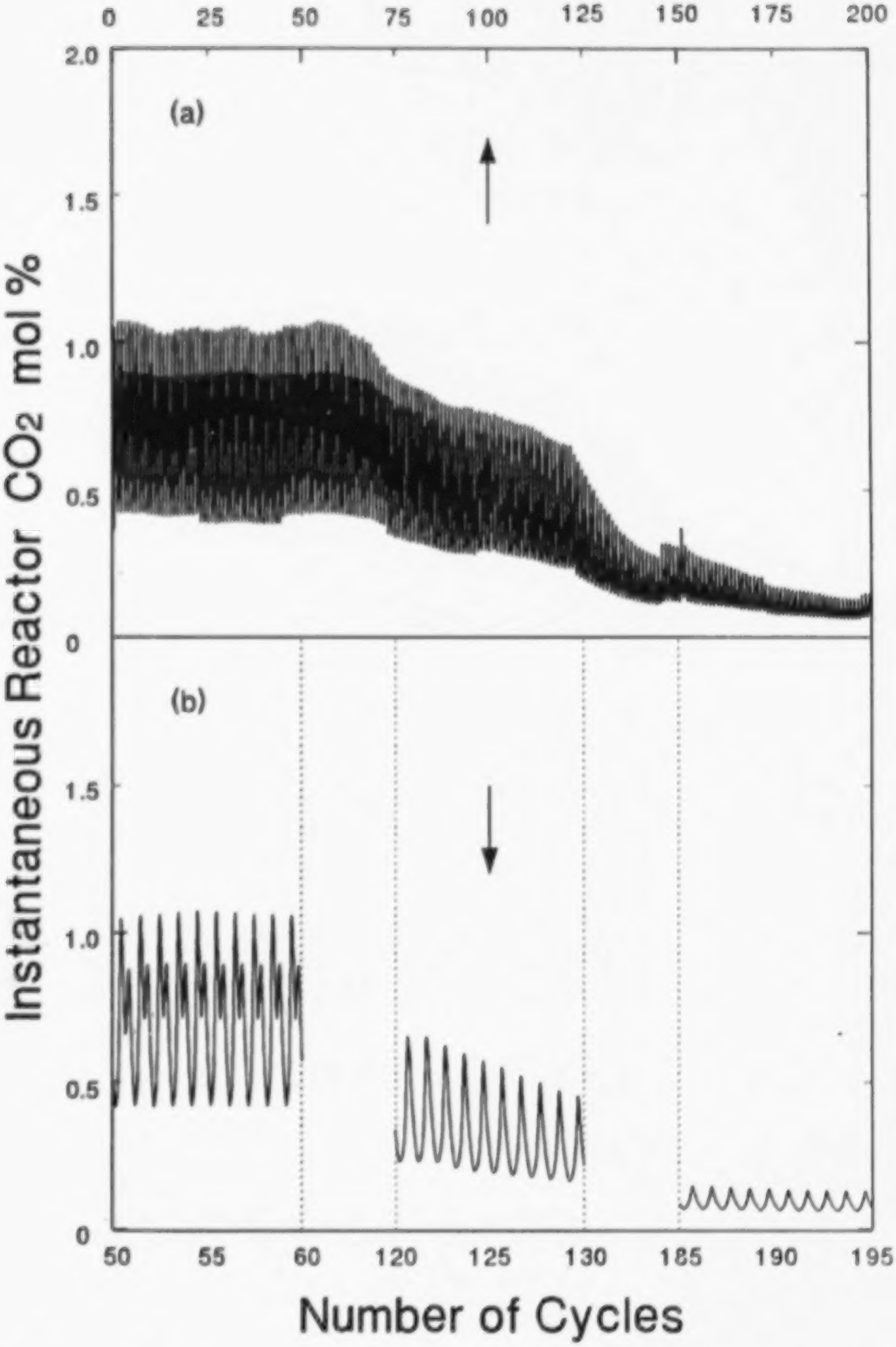

Figure 5.5 Slow Convergence to Cycle-Invariance at a Frequency of 6 mHz. (a) Continuous CO_2 Response, (b) Expanded Views for 10 Cycles

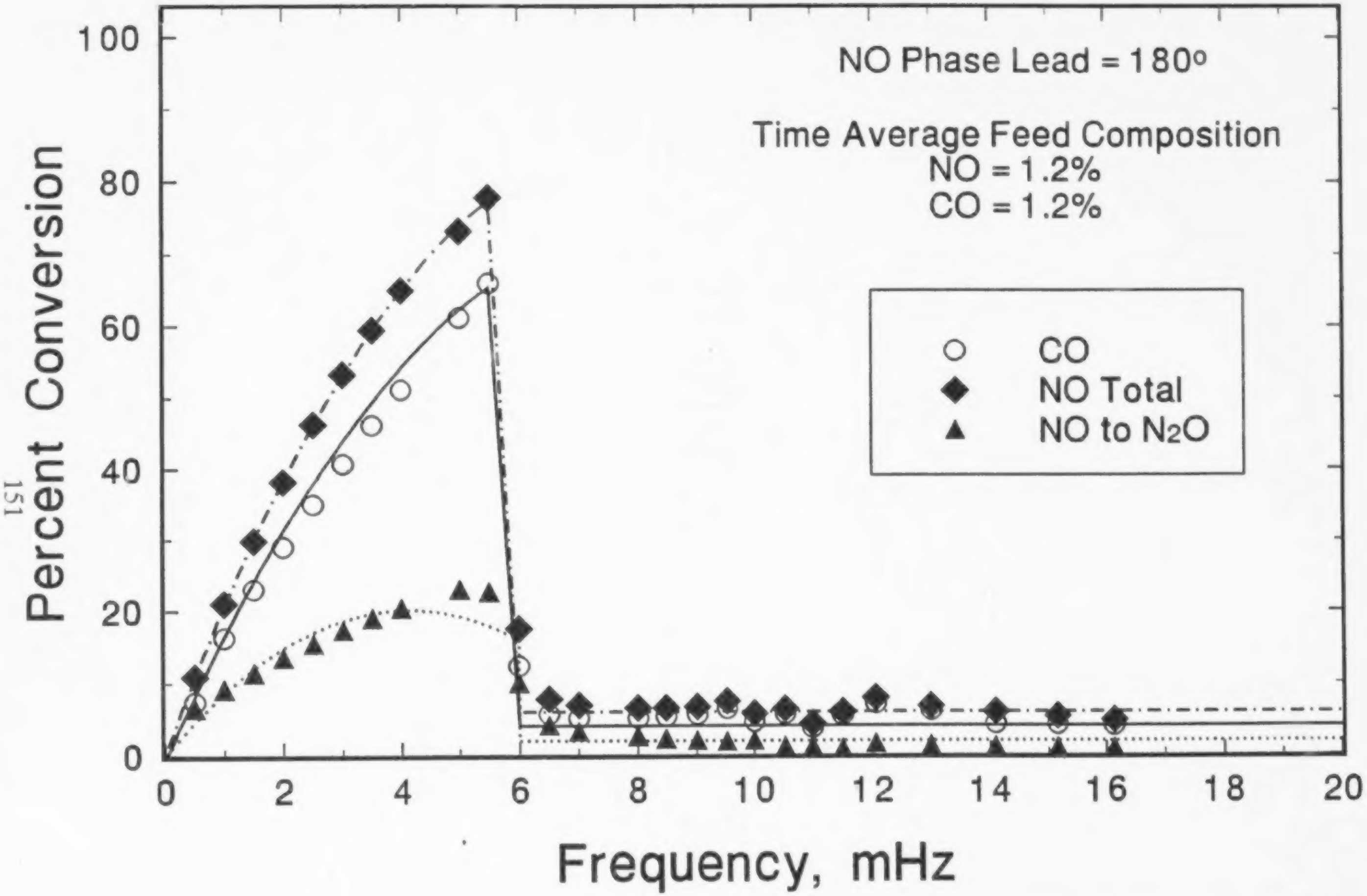

Figure 5.6 Time-Average Conversions for Out-of-Phase Cycling with Time-Average Feed with 1.2% NO and 1.2% CO.

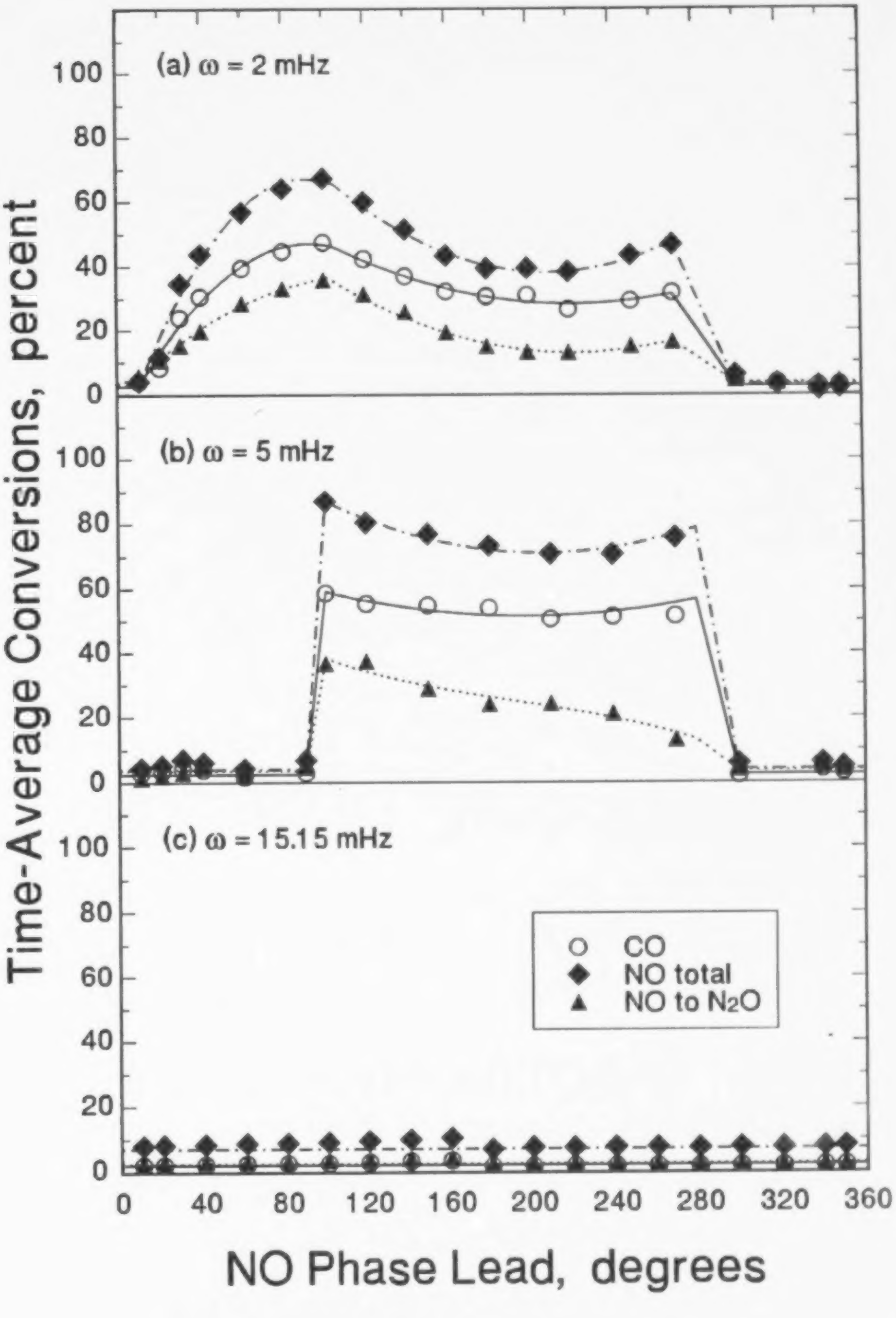

Figure 5.7 Effect of NO Phase Lead on Time-Average Conversions

of the slow convergence to cycle invariance experienced in earlier experiments (Fig. 5.5), the feed cycling was always carried out for at least 9 hours for each set of cycling frequency and NO phase lead. The results in Fig. 5.7(a) show that the NO and CO conversions increased with increasing NO phase leads between 10° and 100°. The conversions then decreased slowly with the stepwise increase in NO phase lead to 180° and remain practically unchanged with a further increase in NO phase lead to 270°. The conversions were consistently low for NO phase leads of higher than 300°. The NO conversion to N_2O varied with NO phase lead in a manner similar to that of the NO and CO conversions. The maximum CO conversion of 47.3% was obtained for the NO phase lead of 100° as compared to 30.8% for the 180° NO phase lead. This observation is similar to that made earlier for the N_2O+CO reaction (Fig. 3.8(a)) in Chapter 3.

The results in Fig. 5.7(b) show that the conversions were consistently low for NO phase leads of lower than 100° and higher than 300°, respectively. Again the maximum CO conversion (58.7%) occurred for the NO phase lead of 100° as compared to 54% for 180° NO phase lead. The CO conversion for the NO phase leads between 180° and 270° remained unchanged while the NO conversion to N_2O appeared to decrease with the increase in NO phase lead. This shows that the NO phase lead has a significant influence on the N_2O selectivity. Therefore, it may be possible to search for a suitable NO phase lead to minimize the N_2O selectivity without significantly reducing the CO conversion during the feed composition cycling. At a high frequency of 15.15 mHz, the time-average conversion was consistently low, approximately equal to the steady-state value, for all of the NO phase leads as can be seen in Fig. 5.7(c). These observations are very similar to those made earlier in Chapter 3 for the N_2O+CO reaction (Fig. 3.8). These results also reinforce the conclusion from the N_2O+CO reaction study that it is possible to obtain a higher time-average conversion for an NO phase lead of less than 180° than the maximum obtainable for a 180° phase lead.

5.3.3 Transient Response

The dynamic response of the reactor concentrations during feed cycling provides valuable information about the reaction mechanism, as was seen earlier for the N_2O+CO reaction in Chapter 3. The infrared analyzers for the measurement of CO_2, NO and N_2O in the reactor were placed in series as shown earlier in Fig. 2.1. Because of the series arrangement of these analyzers, the NO and N_2O responses are delayed relative to the CO_2 response. To derive meaningful conclusions from the transient response curves, it is necessary to know the "transport-lag" for each of the analyzers. Therefore, the experiments were carried out by cycling the feed containing only one component (CO_2, NO or N_2O) and the response curves are shown in Fig. 5.8. It can be seen from Fig. 5.8 that the responses to step-change in the input were delayed by 20 s, 50 s and 70 s for CO_2, NO and N_2O concentrations, respectively.

The dynamic response curves of CO_2, NO and N_2O concentrations for the out-of-phase cycling at four different frequencies are shown in Fig. 5.9. The curves in Fig. 5.9 are drawn after correcting the experimental data for the transport-lags for the CO_2, NO and N_2O analyzers, respectively. For the low frequency cycling at 0.5 mHz (Fig. 5.9(a)), two distinct peaks of CO_2 and N_2O occurred per cycle. The CO_2 formation in each half cycle is approximately equal, as calculated from the area under the CO_2 curve. At the beginning of the NO half-cycle, the surface is almost saturated with adsorbed CO from the previous CO half-cycle. When NO is switched on, the reactor NO concentration rises sharply, because NO cannot adsorb on the surface due to a lack of empty sites. As NO gradually adsorbs and reacts with the adsorbed CO, both CO_2 and N_2O are formed, initially slowly and then rapidly as more sites become available for NO adsorption. The peak in the CO_2 curve coincides with the valley in the NO curve, whereas the N_2O peak occurs before the CO_2 peak. The NO and N_2O curves exhibit similar behavior, in that the peaks and the valleys in both of the curves almost coincide. This shows that the N_2O selectivity is inversely dependent on the NO conversion. It also indicates that N_2O formation occurs from adsorbed NO according to Eq. (5.9).

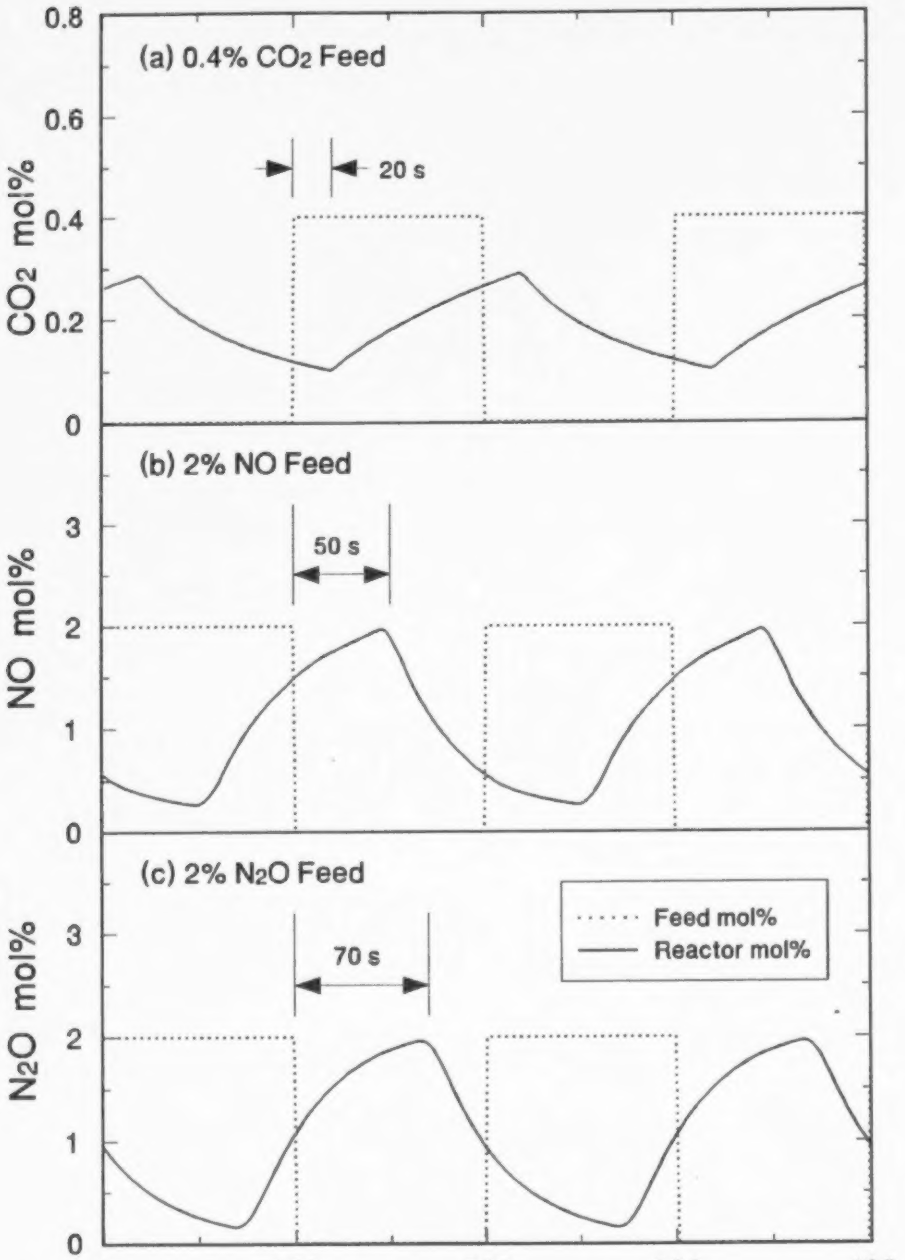

Figure 5.8 Transport-Delays in the Response of CO_2, NO and N_2O Analyzers.

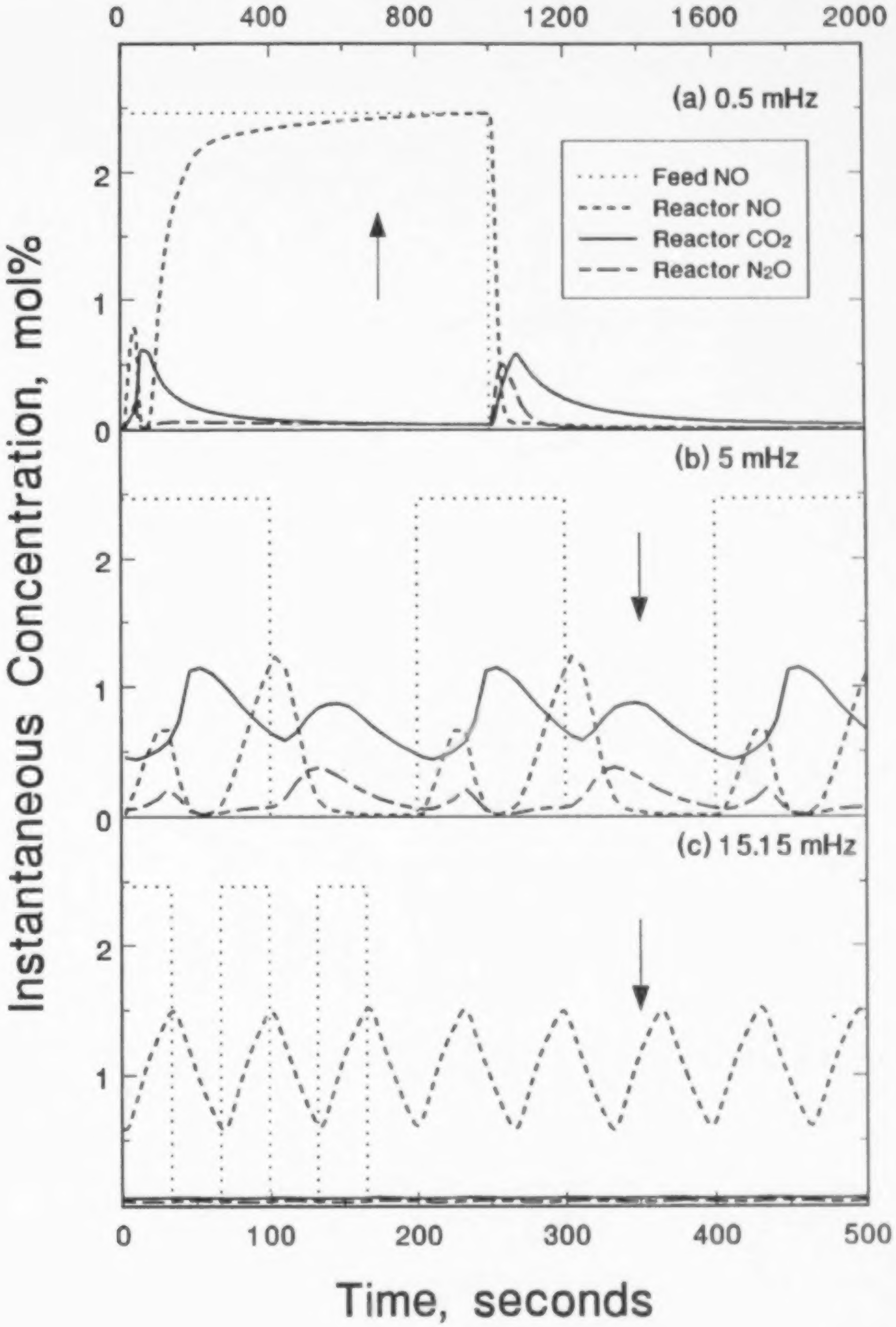

Figure 5.9 Dynamic Response During Out-of-Phase Feed Cycling.

$$M\text{-}NO + M\text{-}N \rightarrow N_2O_{(g)} + 2M \qquad (5.9)$$

However, conclusive proof for such a reaction step can only be obtained through feed cycling experiments using FTIR spectroscopy. After the CO_2 peak is reached, the CO_2 concentration falls almost exponentially, as the CO in the reactor is depleted due to reaction and transport out of the reactor. The CO_2 concentration does not fall to zero even by the end of NO half-cycle due to desorption from the alumina support. The NO and N_2O curves rise sharply, after the CO_2 peak and reach a plateau. The N_2O formation in the absence of CO (towards the end of the NO half-cycle) is due to NO decomposition. It has been shown in other studies (*14, 15*) that the adsorbed NO decomposes almost completely to gaseous N_2 and adsorbed oxygen on Pt/Al_2O_3 catalyst at 500 K, and only small amounts of N_2O formation have been observed (*15*), which is consistent with the observation in Fig 5.9(a). The adsorbed oxygen does not desorb below 700 K (*15*) and therefore accumulates on the catalyst surface. Therefore, the catalyst surface is expected to be largely covered by adsorbed oxygen by the end of the NO half-cycle. It can also be seen from Fig. 5.9(a) that N_2O formation occurs more by the NO+CO reaction (at the beginning of the NO half-cycle) as compared with N_2O formation by NO decomposition (towards the end of the NO half-cycle). This is because the NO decomposition is inhibited by the accumulated oxygen on the catalyst surface whereas CO helps in scavenging the adsorbed oxygen during the NO+CO reaction.

In the CO half-cycle of Fig. 5.9(a), the CO_2 and N_2O concentrations rise sharply and the NO concentration falls rapidly as soon as the CO feed is switched on. This shows that CO is readily adsorbed on the catalyst surface which is largely covered with adsorbed oxygen from the previous NO half-cycle. The peak in the N_2O curve occurs before the peak in the CO_2 curve, which is consistent with the observation in the NO half-cycle. N_2O concentration falls to zero as the gas phase NO concentration depletes due to reaction and transport out of the reactor. A gradual decrease in the CO_2 concentration after the CO_2 peak is due to desorption of CO_2 from the alumina support. However, the NO and N_2O concentrations rapidly decreased to almost zero, suggesting that the adsorption of these species on the alumina support is negligible. The N_2O formation in the CO half-cycle is more than that for the NO half-cycle. The faster reactions in the CO half-cycle compared with those for the NO half-cycle can be understood by examining the gas compositions and the catalyst surface at the beginning of each half-cycle. The gas composition (in the reactor) at the beginning of the NO half cycle is net reducing and the catalyst is pre-treated in a reducing environment (conditions for low-conversion steady-state in Fig. 4.1(b)) whereas the gas composition at the beginning of the CO half-cycle is net oxidizing and the catalyst is pre-treated in an oxidizing environment (conditions for high-conversion steady-state in Fig. 4.1(b)). Therefore, the observations from Fig. 5.9(a) are consistent with those of the steady-state experiments shown in Figs. 4.1, 4.3 and 4.5.

The transient response curves at a higher frequency of 5 mHz (Fig. 5.9(b)) also show two distinct peaks of CO_2 and N_2O per cycle. The N_2O peak in the NO half cycle is smaller than the N_2O peak in the CO half-cycle whereas the CO_2 peak in NO half-cycle is higher than the CO_2 peak in the CO half-cycle. The peak in the N_2O curve coincides with the peak in the NO curve and the valley in the N_2O curve coincides with the valley in the NO curve. These results are consistent with those observed for the lower frequency of 0.5 mHz in Fig. 5.9(a). It is interesting to note that for the N_2O+CO reaction, only a single peak of CO_2 per cycle was observed at the frequency of 5 mHz. This CO_2 peak occurred in the N_2O half-cycle. These results show that the NO+CO reaction is faster than the N_2O+CO reaction under the net reducing environment (CO in excess of the oxidant NO or N_2O) of the CO half cycle. At a high frequency of 15.15 mHz (Fig. 5.9(c)), the CO_2 and N_2O concentrations were consistently low. The cycle period of 62 s, corresponding to a frequency of 15.15 mHz, is smaller than the dominant characteristic time of the system which was estimated to be 81 s. At high frequencies, the catalyst surface is predominantly covered by adsorbed CO which does not get scavenged by the reaction in the short NO half-cycle. Therefore, the CO and NO conversions for high frequency cycling are approximately equal to the steady-state conversions.

The transient response curves for the cycle frequency of 2 mHz at two different NO phase leads of 100° and 270° are shown in Fig. 5.10. The cycle period is divided in four quadrants as shown in Fig. 5.10 for the purpose of discussion. For feed cycling with an NO phase lead of 100° (Fig 5.10(a)), a part of the adsorbed CO from the third quadrant (feed containing only CO) desorbs in the fourth quadrant (feed containing neither NO nor CO). Therefore, in the first quadrant (feed containing only NO), reaction occurs rapidly as seen from the CO_2 response curve because sufficient sites are available for NO adsorption. This is in contrast with the slow initial CO_2 response observed at the beginning of the NO half-cycle for the 180° NO phase lead (Fig. 5.9(a)), where the catalyst surface is essentially saturated with adsorbed CO. Also a short NO peak observed at the beginning of the NO half cycle in Fig 5.9(a) was absent in the first quadrant in Fig. 5.10(a). When CO is switched on in the second quadrant of Fig. 5.10(a), it readily adsorbs on the surface largely covered by adsorbed oxygen and therefore, large peaks of CO_2 and N_2O are obtained in the second quadrant.

For the feed cycling with 270° NO phase lead, the gas-phase NO from the second quadrant (feed containing only NO) is completely depleted in the third quadrant (feed containing neither NO nor CO). However, the adsorbed oxygen does not desorb during the third quadrant. When CO is switched on in the fourth quadrant, the reaction proceeds immediately as shown by the CO_2 and N_2O response curves. However the extent of the reaction in the fourth quadrant is limited by the amount of the adsorbed oxygen on the surface from the second quadrant and therefore relatively smaller peaks of CO_2 and N_2O are observed in the fourth quadrant. When NO is switched on in the first quadrant (feed containing both NO and CO), both NO and CO compete for chemisorption on a small fraction of vacant sites on the surface which is predominantly covered by adsorbed CO from the fourth quadrant. Because CO adsorbs preferentially on the surface, the reaction is slow in the first quadrant. Only after the CO is switched off in the second quadrant (feed containing only NO), can NO adsorb onto the catalyst surface and the reaction then

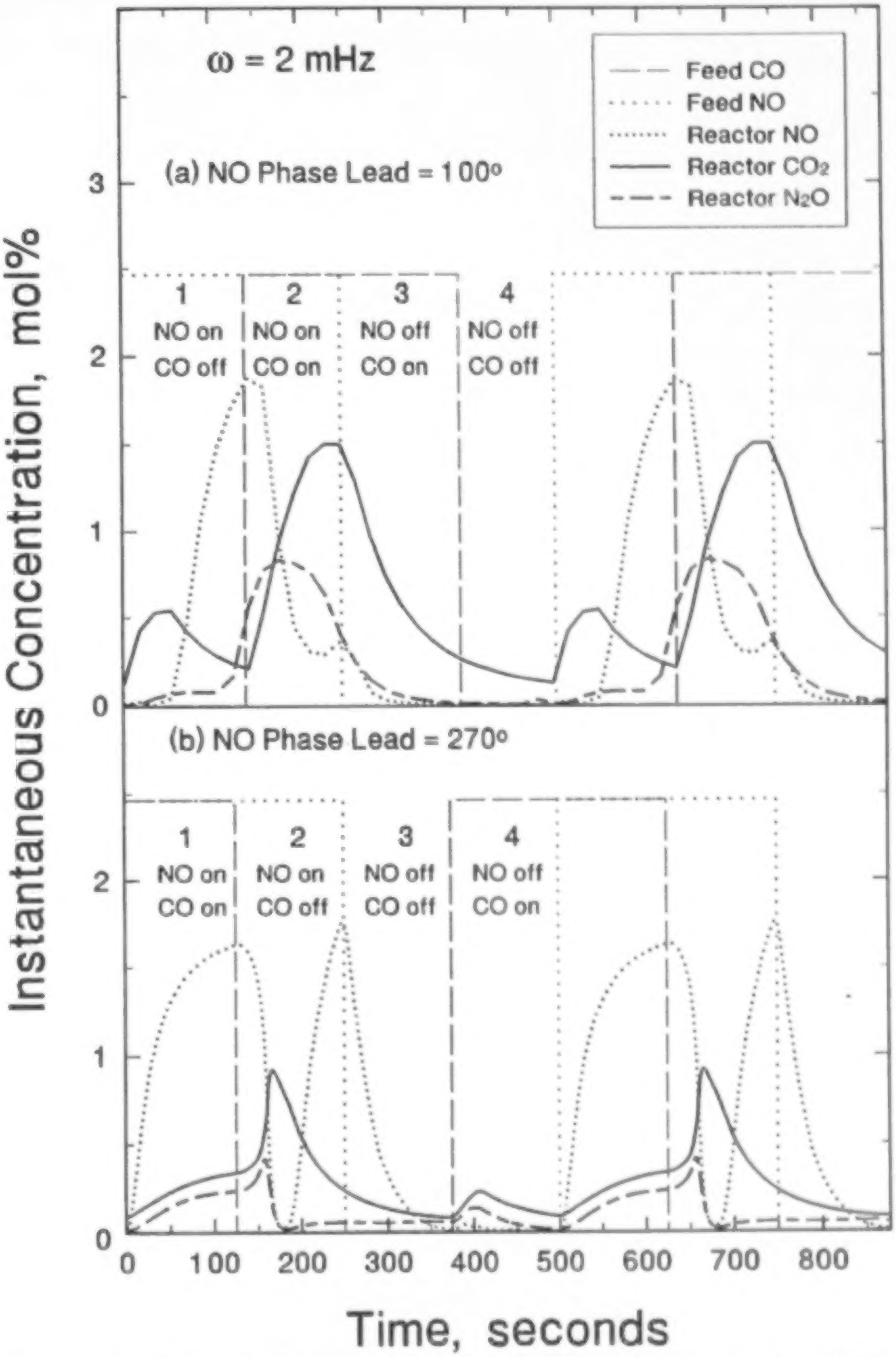

Figure 5.10 Dynamic Response for 100° and 270° NO Phase Leads at 2 mHz.

proceeds to a significant extent as seen from the large peaks in the CO_2 and N_2O curves.

A comparison of Figs 5.10(a) and (b) show that the CO_2 and N_2O production per cycle is more for the NO phase lead of 100° as compared with that for the NO phase lead of 270°. As discussed earlier, the catalyst is predominantly covered by oxygen at the beginning of the overlap part of the cycle (second quadrant) in Fig. 5.10(a) and therefore the reaction rates are high. The catalyst is predominantly covered by adsorbed CO at the beginning of the first quadrant in which the CO and NO feeds overlap for the NO phase lead of 270° and therefore the reaction rates are low.

However, at a higher frequency of 5 mHz, the CO conversion at 100° and 270° are nearly equal as seen from Fig. 5.11. Because of the shorter cycle period, the CO surface coverage in the fourth quadrant is less for the NO phase lead of 270° and this gives more vacant sites for NO adsorption at the beginning of the first quadrant. Therefore, the extent of CO_2 formation in the first quadrant at 5 mHz (Fig. 5.11(b)) is more than that obtained for a frequency of 2 mHz in Fig. 5.10(b). A significant difference in Fig. 5.10(a) and Fig. 5.11(a), is that the reaction between adsorbed CO and adsorbed NO in the second quadrant is carried over to the third quadrant because of a shorter cycle period at the frequency of 5 mHz. The CO_2 production at a frequency of 5 mHz is nearly equal for both the NO phase leads of 270° and 100°. However the N_2O production for 270° NO phase lead is less than that for 100° NO phase leads, as seen from Fig. 5.11. The results of these variable-phase cycling experiments show that NO and CO conversions are generally higher for the NO phase lead of nearly 90° as compared to 180° NO phase lead. However, feed cycling at a frequency of 5 mHz, with NO phase lead in excess of 180° has the advantage of low N_2O selectivity and relatively high conversions as seen from the comparison of Figs. 5.10(a) and (b).

5.3.4 Kinetic Model

The steady-state multiplicity behavior of the NO+CO reaction was described by a

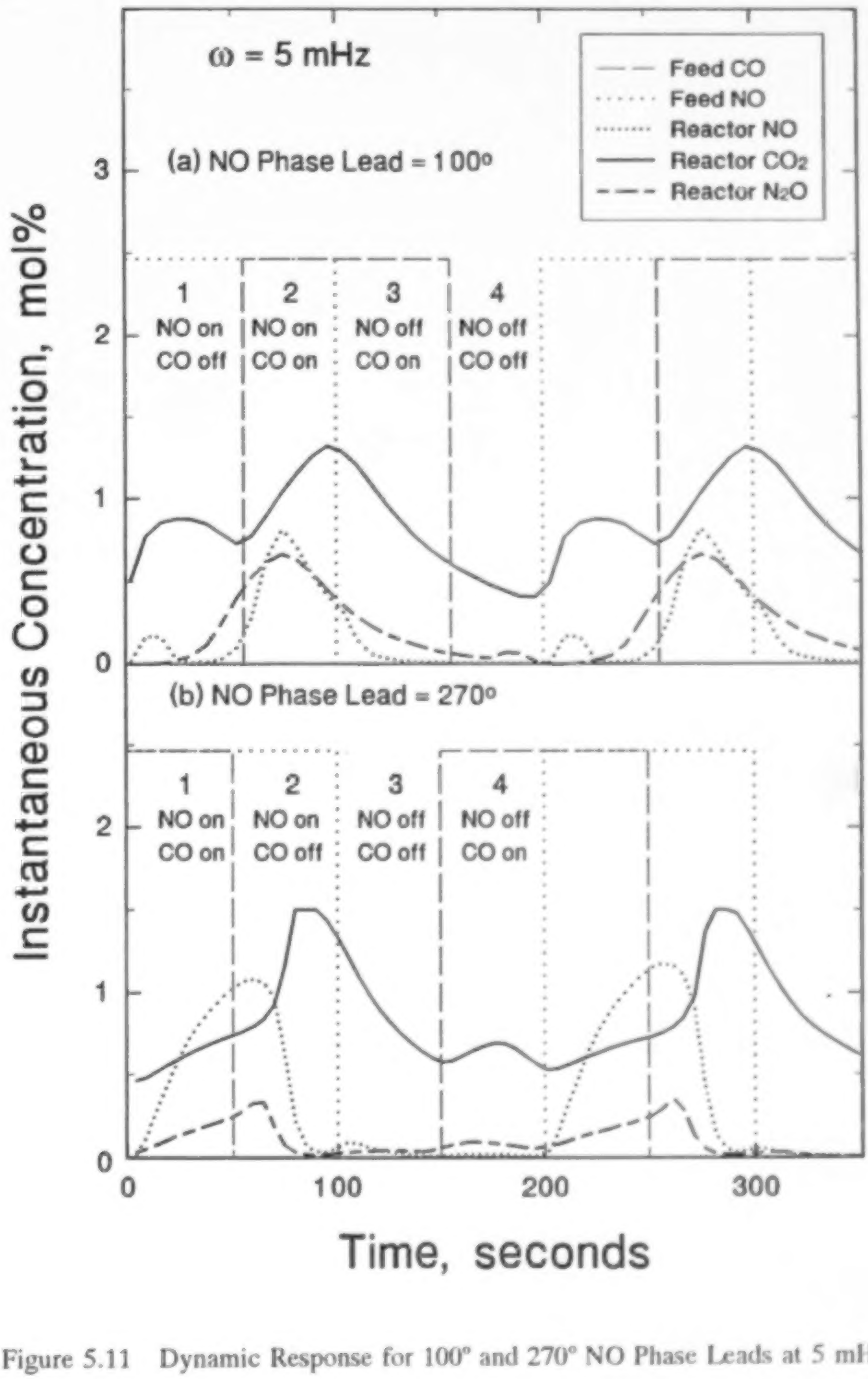

Figure 5.11 Dynamic Response for 100° and 270° NO Phase Leads at 5 mHz.

mechanism consisting of seven reaction steps in Chapter 4. The kinetic model based on this reaction mechanism also included a CO self-exclusion effect. The same model was recast into its dynamic form consisting of nine dimensionless ordinary differential equations described in detail in Appendix I. While modelling the transient behavior of the N_2O+CO reaction in Chapter 3, it was found that such a model adequately describes the time-average conversions at low frequencies (initial linear portion of the curve in Fig 3.4). Therefore, a first attempt was made to use the set of differential equations at a low frequency of 2 mHz. The values of the kinetic rate constants used in the equations were determined using an iterative procedure outlined in Appendix I. It was observed that the system of differential equations for the NO+CO reaction is more difficult to solve as compared with the equations for the N_2O+CO reaction. As many as 50,000 steps per cycle were required for the integration of the equations using the fourth order Runge-Kutta-Fehelberg method for a cycling frequency of 2 mHz. Cycle-invariance was determined using the criterion of percent change in the fractional oxygen surface coverage, as given by Eq. (3.22) for the N_2O+CO reaction system. Table 5.2 shows the comparison of the experimental values of the time-average conversions and the model predictions for a particular set of values of the rate constants given in Appendix I.

The comparison in Table 5.2 shows that the model predictions for CO and NO conversions are approximately 15% higher than the experimental values. The model predictions satisfy the relationship between the CO and NO conversions according to Eq. (5.5). The model-experimental discrepancy for NO conversion to N_2O appears to be large from Table 5.2. However, the observed NO conversion to N_2O of 13.55% is lower than 18.28% calculated by Eq. (5.5) due to errors in measurement of low N_2O concentrations in the reactor by the analyzer equipment. The values of the rate constants can be further optimized to minimize the model-experimental discrepancy. The transient response curves predicted by the model can be compared with the experimental data in Fig. 5.12. The curves in Fig. 5.12(b) represent the solution of eight differential equations (I.9) to (I.16) given in Appendix I. Although the curves in Fig. 5.12(b) do not exactly match with the curves in Fig. 5.12(a), the similarities are apparent. The model predicts two distinct CO_2

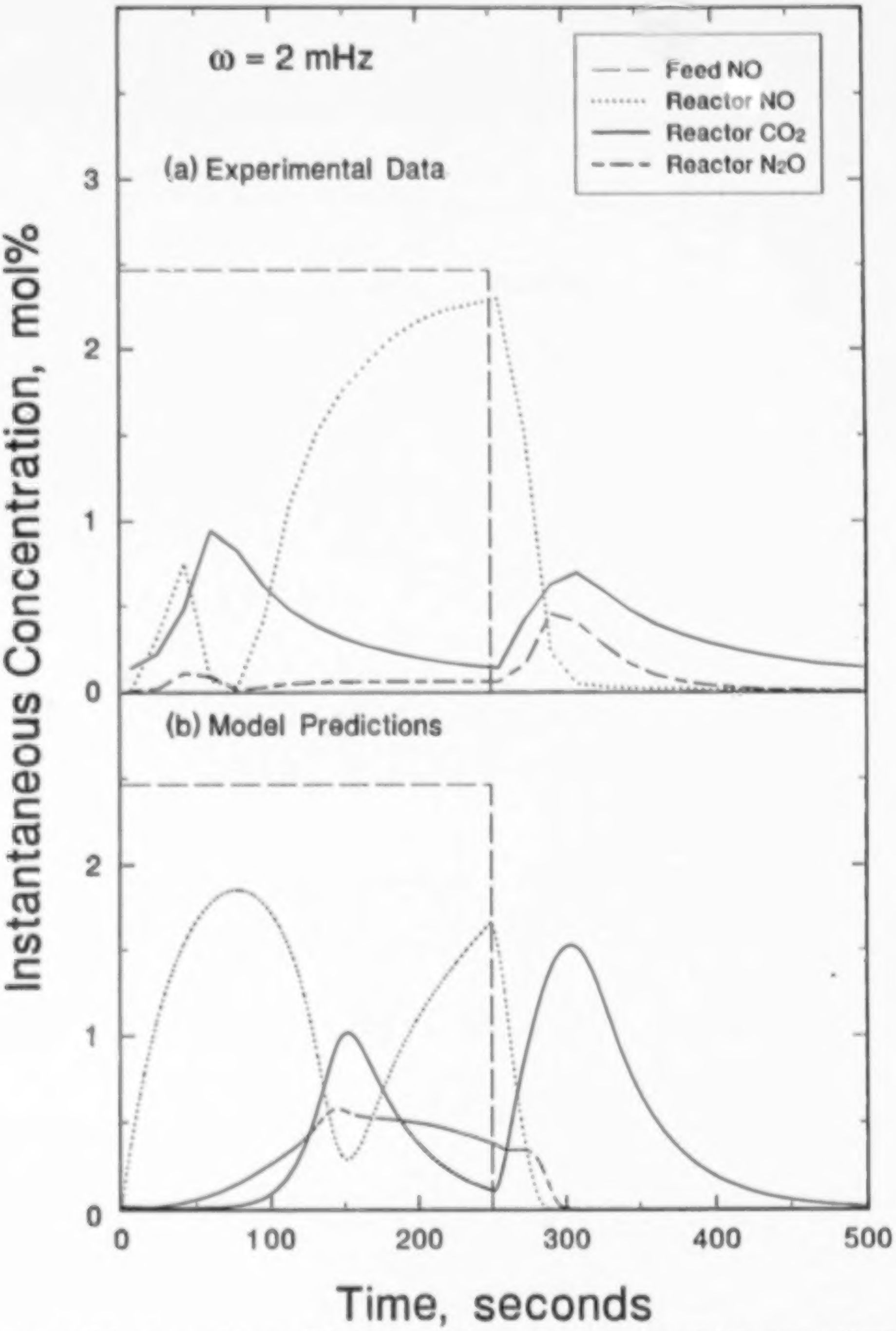

Figure 5.12 Comparison of Model Predictions with Experimental Dynamic Response for Out-of-Phase Feed Cycling at 2 mHz.

peaks per cycle. The shape of the CO_2 curve can be altered by including an additional differential equation (I.17) to account for the adsorption/desorption of CO_2 from the alumina support. The model also predicts a peak and a valley in NO curve in the NO half-cycle, consistent with the experimental observation. The model predicts two peaks of N_2O per cycle, although the N_2O formation in the NO half-cycle is predicted to be larger than that for the CO half-cycle, which is in contrast with the observed behavior. Consistent with the experimental behavior, the model predicts the N_2O peak before the CO_2 peak in each of the two half-cycles. In both Figs 5.12(a) and (b), the CO_2 peak coincides with the valley in the NO curve in the NO half-cycle.

Table 5.2

Comparison of Model Predictions with Experimental Data

for Out-of-Phase Cycling

Time-Average Conversions percent	Experimental Data percent	Model Predictions percent
Cycling Frequency = 2 mHz		
CO	29.06	33.22
NO total	38.20	44.63
NO to N_2O	13.55	23.08
Cycling Frequency = 5 mHz		
CO	61.19	3.55
NO total	73.17	6.27
NO to N_2O	23.08	5.50

The above similarities show that the experimental observations for out-of-cycling at a frequency of 2 mHz can be predicted by a model based on the reaction mechanism used to describe the steady-state multiplicity behavior of the NO+CO reaction. Further optimization of the values of the rate constants may result in the model predictions being in closer agreement with the data, as shown earlier for the N_2O+CO reaction system in Chapter 3. However, the model predictions at 5 mHz are consistently lower than the experimental values, as seen from the comparison in Table 5.2. Therefore, the model needs further improvement, possibly by incorporating a reaction rate enhancement effect due to Pt surface phase transition similar to that used for the N_2O+CO reaction in Chapter 3. A mechanism involving a change of NO sticking coefficient due to Pt(100) phase transition (hex ↔ 1x1) has been suggested to explain rate oscillations of the NO+CO reaction on supported Pt catalyst (*16*). In Chapter 3, while describing the N_2O+CO reaction, it was assumed that the Pt surface phase transition is solely due to the adsorption of CO. However, there is evidence that the adsorbed NO also causes (hex ↔ 1x1) phase transition for Pt(100) (*17, 18*). Therefore, the model should consider the effect of both the adsorbed CO and NO on Pt surface phase transition and the resulting rate enhancement.

5.4 Conclusions

The reduction of NO by CO over Pt/Al_2O_3 catalyst has been investigated using the technique of forced composition cycling. Time-average conversions of both CO and NO, many times larger than the steady state conversions of 2% and 4%, respectively, were obtained during the feed cycling experiments. A significant amount of N_2O was observed as a reaction product. The difference between the NO conversion and CO conversion could be approximately accounted for by the N_2O formation. Higher conversions were obtained for the feeds containing lower concentrations of the reactants. However, the convergence to the cycle-invariant state was very slow for low feed concentrations. This behavior could be explained by considering the relative capacitances of the gas-phase and the catalyst surface. The number of cycles required to reach a cycle-invariant state was found to be strongly and inversely dependent on the ratio of the capacitances of the gas-phase to catalyst surface. The catalyst pretreatment prior to feed cycling has a strong influence on the number of cycles required for convergence. It was also observed that the maximum time-average conversion for the out-of-phase cycling experiments occurred for cycle periods greater than the space-time for the catalyst surface, which is the dominant characteristic time of the system. For cycle periods less than the dominant characteristic time of the system, rate-enhancements were not observed during feed cycling. The time-average conversions for high frequency cycling (short cycle periods) were approximately equal to the steady-state conversions.

By varying the phase angle between the NO and CO feed cycles, it was found that the time-average conversions for 90° NO phase lead are generally greater than those for 180° NO phase lead, especially at low frequencies. It was also observed that the NO phase lead has a significant effect on the N_2O selectivity. Although, the effect of cycling frequency on the reaction selectivity has been reported in the literature (*11*), this study shows that the phase angle also has a significant effect the reaction selectivity. From the transient response curves several observations could be made which are consistent with those made from the steady-state experiments described in Chapter 4. N_2O appears to be formed from the adsorbed NO species. The N_2O selectivity was low for high NO conversions. The reaction proceeds faster on a catalyst surface pre-treated in oxidizing environment as compared with that when the catalyst is pre-treated in a reducing environment.

5.5 Notation

a_m	total Pt surface area of supported catalyst, 9.4 m^2
$[CO]_o$	time-average concentration of CO in feed, mol/m^3
f_{CO}	time-average percent CO conversion
f_{NO}	time-average percent total NO conversion
f_{N_2O}	time-average percent NO conversion to N_2O
L_m	adsorption capacity of platinum surface, 1.42×10^{-5} mol/m^2
M	active site on catalyst surface

M-X	adsorbed species (X=NO or N) on the catalyst surface
$[NO]_o$	time-average NO concentration in feed, mol/m^3
Q_o	volumetric flow rate to the reactor at operating conditions, 5.39x10^{-6}, m^3/s
V	effective free volume of the reactor, 2.15x10^{-4}, m^3

Greek Letters

α_m	ratio of bulk volume to metal surface capacitances
τ_a	catalyst surface space-time, s
τ_v	space-time based on reactor volume, s
ω	cycling frequency, Hz

5.6 References

1. Taylor, K.C. in "Catalysis Science and Technology" (J.R. Anderson and M. Boudart, Eds.) Vol. 5, p 119-170, Springer-Verlag, Berlin, 1984.
2. Muraki, H. and Fujitani, Y., *Ind. Eng. Chem. Prod. Res. Dev.* **25**, 414-419 (1986).
3. Cho, B.K., Shanks, B.H. and Bailey, J.E., *J. Catal.* **115**, 486-499 (1989).
4. Hegedus, L.L., Chang, C.C., McEwen, D.J. and Sloan, E.M., *Ind. Eng. Chem. Fundam.* **19**, 367-373 (1986).
5. Sadhankar, R.R., Ye, J. and Lynch, D.T., *J. Catal.* **146**, 511-522 (1994).
6. Sadhankar, R.R. and Lynch, D.T., *J. Catal.* **149**, 278-291 (1994).
7. Muraki, H., Shinjoh, H. and Fujitani, Y., *Ind. Eng. Chem. Prod. Res. Dev.* **25**, 419-424 (1986).
8. Cho, B.K., *J. Catal.* **148**, 697-708 (1994).
9. Graham, W.R.C. and Lynch, D.T., *AIChE J.* **36**, 1796-1806 (1990).
10. Graham, W.R.C and Lynch, D.T. in "Catalysis 1987 - Proceedings of the Tenth North American Meeting of the Catalysis Society (San Diego 1987)", (J.M. Ward, Ed.), *Stud. Surf. Sci and Catal.* **38**, 693-703, Elsevier, Amsterdam, 1988.
11. Bailey, J.E. in "Chemical Reactor Theory: A review", (L. Lapidus and N.R.

Amundson, Eds.), p. 758-813, Prentice Hall, Engelwood Cliffs, NJ (1977).

12. Lynch, D.T., *Can. J. Chem. Eng.* **64**, 1035-1038 (1986).

13. Lynch, D.T., *Can. J. Chem. Eng.* **62**, 691-698 (1984)

14. Morrow, B.A., Chevrier, J.P. and Moran, L.E., *J. Catal.* **91**, 208-215 (1985).

15. Lööf, P., Kasemo, B., Andersson, S. and Frestad, A., *J. Catal.* **130**, 181-191 (1991).

16. Schüth, F. and Wicke, E. in "Instationary Processes and Dynamic Experimental Methods in Catalysis, Electrochemistry and Corrosion", (G. Sandstede and G. Kreysa, Eds.), Dechema Monogr. vol. 120, p. 429-441 (1989).

17. Gardner, P. Tüshaus, M., Martin, R. and Bradshaw, A.M., *Surf. Sci.* **240**, 112-124 (1990).

18. Bonzel, H.P. and Pirug, G., *Surf. Sci.* **62**, 45-60 (1977).

6. SUMMARY AND RECOMMENDATIONS

The first part of the study deals with the examination of the reduction reaction of N_2O by CO on supported platinum catalyst, as described in Chapters 2 and 3. In the second part of the study, described in Chapters 4 and 5, the NO+CO reaction has been investigated. This chapter summarizes the results and conclusions for both parts of the study. Some recommendations for further work on these reactions have been made towards the end of this chapter.

6.1 N_2O+CO Reaction

There have been several reports in the literature concerning the formation of N_2O as an intermediate in the overall NO+CO reaction at temperatures below 580 K. The N_2O+CO reaction was also recognised as an important sub-reaction of the platinum catalyzed NO+CO reaction (*1*). However, the N_2O+CO reaction on platinum catalysts has not been studied in detail, except for the experimental studies by Lintz and co-workers (*2, 3*). Only recently the importance of the N_2O+CO reaction over rhodium catalyst was recognized due to its importance in automobile catalytic converters which has resulted in a few studies being published (*4-7*). Therefore, one of the objectives of this study was to gain a thorough understanding of the platinum catalyzed N_2O+CO reaction.

The experiments revealed the isothermal steady-state multiplicity behavior of the N_2O+CO reaction in the temperature range of 461-520 K. This is the first report of isothermal steady-state multiplicity of the N_2O+CO reaction. Typically, a high-conversion steady-state was obtained for a net oxidizing ($N_2O > CO$) initial feed composition and a low-conversion steady-state was obtained for an initially net reducing ($N_2O < CO$) feed composition. Four kinetic models were examined to describe the observed multiplicity behavior. Although all four models predicted the existence of multiplicity, only a model based on a CO self-exclusion effect could quantitatively predict the data for low-conversion steady-states. This model was based on a three-step reaction mechanism. The CO self-exclusion effect allows N_2O to adsorb on a CO saturated surface, and therefore, the model predictions of CO conversions for the low-conversion steady-states were as high as the experimental values. For this model, the reaction-rate can be explicitly expressed in terms of the gas-phase concentrations. The reaction rate constants used in the model for four different temperatures showed an Arrhenius-type temperature dependency. However, a constant value of the CO self-exclusion factor, $N_{CO} = 1.025$, was used at the four different temperatures. A low value of the activation energy for CO desorption (41 kJ/mol) was attributed to the abundance of adsorbed CO on the catalyst surface, particularly for low conversion steady-states. A similar observation of low activation energy for high CO surface coverage has been made in a recent study of the NO+CO reaction on platinum foil (*8*). However, two different values of the CO desorption activation energy for the high-rate and low-rate steady-states, respectively, gave a better model-experimental agreement.

To test the applicability of the CO self-exclusion model for describing the reaction transient behavior, further experiments were carried out involving feed composition cycling at 499 K. The CO and N_2O concentrations in the feed were periodically switched between 0% and 2.4% in the form of square-waves. The time-average CO conversion for the out-of-phase cycling showed a resonant behavior. The maximum time-average conversion obtained during out-of-phase cycling was 80% as compared with the steady-state conversion of 20%. This result was expected because several previous studies involving feed composition cycling have reported reaction-rate enhancements for other reactions (*9*). Further experiments were carried out by varying the phase angle between the CO and N_2O feed cycles. Time-average conversion higher than 80% (maximum for out-of-phase cycling) were attained, particularly for N_2O phase leads of less than 180°. It is therefore possible to obtain a global maximum time-average CO conversion for an optimum combination of cycling frequency and the N_2O phase lead. A similar observation has been reported earlier for the platinum-catalyzed CO oxidation reaction

(*10*). The time-average conversions at high cycling frequencies and for high values of N_2O phase leads were consistently low and approximately equal to the steady-state conversion. This is because the gas-phase concentrations in the reactor are nearly time-invariant at high frequencies and resemble the composition for steady-state operation, which gives a low conversion. The CO self-exclusion model based on the steady-state multiplicity data could not describe all of the data for the feed composition cycling experiments. In particular, it could not describe the high conversions obtained for intermediate frequencies for out-of-phase cycling, although the model predictions were better than those from a Langmuir-Hinshelwood type of model. It was found necessary to include a reaction rate enhancement effect due to Pt surface phase transition (1x1 ↔ hex) in the model. It was assumed that the Pt surface switches between two phases, namely a low activity phase (hex) and a high activity phase (1x1) depending on the CO surface coverage during feed cycling. A similar model has been previously used to describe self-sustained oscillations (*11*) and reaction-rate enhancement during feed cycling (*10*) for the $CO+O_2$ reaction on a supported Pt catalyst. A similar mechanism of Pt surface phase transition has also been suggested to explain the oscillations of the NO+CO reaction on Pt/Al_2O_3 catalyst (*12*). The improved model consistently described the transient behavior during feed cycling and the steady-state multiplicity. This demonstrates the usefulness of the feed cycling technique for discrimination among reaction mechanisms. This is apparently the first comprehensive study of the N_2O+CO reaction on alumina supported Pt catalyst. Expanding on the study of the N_2O+CO reaction, further experimental investigation was carried out for the NO+CO reaction.

6.2 NO+CO Reaction

The NO+CO reaction was examined for its steady-state and transient behavior using similar techniques to those used for the N_2O+CO reaction. This reaction was found to exhibit isothermal steady-state multiplicity in the temperature range of 465-520 K. This is a new observation, although there have been earlier reports of rate multiplicity with respect to variation in the temperature (*13-15*). Significant amounts of N_2O were observed as a reaction product, particularly for the high conversion steady-states. Generally, the selectivity towards N_2O formation decreased with increasing NO conversion. An interesting observation for the high-conversion steady-states was that the N_2O selectivity decreased rapidly as the ratio of NO to CO concentrations in the feed decreased below a critical value of approximately 1.5. The experimental values of N_2O selectivity for the feed NO/CO ratios of greater than 1.5 scattered around an average of 0.7 for the high-conversion steady-state. The temperature (in the range of 465-520 K) does not seem to have a significant effect on the N_2O selectivity. A similar observation of average N_2O selectivity of 0.7, with insignificant effect of temperature in the range of 525-675 K has been made in a recent study of the NO+CO reaction on the Rh(111) surface (*16*). The multiplicity behavior of the NO+CO reaction and its selectivity towards N_2O has been described by a mechanism consisting of seven elementary reaction steps which include the three steps used earlier to describe the N_2O+CO reaction. Again it was found necessary to use the CO self-exclusion effect in order to describe the low-to-high bifurcation points and the data for the low-conversion steady-states. The calculated value of the CO desorption activation energy was also low (38 kJ/mol), consistent with the observation for the N_2O+CO reaction. It was possible to eliminate the reaction step for nitrogen desorption (recombination of two adsorbed nitrogen atoms) from the mechanism without affecting the model predictions significantly, particularly for the high-conversion steady-states. This shows that the overall NO+CO reaction can be adequately described by two consecutive reactions, namely the reduction of NO by CO to form N_2O and the subsequent reduction of N_2O by CO. A similar suggestion of consecutive reactions of N_2O formation and subsequent reduction was made earlier by Shelef and Otto (*1*). Subsequently, Cho (*5*, *7*) also reached a similar conclusion while analyzing the role of the N_2O+CO reaction in the overall NO+CO reaction over alumina supported Rh catalyst.

A comparison of the steady-state behavior of the N_2O+CO and NO+CO reactions shows that the CO conversions for the low-conversion steady-states were lower for the NO+CO reaction as compared with the N_2O+CO reaction. This shows a stronger CO inhibition of the NO+CO reaction as compared with the N_2O+CO reaction for the low-conversion steady-states. Secondly, the multiplicity occurred for a wider range of feed compositions for the NO+CO reaction as compared with that for the N_2O+CO reaction. This shows that the multiplicity behavior for the NO+CO reaction could be observed at temperatures higher than that for the N_2O+CO reaction.

The transient behavior of the NO+CO reaction was studied using a feed composition cycling technique similar to that used earlier for the N_2O+CO reaction. Such studies have been performed earlier (*17, 18*), because actual automobile engine exhaust composition oscillates due to the "closed-loop" feed-back control system for the air-to-fuel ratio. However, in this study, there were two unique features, namely, the variable phasing of input cycles and the lower temperature of 485 K which leads to significant N_2O formation. An interesting observation was that the NO+CO reaction exhibits long-term transients during feed cycling, particularly when the catalyst was pre-treated in an oxidizing environment. In general, a large number of cycles was required to reach the cycle-invariant state as compared with the N_2O+CO reaction. The convergence to cycle invariance was very slow for the feed containing lower concentrations of CO and NO (in stoichiometric ratio). This could be explained by comparing the cycle period with the surface residence time, which is the dominant characteristic time of the system and is inversely proportional to the feed concentration. The long-term transients during feed cycling can be correlated to some extent with the transient behavior during non-cycled feed.

The maximum time-average conversion for the out-of-phase cycling experiments occurred for cycle periods greater than the space-time for the catalyst surface. For the out-of-phase cycling experiments, the NO+CO reaction also exhibits resonant behavior for NO and CO conversions, consistent with the observations for the N_2O+CO reaction. The time-average conversions for 90° NO phase lead were generally greater than those for the 180° NO phase lead. The maximum time-average conversions were several times greater than the steady-state conversions of 2% and 4% for CO and NO, respectively. It was also observed that the N_2O selectivity can be altered by changing the NO phase lead. The conversions for the high frequency cycling were approximately equal to the steady-state conversions, consistent with the earlier observations for the N_2O+CO reaction. The observations regarding the N_2O selectivity from the transient response curves were consistent with those made from the steady-state experiments. The instantaneous N_2O selectivity decreased with an increase in instantaneous NO conversion. The transient behavior of the reaction during feed cycling could not be described by the CO self-exclusion model which described the steady-state multiplicity.

6.3 Recommendations for Future Work

The following recommendations are made for further related work on the N_2O+CO reaction and the NO+CO reaction.

1. The kinetic model for the N_2O+CO reaction (Chapter 3) consistently described the steady-state multiplicity and the reaction rate enhancement during feed concentration cycling. One of the main assumptions in this model was that of reaction rate enhancement due to Pt surface phase transition (1x1 ↔ hex). This assumption was based on the experimental evidence from other studies about Pt(100) surface phase transition (hex ↔ 1x1) due to adsorption of CO under high vacuum conditions. However, it is difficult to reconcile an ordered surface reconstruction process under high vacuum conditions on clean Pt(100) surface with the conditions on a supported platinum catalyst at atmospheric pressure (*19*). Therefore, other mechanisms need to be examined. In particular, a mechanism involving a slow oxidation and reduction of the metal surface should be investigated. Such a mechanism has been used to explain the oscillatory oxidation of CO on supported Pt catalyst at atmospheric pressure (*19, 20*).

2. The steady-state multiplicities observed in this study for the N_2O+CO and NO+CO reactions refer to the multiplicities of CO conversion with respect to the direction of change of feed compositions. However, the intrinsic rate multiplicity with respect to the gas-phase concentrations in the reactor has not been investigated. In a theoretical analysis by Eigenberger (*21*), it is shown that the intrinsic-rate multiplicity can exist if the rate

expression is implicit in terms of gas-phase concentrations (i.e. multiple solutions are possible). The steady-state multiplicity for the N_2O+CO reaction in Chapter 2 has been described by an explicit rate expression and therefore intrinsic-rate multiplicity was ruled out. However, for the NO+CO reaction, the rate expression based on the mechanism proposed in Chapter 4, is implicit. Therefore, the NO+CO reaction could exhibit intrinsic-rate multiplicity apart from the conversion-multiplicity investigated in this study. There is some evidence of isothermal intrinsic-rate multiplicity of the NO+CO reaction on polycrystalline platinum under vacuum conditions (*22*). Further experimental work should be performed to investigate the existence of intrinsic-rate multiplicity for the NO+CO reaction. These experiments will involve maintaining the catalyst temperature constant and measuring low concentrations of CO and NO in the reactor accurately, something which was not possible with the gas analyzers employed for this study. The results of such experiments will be useful for further kinetic model development.

3. The reaction rate enhancement observed in this study for the NO+CO reaction could not be described by the kinetic model which described the steady-state multiplicity in Chapter 4. Therefore, the kinetic model needs further improvement for consistently describing both the reaction rate enhancement during feed cycling as well as the steady-state multiplicity. One approach would be to incorporate a reaction rate enhancement effect due to Pt surface phase transition in a manner similar to that used for the N_2O+CO reaction in Chapter 3. The self-sustained oscillations of the NO+CO reaction on Pt(100) (*14*) and on supported Pt catalyst (*12*) have been explained by a Pt surface phase transition mechanism. It has been previously shown for the CO oxidation reaction on Pt/Al_2O_3 that the Pt surface phase transition mechanism could be used to explain both the self-sustained oscillations (*11*), and also the reaction rate enhancement during feed cycling (*10*). Therefore, a similar model has a good chance of describing the NO+CO reaction behavior observed in this study. However, the effect of both the adsorbed CO and NO on the surface-phase transition must be considered because both these species are known to cause hex ↔ 1x1 transition for Pt(100). Alternately, a mechanism based on the autocatalytic behavior of the reaction with coverage dependent adsorption energies for CO

and NO should be investigated. Such a mechanism has been suggested by Fink *et. al.* (*15*) to explain the rate oscillations which occurred when the surface remained in its 1x1 phase all the time.

4. In this study, long-term transients lasting up to 50 hours were observed during the forced concentration cycling of CO and NO. These transients were associated with pretreatment of the catalyst in an oxidizing environment. Similar long-term transients were previously reported for the nickel-catalyzed CO oxidation reaction (*23*) under forced feed concentration cycling conditions. However, the N_2O+CO reaction did not exhibit such long-term transients in this study. The long periods required to reach a cycle-invariant state severely limits the applicability of the forced concentration cycling technique for studying transient behavior, or it may lead to erroneous conclusions as shown in Chapter 5. Some sort of criteria is needed to predict such long-term transients prior to commencing the experiments. Lynch (*24*) suggested such a criteria for the CO+O_2 reaction based on mathematical modelling work. However, in this study, a correlation between the transient behavior during feed cycling and the non-cycled feed was found. The catalyst pretreatment was also found to affect the transient behavior significantly. Therefore, further experimental and modelling work is required to study the effect of the catalyst pretreatment and reactor operating conditions on the transient behavior during cycling, particularly the conditions leading to long-term transients should be clearly identified.

5. The bifurcation points (high-to-low conversion and low-to-high conversion) for the NO+CO reaction at 520 K were farther apart than the bifurcation points for the N_2O+CO reaction at 520 K. Therefore, the bifurcation behavior of the NO+CO reaction could also be observed at temperatures higher than 520 K. However, due to the limitations on the recycle pump, it was not possible to increase the reactor temperature above 520 K in this study. It is recommended that the experiments should be carried out using an internal recycle reactor over a range of temperatures from 450 K to 800 K to study the steady-state bifurcation behavior. The formation of N_2O is expected to be negligible at high

temperatures. The observed multiplicity behavior of the reaction should then be used to verify if the overall reaction can be described by two consecutive reactions, namely, the formation of N_2O and its subsequent reduction by CO, respectively.

6.4 References

1. Shelef, M. and Otto, K., *J. Catal.* **10**, 408-412 (1968).
2. Adlhoch, W., Kohler, R. and Lintz, H.G., *Z. Phys. Chemie Neue Folge* **120**, 111-118 (1980).
3. Lintz, H.G., *Surf. Sci.* **108**, L486-L489 (1981).
4. McCabe, R.W. and Wong, C., *J. Catal.* **121**, 422-431 (1990).
5. Cho, B.K., *J. Catal.* **138**, 255-266 (1992).
6. Belton, D.N. and Schmieg, S.J., *J. Catal.* **138**, 70-78 (1992).
7. Cho, B.K., *J. Catal.* **148**, 697-708 (1994).
8. Scharpf, E.W. and Benziger, J.B., *J. Catal.* **136**, 342-360 (1992).
9. Bailey, J.E. in "Chemical Reactor Theory: A Review" (L. Lapidus and N.R. Amundson, Eds.), p. 758-813, Prentice Hall, Engelwood Cliffs, N.J., 1977.
10. Graham, W.R.C. and Lynch, D.T., *AIChE J.* **36**, 1796-1806 (1990).
11. Lynch, D.T., Emig, G. and Wanke, S.E., *J. Catal.* **97**, 456-468 (1986).
12. Schüth, F. and Wicke, E. in "Instationary Processes and Dynamic Experimental Methods in Catalysis, Electrochemistry and Corrosion", (G. Sandtstede and G. Kreysa, Eds.), Dechema Monogr., Vol. 120, 429-441 (1989).
13. Schwartz, S.B. and Schmidt, L.D., *Surf. Sci.* **183**, L269-L278 (1987).
14. Schwartz, S.B. and Schmidt, L.D., *Surf. Sci.* **206**, 169-186 (1988).
15. Fink, Th., Dath, J.P., Imbihl, R. and Ertl, G., *J. Chem. Phys.* **95**, 2109-2126 (1991).
16. Belton, D.N. and Schmieg, S.J., *J. Catal.* **144**, 9-15 (1993).
17. Muraki, H. and Fujitani, Y., *Ind. Eng. Chem. Prod. Res. Dev.* **25**, 414-419 (1986).
18. Cho, B.K., Shanks, B.H. and Bailey, J.E., *J. Catal.* **115**, 486-499 (1989).

19. Kurtanjek, Ž. and Froment, G.F., *Chem. Eng. Sci.* **40**, 3189-3201 (1991).

20. Sales, B.C., Turner, J.E. and Maple, M.B., *Surf. Sci.* **114**, 381-394 (1982).

21. Eigenberger, G., *Chem. Eng. Sci.* **33**, 1255-1261 (1978).

22. Bolten, H., Hahn, T., LeRoux, J. and Lintz, H.G., *Surf. Sci.* **160**, L529-L532 (1985).

23. Hugo, A.J., Jakelski, D.M., Stanitsas, G., Sullivan, G.R., Hudgins, R.R. and Silveston, P.L., *Can. J. Chem. Eng.* **64**, 349-351 (1986).

24. Lynch, D.T., *Can. J. Chem. Eng.* **64**, 1035-1038 (1986).

APPENDIX A

CALIBRATION OF MASS FLOW CONTROLLERS

The calibration curves for the mass flow meters are presented in this appendix. Each of the flow meters was calibrated using a bubble column. The measured flow was corrected for the ambient temperature and pressure and was expressed at standard conditions of 101.325 kPa and 273.15 K. The calibration data of the measured flow versus the meter reading was fitted using a linear regression of the type

$$Y = aX + b$$

where Y = measured flow, sccm

X = meter reading, sccm

a, b = regression coefficients

The regression coefficients for various flow meters are listed in Table A.1. The calibration curves are presented in Figures A.1 to A.4. The flow transducers use the principle of heat transfer along a capillary tube to develop the flow signal. The heat transfer is a function of the amount of heat added, the mass flow rate and the heat capacity properties of the gas. Therefore, an appropriate correction factor is required for the measured flow if the gas being metered is different from the calibration gas. Based on the data of flow correction factors supplied by Matheson for various gases, no correction was necessary for all the gases used in this study except for the 10% N_2O mixture. The calculated (by regression equation) flow of 10% N_2O (balance N_2) was multiplied by a factor of 0.98 to obtain the actual flow using MFC 3.

Table A.1

Mass flow meter calibration

	MFC 1	MFC 2	MFC 3	MFC 4
Meter Range, sccm	0-500	0-100	0-100	0-30
Matheson Model	8250	8250	8250	8259
Service	N_2	CO, CO_2	N_2O, NO	CO
Calibration gas	N_2	0.982% CO_2 in N_2	2% N_2O in N_2	0.982% CO_2 in N_2
Regression coefficients				
a	0.929283	1.0383	0.994405	1.0059107
b	8.53713	0.0118537	-1.37172	0.35161

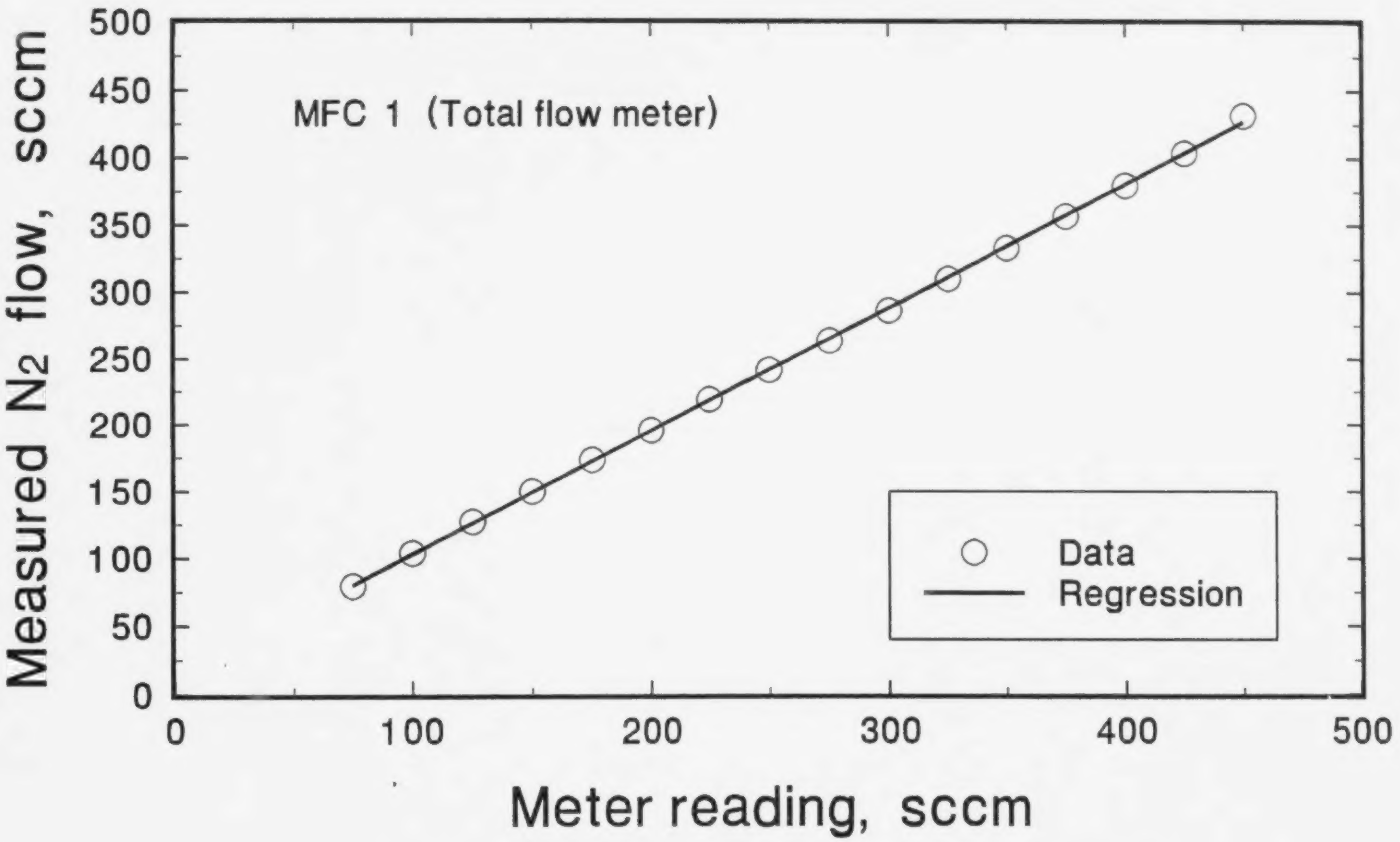

Figure A.1 Calibration of Mass Flow Meter for the Total Flow to the Reactor.

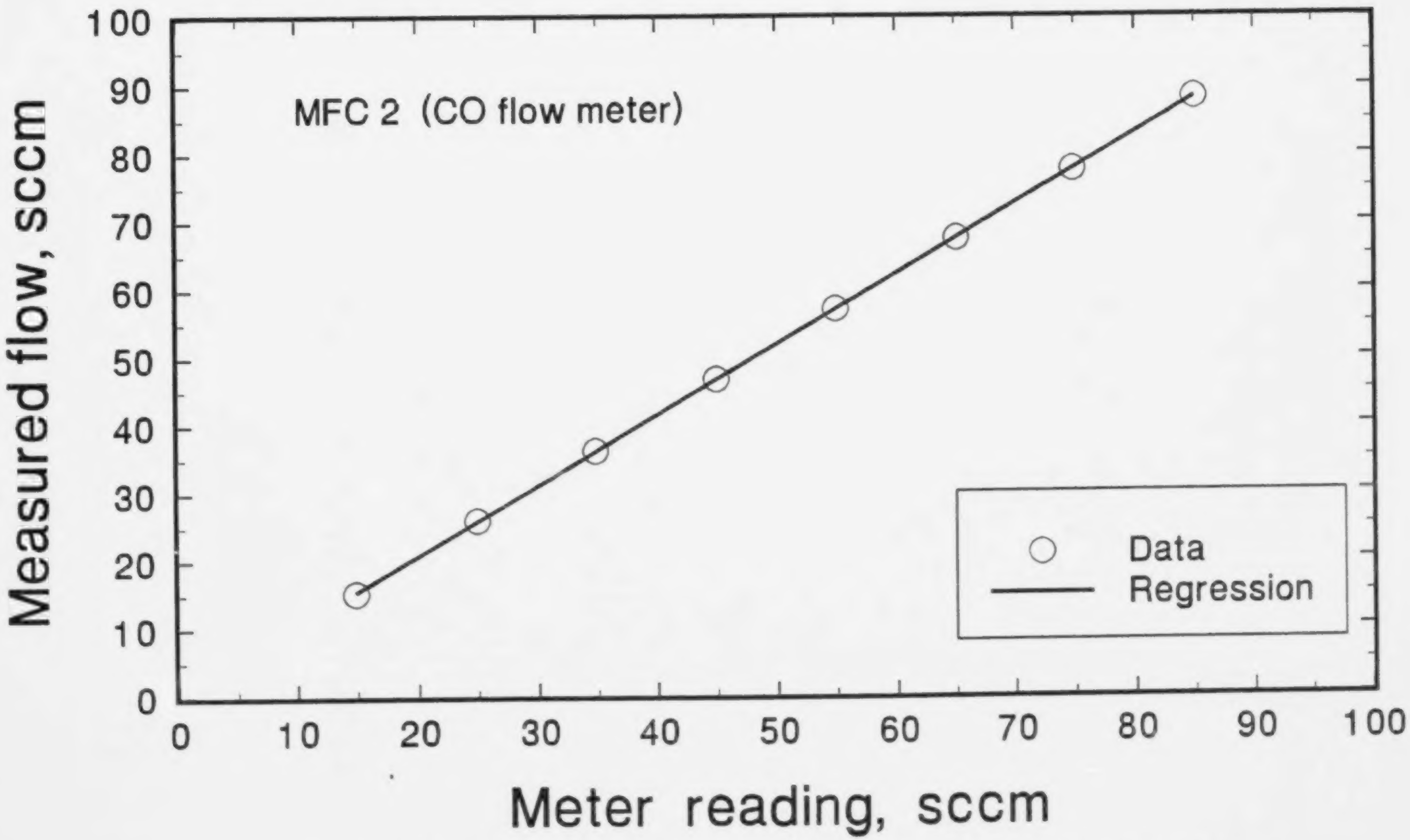

Figure A.2 Calibration of Mass Flow Meter for the Flow of CO or CO_2 Gas Mixtures.

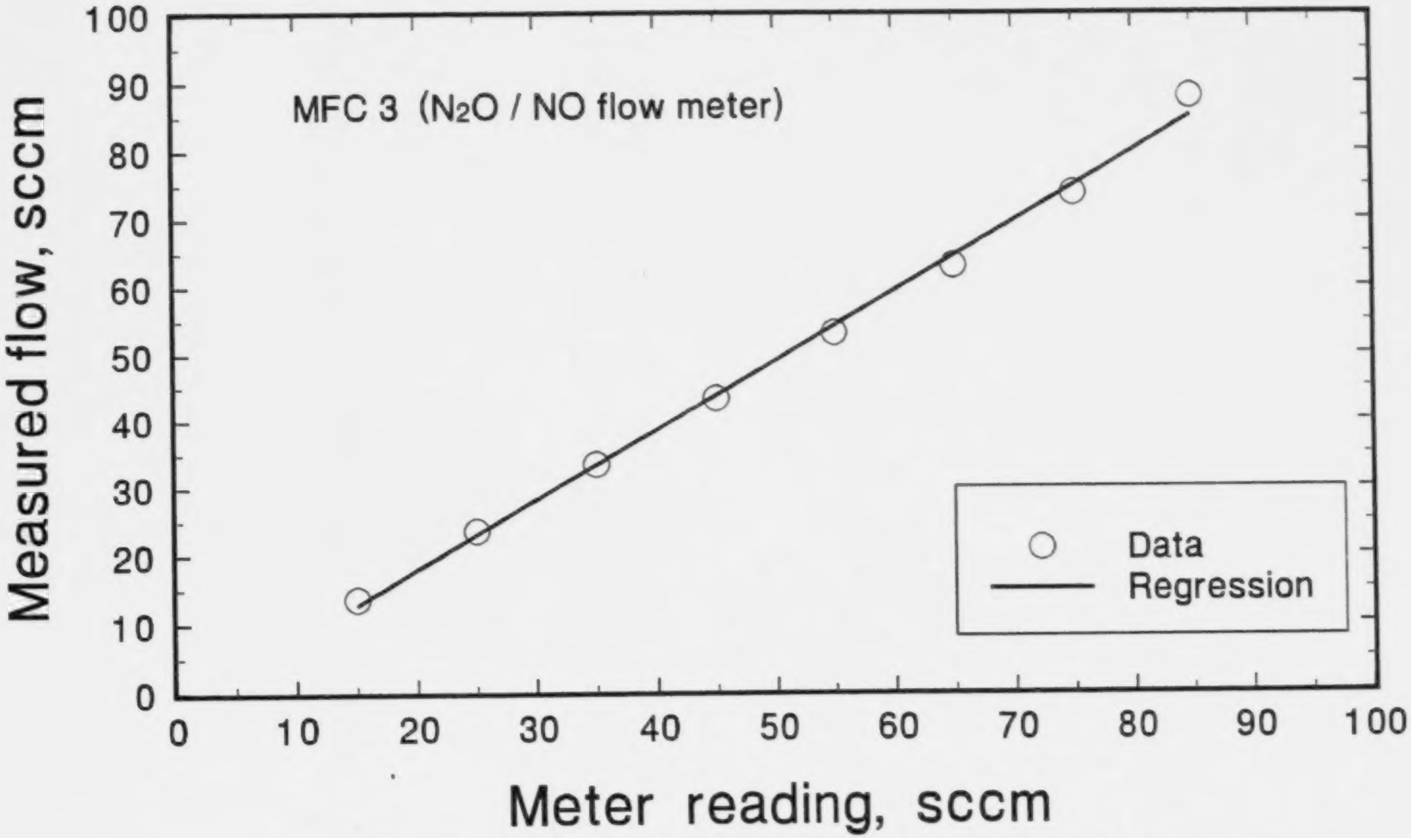

Figure A.3 Calibration of Mass Flow Meter for the Flow of NO or N_2O Gas Mixtures.

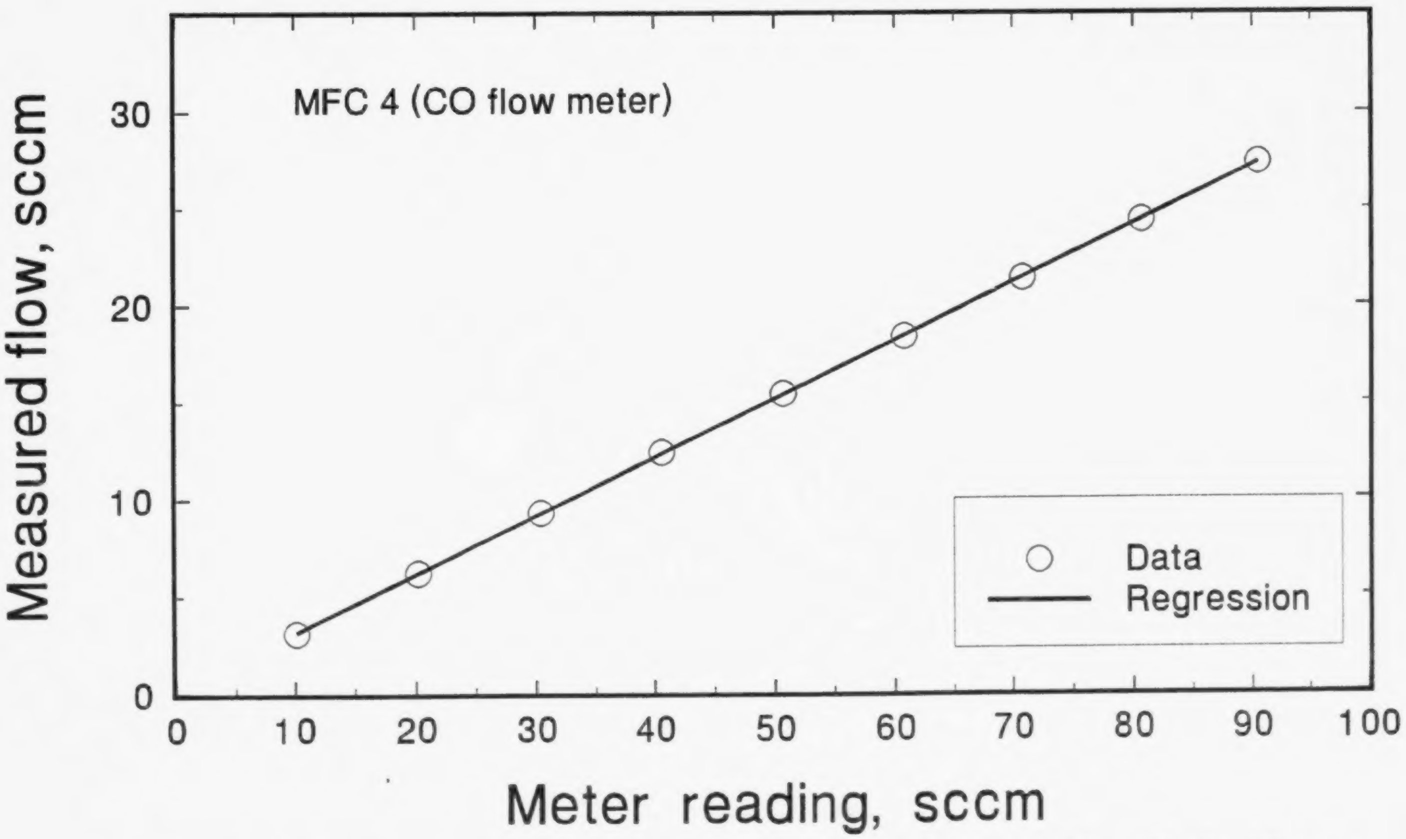

Figure A.4 Calibration of the Auxiliary Mass Flow Meter for the Flow of CO or CO_2 Gas Mixtures.

APPENDIX B

EXPERIMENTAL DATA FOR THE STEADY-STATE MULTIPLICITY OF THE N_2O+CO REACTION

This appendix contains the experimental data of steady-state CO conversion for various feed compositions and temperatures described in Chapter 2.

Table B.1

Steady-State CO Conversions at 499 K with 1.2% N_2O in Feed

Reactor temperature = 499 K
Feed N_2O% = 1.2%
Reactor pressure = 103 kPa
Feed flow rate = 185 sccm

Feed CO% (increasing)	%CO Conversion	Feed CO% (decreasing)	%CO Conversion
0.7475	100	1.9598	9.97
0.7600	100	1.7310	11.08
0.8315	100	1.5315	13.82
0.8337	100	1.3317	16.64
0.9301	100	0.8857	27.92
0.9330	100	0.7858	33.28
1.0289	100	0.6858	39.77
1.0305	100	0.5965	55.78
1.0549	100	0.5861	100
1.0815	20.32	0.5665	100
1.2289	18.49	0.4854	100
		0.3856	100
		0.2859	100
		0.1852	100

Table B.2

Steady-State CO Conversions at 499 K with 0.7% N_2O in Feed

Reactor temperature = 499 K
Feed N_2O% = 0.7%
Reactor pressure = 103 kPa
Feed flow rate = 185 sccm

Feed CO% (increasing)	%CO Conversion	Feed CO% (decreasing)	%CO Conversion
0.1853	100	1.9288	7.23
0.2356	100	1.7300	7.59
0.2856	100	1.5279	8.72
0.3357	100	1.3291	9.98
0.3362	100	1.1284	12.37
0.3853	100	0.7854	24.60
0.5862	100	0.6859	29.24
0.6360	100	0.5856	35.97
0.6568	31.86	0.4864	47.78
		0.4359	61.21
		0.4259	100
		0.4055	100
		0.3859	100
		0.3853	100

Table B.3

Steady-State CO Conversions at 499 K with 0.4% N_2O in Feed

Reactor temperature = 499 K
Feed N_2O% = 0.4%
Reactor pressure = 103 kPa
Feed flow rate = 185 sccm

Feed CO% (increasing)	%CO Conversion	Feed CO% (decreasing)	%CO Conversion
0.1658	100	1.9624	4.63
0.1856	100	1.7341	4.60
0.2358	100	1.5340	5.14
0.2861	100	1.3341	6.17
0.2864	100	1.1337	7.49
0.3263	100	0.9319	9.69
0.3370	100	0.7801	11.98
0.3457	100	0.3849	42.09
0.3662	100	0.3508	44.67
0.3864	41.45	0.3309	50.87
0.4052	38.82	0.3103	56.45
0.4259	33.73	0.2903	62.79
0.4859	24.87	0.2861	100
0.5866	18.18	0.2706	100
0.6864	13.70	0.1859	100

Table B.4

Steady-State CO Conversions at 480 K with 1.2% N_2O in Feed

Reactor temperature = 480 K
Feed N_2O% = 1.2%
Reactor pressure = 103 kPa
Feed flow rate = 185 sccm

Feed CO% (increasing)	%CO Conversion	Feed CO% (decreasing)	%CO Conversion
0.1851	100	1.7333	7.61
0.2862	100	1.5307	8.43
0.3865	100	1.3289	9.72
0.4858	100	1.1299	11.59
0.5859	100	0.9289	14.71
0.6865	100	0.7475	19.83
0.7365	100	0.6860	27.49
0.7852	100	0.5856	33.71
0.8386	100	0.4861	44.02
0.8583	15.03	0.3859	66.03
		0.3658	100
		0.3461	100

Table B.5

Steady-State CO Conversions at 480 K with 0.7% N_2O in Feed

Reactor temperature = 480 K
Feed N_2O% = 0.7%
Reactor pressure = 103 kPa
Feed flow rate = 185 sccm

Feed CO% (decreasing)	%CO Conversion	Feed CO% (increasing)	%CO Conversion
1.9301	4.84	0.1869	100
1.7293	5.15	0.2858	100
1.5268	5.76	0.3863	100
1.3287	6.88	0.4859	100
1.1297	8.36	0.5855	100
0.9291	10.79	0.5867	100
0.8862	12.36	0.6064	97.57
0.7865	13.08	0.6261	20.46
0.6860	15.03	0.7862	14.16
0.5858	18.29	0.8861	11.81
0.4860	24.08		
0.4363	26.99		
0.3857	32.55		
0.3362	40.62		
0.2855	58.54		
0.2660	100		
0.2358	100		
0.1857	100		

Table B.6

Steady-State CO Conversions at 480 K with 0.4% N_2O in Feed

Reactor temperature = 480 K
Feed N_2O% = 0.4%
Reactor pressure = 103 kPa
Feed flow rate = 185 sccm

Feed CO% (increasing)	%CO Conversion	Feed CO% (decreasing)	% CO Conversion
0.1001	100	1.9297	2.91
0.1201	100	1.7284	3.05
0.1401	100	1.5263	3.40
0.1602	100	1.3305	4.04
0.1665	100	1.1305	4.93
0.1801	100	0.9269	6.32
0.1863	100	0.8307	7.13
0.2864	100	0.7859	8.61
0.2967	100	0.6864	9.15
0.3072	100	0.5863	11.03
0.3159	100	0.4855	14.19
0.3256	100	0.3850	20.15
0.3371	100	0.2859	31.37
0.3469	100	0.2663	40.70
0.3569	24	0.2458	45.08
0.3870	18	0.2265	55.06
		0.2201	100.0
		0.2001	100.0

Table B.7

Steady-State CO Conversions at 461 K with 1.2% N_2O in Feed

Reactor temperature = 461 K
Feed N_2O% = 1.2%
Reactor pressure = 103 kPa
Feed flow rate = 185 sccm

Feed CO% (increasing)	%CO Conversion	Feed CO% (decreasing)	%CO Conversion
0.1860	100	0.8862	8.43
0.2361	100	0.8358	8.07
0.2860	100	0.7855	8.19
0.3359	100	0.7358	8.49
0.3859	100	0.6858	8.95
0.4357	100	0.6362	9.65
0.4859	100	0.5861	11.43
0.5359	100	0.5362	12.35
0.5366	100	0.4863	13.64
0.5466	100	0.4361	15.65
0.5564	15.46	0.3861	18.14
0.5760	12.05	0.3364	21.65
		0.2864	26.94
		0.2500	47.60
		0.2362	48.77
		0.2301	55.84
		0.1901	100
		0.1859	100

Table B.8

Steady-State CO Conversions at 461 K with 0.7% N_2O in Feed

Reactor temperature = 461 K
Feed N_2O% = 0.7%
Reactor pressure = 103 kPa
Feed flow rate = 185 sccm

Feed CO% (increasing)	%CO Conversion	Feed CO% (decreasing)	%CO Conversion
0.1863	100	0.8861	4.47
0.2862	100	0.7875	4.61
0.3161	100	0.6861	5.16
0.3363	100	0.5861	6.02
0.3659	100	0.4858	7.72
0.3861	12.71	0.4363	10.03
0.7861	5.26	0.3857	12.07
		0.3362	15.28
		0.2861	19.35
		0.2354	25.57
		0.2012	32.06
		0.1911	33.12
		0.1856	36.34
		0.1610	52.00
		0.1401	100
		0.1302	100

Table B.9

Steady-State CO Conversions at 461 K with 0.4% N_2O in Feed

Reactor temperature = 461 K
Feed N_2O% = 0.4%
Reactor pressure = 103 kPa
Feed flow rate = 185 sccm

Feed CO% (increasing)	%CO Conversion	Feed CO% (decreasing)	%CO Conversion
0.0503	100	0.8860	2.74
0.1002	100	0.7858	2.85
0.1501	100	0.6862	3.26
0.2002	100	0.5858	4.02
0.2356	100	0.4857	4.63
0.2500	100	0.3860	7.41
0.2667	100	0.3362	8.68
0.2854	11.45	0.2854	10.68
		0.2360	13.68
		0.2002	20.33
		0.1802	29.91
		0.1503	38.99
		0.1402	45.43
		0.1303	52.42
		0.1202	61.48
		0.1102	100
		0.1002	100

Table B.10

Steady-State CO Conversions at 520 K with 1.166% CO in Feed

Reactor temperature = 520 K
Feed CO% = 1.1661%
Reactor pressure = 103 kPa
Feed flow rate = 185 sccm

Feed N_2O% (increasing)	%CO Conversion	Feed N_2O% (decreasing)	%CO Conversion
0.1998	9.34	1.8014	100
0.3000	13.01	1.8004	100
0.4003	16.56	1.6999	100
0.5007	20.40	1.5000	100
0.6009	24.47	1.3994	100
0.7009	27.70	1.3486	100
0.8009	31.44	1.3190	100
1.0983	45.08	1.2895	100
1.1989	50.65	1.2586	100
1.2994	55.11	1.2295	56.48
1.3986	60.06	1.1991	51.25
1.4989	64.92	0.9984	41.05
1.5386	69.93	0.8980	36.91
1.5682	74.10		
1.5981	100		
1.6290	100		

Table B.11

Steady-State CO Conversions at 520 K with 0.915% CO in Feed

Reactor temperature = 520 K
Feed CO% = 0.9154%
Reactor pressure = 103 kPa
Feed flow rate = 185 sccm

Feed N_2O% (increasing)	%CO Conversion	Feed N_2O% (decreasing)	%CO Conversion
0.1997	13.89	1.7999	100
0.3001	19.80	1.5982	100
0.4005	24.83	1.4989	100
0.5005	30.71	1.3986	100
0.6007	36.47	1.1076	100
0.7009	42.98	1.0986	100
0.8006	49.03	1.0786	100
0.8287	50.41	1.0486	100
0.8986	55.72	1.0185	100
0.9988	62.57	0.9890	100
1.0995	75.44	0.9570	100
1.1384	100	0.9276	58.90
1.1680	100		
1.2000	100		
1.2286	100		
1.2582	100		
1.3003	100		

Table B.12

Steady-State CO Conversions at 520 K with 0.676% CO in Feed

Reactor temperature = 520 K
Feed CO% = 0.6759%
Reactor pressure = 103 kPa
Feed flow rate = 185 sccm

Feed N_2O% (increasing)	%CO Conversion	Feed N_2O% (decreasing)	%CO Conversion
0.1995	19.50	0.9105	100
0.2998	27.84	0.9004	100
0.3997	35.85	0.8506	100
0.5000	43.75	0.8004	100
0.5501	53.99	0.7504	100
0.6002	59.42	0.7303	100
0.7000	63.40	0.7103	100
0.7304	71.34	0.6902	100
0.7504	73.54	0.6703	100
0.7703	75.06	0.6503	70
0.7905	80.66		
0.8104	100		
0.8306	100		

APPENDIX C

MATLAB PROGRAMS FOR CALCULATING STEADY-STATE CO CONVERSIONS FOR THE N_2O+CO REACTION

The MATLAB programs for the steady-state calculations for the N_2O+CO reaction are listed in this appendix. These programs were used to calculate CO conversion from mechanisms 1, 2, 3 and 4 in Chapter 2. The programs for plotting the bifurcation boundaries and the CO_2 formation rate curve are also listed. The data files for the various programs are listed at the end of the appendix. The various programs and their specific applications are as follows.

MECH1.M	Calculates CO conversion and bifurcation points for Mechanism 1
MECH2.M	Calculates CO conversion and bifurcation points for Mechanism 2
MECH3.M	Calculates CO conversion and bifurcation points for Mechanism 3
MECH4.M	Calculates CO conversion and bifurcation points for Mechanism 4
BIFRMEC4.M	Calculates the bifurcation boundaries at different temperatures
LORATE.M	Calculates CO_2 formation rates for low-conversion region

```
echo off
%PROGRAM : MECH1.M
%THIS PROGRAM CALULATES THE CO% CONVERSION BY MECHANISM 1.
% REACTION STEPS
% CO(g) + M - CO-M   (1)
% N2O(g) + M -- N2(g) + O-M (4)
% CO-M + O-M - CO2(g) + 2M  (8)
a230, b230, c230, % EXPT. DATA AT 499 K
%a210, b210, c210, % EXPT. DATA AT 480 K
%a190, b190, c190, % EXPT. DATA AT 461 K
v=[0,2,0,104]; axis(v)
plot(y(:,1),y(:,2),’o’), hold
plot(x(:,1),x(:,2),’*’)
plot(z(:,1),z(:,2),’x’)
temp=input(’temperature, K’)
mult=103000./(831.4*temp);
k=input(’k1,k21,k23,klh’)
%THE VALUES AT 499 K ARE K1=1000 K21=0.019 K23=8  KLH=17.206
%CONVERT THE INPUT K VALUES TO USE THE MOL% DATA INSTEAD OF mol/cu.m
k1=k(1)*mult;
k2=k(2)*mult;
k23=k(3)*mult;
%TO CONVERT KLH VALUE MUTIPLY BY (W.100.R.T/Q.P)
% =20x100x8.314x1e3x273.15x60/(185x1e-6x101.325)
% = 1.4529731 x 1e7
klh=k(4)*1.4529731;
%DATA FILE d230.m CONTAINS EXPT. BIFURCATION POINTS
d230, %d210, %d190
sumerr=0.0;
for itime=1:3
nrtsav=1;
coi1=data(itime,2);
coi2=data(itime,3);
n2oi=data(itime,1);
xbpll=data(itime,4);
xbplh=data(itime,5);
xbphl=data(itime,6);
xbphh=data(itime,7);
numco=data(itime,8);
for j=1:numco
for l=1:6
xxx(j,l)=0;
end, end
xdelta=(coi2-coi1)/numco;
for i=1:numco
%SOLVE THE CUBIC EQUATION FOR REACTOR N2O%
coi=coi2-xdelta*(i-1);
k12=klh;
k10=k1-(k2+k23);
k11=k1-k2;
del=k1*(coi-n2oi);
aa=-k11*k11;
```

```
bb=k11*k11*n2oi-(1.+2.*del)*k11-k12*k10;
cc=-del*(1.+del)+(1.+2.*del)*k11*n2oi-k12*del;
dd=del*(1.+del)*n2oi;
z=[aa bb cc dd];
zroot=roots(z);
n=0;
for ir=1:3
if imag(zroot(ir))==0.
if real(zroot(ir))>0.
n=n+1;
xroot(n)=zroot(ir);
end,end
end
xxx(i,1)=n;
xxx(i,2)=coi;
xxx(i,3)=xroot(1);
if n>1
xxx(i,4)=xroot(2);
end
if n>2
xxx(i,5)=xroot(3);
end
end
[m,l]=size(xxx);
numco=m;
for i=1:m
for j=1:4
res2(i,j)=0;
res3(i,j)=0;
res4(i,j)=0;
res5(i,j)=0;
end,end
for i=1:m
for j=1:5
res1(i,j)=0;
resa(i,j)=0;
end,end
for i=1:numco
xdelta=(coi2-coi1)/numco;
coi=coi2-xdelta*(i-1);
nroot=0;
for ic=3:5
n2o=xxx(i,ic);
if n2o>0.
co=coi-(n2oi-n2o);
ic=ic-2;
coconv(ic)=(1-co/coi)*100.;
tco(ic)=(k1*co-n2o*(k2+k23))/(1.+k1*co-k2*n2o);
to(ic)=(k23*n2o)/(k1*co-k2*n2o);
rate(ic)=klh*to(ic)*tco(ic);
xcheck(ic)=aa*((xroot(ic))^3)+bb*((xroot(ic))^2)+cc*xroot(ic)+dd;
res2(i,ic)=tco(ic);
```

```
res3(i,ic)=to(ic);
res4(i,ic)=xcheck(ic);
res5(i,ic)=rate(ic);
res1(i,ic)=coconv(ic);
if tco(ic)>=0.0
if tco(ic)<1.
if to(ic)>=0.0
if to(ic)<1.
if(tco(ic)+to(ic))<1.
if coconv(ic)>=0.
if coconv(ic)<100.
nroot=nroot+1;
end,end,end,end,end,end,end,end,end
res1(i,4)=coi;
res1(i,5)=nroot;
if nroot==3
if nrtsav==1
xhbpt=coi+xdelta/2;
nrtsav=3;
num1=i;
end,end
if nroot==1
if nrtsav==3
num2=i;
xlbpt=coi+xdelta/2.;
nrtsav=0;
end,end
end
for i=1:(num2-1)
a1(i)=res1(i,4);
b1(i)=res1(i,1);
end
for i=num1:(num2-1)
b3(i+1-num1)=res1(i,3);
a3(i+1-num1)=res1(i,4);
end
num3=num2-num1;
for i=1:(num3-1)
a2(i)=res1((num2-i),4);
b2(i)=res1((num2-i),2);
end
for i=num2:numco
a4(i+1-num2)=res1(i,4);
b4(i+1-num2)=res1(i,1);
end
a=[a1 a2 a3 a4];
b=[b1 b2 b3 b4];
plot(a,b)
clear a, clear a1, clear a2, clear a3, clear a4
clear b, clear b1, clear b2, clear b3, clear b4
sumerr=sumerr+((((xbpll+xbplh)/2.)-xlbpt)^2)+((((xbphl+xbphh)/2)-xhbpt)^2);
xlb(itime)=xlbpt;
```

```
xhb(itime)=xhbpt;
xlabel('%CO in feed'), ylabel('%CO conversion')
title('CO conversion prediction from Mechanism 1')
% THE FOLLOWING STATEMENTS SAVE THE RESULTS IN ASCII FILES FOR PLOTTING WITH
%A GRAPHICS SOFTWARE.
 for i=1:m
resa(i,1)=res1(i,5);
resa(i,2)=res1(i,4);
resa(i,3)=res1(i,1);
resa(i,4)=res1(i,2);
resa(i,5)=res1(i,3);
end
if itime==1
save resa resa /ascii
end
if itime==2
save resb resa /ascii
end
if itime==3
save resc resa /ascii
end
end, shg
```

```
%PROGRAM MECH2.M
%THIS PROGRAM CALCULATES %CO CONVERSION BY MECHANISM 2.
%REACTION STEPS
% CO(g) + M -- CO-M   (1)
% N2O(g) + M -- N2(g) + O-M   (4)
% CO-M + O-M -- CO2(g) + 2M   (8)
% CO(g) + O-M -- CO2(g) + M  (10)
%THE PROGRAM ALSO HANDLES CO SELF-EXCLUSION MODEL (rnco>1).
a230, b230, c230 ,%EXPT. DATA AT 499 K
%a210, b210, c210 ,%EXPT. DATA AT 480 K
%a190, b190, c190 ,%EXPT. DATA AT 461 K
v=[0,2,0,104]; axis(v)
%plot the experimental CO conversion Vs feed CO
plot(y(:,1),y(:,2),’o’)
hold
plot(x(:,1),x(:,2),’*’)
plot(z(:,1),z(:,2),’x’)
temp=input(’TEMPERATURE, K’)
mult=103000./(831.4*temp);
k=input(’K1 K21 K23 Klh K43 ’)
%THE VALUES OF K AT 499K ARE K1=2115 K21=0.045 K23=8 K43=4.9 KLH=3.891
%CONVERT THE INPUT VALUES OF K TO USE WITH MOL% DATA
k1=k(1)*mult;
k4=k(2)*mult;
k48=k(3)*mult;
klh=k(4)*1.4529731;
rnco=1.0;  %CO SELF-EXCLUSION EFFECT IS NEGLECTED.
k108=k(5)*mult;
%d190, %d210, d230
sumerr=0.0;
for itime=1:3
nrtsav=1;
coi1=data(itime,2);
coi2=data(itime,3);
n2oi=data(itime,1);
xbpll=data(itime,4);
xbplh=data(itime,5);
xbphl=data(itime,6);
xbphh=data(itime,7);
numco=data(itime,8);
for j=1:numco, for l=1:6
xxx(j,l)=0.0 ;
res1(j,l)=0;
res2(j,l)=0;
res3(j,l)=0;
res4(j,l)=0;
res5(j,l)=0;
end, end
count=0;
xdelta=(coi2-coi1)/numco;
% calculate reactor N2O by solving 10th order equation
%with CO self-exclusion effect the polynomial is 10th order.
```

```
for i=1:numco
count=count+1;
coi=coi2-xdelta*(i-1);
m1=coi-n2oi;
a1=klh*k48*k108+k48+k108;
b1=k108*m1*(klh*k48+1.)-n2oi*(k48+k108);
c1=klh*k48*(1.-k108*m1)+1.;
d1=-klh*k48*k108;
e1=-klh*k48;
f1=-n2oi;
g1=-n2oi*m1*k108;
a2=k1*k108;
b2=2.*k1*k108*m1;
c2=k1-2.*rnco*k1*k108*m1-k4-k48-k108;
d2=-rnco*k1*k108;
e2=k4-rnco*k1;
f2=k1*m1-rnco*k1*k108*m1*m1-k108*m1;
g2=k1*k108*m1*m1;
h2=-1.-rnco*k1*m1;
q1=a2*e1-a1*e2;
q2=(e2*d1-d2*e1);
r1=(b2*e1-b1*e2-a1*h2);
r2=e2*c1-e1*c2+d1*h2;
t1=g2*e1-g1*e2-b1*h2;
t2=f1*e2+c1*h2-f2*e1;
s1=-g1*h2;
s2=f1*h2;
p3=d1*d1;
q3=2.*c1*d1-4.*a1*e1;
r3=c1*c1+2.*d1*f1-4.*b1*e1;
t3=2.*c1*f1-4.*g1*e1;
s3=f1*f1;
v5=d1*q2;
v4=2.*e1*q1+c1*q2+d1*r2;
v3=2.*e1*r1+c1*r2+d1*t2+f1*q2;
v2=2.*e1*t1+c1*t2+d1*s2+f1*r2;
v1=2.*e1*s1+c1*s2+f1*t2;
v0=f1*s2;
del(11)=v5*v5;
del(10)=2.*v4*v5;
del(9)=2.*v3*v5+v4*v4;
del(8)=2.*v2*v5+2.*v3*v4;
del(7)=2.*v1*v5+2.*v2*v4+v3*v3;
del(6)=2.*v0*v5+2.*v1*v4+2.*v2*v3;
del(5)=2.*v0*v4+2.*v1*v3+v2*v2;
del(4)=2.*(v0*v3+v1*v2);
del(3)=2.*v0*v2+v1*v1;
del(2)=2.*v0*v1;
del(1)=v0*v0;
gam6=q2*q2;
gam5=2.*q2*r2;
gam4=2.*q2*t2+r2*r2;
```

```
gam3=2.*q2*s2+2.*r2*t2;
gam2=2.*r2*s2+t2*t2;
gam1=2.*t2*s2;
gam0=s2*s2;
beta(11)=gam6*p3;
beta(10)=gam6*q3+gam5*p3;
beta(9)=gam6*p3+gam5*q3+gam4*p3;
beta(8)=gam6*t3+gam5*r3+gam4*q3+gam3*p3;
beta(7)=gam6*s3+gam5*t3+gam4*r3+gam3*q3+gam2*p3;
beta(6)=gam5*s3+gam4*t3+gam3*r3+gam2*q3+gam1*p3;
beta(5)=gam4*s3+gam3*t3+gam2*r3+gam1*q3+gam0*p3;
beta(4)=gam3*s3+gam2*t3+gam1*r3+gam0*q3;
beta(3)=gam2*s3+gam1*t3+gam0*r3;
beta(2)=gam1*s3+gam0*t3;
beta(1)=gam0*s3;
for ii=1:11
alph(12-ii)=del(ii)-beta(ii);
end
zroot=roots(alph);
[m,l]=size(zroot);
for ir=1:10
xroot(ir)=0.0;
end
n=0;
%eliminate imaginary and negative real roots
for ir=1:m
if imag(zroot(ir,1))==0.0
if real(zroot(ir,1))>0.
if real(zroot(ir,1))<=n2oi
n=n+1;
xroot(n)=zroot(ir,1);
end, end, end, end
%matrix xxx stores the positive real roots(N2O)
xxx(i,1)=n;
xxx(i,2)=coi;
xxx(i,3)=xroot(1);
if n>1
xxx(i,4)=xroot(2);
end
if n>2
xxx(i,5)=xroot(3);
end
if n>3
xxx(i,6)=xroot(4);
end
for jj=1:4
tco(jj)=0;
to(jj)=0;
rate(jj)=0;
if xroot(jj)>0.
tco(jj)=(q1*(xroot(jj)^3)+r1*(xroot(jj)^2)+t1*xroot(jj)+s1)/ .....
(q2*(xroot(jj)^3)+r2*(xroot(jj)^2)+t2*xroot(jj)+s2);
```

```
to(jj)=((1-tco(jj))*k48*xroot(jj))/((k48+k108)*xroot(jj)+tco(jj)+k108*m1);
rate(jj)=((n2oi-xroot(jj))*100.)/coi;
res2(i,2+jj)=tco(jj);
res3(i,2+jj)=to(jj);
res4(i,2+jj)=xroot(jj);
res5(i,2+jj)=rate(jj);
end,end
nroot=0;
for jj=1:4
if tco(jj)>=0.
if to(jj)>=0.
if tco(jj)<1.
if to(jj)<1.
if rate(jj)>0.
if rate(jj)<100.
if (to(jj)+tco(jj)) <1.
nroot=nroot+1;
res1(i,2+nroot)=rate(jj);
end,end,end,end,end,end,end,end
res1(i,1)=nroot;
res2(i,1)=nroot;
res3(i,1)=nroot;
res4(i,1)=nroot;
res5(i,1)=nroot;
res1(i,2)=coi;
res2(i,2)=coi;
res3(i,2)=coi;
res4(i,2)=coi;
res5(i,2)=coi;
end
for i=1:numco
if res1(i,1)==3
if nrtsav==1
num1=i;
xhbpt=res1(i,2)+xdelta/2.;
nrtsav=3;
end,end
if res1(i,1)==1
if nrtsav==3
num2=i;
xlbpt=res1(i,2)+xdelta/2.;
nrtsav=1;
end,end,end
%create the vectors a and b for plotting
for i=1:(num2-1)
a1(i)=res1(i,2);
b1(i)=res1(i,3);
end
for i=num1:(num2-1)
b3(i+1-num1)=res1(i,5);
a3(i+1-num1)=res1(i,2);
end
```

```
num3=num2-num1;
for i=1:num3
a2(i)=res1((num2-i),2);
b2(i)=res1((num2-i),4);
end
for i=num2:numco
a4(i+1-num2)=res1(i,2);
b4(i+1-num2)=res1(i,3);
end
a=[a1 a2 a3 a4];b=[b1 b2 b3 b4];plot(a,b,’-’)
title(’%CO prediction by Mechanism 2’)
xlabel(’CO in feed, %’), ylabel(’CO Conversion%’)
sumerr=sumerr+((((xbpll+xbplh)/2.)-xlbpt)^2)+((((xbphl+xbphh)/2.)-xhbpt)^2);
xlb(itime)=xlbpt;xhb(itime)=xhbpt;
clear a a1 a2 a3 a4 b b1 b2 b3 b4
%SAVE THE RESULTS IN ASCII FILES FOR PLOTTING WITH AXUM
if itime==1, save resa res1 /ascii, end
if itime==2, save resb res1 /ascii, end
if itime==3, save resc res1 /ascii , end
end, shg
```

```
%PROGRAM MECH3.M
%THIS PROGRAM CALCULATES THE %CO CONVERSION BY MECHANISM 3.
% REACTIONS STEPS
% CO(g) + M -- CO-M  (1)
% N2O(g) + M -- N2O-M  (5)
% N2O-M -- N2(g) + O-M (6)
% CO-M + O-M -- CO2(g) + 2M (3)
a230, b230, c230
%a210, b210, c210
%a190, b190, c190
v=[0,2,0,104];
axis(v)
%plot the experimental CO conversion Vs feed CO
plot(y(:,1),y(:,2),’o’)
hold
plot(x(:,1),x(:,2),’*’)
plot(z(:,1),z(:,2),’x’)
temp=input(’Temperature, K’)
mult=103000./(831.4*temp);
k=input(’K1 K5 K65 K63 Klh K31’)
%THE VALUES OF K AT 499 K ARE K1=605 : K31=0.00145 : K5=4.8 : K63=2.4 : K65=0.15 : %
%KLH=17.206
%CONVERT THE INPUT K VALUES FOR USE WITH MOL% DATA.
%THIS PROGRAM ALSO HANDLES CO SELF-EXCLUSION EFFECT (rnco >1)
k1=k(1)*mult;
k2=k(2)*mult;
k32=k(3);
k38=k(4)*mult;
k8=k(6);
klh=k(5)*(2.*1.4529731);
rnco=1.0; %FOR CO SELF EXCLUSION EFFECT SET rnco>1.
%read data file d230.m
d230, %d210, %d190
sumerr=0.0;
for itime=3:3
nrtsav=1;
itime
coi1=data(itime,2);
coi2=data(itime,3);
n2oi=data(itime,1);
xbpll=data(itime,4);
xbplh=data(itime,5);
xbphl=data(itime,6);
xbphh=data(itime,7);
numco=data(itime,8);
for j=1:numco
for l=1:6
xxx(j,l)=0.0 ;
res1(j,l)=0;
end
end
count=0;
```

```
xdelta=(coi2-coi1)/numco;
% calculate reactor N2O by solving 5th order equation
for i=1:numco
count=count+1;
coi=coi2-xdelta*(i-1);
m1=coi-n2oi;
q1=k1*(1.+k32)-k2*k38*(1+k8);
t1=k1*m1*(1.+k32);
q2=rnco*k1*(1.+k32)+k2*(1.-k8*k38);
t2=(rnco*k1*m1+1.)*(1.+k32);
a=klh*k2*k38;
a1=a*(q1*(q2-q1));
b1=a*(q1*(t2-t1)+t1*(q2-q1));
c1=a*t1*(t2-t1);
a2=q1*q2*k2+k2*k38*q2*q2;
b2=q1*(t2*k2+q2*(1.+k32))+t1*q2*k2+2.*k2*k38*q2*t2;
c2=q1*t2*(1.+k32)+t1*(t2*k2+q2*(1.+k32))+k2*k38*t2*t2;
d2=t1*t2*(1.+k32);
bb=a1-a2*n2oi+b2;
cc=b1-b2*n2oi+c2;
dd=c1-c2*n2oi+d2;
ee=-d2*n2oi;
zz=[a2 bb cc dd ee];
zroot=roots(zz);
[m,l]=size(zroot);
for ir=1:4
xroot(ir)=0.0;
end
n=0;
%eliminate imaginary and negative real roots
for ir=1:m
if imag(zroot(ir,1))==0.0
if real(zroot(ir,1))>0.
if real(zroot(ir,1))<=n2oi
n=n+1;
xroot(n)=zroot(ir,1);
end
end
end,end
%matrix xxx stores the positive real roots(N2O)
xxx(i,1)=n;
xxx(i,2)=coi;
xxx(i,3)=xroot(1);
if n>1
xxx(i,4)=xroot(2);
end
if n>2
xxx(i,5)=xroot(3);
end
if n>3
xxx(i,6)=xroot(4);
end
```

```
for jj=1:4
tco(jj)=0;
to(jj)=0;
rate(jj)=0;
if xroot(jj)>0.
tco(jj)=(q1*xroot(jj)+t1)/(q2*xroot(jj)+t2);
to(jj)=((1.-tco(jj))*k38*k2*xroot(jj))/ .....
(k38*k2*xroot(jj)+tco(jj)*(1.+k32+k2*xroot(jj)));
rate(jj)=(klh*tco(jj)*to(jj)*100.)/coi;
end,end
nroot=0;
for jj=1:4
if tco(jj)>=0.
if to(jj)>=0.
if tco(jj)<1.
if to(jj)<1.
if rate(jj)>0.
if rate(jj)<100.
if (to(jj)+tco(jj)) <1.
nroot=nroot+1;
res1(i,2+nroot)=rate(jj);
end,end,end,end,end,end,end,end
nroot;
res1(i,1)=nroot;
res1(i,2)=coi;
end
for i=1:numco
if res1(i,1)==3
if nrtsav==1
num1=i;
xhbpt=res1(i,2)+xdelta/2.;
nrtsav=3;
end,end
if res1(i,1)==1
if nrtsav==3
num2=i;
xlbpt=res1(i,2)+xdelta/2.;
nrtsav=1;
end,end,end
%create the vectors a and b for plotting
for i=1:(num2-1)
a1(i)=res1(i,2);
b1(i)=res1(i,3);
end
for i=num1:(num2-1)
b3(i+1-num1)=res1(i,5);
a3(i+1-num1)=res1(i,2);
end
num3=num2-num1;
for i=1:num3
a2(i)=res1((num2-i),2);
b2(i)=res1((num2-i),4);
```

```
end
for i=num2:numco
a4(i+1-num2)=res1(i,2);
b4(i+1-num2)=res1(i,3);
end
a=[a1 a2 a3 a4];
b=[b1 b2 b3 b4];
plot(a,b)
title('CO conversion prediction from Mechanism 3')
xlabel('CO in feed, %'),ylabel('CO Conversion, %')
sumerr=sumerr+((((xbpll+xbplh)/2.)-xlbpt)^2)+((((xbphl+xbphh)/2.)-xhbpt)^2);
xlb(itime)=xlbpt;
xhb(itime)=xhbpt;
if itime==1
save resa res1 /ascii
end
if itime==2
save resb res1 /ascii
end
if itime==3
save resc res1 /ascii
end
clear a,clear a1,clear a2, clear a3, clear a4
clear b, clear b1, clear b2, clear b3, clear b4
end
shg
```

```
%PROGRAM: MECH4.M
%THIS PROGRAM CALCULATES CO CONVERSION BY MECHANISM 4
% REACTIONS STEPS SIMILAR TO MECHANISM #1
% CO SELF-EXCLUSION EFFECT IS INCLUDED
% A SIMILAR PROGRAM "MECH4B.M" IS USED FOR CALULATIONS AT 520 K WITH FIXED
%FEED %CO AND VARIABLE FEED %N2O
a230, b230, c230
%a210,b210,c210
%a190, b190, c190
v=[0,2.,0,104];axis(v)
%plot the experimental CO conversion Vs feed CO
plot(y(:,1),y(:,2),’o’),hold
plot(x(:,1),x(:,2),’*’)
%temp=input(’enter temperature, K’)
temp=499.0;
mult=(103000.)/(831.4*temp);
plot(z(:,1),z(:,2),’x’)
%Enter the value of KLH after multiplying by 10e7 .
k=input(’K1 K4 K48 Klh Nco’)
%THE VALUES OF K AT 499K ARE K1=1200 K21=0.0173 K23=8 KLH=13.076 %Nco=1.025
%convert the parameters for use with mol% data
k1=k(1)*mult;
k3=k(2)*mult;
k37=k(3)*mult;
k12=k(4)*1.4529731
rnco=k(5);
%read data file d230.m
d230, %d210, %d190
sumerr=0.0;
for itime=1:3
nrtsav=1;
coi1=data(itime,2);
coi2=data(itime,3);
n2oi=data(itime,1);
xbpll=data(itime,4);
xbplh=data(itime,5);
xbphl=data(itime,6);
xbphh=data(itime,7);
numco=data(itime,8);
for j=1:numco, for l=1:6
xxx(j,l)=0.0 ;
end,end
for j=1:numco, for l=1:5
resa(j,l)=0;res1(j,l)=0;
end,end
count=0;
xdelta=(coi2-coi1)/numco;
% calculate reactor N2O by solving 4th order equation
for i=1:numco
count=count+1;
coi=coi2-xdelta*(i-1);
k7=k3/k37;
```

```
del=k1*(coi-n2oi);
k10=k1-(1.+1./k7)*k3;
k11=k1-k3;
k37=k3/k7;
gamma=1.+rnco*del;
k14=rnco*k1-k3;
k15=(rnco-1.)*k1+k3/k7;
k16=k1-k3+rnco*del*k3/k7;
aa=-k14*k14*k37;
bb=k14*k14*k37*n2oi-k14*(gamma*k37+k16)-k12*k10*k15;
cc=(gamma*k37+k16)*k14*n2oi-gamma*k16-del*k14-k12*(del*k15+(gamma-del)*k10);
dd=(gamma*k16+del*k14)*n2oi-gamma*del-k12*del*(gamma-del);
ee=gamma*del*n2oi;
z=[aa,bb,cc,dd,ee];
zroot=roots(z);
[m,l]=size(zroot);
for ir=1:4
xroot(ir)=0.0;
end
n=0;
%eliminate imaginary and negative real roots
for ir=1:m
if imag(zroot(ir,1))==0.0
if real(zroot(ir,1))>0.
n=n+1;xroot(n)=zroot(ir,1);
end,end,end
%matrix xxx stores the positive real roots(N2O)
xxx(i,1)=count; xxx(i,2)=n; xxx(i,3)=xroot(1);
if n>1, xxx(i,4)=xroot(2); end
if n>2, xxx(i,5)=xroot(3);end
if n>3, xxx(i,6)=xroot(4),end
end
%res1 stores the CO conversions, res2 stores CO coverages
%res4 stores the value of the polynomial (should be zero)
for i=1:numco
for j=1:4
res1(i,j)=0.0; res2(i,j)=0.0
res3(i,j)=0.0;%res4(i,j)=0.0
resa(i,j)=0.0;
res5(i,j)=0.0;
end, end
for i=1:numco
xdelta=(coi2-coi1)/numco;
coi=coi2-xdelta*(i-1);
nroot=0;
for ic=3:5
n2o=xxx(i,ic);
if n2o>0.
co=coi-(n2oi-n2o);
ic=ic-2;
coconv(ic)=(1-co/coi)*100.;
%rate(ic)=(coi-co)*68.824404;
```

```
tco(ic)=(k1*co-k3*(1.+1./k7)*n2o)/(1.+rnco*k1*co-k3*n2o);
to(ic)=k3*n2o*(1.+rnco*k1*co-k1*co+k3*n2o/k7)/ ....
(k7*(k1*co-k3*n2o)+k3*n2o*(rnco*k1*co-k3*n2o));
rate(ic)=k12*to(ic)*tco(ic);
res2(i,ic)=co;
res3(i,ic)=to(ic);
res5(i,ic)=rate(ic);
res1(i,ic)=coconv(ic);
if tco(ic)>=0.0
if tco(ic)<1.
if to(ic)>=0.0
if to(ic)<1.
if (tco(ic)+to(ic))<1.
if coconv(ic)>=0.
if coconv(ic)<100.
nroot=nroot+1;
end, end, end, end, end, end, end, end, end
% determine the lower and upper bifurcation points
res1(i,4)=coi;
res1(i,5)=nroot;
res2(i,4)=nroot;
if nroot==3
if nrtsav==1
xhbpt=coi+xdelta/2;
nrtsav=3; num1=i;
end,end
if nroot==1
if nrtsav==3
num2=i; nrtsav=0;
xlbpt=coi+xdelta/2;
end,end
end
%create the vectors a and b for plotting
for i=1:(num2-1)
a1(i)=res1(i,4);
b1(i)=res1(i,1);
end
for i=num1:(num2-1)
b3(i+1-num1)=res1(i,3);
a3(i+1-num1)=res1(i,4);
end
num3=num2-num1;
for i=1:num3-1
a2(i)=res1((num2-i),4);
b2(i)=res1((num2-i),2);
end
for i=num2:numco
a4(i+1-num2)=res1(i,4);
b4(i+1-num2)=res1(i,1);
end
a=[a1 a2 a3 a4];
b=[b1 b2 b3 b4];
```

```
plot(a,b)
xlabel(’CO % in feed’),ylabel(’% CO Conversion’)
sumerr=sumerr+((((xbpll+xbplh)/2.)-xlbpt)^2)+((((xbphl+xbphh)/2.)-xhbpt)^2);
xlb(itime)=xlbpt;
xhb(itime)=xhbpt;
clear a a1 a2 a3 a4 b b1 b2 b3 b4
for i=1:numco
resa(i,1)=res1(i,5);
resa(i,2)=res1(i,4);
resa(i,3)=res1(i,1);
resa(i,4)=res1(i,2);
resa(i,5)=res1(i,3);
end
%SAVE THE RESULTS IN ASCII FILE FOR PLOTTING
if itime==1, save resa resa /ascii, end
if itime==2, save resb resa /ascii, end
if itime==3, save resc resa /ascii, end
end
shg
```

```
%PROGRAM BIFRMEC4.M
% This program generates data for the lower
% and upper bifurcation curves for Mechanism 4
temp=input('enter temperature, K')
mult=(103000.)/(831.4*temp);
k=input('K1 K21 K23 KLH Nco')
% convert the parameters for use with mol% data
k1=k(1)*mult;
k3=k(2)*mult;
k37=k(3)*mult;
k12=k(4)*1.4529731;
rnco=k(5);
for jtime=1:100, for i=1:3
res2(jtime,i)=0;
end,end
for jtime=1:100
n2oi=0.3+(1.3/99)*(jtime-1);
nrtsav=1;
%SELECT THE MIN.(coi1) AND MAX.(coi2) CO% IN FEED
coi1=0.05; coi2=1.0;
numco=100; %numco = NO. OF STEPS BETWEEN coi1 AND coi2.
for j=1:numco, for l=1:6
xxx(j,l)=0.0 ;
end, end
for j=1:numco, for l=1:5
res1(j,l)=0;
end,end
count=0;
xdelta=(coi2-coi1)/numco;
% calculate reactor N2O by solving 4th order equation
for i=1:numco
count=count+1;
coi=coi2-xdelta*(i-1);
k7=k3/k37;
del=k1*(coi-n2oi);
k10=k1-(1.+1./k7)*k3;
k11=k1-k3;
k37=k3/k7;
gamma=1.+rnco*del;
k14=rnco*k1-k3;
k15=(rnco-1.)*k1+k3/k7;
k16=k1-k3+rnco*del*k3/k7;
aa=-k14*k14*k37;
bb=k14*k14*k37*n2oi-k14*(gamma*k37+k16)-k12*k10*k15;
cc=(gamma*k37+k16)*k14*n2oi-gamma*k16-del*k14-k12*(del*k15+(gamma-del)*k10);
dd=(gamma*k16+del*k14)*n2oi-gamma*del-k12*del*(gamma-del);
ee=gamma*del*n2oi;
z=[aa,bb,cc,dd,ee];
zroot=roots(z);
[m,l]=size(zroot);
for ir=1:4
xroot(ir)=0.0;
```

```
end
n=0;
%eliminate imaginary and negative real roots
for ir=1:m
if imag(zroot(ir,1))==0.0
if real(zroot(ir,1))>0.
n=n+1;
xroot(n)=zroot(ir,1);
end ,end, end
%matrix xxx stores the positive real roots(N2O)
xxx(i,1)=count;
xxx(i,2)=n;
xxx(i,3)=xroot(1);
if n>1, xxx(i,4)=xroot(2);end
if n>2, xxx(i,5)=xroot(3);end
if n>3, xxx(i,6)=xroot(4);end
end
%res1 stores the CO conversions, res2 stores CO coverages
for i=1:numco
xdelta=(coi2-coi1)/numco;
coi=coi2-xdelta*(i-1);
nroot=0;
for ic=3:5
n2o=xxx(i,ic);
if n2o>0.
co=coi-(n2oi-n2o);
ic=ic-2;
coconv(ic)=(1-co/coi)*100.;
tco(ic)=(k1*co-k3*(1.+1./k7)*n2o)/(1.+rnco*k1*co-k3*n2o);
to(ic)=k3*n2o*(1.+rnco*k1*co-k1*co+k3*n2o/k7)/(k7*(k1*co-k3*n2o)+k3*n2o*(rnco*k1*co-k3*n2o));
rate(ic)=k12*to(ic)*tco(ic);
res1(i,ic)=coconv(ic);
if tco(ic)>=0.0
if tco(ic)<1.
if to(ic)>=0.0
if to(ic)<1.
if (tco(ic)+to(ic))<1.
if coconv(ic)>=0.
if coconv(ic)<100.
nroot=nroot+1;
end, end, end, end, end, end, end, end, end
% determine the lower and upper bifurcation points
res1(i,4)=coi;
res1(i,5)=nroot;
if nroot==3
if nrtsav==1
xhbpt=coi+xdelta/2;
nrtsav=3; num1=i;
end,end
if nroot==1
if nrtsav==3
num2=i;nrtsav=0;
```

```
xlbpt=coi+xdelta/2;
end,end
end
%create the vectors a and b for plotting
for i=1:(num2-1)
a1(i)=res1(i,4);
b1(i)=res1(i,1);
end
for i=num1:(num2-1)
b3(i+1-num1)=res1(i,3);
a3(i+1-num1)=res1(i,4);
end
num3=num2-num1;
for i=1:num3-1
a2(i)=res1((num2-i),4);
b2(i)=res1((num2-i),2);
end
for i=num2:numco
a4(i+1-num2)=res1(i,4);
b4(i+1-num2)=res1(i,1);
end
a=[a1 a2 a3 a4];
b=[b1 b2 b3 b4];
%res2 STORES THE CALCULATED BIFURCATION POINTS.
res2(jtime,1)=n2oi;
res2(jtime,2)=xlbpt;
res2(jtime,3)=xhbpt;
clear a a1 a2 a3 a4 b b1 b2 b3 b4 res1 num1 num2 num3
end, %SAVE THE RESULTS IN ASCII FILE FOR PLOTTING
save bifr1 res2 /ascii
```

```
%PROGRAM: LORATE.M
 echo off
%THIS PROGRAM CALULATES THE CO2 FORMATOION RATE BY MECHANISM 4.
%RATES FOR HIGH CONVERSION BRANCH CAN BE FOUND FROM PROGRAM   mech1.m
%THIS PROGRAM CALULATES THE RATE FOR LOW CONVERSION BRANCH ONLY
%BY USING EQUATION (28).
c230,  % EXPT. DATA AT 490 K WITH FEED N2O=1.2%
v=[0.6,2,0,40];
axis(v)
for ii=1:25
z(ii,3)=z(ii,1)*z(ii,2)*0.6875;
end
plot(z(:,1),z(:,3),'o')
hold
temp=499;
mult=103000./(831.4*temp);
k=input('k1,k23,klh')
%CONVERT THE INPUT K VALUES TO USE THE MOL% DATA INSTEAD
%INSTEAD OF mol/cu.m
k1=k(1)*mult;
k23=k(2)*mult;
%TO CONVERT KLH VALUE MUTIPLY BY (100.R.T/Q.P)
klh=k(3)*1.4529731/2;
%DATA FILE d230.m CONTAINS EXPT. BIFURCATION POINTS
d230
sumerr=0.0;
for itime=3:3
nrtsav=1;
coi1=data(itime,2);
coi2=data(itime,3);
n2oi=data(itime,1);
xbpll=data(itime,4);
xbplh=data(itime,5);
xbphl=data(itime,6);
xbphh=data(itime,7);
numco=data(itime,8);
for j=1:numco
for l=1:6
xxx(j,l)=0;
end
end
xdelta=(coi2-coi1)/numco;
for i=1:numco
%SOLVE THE CUBIC EQUATION FOR REACTOR N2O%
coi=coi2-xdelta*(i-1);
m1=coi-n2oi;
 nco=1.025;
aa=-nco*nco*k1*k23;
bb=nco*k1*(n2oi*k23*nco-(1+k23*nco*m1))-klh*k23*((nco-1)*k1+k23);
cc=nco*k1*(n2oi*(1+k23*nco*m1)-m1)-klh*k23*(1+k1*m1*(nco-1));
dd=nco*k1*n2oi*m1;
z=[aa bb cc dd];
```

```
zroot=roots(z);
n=0;
for ir=1:3
if imag(zroot(ir))==0.
if real(zroot(ir))>0.
n=n+1;
xroot(n)=zroot(ir);
end,end
end
xxx(i,1)=n;
xxx(i,2)=coi;
xxx(i,3)=xroot(1);
if n>1
xxx(i,4)=xroot(2);
end
if n>2
xxx(i,5)=xroot(3);
end
end
[m,l]=size(xxx);
numco=m;
for i=1:m
for j=1:4
res2(i,j)=0;
res3(i,j)=0;
res4(i,j)=0;
res5(i,j)=0;
end,end
for i=1:m
for j=1:5
res1(i,j)=0;
resa(i,j)=0;
end,end
for i=1:numco
xdelta=(coi2-coi1)/numco;
coi=coi2-xdelta*(i-1);
nroot=0;
res1(i,4)=coi;
for ic=2:4
n2o=xxx(i,ic);
if n2o>0.
co=coi-(n2oi-n2o);
ic=ic-1;
rate(ic)=(coi-co)*68.75;
res1(i,ic)=rate(ic);
end, end
end
end
plot(res1(:,4),res1(:,2))
xlabel('%CO in the feed')
ylabel('Rate of CO2 formation, nano mol/g.s.')
shg
```

```
%FILE a190.m
%EXPERIMENTAL DATA AT 461 K WITH 0.4% N2O IN THE FEED
x=[0.0503 0.1002 0.1501 0.2002 0.2356 0.2500 0.2667 0.2854 0.8860 0.7858  0.6862 0.5858 0.4877 .......
   0.3860 0.3362 0.2854 0.2360 0.2002 0.1802 0.1503  0.1402 0.1303 0.1202 0.1102 0.1002
   100 100 100 100 100 100 100 11.45 2.74 2.85 3.26 4.02 4.63 7.41 8.68 10.68 13.68 20.33 29.91 ........
   38.99 45.43 52.42 61.48 100 100].';

%FILE b190.m
%EXPERIMENTAL DATA AT 461 K WITH 0.7% N2O IN THE FEED
y=[0.1863 0.2862 0.3161 0.3363 0.3659 0.3861 0.7861 0.8861 0.7875 0.6861 0.5861 0.4858 0.4363 ......
   0.3857 0.3362 0.2861 0.2354 0.2012 0.1911 0.1856 0.1610 0.1401 0.1302
   100 100 100 100 100 12.71 5.26 4.47 4.61 5.16 6.02 7.72 10.03 12.07 15.28 19.35 25.57 32.06 ......
   33.12 36.34 52.00 100 100].';

%FILE c190.m
%EXPERIMENTAL DATA AT 461 K WITH 1.2% N2O IN THE FEED
z=[0.1860 0.2361 0.2860 0.3359 0.3859 0.4357 0.4859 0.5359 0.5366 0.5466 0.5564 0.5760 0.8862 ......
  0.8358 0.7855 0.7358 0.6858 0.6362 0.5861 0.5362  0.4863 0.4361 0.3861 0.3364 0.2864 0.2500 .....
  0.2362 0.2301 0.1901 0.1859
   100 100 100 100 100 100 100 100 100 100 15.46 12.05 8.43 8.07 8.19 8.49 8.95 9.65 11.43 12.35 ......
    13.64 15.65 18.14 21.65 26.94 47.60 48.77 55.84 100 100].';


%FILE a210.m
%EXPERIMENTAL DATA AT 480 K WITH 0.4% N2O IN THE FEED
x=[0.1001 0.1201 0.1401 0.1602 0.1665 0.1801 0.1863 0.2864 0.2967 0.3072 0.3159 0.3256 0.3371 .....
   0.3469 0.3569 0.3870 1.9297 1.7284 1.5263 1.3305 1.1305 0.9269 0.8307 0.7859 0.6864 0.5863 ......
   0.4855 0.3850 0.2859 0.2663 0.2458 0.2265 0.2201 0.2001
   100 100 100 100 100 100 100 100 100 100 100 100 100 100 24 18 2.91 3.05 3.4 4.04 4.93 6.32 ......
   7.13 8.61 9.15 11.03 14.19 20.15 31.37 40.7 45.08 55.06 100 100].';


%FILE b210.m
%EXPERIMENTAL DATA AT 480 K WITH 0.7% N2O IN THE FEED
y=[0.1869 0.2858 0.3863 0.4859 0.5855 0.5857 0.6064 0.6261 0.7862 0.8861 1.9301 1.7293 1.5268 ......
   1.3287 1.1297 0.9291 0.8862 0.7865 0.6860 0.5858 0.4860 0.4363 0.3857 0.3362 0.2855 0.2660 ......
   0.2358 0.1857
   100 100 100 100 100 100 97.57 20.46 14.16 11.81 4.84 5.15 5.76 6.88 8.36 10.79 12.36 13.08 ....
   15.03 18.29 24.08 26.99 32.55 40.62 58.54 100 100 100].';


%FILE c210.m
%EXPERIMENTAL DATA AT 480 K WITH 1.2% N2O IN THE FEED
z=[0.1851 0.2862 0.3865 0.4858 0.5859 0.6865 0.7365 0.7852 0.8386 0.8583  1.7333 1.5307 1.3289 .....
  1.1299 0.9289 0.7475 0.6860 0.5856 0.4861 0.3859 0.3658 0.3461
   100 100 100 100 100 100 100 100 100 15.03 7.61 8.43 9.72 11.59 14.71 19.83 27.49 33.71 44.02 ....
   66.03 100 100].';
```

```
% FILE a230.m
% EXPERIMENTAL DATA AT 499 K WITH FEED N2O=0.4%
x=[0.1658 0.1856 0.2358 0.2861 0.2864 0.3263 0.3370 0.3457 0.3662 0.3864 0.4052 0.4259 0.4859 .....
  0.5866 0.6864 1.9624 1.7341 1.5340 1.3341 1.1337 0.9319 0.7801 0.3849 0.3508 0.3309 0.3103 .....
  0.2903 0.2861 0.2706 0.1859
   100 100 100 100 100 100 100 100 100 41.45 38.82  33.73 24.87 18.18 13.70 4.63 4.60 5.14 6.17 ....
   7.49 9.69 11.98 42.09 44.67 50.87 56.45 62.79 100 100 100].';
```

```
% FILE b230.m
% EXPERIMENTAL DATA AT 499 K WITH FEED N2O=0.7%
y=[0.1853 0.2356 0.2856 0.3357 0.3362 0.3853 0.5862 0.6360 0.6568 1.9288  1.7300 ......
1.5279   1.3291 1.1284 0.7854 0.6859 0.5856 0.4864 0.4359 0.4259 0.4055 0.3859 0.3853
100 100 100 100 100 100 100 100 31.86 7.23 7.59 8.72 9.98 12.37 24.60 29.24 35.97 47.78 .......
61.21 100 100 100 100].';
```

```
% FILE c230.m
% EXPERIMENTAL DATA AT 499 K WITH FEED N2O=1.2%
z=[0.7475 0.76 0.8315 0.8337 0.9301 0.9330 1.0289 1.0305 1.0549 1.0815 1.2289 1.9598 1.7310 .....
  1.5315 1.3317 0.8857 0.7858 0.6858 0.5965 0.5861 0.5665 0.4854 0.3856 0.2859 0.1852
   100 100 100 100 100 100 100 100 100 20.32 18.49 9.97 11.08 13.82 16.64 27.92 33.28 39.77 ......
   55.78 100 100 100 100 100 100].';
```

```
%FILE a245.m
%EXPERIMENTAL DATA AT 520 K WITH 0.6759% CO IN THE FEED
x=[0.1995 0.2998 0.3997 0.5000 0.5501 0.6002 0.7000 0.7304 0.7504 0.7703  0.7905 0.8104 0.8306 .....
  0.9105 0.9004 0.8506 0.8004 0.7504 0.7303 0.7103  0.6902 0.6703 0.6503
   19.50 27.84 35.85 43.75 53.99 59.42 63.40 71.34 73.54 75.06 80.66 100  100 100 100 100 100 .....
   100 100 100 100 100 70].';
```

```
%FILE b245.m
%EXPERIMENTAL DATA AT 520 K WITH 0.915% CO IN THE FEED
y=[1.7992 1.5982 1.4989 1.3986 1.3003 1.2582 1.2286 1.2000  1.1686 1.1384 1.1076 1.0995 1.0986 ....
   1.0786 1.0486 1.0185  0.9988 0.9890 0.9570 0.9276 0.8986 0.8287 0.8006 0.7009 0.6007 0.5005 ....
   0.4005 0.3001 0.1997
   100 100 100 100 100 100 100 100 100 100 100 75.44 100 100 100 100 62.57 100 100 58.90 55.72 .....
    50.41 49.03 42.98 36.47 30.71 24.83 19.80 13.89];
```

```
%FILE c245.m
%EXPERIMENTAL DATA AT 520 K WITH 1.166% CO IN THE FEED
z=[1.8014 1.8004 1.6999 1.6290 1.5981 1.5682 1.5386 1.5000 1.4989 1.3994 1.3989 1.3486 1.3190 .....
   1.3008 1.2994 1.2895 1.2586 1.1989 1.0983 0.9984 0.8980 0.8009 0.7009 0.6009 0.5007 0.4003 ....
   0.3000 0.1998
   100 100 100 100 69.93 100 64.92 100 60.06 100 100 100 55.11 100 100 50.65 45.08 41.05 36.91 ....
   31.44 27.70 24.47 20.40 16.56 13.01 9.34].';
```

```
%The following data files contain Program inputs
%Each row contains %CO in feed, Low anf high limits
%of feed %CO, experimental lower and upper bifurcation
%points and the number of points to be used to draw
%a smmoth curve

%DATA FILE d190.m for experiments at 461 k
data=[.3999 .01  1. .1102 .1202 .2667 .2854 200
       .7000 .01  1. .1401 .1610 .3659  .3860 200
      1.1992 .010 1. .1901 .2301  .5466  .5564 200];

%DATA FILE d210.m for experiments at 480 K
data=[.3999 .080 2. .2201 .2265 .3469 .3569 200
       .7000 .080 2. .2660 .2855  .6064 .6261 200
      1.1992 .080 2. .3658 .3866  .8386  .8583 200];


%DATA file d230.m for experiments at 499 K
data=[0.40  .08 2. .2861 .2903 .3662 .3864 200
       0.7   .08 2. .4259 .4359  .6360 .6568 200
      1.19920  .08 2.0  .5861 .5965 1.0549 1.0815 200];


%DATA file d245.m for experiments at 245 K
%To be used for Program mech4b.m
data=[0.6759 0.2 2 0.6503 0.6703 0.7905 0.8104 200
       0.9154 0.2 2 0.9276 0.9570 1.0483 1.0786 200
       1.1661 0.2 2 1.2295 1.2586 1.5682 1.5980 200];
```

APPENDIX D

EXPERIMENTAL TIME-AVERAGE CO CONVERSIONS FOR THE N_2O+CO REACTION DURING FEED COMPOSITION CYCLING

The experimental values of time-average CO conversions during feed composition cycling experiments are listed in this Appendix. The instantaneous experimental data of time versus feed flows and reactor concentrations are available in the form of compressed ASCII files on a magnetic tape.

The following conditions were always maintained for all of the experiments.

Reactor temperature		499 K
Reactor pressure		103 kPa
Feed flow		185 sccm
Feed composition during cycling,		
	N_2O	0 - 2.4%
	CO	0 - 2.4%
	N_2	balance

Table D.1

Time-Average CO Conversions During Out-of-Phase Cycling

(with N_2O Phase-Lead of 180°)

Frequency, mHz	Time-Average CO Conversion, percent	Frequency, mHz	Time-Average CO Conversion, percent
0.7689	18.98	5.0231	77.10
0.8347	19.65	5.7444	79.62
0.9084	21.72	6.7349	79.49
1.1097	25.97	6.7349	78.94
1.1765	27.11	7.5120	76.55
1.3377	30.40	7.8125	76.99
1.5379	34.11	8.1380	76.40
1.5379	34.17	8.4984	75.22
1.6693	36.39	9.2798	73.26
1.8253	39.13	9.7656	71.38
1.9929	42.20	9.7656	70.94
1.9929	42.49	10.8507	68.45
2.2194	46.01	10.8507	67.92
2.5040	50.96	11.4889	66.00
2.5040	52.11	12.2070	30.83
2.8722	56.92	13.0208	29.19
3.1001	60.13	13.0208	30.76
3.3103	62.91	13.9509	29.01
3.9859	70.29	16.2760	28.59
3.9859	72.42	17.7556	26.95
4.1555	73.71	19.5312	28.84

Table D.2

Time-Average CO Conversions for Cycling with 90° N_2O Phase-Lead

Frequency, mHz	Time-Average CO Conversion, percent	Frequency, mHz	Time-Average CO Conversion, percent
0.1000	21.82	4.2553	91.03
0.1250	25.39	4.5000	93.00
0.2500	35.73	4.6511	91.36
0.3333	44.50	5.0000	92.11
0.5000	52.15	5.5000	91.88
0.6667	54.75	6.0000	91.24
1.2500	64.19	6.5000	90.59
1.6667	69.38	7.0000	89.35
1.8182	71.49	7.5000	88.53
1.8182	70.98	8.0000	87.72
2.0000	73.91	8.0000	25.41
2.2222	77.19	9.0000	22.86
2.5000	80.19	10.000	22.42
2.8571	83.63	11.000	20.93
3.3333	87.50	12.000	20.76
3.5000	90.06	14.000	20.53
4.0000	91.44	16.000	20.92
4.0000	90.00	18.000	20.74

Table D.3

Time-Average CO Conversion for Cycling with 270° N_2O Phase-Lead

Frequency, mHz	Time-Average CO Conversion, percent	Frequency, mHz	Time-Average CO Conversion, percent
0.2000	12.39	3.3333	52.07
0.3333	16.18	4.0000	51.19
0.4000	17.20	5.0000	48.39
0.5000	18.64	5.7143	41.96
0.6667	21.40	6.2500	39.81
0.6667	22.01	7.1428	36.87
0.8333	24.16	7.6923	36.66
1.0000	26.80	8.3333	36.06
1.1111	28.68	9.0909	24.94
1.1111	29.25	10.000	23.31
1.2500	31.54	12.500	21.58
1.4285	33.65	14.286	21.43
1.6667	37.08	16.667	20.82
1.8182	39.65	20.000	20.44
2.0000	42.87		

Table D.4

Time-Average CO Conversion for Cycling Frequency of 2 mHz

N_2O Phase Lead, degree	Time-Average CO Conversion, percent	N_2O Phase Lead, degree	Time-Average CO Conversion, percent
10	46.84	190	42.79
20	76.23	200	41.76
30	92.48	210	41.23
40	93.44	220	41.10
50	92.61	230	41.47
60	89.64	240	41.92
70	85.80	250	42.31
80	81.49	260	42.77
90	77.25	270	43.33
100	72.72	280	43.80
110	68.71	290	44.40
120	64.45	300	41.82
130	60.18	310	37.08
140	56.40	320	31.70
150	52.76	330	27.22
160	48.72	340	22.60
170	46.07	350	19.48
180	44.25	360	18.90

Table D.5

Time-Average CO Conversions for Cycling Frequency of 5 mHz

N_2O Phase Lead, degrees	Time-Average CO Conversion, percent	N_2O Phase Lead, degrees	Time-Average CO Conversion, percent
10	21.95	190	77.07
20	24.84	200	74.54
25	54.14	210	70.56
30	68.23	220	66.64
35	83.17	230	62.49
40	85.50	240	58.05
45	89.90	250	53.77
50	91.36	260	50.33
60	92.28	270	46.00
70	92.58	280	41.20
80	92.20	290	36.67
90	92.20	300	31.70
100	91.64	310	27.99
110	90.95	320	24.98
120	90.21	330	22.85
130	89.17	335	23.19
140	88.00	340	21.05
150	86.27	345	20.19
160	83.73	350	20.29
170	81.56	355	19.88
180	79.49	359	20.19

Table D.6

Time-Average CO Conversion for Cycling Frequency of 7.04 mHz

N_2O Phase Lead, degrees	Time-Average CO Conversion, percent	N_2O Phase Lead, degrees	Time-Average CO Conversion, percent
10	24.70	160	81.58
20	22.73	170	78.70
30	22.29	180	76.78
40	23.64	190	72.98
45	27.53	200	68.60
50	26.60	210	64.67
50	24.52	220	60.10
55	87.34	230	56.99
60	88.84	240	52.40
60	89.00	250	47.78
65	89.29	260	42.90
70	88.77	270	38.73
70	89.83	280	34.63
80	90.10	290	30.94
90	89.62	300	26.85
100	89.50	310	27.10
110	88.86	320	23.10
120	88.24	330	22.64
130	87.11	340	21.65
140	85.32	350	21.14
150	83.33	359	20.49

Table D.7

Time-Average CO Conversion for Cycling Frequency of 11.11 mHz

N_2O Phase Lead, degrees	Time-Average CO Conversion, percent	N_2O Phase Lead, degrees	Time-Average CO Conversion, percent
5	26.75	180	60.46
10	23.51	180	60.58
20	23.41	185	58.01
30	22.64	190	55.88
40	22.96	190	59.06
50	22.80	195	52.75
60	22.63	200	54.36
70	23.00	205	48.29
80	23.49	210	28.57
90	23.85	215	26.19
100	24.12	220	26.36
110	24.10	220	27.64
120	24.45	230	26.57
130	25.28	240	25.37
140	25.27	250	25.32
150	26.82	260	24.39
150	26.17	270	23.61
155	65.82	280	23.55
160	65.79	290	21.92
160	64.18	300	23.33
165	65.51	310	22.06
170	63.56	320	21.66
170	65.14	340	21.16
175	60.39	350	19.57

Table D.8

Time-Average CO Conversion for Cycling Frequency of 15.15 mHz

N_2O Phase Lead, degrees	Time-Average CO Conversion, percent	N_2O Phase Lead, degrees	Time-Average CO Conversion, percent
10	26.78	160	23.95
20	24.79	170	24.26
30	23.41	180	23.55
40	23.33	190	22.97
50	23.23	200	23.00
60	22.74	210	23.03
70	23.11	220	22.06
80	23.18	230	22.12
90	23.05	240	21.98
100	23.05	260	21.72
110	22.68	280	21.44
120	23.80	300	20.73
130	23.36	320	20.22
140	23.91	340	20.04
150	23.30	359	20.02

APPENDIX E

MATLAB PROGRAMS FOR THE N_2O+CO REACTION FEED CYCLING

The computer programs used for the calculations in chapter 3 are listed in this Appendix. All the programs are written for use with MATLAB version 4.0a. The various programs and their respective applications are as follows.

PHASE.M:	Calculates the time-average CO conversion from the experimental data
TRANS1.M:	Calculates the steady-state CO conversion and the bifurcation points for the surface-phase transition model
TRANSBF.M:	Determines the bifurcation boundaries at a given temperature based on surface-phase transition model
DYNSOL.M:	Calculates the time-average CO conversion for variable-phase feed composition cycling. The function N2ODYN.M evaluates the values of the derivatives for the differential equations

```
% Program PHASE.M
% This program calculates the time-average CO conversion
% from the experimental data stored in the file PHA.M
pha
sco=4.99;% percentage CO in the cylinder
sn2o=10.01;% percentage N2O in the cylinder
tt=input(’Cycle period in seconds’)
nphi=input(’Phase lead =  ’)
[m n]=size(xx);
for i=1:m
time(i)=xx(i,1)-xx(1,1);
coi(i)=(xx(i,3)*sco)/xx(i,2);
n2oi(i)=(xx(i,4)*sn2o)/xx(i,2);
co2(i)=xx(i,6);
end
coiav=0;
n2oav=0;
for i=1:m
coiav=coiav+coi(i);
n2oav=n2oav+n2oi(i);
end
coiav=coiav/m;
n2oav=n2oav/m;
for i=1:m
co(i)=0;
n2o(i)=0;
end
for i=1:m
if xx(i,8)==0
co(i)=coi(i);
end
if xx(i,9)==0
n2o(i)=n2oi(i);
end,end
plot(time,co,’--’,time,co2,’-’,time,n2o,’:’)
xlabel(’Time, sec.’),ylabel(’% CO2 in reactor’)
pause
k=input(’start and end cycle for time integration’)
% example k=[3 15];
n1=k(1);
n2=k(2);
n11=0;
for i=1:m
if co(i)==0
if co(i+1)>0
n11=n11+1;
end,end
m1=i;
if n11==n1, break, end
end
n22=0;
for i=1:m
```

```
if co(i)==0
if co(i+1)>0
n22=n22+1;
end, end
m2=i;
if n22==n2, break, end
end
co21=0;
co1=0;
for i=m1:(m2-1)
co21=co21+((co2(i)+co2(i+1))/2.)*(time(i+1)-time(i));
co1=co1+((co(i)+co(i+1))/2.)*(time(i+1)-time(i));
end
conv=(co21*100.)/co1;
w=1000./tt;
coiav
n2oav
w
conv
s1=['Phase lead =',num2str(nphi),' w = ',num2str(w)];
s2=['%CO Conversion = 'num2str(conv)];
s3=['Feed %CO = 'num2str(coiav),' %N2O = 'num2str(n2oav)];
v=axis;
vx=v(2)/2;
vy1=0.95*v(4);
vy2=0.91*v(4);
vy3=0.87*v(4);
text(vx,vy1,s1)
text(vx,vy2,s2)
text(vx,vy3,s3)
name=input('Data file name:','s'), % Enter the data file name
vy4=1.02*v(4);
text(0,vy4,name)
```

```
% Program TRANS1.M
% This program calculates the steady-state CO conversion
% and bifurcation points for the phase-transition model
% For the predictions at 520 K use program TRANS2.M
%
% The experimental data files are listed in Appendix C
%a190, b190, c190, % data files for 461 K
%a210, b210, c210, % data files for 480 K
a230, b230, c230, % data files at 499 K
temp=499;% enter the temperature K
v=[0,2.,0,104];% for 461 K use v=[0, 1, 0, 104]
axis(v)
%plot the experimental CO conversion Vs feed CO
plot(y(:,1),y(:,2),’o’)
hold
plot(x(:,1),x(:,2),’*’)
plot(z(:,1),z(:,2),’+’)
%d190, % input data file for the program
%d210
d230
sumerr=0.0;
psi1=5; psi2=100;
%kin=input(’ K1,K-1, K2, K3,Nco’)
kin=[28000 15.75 118 2000  1.0015];
for itime=1:1
for jtime=1:2
nrtsav=1;
itime
coi1=data(itime,2);
coi2=data(itime,3);
n2oi=data(itime,1);
xbpll=data(itime,4);
xbplh=data(itime,5);
xbphl=data(itime,6);
xbphh=data(itime,7);
numco=data(itime,8);
for j=1:numco
for l=1:6
xxx(j,l)=0.0 ;
end
end
for j=1:numco
for l=1:5
res1(j,l)=0;
end,end
count=0;
xdelta=(coi2-coi1)/numco;
% calculate reactor N2O by solving 4th order equation
for i=1:numco
count=count+1;
cop=coi2-xdelta*(i-1);
n2op=n2oi;
```

```
k1=kin(1)*((temp/499)^0.5);
k1a=kin(2)/cop;
k2=kin(3);
k3=kin(4)/cop;
if jtime==2
k2=kin(3)/psi1;k3=kin(4)/(psi2*cop);
end
f=n2op/cop;
nco=kin(5);
del=k1*(1-f);
k10=f*k1-f*k2*(1+k1a/k3);
gama=k1a+nco*del;
k15=k1*f*(nco-1)+k2*k1a*f/k3;
k14=f*k1*nco-f*k2;
k11=f*(k1-k2);
k16=k11+f*nco*del*k2/k3;
aa=-f*k2*k14*k14/k3;
bb=f*k2*k14*k14/k3-f*gama*k2*k14/k3-k14*k16-k2*k10*k15;
cc=k14*(gama*k2*f/k3+k16)-(gama*k16+del*k14)-k2* ...
(del*k15+k10*(gama-del));
dd=gama*k16+del*k14-gama*del-k2*del*(gama-del);
ee=gama*del;
z=[aa,bb,cc,dd,ee];
zroot=roots(z);
[m,l]=size(zroot);
for ir=1:4
xroot(ir)=0.0;
end
n=0;
%eliminate imaginary and negative real roots
for ir=1:m
if imag(zroot(ir,1))==0.0
if real(zroot(ir,1))>0.
n=n+1;
xroot(n)=zroot(ir,1);
end
end
end
%matrix xxx stores the positive real roots(N2O)
xxx(i,1)=count;
xxx(i,2)=n;
xxx(i,3)=xroot(1);
if n>1
xxx(i,4)=xroot(2);
end
if n>2
xxx(i,5)=xroot(3);
end
if n>3
xxx(i,6)=xroot(4);
end
end
```

```
for i=1:numco
xdelta=(coi2-coi1)/numco;
coi=coi2-xdelta*(i-1);
k1a=kin(2)/coi;
k3=kin(4)/coi;
if jtime==2
k3=kin(3)/(cop*psi2);
end
nroot=0;
for ic=3:5
n2o=xxx(i,ic);
if n2o>0.
f=n2oi/coi;
co=1-f*(1-n2o);
ic=ic-2;
coconv(ic)=(1-co)*100.;
tco(ic)=(k1*co-k2*(1+k1a/k3)*f*n2o)/(k1a+k1*nco*co-k2*f*n2o);
to(ic)=(1-tco(ic))/(1+k3*tco(ic)/(k2*n2o*f));
coco2(ic)=k3*to(ic)*tco(ic)*100;
res5(i,ic)=tco(ic);
res1(i,ic)=coconv(ic);
if tco(ic)>=0.0
if tco(ic)<1.001
if to(ic)>=0.0
if to(ic)<1.001
if (tco(ic)+to(ic))<1.001
if coconv(ic)>=0.
if coconv(ic)<100.
nroot=nroot+1;
end, end, end, end, end, end, end, end, end
% determine the lower and upper bifurcation points
res1(i,4)=coi;
res1(i,5)=nroot;
if jtime==1
res2=res1;
res5a=res5;
end
end
end
xdelta=(coi2-coi1)/numco;
for i=1:numco
coi=res2(i,4);
nroot=res2(i,5);
if nroot==3
if nrtsav==1
xhbpt=coi+xdelta/2;
nrtsav=3;
num1=i;
end,end
if nroot==1
if nrtsav==3
num2=i;
```

```
xlbpt=coi+xdelta/2;
nrtsav=0;
end,end
end
nrtsav=1;
num4=0;
for i=1:numco
coi=res1(i,4);
nroot=res1(i,5);
if nroot==3
if nrtsav==1
num3=i;
nrtsav=3;
xhbpt1=coi+xdelta/2;
end,end
if nroot==1
if nrtsav==3
num4=i;
xlbpt1=coi+xdelta/2;
nrtsav=0;
end, end
end
if num4==0, num4=numco;end
%create the vectors a and b for plotting
for i=1:(num2-1)
a1(i)=res2(i,4);
b1(i)=res2(i,1);
end
for i=num3:(num4-1)
b3(i+1-num3)=res1(i,3);
a3(i+1-num3)=res1(i,4);
if res1(i,3)==0
b3(i+1-num3)=res1(i,1);
end
end
num3a=num2-num3;
for i=1:num3a-1
a2(num3a-i)=res2((num3+i),4);
b2(num3a-i)=res2((num3+i),2);
end
for i=num4:numco
a4(i+1-num4)=res1(i,4);
b4(i+1-num4)=res1(i,1);
end
a=[a1 a2 a3 a4];
b=[b1 b2 b3 b4];
plot(a,b)
ra1=[a1' b1'];
ra2=[a2' b2'];
a5=[a3 a4];
b5=[b3 b4];
ra3=[a5' b5'];
```

```
xlabel('CO % in feed'),ylabel('% CO Conversion')
xlb(itime)=xlbpt;
xhb(itime)=xhbpt1;
% save the data in ASCII files
save res56 res2 /ascii
save res55 res1 /ascii
end
```

```
% Program TRANSBF.M
% This program generates the upper and lower bifuraction
% boundaries at the specified temperature using the
% phase-transition model
temp=input(’Temperatere, k’), %Enter the temperature value
for japan=1:50
%Generate 50 points for drawing a smooth curve
sumerr=0.0;
psi1=5; psi2=100;
%kin=input(’ K1,K-1, K2, K3,Nco’)
kin=[28000 15.75 118 2000 1.0015];
for itime=1:1
for jtime=1:2
nrtsav=1;
coi1=0.0;
coi2=1.0;
n2oi=0.25+0.028*japan;
numco=500;
for j=1:numco
for l=1:6
xxx(j,l)=0.0 ;
end, end
for j=1:numco
for l=1:5
res1(j,l)=0;
end,end
count=0;
xdelta=(coi2-coi1)/numco;
% calculate reactor N2O by solving 4th order equation
for i=1:numco
count=count+1;
cop=coi2-xdelta*(i-1);
n2op=n2oi;
k1=kin(1)*((temp/499)^0.5);
k1a=kin(2)/cop;
k2=kin(3);
k3=kin(4)/cop;
if jtime==2
k2=kin(3)/psi1;k3=kin(4)/(psi2*cop);
end
f=n2op/cop;
nco=kin(5);
del=k1*(1-f);
k10=f*k1-f*k2*(1+k1a/k3);
gama=k1a+nco*del;
k15=k1*f*(nco-1)+k2*k1a*f/k3;
k14=f*k1*nco-f*k2;
k11=f*(k1-k2);
k16=k11+f*nco*del*k2/k3;
aa=-f*k2*k14*k14/k3;
bb=f*k2*k14*k14/k3-f*gama*k2*k14/k3-k14*k16-k2*k10*k15;
cc=k14*(gama*k2*f/k3+k16)-(gama*k16+del*k14)-k2* ...
```

```
(del*k15+k10*(gama-del));
dd=gama*k16+del*k14-gama*del-k2*del*(gama-del);
ee=gama*del;
z=[aa,bb,cc,dd,ee];
zroot=roots(z);
[m,l]=size(zroot);
for ir=1:4
xroot(ir)=0.0;
end
n=0;
%eliminate imaginary and negative real roots
for ir=1:m
if imag(zroot(ir,1))==0.0
if real(zroot(ir,1))>0.
n=n+1;
xroot(n)=zroot(ir,1);
end, end, end
%matrix xxx stores the positive real roots(N2O)
xxx(i,1)=count;
xxx(i,2)=n;
xxx(i,3)=xroot(1);
if n>1
xxx(i,4)=xroot(2);
end
if n>2
xxx(i,5)=xroot(3);
end
if n>3
xxx(i,6)=xroot(4);
end
end
for i=1:numco
xdelta=(coi2-coi1)/numco;
coi=coi2-xdelta*(i-1);
k1a=kin(2)/coi;
k3=kin(4)/coi;
if jtime==2
k3=kin(3)/(cop*psi2);
end
nroot=0;
for ic=3:5
n2o=xxx(i,ic);
if n2o>0.
f=n2oi/coi;
co=1-f*(1-n2o);
ic=ic-2;
coconv(ic)=(1-co)*100.;
tco(ic)=(k1*co-k2*(1+k1a/k3)*f*n2o)/(k1a+k1*nco*co-k2*f*n2o);
to(ic)=(1-tco(ic))/(1+k3*tco(ic)/(k2*n2o*f));
coco2(ic)=k3*to(ic)*tco(ic)*100;
res5(i,ic)=tco(ic);
res1(i,ic)=coconv(ic);
```

```
if tco(ic)>=0.0
if tco(ic)<1.001
if to(ic)>=0.0
if to(ic)<1.001
if (tco(ic)+to(ic))<1.001
if coconv(ic)>=0.
if coconv(ic)<100.
nroot=nroot+1;
end, end, end, end, end, end, end, end, end
% determine the lower and upper bifurcation points
res1(i,4)=coi;
res1(i,5)=nroot;
if jtime==1
res2=res1;
res5a=res5;
end, end, end
xdelta=(coi2-coi1)/numco;
for i=1:numco
coi=res2(i,4);
nroot=res2(i,5);
if nroot==3
if nrtsav==1
xhbpt=coi+xdelta/2;
nrtsav=3;
num1=i;
end,end
if nroot==1
if nrtsav==3
num2=i;
xlbpt=coi+xdelta/2;
nrtsav=0;
end,end, end
nrtsav=1;
num4=0;
for i=1:numco
coi=res1(i,4);
nroot=res1(i,5);
if nroot==3
if nrtsav==1
num3=i;
nrtsav=3;
xhbpt1=coi+xdelta/2;
end,end
if nroot==1
if nrtsav==3
num4=i;
xlbpt1=coi+xdelta/2;
nrtsav=0;
end, end, end
if num4==0, num4=numco;end
bfres(japan,1)=xlbpt;
bfres(japan,2)=xhbpt1;
bfres(japan,3)=n2oi;
clear a a1 a2 a3 a4 b b1 b2 b3 b4
% save the results in an ASCII file
save bfr230 bfres /ascii
end, end
exit
```

```
%               Program 'DYNSOL.M'
%        This program solves the differential equations for the dynamic
%        system. The equations are defined in a function file'N3ODYN.M'
%        The program furhter calculates the time average CO conversion
%        for the specified number of cycles.
%
%        The program inputs include the model parameter values for the
%        differential equations, N2O phase lead, Cycle period and the
%        number of cycles for integration.
%
global x10 x20
global k1 k11 k2 k3 nco am n2op cop factor
global as k4 k41
diary n2o36
omgin=[ .15 0.25];% omgin contains the values of frequencies
result=[0 0 0 0 0 0];% stores the results
cosh=0.95; cosl=0.1;% limits of surface CO for phase-transition model
%Enter the initial conditions for integration.x0
%where x0(1)=CO x0(2)=N2O x0(3)=CO2 xo(4)=surface CO
%x0(5)=surface oxygen  x0(6)=adsorbed CO2
x0=[ 0.003 0.000001 0.000011 0.85 0.000001 0.00009].';
for ii=1:2
n2op=1.2364;
cop=1.2157;
%        define the model parameters as global variables
psi1=1; psi2=1;
psin1=5; psin2=100;%enhancement factors for (1x1) surface-phase
k1=28000;%dimensionless CO adsorption rate parameter
k11=15.75;%dimensionless CO desorption rate parameter
k2in=118;% dimensionless N2O dissociation rate parameter
k3in=2000/cop;% dimensionless surface reaction rate parameter
am=0.4*cop;%ratio of bulk volume to metal surface capacitances
nco=1.0015;% CO self-exclusion factor
factor=n2op/cop;% ratio of feed N2O to feed CO
k4=400;% dimensionless CO2 adsorption rate parameter
k41=12000;% dimensionless CO2 desorption rate parameter
as=0.024; % ratio of bulk volume to alumina surface capacitances
omega=omgin(ii);% cycling frequency mHz
cycle=1000/omega;% cycle period in seconds
angle=90;% N2O phase lead
%num=input('number of cycles for integration')
%num1=input('No. of steps per cycle')
num1=1000.;
num=8;
%        The following values of v, q0, tk and p should be
%        changed depending on experimental conditions
v=2.15*1e-4; % v=volume of the reactor cu.m.
tk=499; % temperature of the reactor K
p=103; % pressure in the reactor kPa
q0=185; %total feed flow to the reactor sccm
tt=(q0*1e-6/60)*(tk/273.15)*(101.325/p)*(cycle/v);
t0=0; tf=tt;nlead=(angle*tt)/360;
```

```
%tol    -accuracy used to calculate desirable error. A very low
%       -value of 'tol' will prevent integration of diff. equations
%       using Runge-Kutta-Fehlberg method
%
tol=0.0001;
%
%       Integrate a system of ordinary differential equations using
%       4th and 5th order Runge-Kutta formulas. The differential equations
%       (any number) are listed in a separate function file 'n2odyn.m'
% INPUT:
% t0    - Initial value of t: dimensionless
% tf    - Final value of t: dimensionless
% x0    - Initial value column-vector.
% tol   - The desired accuracy.
%
% The Fehlberg coefficients:
%
alpha = [1/4  3/8  12/13  1  1/2]';
beta  = [ [    1      0      0     0      0    0]/4
          [    3      9      0     0      0    0]/32
          [ 1932  -7200   7296     0      0    0]/2197
          [ 8341 -32832  29440  -845      0    0]/4104
          [-6080  41040 -28352  9295  -5643    0]/20520 ]';
gamma = [ [902880  0  3953664  3855735  -1371249  277020]/7618050
          [ -2090  0    22528    21970    -15048  -27360]/752400 ]';
pow = 1/5;

% Initialization
t = t0;
hmax = (tf - t)/(5);
hmin = (tf - t)/(num*100000);
h0 = (tf - t)/(num1) ;h=h0;
%count=1; %counts the number of cycles
x00=[0 0 0 0 0 0 0 0];
% matrix x00 stores the values at the begining of each
% quadrant for all the cycles.
flag=1;% flag=1 for N2O phase lead of less than 180 degree
% flag=2 for N2O phase lead of greater than 180 degree
% flag=3 for N2O phase lead of 180 degree
if nlead>tt/2
nlead=tt-nlead;
flag=2; end
for i=1:num
sum1=0; sum2=0; sum3=0;
osold=x0(5);% surface oxygen value at the start of the cycle
h=h0;
nk=0;% counts the number of integration steps per cycle
jk=1;
if (nlead==tt/2) | (angle==180)
jk=2; flag=3;end
% perform the integration for each of the four quadrants
for jj=1:jk:4
```

```
if jj==1
x10=0;x20=2;t0=0;tf=nlead;
end
if jj==2
x10=2;x20=2;t0=nlead;tf=tt/2;
end
if jj==3
x10=2;x20=0;t0=tt/2;tf=t0+nlead;
end
if jj==4
x10=0;x20=0;t0=nlead+tt/2;tf=tt;
end
if flag==2
dummy=x20; x20=x10; x10=dummy; end
h=h0;
t=t0;
x00=[x00; i jj x0.'];
x = x0(:);cos=x(4);
if cos>=cosh, iflag=1; end, % iflag=1 for (1x1) phase
if cos<=cosl, iflag=0; end, % iflag=0 for (5x20) phase
f = x*zeros(1,6);
tout0=t0;
xout0=x.';
tau = tol * max(norm(x, 'inf'), 1);
n=0;
rout=[ 0 0];% stores the integration results of time Vs CO2
%  for plotting pupose. The number of colums of rout should
%  be adjusted to include other results i.e. CO, N2O, surface
%  oxygen, surface CO etc.
%
% The main loop
%
   while (t < tf ) & (h >= hmin)
      if t + h > tf, h = tf - t; end
% Check for the surface-phase transition
if iflag==1
if cos<=cosl
iflag=0;
end, end
if iflag==0
if cos>=cosh
iflag=1
end, end
if iflag==1, psi1=1; psi2=1; end
if iflag==0, psi1=psin1; psi2=psin2; end
    k2=k2in/psi1; k3=k3in/psi2;
     n=n+1;
        nk=nk+1;
%  Corrections for physically unreasonable values
if x(4)>1, x(4)=1/1.00001; end
if x(4)<0, x(4)=1e-8; end
if x(5)<0, x(5)=1e-8; end
if x(5)>1, x(5)=1/1.00001; end
if x(1)>2, x(1)=2/1.000001; end
if x(1)<0, x(1)=1e-8; end
if x(2)<0, x(2)=1e-8; end
if x(2)>2, x(2)=2/1.000001; end
if x(3)<0, x(3)=1e-8; end
if x(6)<0, x(6)=1e-8; end
    % Compute the slopes
    temp = n2odyn(t,x);
    f(:,1) = temp(:);
    for j = 1:5
      temp = n2odyn( t+alpha(j)*h, x+h*f*beta(:,j));
      f(:,j+1) = temp(:);
    end

    % Estimate the error and the acceptable error
    delta = norm(h*f*gamma(:,2),’inf’);
    tau = tol*max(norm(x,’inf’),1.0);
    temp2=x+h*f*gamma(:,1);
    % Update the solution only if the error is acceptable
    if (delta <= tau)
      t = t + h;
      x = temp2;
  yy=x.’;
  sum1=sum1+(t-tout0)*(yy(1)+xout0(1))/2;% Area under CO curve
  sum2=sum2+(t-tout0)*(yy(2)+xout0(2))/2;% Area under N2O curve
  sum3=sum3+(t-tout0)*(yy(3)+xout0(3))/2;% Area under CO2 curve
  tout0=t;
  xout0=yy;
if i==(num-1), zf=[t  yy(3)];
rout=[rout;zf];
end
     x0=x;
     h0=h; cos=x0(4);
     end
     % Update the step size
    if delta ~= 0.0
      h = min(hmax, 0.8*h*(tau/delta)^pow);
    end
  end
  if (t < tf)
    disp(’SINGULARITY LIKELY.’)
    t
  end
% save the results for plotting the CO2 response curve for
% the second last cycle
if i==(num-1)
if jj==1, save res11 rout /ascii, end
if jj==2, save res12 rout /ascii, end
if jj==3, save res13 rout /ascii, end
if jj==4, save res14 rout /ascii, end
clear rout
```

```
end
        if (t < tf), break, end
        clear  x
    end
        if (t<tf),break,end
        conv(i,1)=i;
        conv(i,2)=(tt-sum1)*100./tt;% conversion based on CO curve
        conv(i,3)=(tt-sum2)*factor*100./tt;% conversion based on N2O curve
        conv(i,4)=sum3*100./tt;% conversion based on CO2 curve
       pctos=(x0(5)-osold)*100./osold;% change in surface oxygen
        conv(i,5)=pctos; conv(i,6)=angle;
        conv(i,:),nk
     x0
        end
    angle
        conv
result=[result
conv];
clear conv
        end
% save the time-average conversions in ASCII file
save res31 result /ascii
diary off
exit


%Function N2ODYN.M
function xdot=n2odyn(t,x)
% This function evaluates the derivatives
global x10 x20 k1 k11 k2 k3 nco am factor k4 k41 as
xdot(1)=x10-x(1)-k1*x(1)*(1-x(4)-x(5))*((1-nco*x(4))/ ...
(1-x(4)))+k11*x(4);
xdot(2)=x20-x(2)-k2*x(2)*(1-x(4)-x(5));
xdot(3)=k3*x(4)*x(5)-x(3)-k4*x(3)*(1-x(6))+k41*x(6);
xdot(4)=am*(k1*x(1).*(1-x(4)-x(5))*((1-nco*x(4))/ ...
(1-x(4)))-k11*x(4)-k3*x(4).*x(5));
xdot(5)=am*(factor*k2*x(2).*(1-x(4)-x(5))-k3*x(4).*x(5));
xdot(6)=as*(k4*x(3)*(1-x(6))-k41*x(6));
```

APPENDIX F

STEADY-STATE EXPERIMENTAL DATA FOR THE NO+CO REACTION

This appendix contains the experimental data for the NO+CO reaction steady-state multiplicity described in Chapter 4. All of the experiments were carried out with a constant feed flow of 185 cm^3 (STP)/min and at a constant reactor pressure of 103 kPa. A total of 26 sets of experiments were carried out in the temperature range of 465-520 K. Each set of experiments was carried out at a constant reactor temperature by holding the feed concentration of one of the reactants (NO or CO) constant while varying (stepwise increasing or decreasing) the feed concentration of the other reactant. The results for each set of experiments are listed in the individual tables. A time of 4 hours was allowed to reach the steady-state, however, it was observed that the steady-state was not achieved in 4 hours immediately following the high-to-low or low-to-high conversion bifurcation. The data for the experiments where the steady-state was not reached in 4 hours, is also tabulated with asterisk marks but was not used in the figures in Chapter 4. The conversions and the selectivity are calculated as follows.

F.1 CO conversion:

$$CO\ Conversion = \frac{Reactor\ CO_2\%}{Feed\ CO\%} \times 100\ \% \qquad (F.1)$$

F.2 NO Conversion:

It is possible to calculate the feed NO% from the reactor compositions. Therefore, the NO conversion was calculated by two different methods as follows.

$$NO\ Conversion = \frac{(Feed\ NO\% - Reactor\ NO\%)}{Feed\ NO\%} \times 100\% \quad (F.2)$$

$$NO\ Conversion = \frac{(Feed\ NO\% - Reactor\ NO\%)}{Calculated\ Reactor\ NO\%} \times 100\% \quad (F.3)$$

where

$$Calculated\ Feed\ NO\% = Reactor\ NO\% + Reactor\ N_2O\% + Reactor\ CO_2\% \quad (F.4)$$

Equation (F.4) can be easily derived from equation (4.) of Chapter 4. It was found that the NO conversion calculated by these two methods matched within 5%. The NO conversions listed in the tables is the average of the two values.

F.3 N_2O Selectivity:

$$N_2O\ Selectivity = \frac{2 \times Reactor\ N_2O\%}{(Feed\ NO\% - Reactor\ NO\%)} \quad (F.5)$$

In the above equation the feed NO% is the average value of the measured feed NO% and the calculated feed NO% from equation (F.4)

Table F.1

NO+CO High-Conversion Steady-State Data at 465 K with 0.45% NO in the Feed

Feed CO%	Reactor N_2O%	Reactor NO%	CO Conversion	NO Conversion	N_2O Selectivity
0.0839	0.0448	0.2964	100.00	32.20	0.6348
0.1356	0.0775	0.2270	100.00	48.99	0.7108
0.1867	0.1051	0.1556	100.00	65.32	0.7172
0.2373	0.1248	0.0875	100.00	80.55	0.6889
0.2662	0.1289	0.0540	100.00	87.99	0.6518
0.2962	0.1242	0.0319	100.00	92.93	0.5925
0.3267	0.1126	0.0212	100.00	95.34	0.5188
0.3554	0.1102	0.0277	100.00	94.11	0.4965
0.3864*	0.0319	0.3100	20.28	28.67	0.5098
0.4165*	0.0178	0.3425	11.61	20.04	0.4100
0.4458	0.0111	0.3583	7.96	15.94	0.3210
0.6563	0.0090	0.3627	4.97	14.84	0.2793

(* indicates steady-state was not reached)

Table F.2

NO+CO Low-conversion Steady-State Data at 465 K with 0.45% NO in the Feed

Feed CO%	Reactor N_2O%	Reactor NO%	CO Conversion	NO Conversion	N_2O Selectivity
0.9656	0.0164	0.3533	4.00	17.48	0.4324
0.8640	0.0123	0.3632	3.25	14.65	0.3868
0.7638	0.0105	0.3670	3.25	13.61	0.3550
0.6656	0.0093	0.3698	3.32	12.82	0.3333
0.5641	0.0100	0.3688	4.13	13.16	0.3493
0.4865	0.0142	0.3636	7.65	15.79	0.4122
0.3866	0.0147	0.3637	9.47	15.77	0.4273
0.3361	0.0146	0.3631	11.10	15.91	0.4207
0.2865	0.0151	0.3634	12.74	15.84	0.4370
0.2371	0.0159	0.3623	15.52	16.09	0.4530
0.1865	0.0183	0.3582	20.64	17.04	0.4926
0.1555	0.0207	0.3536	26.17	18.11	0.5247
0.1254	0.0277	0.3381	39.23	21.70	0.5869
0.0958	0.0646	0.2300	100.00	44.99	0.6793
0.0664	0.0504	0.2702	100.00	35.07	0.6797

Table F.3

NO+CO High-Conversion Steady-State Data at 465 K with 0.7% NO in the Feed

Feed CO%	Reactor N_2O%	Reactor NO%	CO Conversion	NO Conversion	N_2O Selectivity
0.0744	0.0471	0.5397	100.00	20.64	0.6686
0.1359	0.0885	0.4379	100.00	35.66	0.7276
0.2366	0.1531	0.2993	100.00	56.90	0.7748
0.3351	0.2024	0.1597	100.00	77.14	0.7512
0.4358	0.2111	0.0607	100.00	91.38	0.6565
0.4666	0.2066	0.0643	100.00	91.05	0.6314
0.4965*	0.0527	0.5036	19.59	25.50	0.6086
0.5262	0.0327	0.5625	11.25	16.84	0.5702
0.5563	0.0237	0.5893	7.78	13.01	0.5335
0.5657	0.0188	0.6044	6.15	10.90	0.5040
0.5965	0.0149	0.6153	4.90	9.39	0.4627
0.6266	0.0139	0.6227	4.44	8.66	0.4672

(* indicates steady-state was not reached)

Table F.4

NO+CO Low-Conversion Steady-State Data at 465 K with 0.7% NO in the Feed

Feed CO%	Reactor N_2O%	Reactor NO%	CO Conversion	NO Conversion	N_2O Selectivity
0.9657	0.0274	0.5885	5.25	13.82	0.5781
0.8650	0.0214	0.6058	4.52	11.27	0.5533
0.7639	0.0182	0.6160	4.54	9.95	0.5318
0.6669	0.0167	0.6158	4.99	9.77	0.4978
0.5648	0.0178	0.6109	6.04	10.28	0.5050
0.4958	0.0203	0.5961	10.95	12.98	0.4549
0.4048	0.0193	0.5981	12.62	12.54	0.4481
0.3732	0.0162	0.6054	12.11	11.36	0.4154
0.3434	0.0139	0.6155	12.29	10.21	0.3954
0.3117	0.0126	0.6160	12.58	9.88	0.3711
0.2817	0.0119	0.6190	12.78	9.38	0.3693
0.2512	0.0116	0.6198	14.49	9.32	0.3619
0.2207	0.0118	0.6206	16.27	9.24	0.3714
0.1993	0.0121	0.6198	17.31	9.22	0.3817
0.1703	0.0135	0.6176	20.73	9.55	0.4116
0.1398	0.0181	0.6043	30.62	11.41	0.4623
0.1083*	0.0606	0.4689	100.0	29.75	0.6060

(* indicates steady-state was not reached)

Table F.5

NO+CO High-Conversion Steady-State Data at 465 K with 1.2% NO in the Feed

Feed CO%	Reactor N_2O%	Reactor NO%	CO Conversion	NO Conversion	N_2O Selectivity
0.0833	0.0578	1.0557	100.00	11.91	0.8101
0.1862	0.1313	0.8853	100.00	26.31	0.8307
0.2858	0.2040	0.7118	100.00	40.72	0.8344
0.3858	0.2707	0.5280	100.00	55.71	0.8151
0.4164	0.2904	0.4726	100.00	60.27	0.8099
0.4465	0.3079	0.4269	100.00	64.14	0.8063
0.4768	0.3238	0.3893	100.00	67.42	0.8038
0.5071	0.3357	0.3502	100.00	70.73	0.7933
0.5363	0.3493	0.3181	100.00	73.53	0.7905
0.5663	0.3598	0.2874	100.00	76.18	0.7827
0.5962	0.3649	0.2645	100.00	78.19	0.7696
0.6256	0.3514	0.2954	100.00	76.08	0.7470
0.6566*	0.0689	1.0099	18.11	15.76	0.7293
0.6862	0.0507	1.0543	12.47	11.79	0.7191
0.7161	0.0507	1.0543	11.91	11.78	0.7199

(* indicates steady-state was not reached)

Table F.6

NO+CO Low-Conversion Steady-State Data at 465 K with 1.2% NO in the Feed

Feed CO%	Reactor N_2O%	Reactor NO%	CO Conversion	NO Conversion	N_2O Selectivity
1.1656	0.0554	1.0524	7.91	12.30	0.7507
1.0649	0.0388	1.0927	5.88	8.72	0.7437
0.9646	0.0311	1.1125	5.09	7.01	0.7418
0.8644	0.0265	1.1343	5.06	5.65	0.7800
0.7646	0.0235	1.1393	5.18	5.15	0.7593
0.6664	0.0218	1.1427	5.36	4.78	0.7596
0.5662	0.0209	1.1416	5.79	4.68	0.7458
0.4860	0.0352	1.1042	11.01	7.71	0.7631
0.4361	0.0328	1.1081	11.42	7.30	0.7519
0.3959	0.0310	1.1107	12.02	7.03	0.7385
0.3659	0.0293	1.1134	12.27	6.73	0.7289
0.3355	0.0279	1.1166	12.55	6.42	0.7275
0.3062	0.0267	1.1195	13.16	6.18	0.7241
0.2756	0.0263	1.1205	14.08	6.06	0.7275
0.2448	0.0268	1.1183	16.38	6.23	0.7214
0.2164	0.0270	1.1187	18.85	6.24	0.7243
0.1967	0.0283	1.1072	21.50	6.86	0.6928
0.1664	0.0320	1.1027	28.31	7.40	0.7256
0.1348	0.0432	1.0780	46.36	9.55	0.7589
0.1046*	0.0729	1.0072	100.00	15.52	0.7874

(* indicates steady-state was not reached)

Table F.7

NO+CO High-Conversion Steady-State Data at 485 K with 0.45% NO in the Feed

Feed CO%	Reactor N_2O%	Reactor NO%	CO Conversion	NO Conversion	N_2O Selectivity
0.0582	0.0320	0.3285	100.00	24.27	0.6046
0.1369	0.0804	0.2232	100.00	49.87	0.7242
0.2068	0.1133	0.1281	100.00	71.48	0.7059
0.2565	0.1253	0.0671	100.00	85.07	0.6554
0.2860	0.1234	0.0385	100.00	91.42	0.6013
0.3153	0.1114	0.0201	100.00	95.52	0.5202
0.3456	0.0917	0.0112	100.00	97.51	0.4187
0.3761	0.0715	0.0075	100.00	98.34	0.3213
0.3963	0.0558	0.0066	100.00	98.55	0.2492
0.4263	0.0476	0.0096	100.00	97.94	0.2082
0.4562*	0.0487	0.2597	27.72	41.28	0.5330

(* indicates steady-state was not reached)

Table F.8

NO+CO Low-Conversion Steady-State Data at 485 K with 0.45% NO in the Feed

Feed CO%	Reactor N_2O%	Reactor NO%	CO Conversion	NO Conversion	N_2O Selectivity
0.9858	0.0202	0.3522	4.45	18.57	0.4991
0.8863	0.0175	0.3585	4.24	16.83	0.4775
0.7856	0.0153	0.3635	4.06	15.36	0.4577
0.6861	0.0142	0.3650	4.21	14.73	0.4434
0.5852	0.0134	0.3673	4.56	14.11	0.4365
0.4866	0.0130	0.3678	5.24	13.87	0.4308
0.3852	0.0134	0.3668	6.62	14.04	0.4390
0.2851	0.0147	0.3642	8.91	14.49	0.4670
0.2360	0.0155	0.3633	11.10	14.78	0.4829
0.1858	0.0170	0.3607	16.36	15.73	0.4974
0.1564	0.0182	0.3569	20.27	16.48	0.5091
0.1251	0.0236	0.3432	32.45	19.75	0.5520
0.0964	0.0784	0.1845	100.00	53.83	0.7122
0.0677	0.0534	0.2795	100.00	34.06	0.7325
0.0463	0.0341	0.3283	100.00	23.36	0.6749

Table F.9

NO+CO High-Conversion Steady-State Data at 485 K with 0.7% NO in the Feed

Feed CO%	Reactor N_2O%	Reactor NO%	CO Conversion	NO Conversion	N_2O Selectivity
0.0764	0.0349	0.5454	100.00	19.52	0.5250
0.1356	0.0736	0.4449	100.00	34.21	0.6341
0.1956	0.1099	0.3644	100.00	46.77	0.6857
0.2554	0.1433	0.2829	100.00	59.04	0.7026
0.3156	0.1727	0.1989	100.00	71.32	0.6982
0.3754	0.1888	0.1217	100.00	82.44	0.6610
0.4361	0.1858	0.0591	100.00	91.44	0.5885
0.4963	0.1576	0.0245	100.00	96.44	0.4742
0.5262	0.1359	0.0159	100.00	97.69	0.4038
0.5558	0.1092	0.0114	100.00	98.34	0.3227
0.5858	0.0930	0.0102	100.00	98.53	0.2718
0.6152	0.1052	0.0232	100.00	96.78	0.3012
0.6455*	0.0408	0.4891	19.89	27.91	0.4293
0.6758*	0.0199	0.5617	11.04	17.08	0.3419
0.6962	0.0111	0.5908	7.66	12.71	0.2558
0.7258	0.0065	0.6083	5.64	10.16	0.1869

(* indicates steady-state was not reached)

Table F.10

NO+CO Low-Conversion Steady-State Data at 485 K with 0.7% NO in the Feed

Feed CO%	Reactor N_2O%	Reactor NO%	CO Conversion	NO Conversion	N_2O Selectivity
1.0617*	0.0365	0.5620	8.44	19.02	0.5529
0.9861	0.0226	0.6073	5.66	12.34	0.5283
0.9046	0.0179	0.6221	4.93	10.13	0.5161
0.8021	0.0144	0.6354	4.45	8.27	0.5023
0.6995	0.0135	0.6351	4.96	8.16	0.4775
0.5979	0.0126	0.6342	5.18	7.92	0.4607
0.4952	0.0125	0.6349	6.09	7.80	0.4641
0.3934	0.0131	0.6334	7.44	7.89	0.4809
0.2916	0.0144	0.6289	10.63	8.45	0.4944
0.2399	0.0153	0.6277	13.28	8.66	0.5123
0.2094	0.0164	0.6226	16.65	9.33	0.5098
0.1797	0.0177	0.6184	20.29	9.86	0.5215
0.1485	0.0210	0.6070	27.83	11.30	0.5408
0.1204	0.0903	0.3705	100.00	41.66	0.6686
0.0884	0.0740	0.4433	100.00	31.74	0.7063
0.0574	0.0460	0.5397	100.00	19.49	0.6978

(* indicates steady-state was not reached)

Table F.11

NO+CO High-Conversion Steady-State Data at 485 K with 1.2% NO in the Feed

Feed CO%	Reactor N_2O%	Reactor NO%	CO Conversion	NO Conversion	N_2O Selectivity
0.0862	0.0621	1.0545	100.00	12.23	0.8455
0.1860	0.1340	0.8938	100.00	25.94	0.8560
0.2868	0.2036	0.7222	100.00	40.13	0.8411
0.3860	0.2697	0.5364	100.00	55.15	0.8177
0.4859	0.3254	0.3816	100.00	68.11	0.7987
0.5366	0.3474	0.3172	100.00	73.58	0.7865
0.5859	0.3619	0.2566	100.00	78.66	0.7654
0.6159	0.3692	0.2191	100.00	81.77	0.7512
0.6460	0.3733	0.1852	100.00	84.60	0.7341
0.6769	0.3754	0.1555	100.00	87.08	0.7161
0.6958	0.3745	0.1364	100.00	88.66	0.7020
0.7255	0.3698	0.1131	100.00	90.61	0.6778
0.7565	0.3632	0.0980	100.00	91.89	0.6539
0.7858	0.3601	0.0982	100.00	91.96	0.6408
0.8157*	0.0694	1.0181	17.37	16.16	0.7063
0.8465	0.0434	1.0898	10.11	9.88	0.7258
0.8765	0.0319	1.1227	7.01	7.06	0.7479
0.9067	0.0320	1.0889	7.01	8.66	0.6193

(* indicates steady-state was not reached)

Table F.12

NO+CO Low-Conversion Steady-State Data at 485 K with 1.2% NO in the Feed

Feed CO%	Reactor N_2O%	Reactor NO%	CO Conversion	NO Conversion	N_2O Selectivity
1.0560	0.0120	1.0173	11.40	13.37	0.1523
1.0060	0.0076	1.0716	7.41	8.91	0.1444
0.9459	0.0060	1.0915	6.12	7.29	0.1392
0.8863	0.0048	1.1053	5.24	6.16	0.1316
0.7857	0.0219	1.1229	5.37	5.91	0.6204
0.6866	0.0196	1.1181	5.24	5.78	0.5702
0.5855	0.0196	1.1178	5.93	5.74	0.5744
0.4864	0.0196	1.1177	6.91	5.70	0.5786
0.3857	0.0210	1.1143	9.07	5.96	0.5928
0.2855	0.0241	1.1116	14.12	6.42	0.6309
0.2358	0.0264	1.1045	19.08	7.02	0.6327
0.2061	0.0268	1.1018	21.45	7.12	0.6336
0.1749	0.0320	1.0883	30.36	8.28	0.6504
0.1460	0.1040	0.8886	100.00	23.95	0.7410
0.1144	0.1026	0.8943	100.00	22.50	0.7852
0.0861	0.0798	0.9687	100.00	16.95	0.8036

Table F.13

NO+CO High-Conversion Steady-state Data at 505 K with 0.45% NO in the Feed

Feed CO%	Reactor N_2O%	Reactor NO%	CO Conversion	NO Conversion	N_2O Selectivity
0.0840	0.0474	0.3002	100.00	32.59	0.6743
0.1864	0.1016	0.1658	100.00	63.71	0.7102
0.2858	0.1236	0.0434	100.00	90.49	0.6059
0.3164	0.1128	0.0222	100.00	95.13	0.5265
0.3454	0.0950	0.0104	100.00	97.72	0.4318
0.3762	0.0692	0.0057	100.00	98.75	0.3111
0.3961	0.0516	0.0043	100.00	99.06	0.2310
0.4258	0.0280	0.0034	100.00	99.26	0.1244
0.4555	0.0063	0.0034	100.00	99.26	0.0277
0.4960*	0.0067	0.0074	86.74	98.35	0.0304
0.5060*	0.0815	0.3308	16.28	29.81	1.1500

(* indicates steady-state was not reached)

Table F.14

NO+CO Low-Conversion Steady-State Data at 505 K with 0.45% NO in the Feed

Feed CO%	Reactor N_2O%	Reactor NO%	CO Conversion	NO Conversion	N_2O Selectivity
1.0256	0.0185	0.3506	4.87	19.21	0.4410
0.9858	0.0151	0.3588	4.06	16.79	0.4128
0.8857	0.0135	0.3632	3.99	15.57	0.3982
0.7856	0.0125	0.3696	4.23	14.44	0.3965
0.6853	0.0114	0.3662	4.26	14.30	0.3666
0.5857	0.0112	0.3662	4.64	14.06	0.3666
0.4856	0.0115	0.3653	5.56	14.18	0.3734
0.3859	0.0125	0.3626	7.54	14.86	0.3876
0.2864	0.0145	0.3580	11.24	15.99	0.4182
0.2356	0.0161	0.3534	15.03	17.09	0.4348
0.2051	0.0173	0.3502	18.48	17.90	0.4464
0.1753	0.0191	0.3459	22.82	18.86	0.4681
0.1460	0.0292	0.3174	41.30	25.73	0.5259
0.1139	0.0812	0.1741	100.00	57.08	0.6896
0.0853	0.0553	0.2711	100.00	36.95	0.6923
0.0571	0.0315	0.3285	100.00	24.12	0.5997

Table F.15

NO+CO High-Conversion Steady-State Data at 505 K with 0.7% NO in the Feed

Feed CO%	Reactor N_2O%	Reactor NO%	CO Conversion	NO Conversion	N_2O Selectivity
0.0864	0.0492	0.5319	100.00	22.16	0.6480
0.1857	0.1114	0.3759	100.00	45.22	0.7173
0.2874	0.1628	0.2407	100.00	65.39	0.7160
0.3856	0.1925	0.1081	100.00	84.40	0.6581
0.4365	0.1898	0.0560	100.00	91.90	0.5977
0.4662	0.1786	0.0348	100.00	94.95	0.5453
0.4964	0.1584	0.0206	100.00	97.00	0.4749
0.5267	0.1358	0.0122	100.00	98.22	0.4023
0.5572	0.1098	0.0075	100.00	98.91	0.3231
0.5864	0.0853	0.0051	100.00	99.26	0.2497
0.6160	0.0584	0.0044	100.00	99.36	0.1705
0.6468	0.0391	0.0050	100.00	99.28	0.1133
0.6763	0.0423	0.0114	100.00	98.40	0.1202
0.6972*	0.0548	0.4562	22.80	33.37	0.4790
0.7465	0.0213	0.5864	7.68	14.02	0.4433

(* indicates steady-state was not reached)

Table F.16

NO+CO Low-Conversion Steady-State Data at 505 K with 0.7% NO in the Feed

Feed CO%	Reactor N_2O%	Reactor NO%	CO Conversion	NO Conversion	N_2O Selectivity
0.9458	0.0200	0.5741	7.44	15.79	0.3699
0.8855	0.0148	0.5972	5.54	12.18	0.3551
0.7856	0.0128	0.6059	5.14	10.76	0.3476
0.6864	0.0119	0.6108	5.16	9.97	0.3487
0.5858	0.0114	0.6144	5.58	9.46	0.3516
0.4855	0.0119	0.6133	6.47	9.49	0.3662
0.3858	0.0131	0.6096	8.48	9.95	0.3847
0.2860	0.0160	0.5999	12.90	11.20	0.4183
0.2360	0.0179	0.5938	16.99	12.03	0.4361
0.2062	0.0215	0.5934	24.15	12.98	0.4834
0.1752	0.0244	0.5822	31.28	14.40	0.4954
0.1467	0.1123	0.3082	100.00	50.82	0.6902
0.1147	0.0785	0.4344	100.00	34.36	0.6844
0.0864	0.0523	0.5184	100.00	23.53	0.6531
0.0578	0.0304	0.5867	100.00	14.63	0.6035

Table F.17

NO+CO High-Conversion Steady-state Data at 505 K with 1.2% NO in the Feed

Feed CO%	Reactor N_2O%	Reactor NO%	CO Conversion	NO Conversion	N_2O Selectivity
0.0860	0.0578	1.0399	100.00	12.75	0.7608
0.1834	0.1219	0.8878	100.00	25.80	0.7896
0.2858	0.1877	0.7186	100.00	39.92	0.7863
0.3863	0.2466	0.5400	100.00	54.48	0.7629
0.4858	0.2977	0.3864	100.00	67.39	0.7456
0.5856	0.3331	0.2657	100.00	77.71	0.7191
0.6861	0.3469	0.1498	100.00	87.43	0.6661
0.7366	0.3392	0.1020	100.00	91.42	0.6242
0.7856	0.3225	0.0632	100.00	94.67	0.5746
0.8156	0.3083	0.0476	100.00	95.99	0.5418
0.8464	0.2840	0.0365	100.00	96.92	0.4952
0.8765	0.2665	0.0278	100.00	97.65	0.4604
0.9054	0.2439	0.0223	100.00	98.12	0.4193
0.9359	0.2209	0.0197	100.00	98.34	0.3781
0.9659	0.2086	0.0239	100.00	98.01	0.3550
0.9956*	0.0614	0.9792	16.57	18.50	0.5492
1.0257	0.0353	1.0593	9.04	11.25	0.5255
1.0558	0.0258	1.0888	6.24	8.52	0.5086
1.0771	0.0206	1.1049	4.68	6.98	0.4961

(* indicates steady-state was not reached)

Table F.18

NO+CO Low-Conversion Steady-State Data at 505 K with 1.2% NO in the Feed

Feed CO%	Reactor N_2O%	Reactor NO%	CO Conversion	NO Conversion	N_2O Selectivity
1.0258	0.0416	1.0446	10.59	12.76	0.5445
0.9862	0.0310	1.0777	8.12	9.77	0.5313
0.8860	0.0259	1.0953	7.28	8.17	0.5310
0.7856	0.0239	1.1032	7.33	7.47	0.5362
0.6860	0.0230	1.1118	7.99	6.95	0.5542
0.5854	0.0217	1.1155	8.49	6.53	0.5568
0.4854	0.0231	1.1152	10.65	6.68	0.5789
0.3859	0.0266	1.1015	14.59	7.60	0.5865
0.2852	0.0328	1.0822	23.81	9.16	0.6005
0.2555	0.0373	1.0670	30.96	10.46	0.5982
0.2259	0.0430	1.0513	40.11	11.83	0.6093
0.1954	0.1748	0.6557	100.00	40.72	0.7646
0.1670	0.1262	0.8499	100.00	27.41	0.7847
0.1353	0.0952	0.9460	100.00	20.38	0.7860
0.1072	0.0697	1.0151	100.00	15.12	0.7706
0.0759	0.0468	1.0693	100.00	10.59	0.7388

Table F.19

NO+CO High-Conversion Steady-State Data at 520 K with 0.235% CO in the Feed

Feed NO%	Reactor N_2O%	Reactor NO%	CO Conversion	NO Conversion	N_2O Selectivity
1.9010	0.1508	1.4589	100.00	22.09	0.7286
1.8006	0.1489	1.3647	100.00	23.08	0.7265
1.7004	0.1480	1.2788	100.00	23.92	0.7358
1.6007	0.1475	1.1910	100.00	24.95	0.7448
1.4998	0.1459	1.1006	100.00	26.16	0.7481
1.3999	0.1452	1.0069	100.00	27.74	0.7512
1.3006	0.1426	0.9115	100.00	29.60	0.7440
1.2000	0.1423	0.8120	100.00	32.03	0.7438
1.0996	0.1379	0.7189	100.00	34.39	0.7320
1.0005	0.1364	0.6115	100.00	38.33	0.7175
0.9001	0.1338	0.5038	100.00	43.15	0.6995
0.7992	0.1316	0.4101	100.00	47.94	0.6966
0.6997	0.1274	0.3324	100.00	52.33	0.6984
0.5987	0.1224	0.2468	100.00	58.96	0.6903
0.4991	0.1157	0.1581	100.00	68.62	0.6691
0.3995	0.1010	0.0707	100.00	82.46	0.6077
0.3490	0.0864	0.0320	100.00	90.89	0.5414
0.2989	0.0584	0.0085	100.00	97.17	0.4001
0.2689	0.0325	0.0025	100.00	99.07	0.2435
0.2388	0.0021	0.0008	100.00	99.66	0.0177
0.2087*	0.0010	0.0005	75.08	99.74	0.0104
0.1787*	0.0001	0.0008	69.30	99.53	0.0012

(* indicates steady-state was not reached)

Table F.20

NO+CO Low-Conversion Steady-State Data at 520 K with 0.235% CO in the Feed

Feed NO%	Reactor N_2O%	Reactor NO%	CO Conversion	NO Conversion	N_2O Selectivity
0.1393	0.0086	0.1062	6.06	20.73	0.6148
0.1887	0.0098	0.1529	6.07	16.27	0.6552
0.2388	0.0109	0.1987	7.18	14.52	0.6426
0.2889	0.0120	0.2440	8.67	13.62	0.6214
0.3390	0.0130	0.2883	9.33	12.88	0.6072
0.3891	0.0141	0.3320	10.04	12.43	0.5953
0.4393	0.0147	0.3755	10.06	11.89	0.5758
0.4890	0.0152	0.4168	10.33	11.71	0.5446
0.5388	0.0169	0.4585	11.88	11.91	0.5401
0.5895	0.0183	0.5102	13.18	11.13	0.5692
0.6898	0.0201	0.6136	14.28	9.54	0.6192
0.7891	0.0241	0.7072	18.10	9.50	0.6488
0.8901	0.0257	0.8058	19.69	8.84	0.6578
0.9904	0.0299	0.8927	23.84	9.32	0.6515
1.0404	0.0316	0.9379	25.67	9.39	0.6502
1.1397	0.0334	1.0192	27.28	9.65	0.6128
1.2405	0.0417	1.0864	35.78	11.40	0.5959
1.3409	0.0457	1.1673	40.28	11.84	0.5822
1.4402	0.1753	0.8337	100.00	37.55	0.6896

Table F.21

NO+CO High-Conversion Steady-State Data at 520 K with 0.31% CO in the Feed

Feed NO%	Reactor N_2O%	Reactor NO%	CO Conversion	NO Conversion	N_2O Selectivity
2.4015	0.2381	1.7039	100.00	26.69	0.7646
2.2013	0.2244	1.5529	100.00	27.53	0.7589
1.9999	0.2155	1.3797	100.00	29.30	0.7524
1.8068	0.2100	1.2192	100.00	31.21	0.7584
1.6002	0.2026	1.0400	100.00	34.01	0.7554
1.3996	0.1982	0.8548	100.00	38.11	0.7529
1.2000	0.1923	0.6656	100.00	43.77	0.7420
1.0003	0.1856	0.4657	100.00	52.50	0.7206
0.7992	0.1748	0.3059	100.00	61.52	0.7149
0.6997	0.1685	0.2218	100.00	68.31	0.7048
0.5989	0.1609	0.1380	100.00	77.15	0.6907
0.4994	0.1372	0.0576	100.00	88.53	0.6173
0.4499	0.1151	0.0274	100.00	93.93	0.5432
0.3998	0.0819	0.0085	100.00	97.88	0.4183
0.3492	0.0379	0.0014	100.00	99.60	0.2180
0.2989	0.0042	0.0003	96.54	99.90	0.0279
0.2488*	0.0039	0.0006	76.86	99.76	0.0318
0.1987*	0.0362	0.0535	33.58	72.73	0.5075
0.1486	0.0198	0.0670	16.04	52.92	0.5240

(* indicates steady-state was not reached)

Table F.22

NO+CO Low-Conversion Steady-State Data at 520 K with 0.31% CO in the Feed

Feed NO%	Reactor N_2O%	Reactor NO%	CO Conversion	NO Conversion	N_2O Selectivity
0.1393	0.0046	0.1203	2.00	10.94	0.6174
0.1887	0.0057	0.1665	2.65	9.74	0.6315
0.2388	0.0070	0.2112	3.29	9.54	0.6250
0.2889	0.0080	0.2555	3.07	8.99	0.6285
0.3389	0.0089	0.2981	4.93	9.77	0.5477
0.3891	0.0099	0.3401	5.48	9.96	0.5218
0.4393	0.0105	0.3803	5.36	10.04	0.4878
0.4891	0.0114	0.4197	6.48	10.59	0.4519
0.5390	0.0122	0.4633	7.10	10.46	0.4440
0.5895	0.0131	0.5154	7.24	9.51	0.4778
0.6897	0.0148	0.6218	8.71	8.07	0.5397
0.7892	0.0163	0.7241	9.62	7.12	0.5862
0.8898	0.0181	0.8214	11.09	6.85	0.5990
0.9904	0.0200	0.9172	12.09	6.64	0.6122
1.0404	0.0206	0.9646	12.27	6.51	0.6129
1.1398	0.0221	1.0436	13.76	7.14	0.5493
1.2400	0.0237	1.1243	15.05	7.61	0.5095
1.3403	0.0244	1.2147	15.25	7.47	0.4947
1.4404	0.0260	1.3003	16.27	7.64	0.4803
1.5409	0.0292	1.3828	18.38	8.06	0.4782
1.6410	0.0324	1.4716	20.86	8.26	0.4864
1.7400	0.0314	1.5745	20.14	7.57	0.4843
1.8406	0.0354	1.6596	23.64	7.99	0.4888
1.9407	0.0377	1.7437	25.38	8.20	0.4812
2.0402	0.0393	1.8337	26.44	8.16	0.4796
2.1409	0.0418	1.9575	27.80	7.35	0.5369
2.2416	0.0432	2.1085	28.76	5.92	0.6510
2.3406	0.0463	2.2103	31.65	5.85	0.6742
2.4407	0.0476	2.2899	33.29	6.18	0.6313

Table F.23

NO+CO High-Conversion Steady-Sate Data at 520 K with 0.435% CO in the Feed

Feed NO%	Reactor N_2O%	Reactor NO%	CO Conversion	NO Conversion	N_2O Selectivity
2.4010	0.3091	1.5625	100.00	33.59	0.7812
2.2013	0.2981	1.3939	100.00	35.57	0.7740
2.0008	0.2928	1.2233	100.00	38.08	0.7781
1.8005	0.2884	1.0417	100.00	41.56	0.7783
1.6007	0.2787	0.8580	100.00	45.90	0.7654
1.4997	0.2794	0.7654	100.00	48.62	0.7715
1.4000	0.2757	0.6662	100.00	52.02	0.7634
1.3008	0.2700	0.5633	100.00	56.14	0.7487
1.2001	0.2627	0.4605	100.00	60.93	0.7311
1.0999	0.2554	0.3789	100.00	65.06	0.7238
1.2000	0.2579	0.4305	100.00	62.90	0.7054
1.0995	0.2487	0.3729	100.00	65.40	0.7054
1.0003	0.2383	0.3043	100.00	69.23	0.6961
0.8995	0.2281	0.2261	100.00	74.72	0.6827
0.7992	0.2118	0.1481	100.00	81.42	0.6527
0.6995	0.1862	0.0748	100.00	89.28	0.5978
0.5988	0.1365	0.0227	100.00	96.19	0.4758
0.4987	0.0569	0.0032	100.00	99.36	0.2305
0.5492	0.0960	0.0090	100.00	98.35	0.3585
0.4987	0.0534	0.0031	100.00	99.37	0.2171
0.4493	0.0095	0.0011	100.00	99.75	0.0426
0.3992	0.0027	0.0015	97.69	99.64	0.0131
0.3490*	0.0068	0.0042	79.24	98.81	0.0391
0.2989*	0.0330	0.1694	22.40	43.41	0.5078
0.2488	0.0187	0.1742	11.25	28.98	0.5258
0.1987	0.0121	0.1487	6.42	23.19	0.5375

(* indicates steady-state was not reached)

Table F.24

NO+CO Low-Conversion Steady-State Data at 520 K with 0.435% CO in the Feed

Feed NO%	Reactor N_2O%	Reactor NO%	CO Conversion	NO Conversion	N_2O Selectivity
0.1480*	0.0220	0.0328	20.88	77.48	0.3859
0.3996	0.0251	0.2942	16.59	24.85	0.4954
0.4987	0.0229	0.3900	14.01	17.69	0.4757
0.5988	0.0239	0.4773	14.12	15.16	0.4623
0.6997	0.0238	0.5913	13.46	12.23	0.4990
0.7993	0.0242	0.6997	13.37	10.53	0.5319
0.9002	0.0250	0.8018	13.56	9.48	0.5483
1.0002	0.0261	0.9147	14.33	8.82	0.6001
1.0998	0.0257	1.0147	13.83	7.80	0.6013
1.2000	0.0264	1.1064	14.03	7.32	0.5833
1.2002	0.0410	1.0294	19.53	10.90	0.5526
1.3504	0.0421	1.1649	19.92	9.95	0.5359
1.5003	0.0428	1.2952	19.99	9.11	0.5113
1.6509	0.0424	1.4401	19.65	8.16	0.5008
1.8008	0.0428	1.5913	19.70	7.47	0.5065
1.9519	0.0466	1.7264	22.02	7.62	0.5067
2.1010	0.0460	1.8881	21.34	6.85	0.5231
2.2520	0.0492	2.1102	23.25	6.65	0.6736
2.4014	0.0518	2.4014	25.10	6.28	1.2870

(* indicates steady-state was not reached)

Table F.25

NO+CO High-Conversion Steady-State Data at 520 K with 0.685% CO in the Feed

Feed NO%	Reactor N_2O %	Reactor NO%	CO Conversion	NO Conversion	N_2O Selectivity
2.4016	0.4542	1.2108	100.00	49.03	0.7797
2.2018	0.4481	1.0246	100.00	52.99	0.7758
2.0009	0.4348	0.8411	100.00	57.54	0.7629
1.8008	0.4230	0.6446	100.00	63.71	0.7473
1.6006	0.4026	0.4497	100.00	71.33	0.7194
1.4999	0.3885	0.3770	100.00	74.44	0.7075
1.3996	0.3748	0.3053	100.00	77.91	0.6960
1.3005	0.3581	0.2318	100.00	82.00	0.6783
1.3003	0.3424	0.2405	100.00	81.27	0.6562
1.1999	0.3217	0.1713	100.00	85.59	0.6322
1.0996	0.2885	0.1071	100.00	90.17	0.5870
1.0001	0.2418	0.0545	100.00	94.50	0.5166
0.8997	0.1767	0.0194	100.00	97.82	0.4057
0.8492	0.1354	0.0102	100.00	98.79	0.3264
0.7991	0.0902	0.0055	100.00	99.30	0.2300
0.7497	0.0459	0.0032	100.00	99.57	0.1243
0.7197	0.0159	0.0023	100.00	99.68	0.0448
0.6897	0.0022	0.0024	100.00	99.65	0.0064
0.6596	0.0015	0.0039	96.29	99.41	0.0046
0.6292	0.0045	0.0109	91.85	98.29	0.0144
0.5988	0.0354	0.4321	16.46	26.69	0.4497
0.5695	0.0219	0.4510	9.50	18.49	0.4263
0.5386	0.0158	0.4439	6.33	14.67	0.4107
0.4986	0.0126	0.4201	4.80	12.75	0.4066

(* indicates steady-state was not reached)

Table F.26

NO+CO Low-Conversion Steady-State Data at 520 K with 0.685% CO in the Feed

Feed NO %	Reactor N_2O%	Reactor NO%	CO Conversion	NO Conversion	N_2O Selectivity
0.1390*	0.0117	0.0761	6.97	44.55	0.3826
0.1981	0.0130	0.1410	6.60	29.03	0.4509
0.2989	0.0148	0.2390	6.63	20.08	0.4928
0.3991	0.0150	0.3322	6.31	15.84	0.4795
0.4986	0.0150	0.4149	6.14	14.44	0.4263
0.5492	0.0139	0.4635	5.71	12.94	0.4007
0.6995	0.0260	0.5757	9.80	15.81	0.4795
0.7992	0.0230	0.6942	8.53	11.82	0.4935
0.8995	0.0217	0.7996	7.92	9.89	0.4937
1.0002	0.0212	0.9124	7.76	8.16	0.5231
1.0997	0.0205	1.0106	7.22	7.29	0.5156
1.1998	0.0203	1.1040	6.95	6.89	0.4959
1.3007	0.0202	1.1976	6.76	6.59	0.4763
1.3999	0.0201	1.2889	6.63	6.38	0.4554
1.4999	0.0207	1.3771	6.84	6.43	0.4350
1.6008	0.0214	1.4777	6.98	6.08	0.4451
1.7000	0.0217	1.6299	7.06	4.12	0.6194
1.8010	0.0222	1.7300	7.11	3.94	0.6257
1.9012	0.0232	1.8277	7.33	3.86	0.6316
2.0009	0.0242	1.9239	7.70	3.85	0.6289
2.1014	0.0246	2.0228	7.87	3.74	0.6263
2.2016	0.0258	2.1207	8.03	3.67	0.6381
2.3009	0.0266	2.2169	8.37	3.65	0.6336

(* indicates steady-state was not reached)

APPENDIX G

MATLAB PROGRAMS FOR STEADY-STATE CALCULATIONS FOR THE NO+CO REACTION

The programs for the steady-state calculations for the NO+CO reaction described in Chapter 4 are listed in this appendix. The programs can be run on MATLAB version 3.5j. The program NOSS1.M is used for calculations with fixed feed CO% and program NOSS2.M is used for calculations with fixed feed NO%.

```
%   xxxxxxxxxxxxxxxxxxxxxxxxxxxxxxxxxxxxxxx
%   x              NOSS1.M                        x
%   x xxxxxxxxxxxxxxxxxxxxxxxxxxxxxxxxxxxxx
%This program solves a set of six non-linear equations
%for the steady-state modelling of NO+CO reaction
%by Newton-Raphson (False-Position) method.
%The non-linear equations are defined by the function 'NOEQTN.M
%The program can only be used for fixed feed CO% and varying feed NO%.
%The program can be run to generate either the high-conversion
%branch or the low conversion branch with appropriate inputs.
%This program listing is for the calculation of the high-conversion
%branch at 465 K.
global l am q co0 no0 nco
global k1, k11, k2, k21, k3, k4, k5, k6, k7
t=465;% Reactor temperature, 465, 485 or 505 K
nco=1.05; %CO self-exclusion factor
flag1=1; %ends the program if the number of iterations exceed 500
no0m=input(' NO mol percent in the feed i.e. 0.45, 0.7 or 1.2%')
% Define a Jacobian matrix "a"
for i=1:6
for j=1:6
a(i,j)=0;
end
end
am=9.4;% total surface area of the catalyst (square meter)
l=2e-5;% adsorption capacity of catalyst (mol/sq. m.)
q=(185/60)*(101.325/104)*(t/273)*1e-6;% Total feed flow (cu.m./s)
no0=(no0m/100)*(104000/(8.314*t));%Convert mol% to mol/cu.m.
k=input('values of kinetic parameters')
%k=[74072 0.48 71600 250 61000 3800 20 0.50 5500] at 465 K;
%k=[77192 1.0412 74616 1050 667816 20168 101 2.2 24612]at 505 K;
%k=[75648 0.72 73123 500  212046 9061 46.5 1.08 12000] at 485 K;
k1=k(1);
k11=k(2);
k2=k(3);
k21=k(4);
k3=k(5);
k4=k(6);
k5=k(7);
k6=k(8);
k7=k(9);
% dx step size for evaluating the partial derivative
for i=1:6
dx(i)=0.00001;
end
x0=input('guess values of solutions')
%x0=[0.8173 0.0091 0.0304 0.0067 0 0.22] typical values for
% high conversion branch
%x0=[0.0002 0.94 0.0131 0.0343 0 0.002] typical values for
% low conversion branch;
x0(5)=no0m*0.9;
for i=5:6
```

```
x0(i)=x0(i)*1040./(8.314*t);% convert mol% to cu.m./mol
end
for jj=1:99
if flag1>=2, break, end
co0m=1.2-1.20*(jj)/100; % range of feed CO mole percent for low conversion branch
%for high conversion branch use co0m=1.2*jj/100
co0=co0m*1040./(8.314*t);
err=100.;% average change in x-values of two consecutive iterations
n=0;% counts the number of iterations
% Main loop
while err>0.00001
% verify that the guess values are physically reasonable
for i=1:4
x(i)=x0(i);%fractional surface coverage must be between 0 and 1
if x(i)<0, x(i)=1e-8; end
if x(i)>=1, x(i)=1/1.00001; end
end
for i=5:6
x(i)=x0(i);% Gas phase concentrations must be between 0 and feed concentration.
nochk(i)=x(i)*8.314*t/1040.;
if nochk(i)<0, x(i)=1e-8; end
end
if nochk(5)>no0m, x(5)=no0/1.00001; end
if nochk(6)>no0m/2, x(6)=no0/2.00002; end
% function evaluation
temp=noeqtn(x);
for i=1:6
b(i,1)=-1.*temp(i);
x0(i)=x(i);
end
for j=1:6
for i=1:6
x(i)=x0(i);
end
% evaluate the partial derivatives
x(j)=x(j)+dx(j);
temp=noeqtn(x);
for i=1:6
a(j,i)=temp(i);
end
end
for i=1:6
for j=1:6
a(i,j)=(a(i,j)+b(j))/dx(j);
end,end
aa=a';
% Estimate the condition of the matrix for singularity
% escond is the estimate of the reciprocal of the matrix condition
% stop the calculation if "escond" is very low
escond=rcond(aa);
if escond<1e-12, break, end
% solve the linear system A.x = B using LU decomposition
```

```
xs=aa\b;
sum=0;
for i=1:6
sum=sum+abs(xs(i));
end
err=sum/6;
% abandon the calculations after 500 iterations
if n>500, err=0.000001; flag1=2;end
n=n+1;
if (err>=0.00001)
x0(:)=x0(:)+xs(:);% Guess value of the solution for the next iteration
end
end
xout=x0;
for i=5:6
xout(i)=(xout(i)*8.314*t)/(1040.);
end
%calculate CO and NO percent conversions
coconv=(no0m-xout(5)-xout(6))*(100/co0m);
noconv=(no0m-xout(5))*100/no0m;
coconv, noconv, n, xout, % display the results after each iteration
% store the results in the matrix "res"
if n>0
if n<500
res(jj,1)=co0m;
for ii=2:7
res(jj,ii)=xout(ii-1);
end
res(jj,8)=coconv;
res(jj,9)=noconv;
res(jj,10)=n;
end
end
end
% read the experimental data from the respective data files
% experimental data files at 465 K are
% tf1.m, tf2.m, tf3.m, tf4.m, tf5.m, tf6.m
% experimental data files at 485 K are
% tf7.m, tf8.m, tf9.m, tf10.m, tf11.m, tf12.m
% experimental data files at 505 K are
% tf13.m, tf14.m, tf15.m, tf16.m, tf17.m, tf18.m
% the above data files correspond to the tables in Appendix F.
tf1
tf2
tf3
tf4
tf5
tf6
% graphically compare the results with the experimental data
v=[0 1.3 0 110];
axis(v)
plot(yy(:,1),yy(:,5),'o'),hold
```

```
xlabel('Feed CO%'), ylabel('% NO Conversion')
plot(xx(:,1),xx(:,5),'o')
plot(xx1(:,1),xx1(:,5),'*')
plot(yy1(:,1),yy1(:,5),'*')
plot(xx2(:,1),xx2(:,5),'+')
plot(yy2(:,1),yy2(:,5),'+')
plot(res(:,1),res(:,9),'-')
pause
hold
v=[0 1.3 0 0.5];
axis(v)
plot(yy(:,1),yy(:,2),'o')
hold
xlabel('Feed CO%'), ylabel('Reactor N2O%')
plot(xx(:,1),xx(:,2),'o')
plot(yy1(:,1),yy1(:,2),'*')
plot(xx1(:,1),xx1(:,2),'*')
plot(xx2(:,1),xx2(:,2),'+')
plot(yy2(:,1),yy2(:,2),'+')
plot(res(:,1),res(:,7),'-')
pause
hold
v=[0 1.3 0 110];
axis(v)
plot(xx(:,1),xx(:,4),'o'),hold
xlabel('Feed CO%'), ylabel('%CO Conversion')
plot(yy(:,1),yy(:,4),'o')
plot(xx1(:,1),xx1(:,4),'*')
plot(yy1(:,1),yy1(:,4),'*')
plot(xx2(:,1),xx2(:,4),'+')
plot(yy2(:,1),yy2(:,4),'+')
plot(res(:,1),res(:,4),'-')



% xxxxxxxxxxxxxxxxxxxxxxxxxxxxxxxx
% x        NOEQTN.M              x
% xxxxxxxxxxxxxxxxxxxxxxxxxxxxxxxx
function f=noeqtn(x)
%global k1 k11 k2 k21 k3 k4 k5 k6 k7 co0 no0 am q l
%x(1)=fractional surface coverage of Oxygen
%x(2)=fractional surface coverage of CO
%x(3)=fractional surface coverage of NO
%x(4)=fractional surface coverage of Nitrogen
%x(5)=gas phase NO, mol/cu.m.
%x(6)=gas phase N2O, mol/cu.m.
f(1)=l*k3*x(3)*(1-x(1)-x(2)-x(3)-x(4))+k4*l*x(3)*x(4) ...
     +k6*x(6)*(1-x(1)-x(2)-x(3)-x(4))-k7*l*x(1)*x(2);
f(2)=k1*(co0-no0+x(5)+x(6))*(1-x(1)-x(2)-x(3)-x(4)) .....
     *((1-nco*x(2))/(1-x(2)))-k11*x(2);
f(3)=k2*x(5)*(1-x(1)-x(2)-x(3)-x(4))-k21*x(3) .....
 -k3*l*x(3)*(1-x(1)-x(2)-x(3)-x(4))-k4*l*x(3)*x(4);
```

```
f(4)=k3*x(3)*(1-x(1)-x(2)-x(3)-x(4))-k4*x(3)*x(4)-k5*x(4)*x(4);
f(5)=q*(x(5)-no0)+am*k2*l*x(5)*(1-x(1)-x(2)-x(3)-x(4)) ....
     -am*k21*l*x(3);
f(6)=q*x(6)-am*k4*l*l*x(3)*x(4)+am*k6*l*x(6)* ....
        (1-x(1)-x(2)-x(3)-x(4));




%   xxxxxxxxxxxxxxxxxxxxxxxxxxxxxxxxxxxxx
%   x             NOSS2.M                    x
%   x xxxxxxxxxxxxxxxxxxxxxxxxxxxxxxxxxxx
%This program solves a set of six non-linear equations
%for the steady-state modelling of NO+CO reaction
%by Newton-Raphson (False-Position) method.
%The non-linear equations are defined by the function 'NOEQTN.M'
%The program performs calculations for fixed feed NO% and varying feed CO% at 520 K.
global l am q co0 no0 nco
global k1, k11, k2. k21, k3, k4, k5, k6, k7
t=465;% Reactor temperature, 465, 485 or 505 K
nco=1.05; %CO self-exclusion factor
flag1=1; %ends the program if the number of iterations exceed 500
co0m=input(' CO mol percent in the feed i.e. 0.235, 0.31, 0.435 or 0.685%')
% Define a Jacobian matrix "a"
for i=1:6
for j=1:6
a(i,j)=0;
end
end
am=9.4;% total surface area of the catalyst (square meter)
l=2e-5;% adsorption capacity of catalyst (mol/sq. m.)
q=(185/60)*(101.325/104)*(t/273)*1e-6;% Total feed flow (cu.m./s)
co0=(co0m/100)*(104000/(8.314*t));%Convert mol% to mol/cu.m.
k=input('values of kinetic parameters')
%k=[78330 1.35 75716 1500 1490000 35300 174 3.6 40682] at 520 K;
k1=k(1);
k11=k(2);
k2=k(3);
k21=k(4);
k3=k(5);
k4=k(6);
k5=k(7);
k6=k(8);
k7=k(9);
% dx step size for evaluating the partial derivative
for i=1:6
dx(i)=0.00001;
end
x0=input('guess values of solutions')
%x0=[0.8173 0.0091 0.0304 0.0067 1.4275 0.2222] typical values for
% high conversion branch
%x0=[0.0002 0.94 0.0131 0.0343 0.008 0.002] typical values for
```

```
% low conversion branch;
x0(5)=no0m*0.9;
for i=5:6
x0(i)=x0(i)*1040./(8.314*t);% convert mol% to cu.m./mol
end
for jj=1:199
if flag1>=2, break, end
no0m=2.5-2.5*(jj)/200; % range of feed NO mole percent for low conversion branch
%for high conversion branch use co0m=1.2*jj/100
no0=no0m*1040./(8.314*t);
err=100.;% average change in x-values of two consecutive iterations
n=0;% counts the number of iterations
% Main loop
while err>0.00001
% verify that the guess values are physically reasonable
for i=1:4
x(i)=x0(i);%fractional surface coverage must be between 0 and 1
if x(i)<0, x(i)=1e-8; end
if x(i)>=1, x(i)=1/1.00001; end
end
for i=5:6
x(i)=x0(i);% Gas phase concentrations must be between 0 and feed concentration.
nochk(i)=x(i)*8.314*t/1040.;
if nochk(i)<0, x(i)=1e-8; end
end
if nochk(5)>no0m, x(5)=no0/1.00001; end
if nochk(6)>no0m/2, x(6)=no0/2.00002; end
% function evaluation
temp=noeqtn(x);
for i=1:6
b(i,1)=-1.*temp(i);
x0(i)=x(i);
end
for j=1:6
for i=1:6
x(i)=x0(i);
end
% evaluate the partial derivatives
x(j)=x(j)+dx(j);
temp=noeqtn(x);
for i=1:6
a(j,i)=temp(i);
end
end
for i=1:6
for j=1:6
a(i,j)=(a(i,j)+b(j))/dx(j);
end,end
aa=a';
% Estimate the condition of the matrix for singularity
% escond is the estimate of the reciprocal of the matrix condition
% stop the calculation if "escond" is very low
```

```
escond=rcond(aa);
if escond<1e-12, break, end
% solve the linear system A.x = B using LU decomposition
xs=aa\b;
sum=0;
for i=1:6
sum=sum+abs(xs(i));
end
err=sum/6;
% abandon the calculations after 500 iterations
if n>500, err=0.000001; flag1=2;end
n=n+1;
if (err>=0.00001)
x0(:)=x0(:)+xs(:);% Guess value of the solution for the next iteration
end
end
xout=x0;
for i=5:6
xout(i)=(xout(i)*8.314*t)/(1040.);
end
%calculate CO and NO percent conversions
coconv=(no0m-xout(5)-xout(6))*(100/co0m);
noconv=(no0m-xout(5))*100/no0m;
coconv, noconv, n, xout, % display the results after each iteration
% store the results in the matrix "res"
if n>0
if n<500
res(jj,1)=no0m;
for ii=2:7
res(jj,ii)=xout(ii-1);
end
res(jj,8)=coconv;
res(jj,9)=noconv;
res(jj,10)=n;
end
end
end
% read the experimental data from the respective data sheets
% experimental data files at 520 K are
% tf19.m, tf20.m, tf21.m, tf22.m, tf23.m, tf24.m, tf25.m, tf26.m
tf19
tf20
tf21
tf22
tf23
tf24
tf25
tf26
% graphically compare the results with the experimental data
v=[0 2.3 0 110];
axis(v)
plot(yy(:,1),yy(:,5),'o'),hold
```

```
xlabel(’Feed NO%’), ylabel(’% NO Conversion’)
plot(xx(:,1),xx(:,5),’o’)
plot(xx1(:,1),xx1(:,5),’*’)
plot(yy1(:,1),yy1(:,5),’*’)
plot(xx2(:,1),xx2(:,5),’+’)
plot(yy2(:,1),yy2(:,5),’+’)
plot(xx3(:,1),xx3(:,5),’x’)
plot(yy3(:,1),yy3(:,5),’x’)
plot(res(:,1),res(:,9),’-’)
pause
hold
v=[0 2.5 0 0.5];
axis(v)
plot(yy(:,1),yy(:,2),’o’)
hold
xlabel(’Feed NO%’), ylabel(’Reactor N2O%’)
plot(xx(:,1),xx(:,2),’o’)
plot(yy1(:,1),yy1(:,2),’*’)
plot(xx1(:,1),xx1(:,2),’*’)
plot(xx2(:,1),xx2(:,2),’+’)
plot(yy2(:,1),yy2(:,2),’+’)
plot(xx3(:,1),xx3(:,2),’x’)
plot(yy3(:,1),yy3(:,2),’x’)
plot(res(:,1),res(:,7),’-’)
pause
hold
v=[0 2.5 0 110];
axis(v)
plot(xx(:,1),xx(:,4),’o’),hold
xlabel(’Feed NO%’), ylabel(’%CO Conversion’)
plot(yy(:,1),yy(:,4),’o’)
plot(xx1(:,1),xx1(:,4),’*’)
plot(yy1(:,1),yy1(:,4),’*’)
plot(xx2(:,1),xx2(:,4),’+’)
plot(yy2(:,1),yy2(:,4),’+’)
plot(xx3(:,1),xx3(:,4),’x’)
plot(yy3(:,1),yy3(:,4),’x’)
plot(res(:,1),res(:,8),’-’)
```

```
% An example of the experimental data file.
%   xxxxxxxxxxxxxxxxxxxxxxxxxxxxxxxx
%   x           tf1.m                x
%   xxxxxxxxxxxxxxxxxxxxxxxxxxxxxxxx
% experimental data at 465 K and 0.45% NO feed
xx=[0.0839 0.0448 0.2964 100 32.2 0.6348
0.1356 0.0775 0.2270 100 48.99 0.7108
0.1867 0.1051 0.1556 100 65.32 0.7172
0.2373 0.1248 0.0875 100 80.55 0.6889
0.2662 0.1289 0.054 100 87.99 0.6518
0.2962 0.1242 0.0319 100 92.93 0.5925
0.3267 0.1126 0.0212 100 95.34 0.5188
0.3554 0.1102 0.0277 100 94.11 0.4965
0.3864 0.0319 0.31 20.28 28.67 0.5098
0.4165 0.0178 0.3425 11.61 20.04 0.41
0.4458 0.0111 0.3583 7.96 25.94 0.3210
0.6563 0.009 0.3627 4.97 14.84 0.2793];
%this data file corresponds to Table F.1
%other data files are not printed here
```

APPENDIX H

EXPERIMENTAL TIME-AVERAGE CONVERSIONS FOR THE NO+CO REACTION DURING FEED COMPOSITION CYCLING

The experimental values of the instantaneous feed flows, concentrations in the reactor and reactor temperatures are available in the form of compressed ASCII files on a magnetic tape. The time-average conversions of CO, NO and NO conversion to N_2O were calculated from the transient response curves of reactor CO_2, NO and N_2O concentrations, respectively, using a MATLAB program which is listed in this Appendix. The values of the time-average conversions are tabulated in Tables H.1 to H.10. The reactor temperature, pressure and the total feed flow to the reactor were always maintained at 485 K, 103 kPa and 185 cm^3(STP)/min respectively.

Table H.1

Time-Average Conversions During Out-of-Phase Cycling

(Time-Average Feed Composition 1.2% NO and 1.2% CO)

Cycle Period	Frequency	Time-Average Conversions, percent		
sec	mHz	CO	NO total	NO to N_2O
2000	0.5000	7.44	10.86	6.58
1000	1.0000	16.33	21.10	9.19
667	1.4993	23.07	29.86	11.45
500	2.0000	29.06	38.20	13.55
400	2.5000	35.03	46.26	15.52
333	3.0030	40.77	53.30	17.45
286	3.4965	46.17	59.51	19.07
250	4.0000	51.15	65.02	20.47
222	4.5045	55.41	69.93	21.58
200	5.0000	59.48	74.27	22.11
182	5.4945	63.08	77.78	22.72
167	5.9880	65.71	80.08	23.20
154	6.4935	68.37	83.50	23.49
143	6.9930	70.15	85.71	23.03
133	7.5188	69.00	85.59	26.70
125	8.0000	67.63	85.72	26.59
118	8.4746	64.30	83.84	29.88
111	9.0090	61.01	81.31	30.10
105	9.5238	32.01	45.13	28.58
100	10.0000	8.67	16.81	9.04
95	10.5263	5.70	12.74	6.22
91	10.9890	5.05	13.40	5.54
87	11.4943	3.74	11.65	4.26
83	12.0482	7.51	10.00	8.05
77	12.9870	6.05	9.50	6.68
71	14.0845	5.39	7.80	5.95
66	15.1515	4.76	5.31	5.30
62	16.1290	4.35	6.00	4.88
59	16.9492	4.05	6.20	4.52
55	18.1818	3.89	5.80	4.22
53	18.8679	3.59	5.50	3.91
50	20.0000	3.44	3.60	3.66

Table H.2

Time-Average Conversions During Out-of-Phase Cycling

(Time-Average Feed Composition 0.7% NO and 0.7% CO)

Cycle Period	Frequency	Time-Average Conversions, percent		
sec	mHz	CO	NO total	NO to N_2O
2000	0.5000	23.23	24.02	8.74
1000	1.0000	22.11	34.85	11.14
667	1.4993	30.84	44.29	12.97
500	2.0000	39.26	53.47	14.51
400	2.5000	47.43	62.38	15.51
333	3.0030	55.13	70.17	16.43
286	3.4965	61.31	76.91	17.17
250	4.0000	67.46	83.03	16.74
222	4.5045	72.43	87.77	16.03
200	5.0000	76.39	91.06	14.86
182	5.4945	79.32	93.51	14.31
167	5.9880	82.27	95.70	11.97
154	6.4935	84.33	97.01	10.66
143	6.9930	86.78	97.64	9.77
133	7.5188	86.39	98.41	9.11
125	8.0000	86.34	98.74	8.14
118	8.4746	87.05	99.00	5.94
111	9.0090	87.70	99.23	5.31
105	9.5238	87.17	99.38	3.46
100	10.0000	88.40	99.69	6.43
95	10.5263	86.72	99.53	5.00
91	10.9890	85.49	99.42	8.00
87	11.4943	85.03	99.30	6.60
83	12.0482	84.75	99.34	6.17
77	12.9870	84.21	99.24	7.60
71	14.0845	85.81	99.43	5.31
66	15.1515	85.49	99.58	6.31
62	16.1290	85.14	99.48	7.77
56	17.8571	86.50	99.47	7.06
50	20.0000	85.70	99.54	6.14

Table H.3

Time-Average Conversions During Out-of-Phase Cycling

(Time-Average Feed Composition 0.45% NO and 0.45% CO)

Cycle Period	Frequency	Time-Average Conversions, percent		
sec	mHz	CO	NO total	NO to N_2O
2000	0.5000	19.28	30.95	10.48
1000	1.0000	32.75	46.78	12.84
667	1.4993	45.48	60.10	13.66
500	2.0000	57.66	72.20	13.75
400	2.5000	68.07	82.43	13.05
333	3.0030	77.58	89.43	11.54
286	3.4965	83.57	94.79	9.47
256	3.9063	87.72	97.82	6.09
222	4.5045	90.15	98.77	3.39
200	5.0000	90.63	99.17	2.67
182	5.4945	91.18	99.35	1.82
167	5.9880	90.98	99.41	1.88
154	6.4935	91.37	99.48	1.88
143	6.9930	89.37	99.45	1.92
133	7.5188	91.59	99.51	1.92
125	8.0000	90.87	99.37	2.23
118	8.4746	90.39	99.22	2.52
111	9.0090	90.49	99.25	2.40
105	9.5238	89.94	99.14	2.58
100	10.0000	89.66	98.83	2.98
95	10.5263	89.27	98.65	3.42
91	10.9890	89.33	98.47	3.38
87	11.4943	87.96	98.22	3.56
72	13.8889	91.71	99.42	2.04
62	16.1290	91.36	99.31	2.40
56	17.8571	90.80	99.23	2.64
50	20.0000	89.96	98.99	3.11

Table H.4

Time-Average Conversions for Out-of-Phase Cycling at 10 mHz

(Time-Average Feed Composition 1.2% NO and 1.2% CO)

Number of Cycles	Time-Average Conversions, percent	
	CO	NO total
25	87.14	92.33
50	83.47	90.09
75	80.13	88.49
100	72.15	83.49
125	19.67	22.19
150	9.05	10.48
175	5.69	6.38
200	3.91	4.14
225	3.11	2.68
250	2.42	3.00
275	2.00	3.00
300	2.00	3.00
325	2.00	3.00

Table H.5

Time-Average Conversions for Out-of-Phase Cycling at 10 mHz

(Feed Composition 0.7% NO and 0.7% CO)

Number of Cycles	Time-Average Conversions, percent	
	CO	NO total
5	80.14	97.45
50	82.75	96.78
100	81.00	93.35
150	81.95	92.97
200	81.99	93.03
250	80.72	92.27
300	79.85	91.97
350	79.62	91.84
400	79.04	91.37
450	78.28	90.48
500	76.13	90.05
550	74.17	88.30
600	68.37	84.52
650	64.79	82.70
700	62.34	81.35
750	13.54	17.62
800	7.46	10.62
840	6.09	8.59

Table H.6

Time-Average Conversions for Out-of-Phase Cycling at 10 mHz

(Feed Composition 0.45% NO and 0.45% CO)

Number of Cycles	Time-Average Conversions, percent	
	CO	NO total
5	89.68	99.38
50	92.46	99.43
100	91.41	99.33
150	91.14	99.39
200	90.93	99.16
250	91.10	99.31
300	91.95	99.35
350	92.38	98.86
400	88.67	98.73
450	92.28	98.90
500	88.20	98.59
550	89.78	98.88
600	91.73	98.74
650	88.60	98.85
700	89.55	98.75
750	89.98	98.91
800	89.41	98.64
850	89.32	98.56
900	89.95	98.82
950	90.15	98.83
1000	92.05	98.98
1050	88.09	98.78
1100	91.15	98.89
1150	89.53	98.83
1200	88.21	98.67
1250	88.96	98.79
1300	88.83	98.72

Table H.7

Time-Average Conversions During Out-of-Phase Cycling

(Feed Composition 1.2% NO and 1.2% CO)

Cycle Period sec	Frequency mHz	Time-Average Conversions, percent CO	NO total	NO to N_2O
200	5.0000	61.19	73.17	23.08
182	5.4945	65.98	77.78	22.73
167	5.9880	12.33	17.54	10.03
154	6.4935	5.62	7.78	4.15
143	6.9930	5.13	6.83	3.29
125	8.0000	5.15	6.53	2.65
118	8.4746	5.31	6.49	2.27
111	9.0090	5.58	6.68	2.10
105	9.5238	6.42	7.42	1.94
100	10.0000	4.64	5.72	2.09
95	10.5263	5.70	6.33	1.22
91	10.9890	3.74	4.32	1.12
87	11.4943	5.50	5.94	0.85
83	12.0482	7.11	7.95	1.61
77	12.9870	6.14	6.74	1.33
71	14.0845	4.30	6.01	1.19
66	15.1515	4.20	5.31	1.06
62	16.1290	4.04	4.85	0.98

Table H.8

Time-Average Conversions During Variable Phase Cycling at 2 mHz

(Time-Average Feed Composition 1.2% NO and 1.2% CO)

NO Phase Lead degree	Time-Average Conversions, percent CO	NO total	NO to N_2O
10	3.94	3.93	5.53
20	8.05	11.34	10.47
30	23.82	34.53	15.07
40	30.48	43.74	19.68
60	39.41	56.70	28.38
80	44.65	63.90	32.98
100	47.32	67.13	35.70
120	42.27	59.74	31.32
140	36.79	51.24	25.58
160	32.01	43.20	19.03
180	30.36	39.23	14.81
180	30.76	39.43	14.79
200	30.98	39.26	12.83
220	26.43	38.31	12.69
250	29.13	43.34	14.82
270	31.73	46.61	16.24
300	4.72	5.85	4.39
320	3.34	3.14	3.52
340	2.46	1.18	3.45
350	2.72	1.94	3.81

Table H.9

Time-Average Conversions During Variable Phase Cycling at 5 mHz

(Time-Average Feed Composition 1.2% NO and 1.2% CO)

NO Phase Lead degree	Time-Average Conversions, percent CO	NO total	NO to N_2O
10	2.83	4.36	1.41
20	3.31	5.26	2.04
30	4.05	7.04	3.10
40	4.00	6.00	5.18
60	1.72	4.25	2.98
90	2.85	6.87	4.67
100	58.68	86.88	36.63
120	55.42	80.27	37.43
150	54.81	76.81	28.83
180	54.02	73.17	23.97
210	50.54	70.67	24.25
240	51.29	70.58	21.20
270	51.42	75.63	13.04
300	2.23	5.73	3.89
340	4.00	6.00	5.40
350	2.98	4.77	4.01

Table H.10

Time-Average Conversions During Variable Phase Cycling at 15.15 mHz

(Time-Average Feed Composition 1.2% NO and 1.2% CO)

NO Phase Lead degree	Time-Average Conversions, percent CO	 NO total	 NO to N_2O
10	1.91	7.89	2.74
20	2.01	8.10	2.82
40	2.19	8.41	3.00
60	2.37	8.65	3.18
80	2.43	8.80	3.32
100	2.51	9.02	3.48
120	2.80	9.55	3.73
140	3.14	9.78	4.07
160	3.40	10.30	4.30
180	1.54	6.90	2.30
200	1.59	7.44	2.32
220	1.59	7.39	2.32
240	1.62	7.52	2.35
260	1.69	7.58	2.40
280	1.63	7.40	2.40
300	1.78	7.53	2.45
320	1.73	7.45	2.40
340	1.92	7.72	2.55
350	1.88	7.88	2.58

```
%       program ’PHANO.M’
%       this program calculates the time-average CO and NO
%       conversions by time integration of the instantaneous
%       CO2 and NO data.  The time-average N2O mol% in the reactor
%       is also calculated.
pha
% file ’PHA.M’ contains experimental data in the form of matrix XX
%       Matrix xx  is a ten column matrix
%       Column 1: time
%       Column 2: total feed flow
%       Column 3: CO feed flow
%       Column 4: NO feed flow
%       Column 5: Reactor N2O mol%
%       Column 6: Reactor NO mol%
%       Column 7: Reactor CO2 mol%
%       Column 8: Reactor temperature
%       Column 9: CO four-way valve position (on/off)
%       Column 10: NO four-way valve position (on/off)
%sco=input(’stock CO%’)
%sno=input(’stock NO%’)
sco=5.94;
sno=7.89;
%tt=input(’Cycle period’)
tt=100;
%nphi=input(’Phase lead =  ’)
nphi=180;
[m n]=size(xx);
for i=1:m
time(i)=xx(i,1)-xx(1,1);
coi(i)=(xx(i,3)*sco)/xx(i,2);
noi(i)=(xx(i,4)*sno)/xx(i,2);
co2(i)=xx(i,7);
n2o(i)=xx(i,5);
no(i)=xx(i,6);
end
coiav=0;
noiav=0;
for i=1:m
coiav=coiav+coi(i);
noiav=noiav+noi(i);
end
coiav=coiav/m;
noiav=noiav/m;
for i=1:m
coin(i)=0;
noin(i)=0;
end
for i=1:m
if xx(i,9)==0
coin(i)=coi(i);
end
if xx(i,10)==0
```

```
noin(i)=noi(i);
end,end
plot(time, co2)
xlabel('Time, sec.'), ylabel('Reactor %CO2')
pause
%k=input('start and end cycle for time integration')
k=[25 35];
n1=k(1);
n2=k(2);
n11=0;
for i=1:m
if coin(i)==0
if coin(i+1)>0
n11=n11+1;
end,end
m1=i;
if n11==n1, break, end
end
n22=0;
for i=1:m
if coin(i)==0
if coin(i+1)>0
n22=n22+1;
end, end
m2=i;
if n22==n2, break, end
end
co21=0;
co1=0;
no1=0;
no11=0;
n2oav=0;
for i=m1:(m2-1)
co21=co21+((co2(i)+co2(i+1))/2.)*(time(i+1)-time(i));
co1=co1+((coin(i)+coin(i+1))/2.)*(time(i+1)-time(i));
no11=no11+((no(i)+no(i+1))/2.)*(time(i+1)-time(i));
no1=no1+((noin(i)+noin(i+1))/2.) .....
*(time(i+1)-time(i));
n2oav= n2oav+((n2o(i)+n2o(i+1))*(time(i+1)-time(i)));
end
conv=(co21*100.)/co1;
noconv=(no1-no11)*100/no1;
n2oav=n2oav/(2*(time(m2)-time(m1)));
w=1000./tt;
coiav
noiav
w
conv
noconv
n2oav
v=[time(m1),time(m2),0,2.5];
axis(v)
```

```
plot(time,co2,'-',time,coin,':')
xlabel('TIME, sec')
ylabel('REACTOR %CO2')
s1=['Phase lead =',num2str(nphi),' w = ',num2str(w) .....
' Period = ',num2str(tt)];
s2=['%CO Conversion = 'num2str(conv), ' %NO Conversion = ' .....
num2str(noconv)];
s3=['Feed %CO = 'num2str(coiav),' %NO = 'num2str(noiav)];
s4=['Time Average N2O% = 'num2str(n2oav)];
v=axis;
vx=v(1)+(v(2)-v(1))/5;
vy1=0.95*v(4);
vy2=0.91*v(4);
vy3=0.87*v(4);
vy4=0.83*v(4);
text(vx,vy1,s1)
text(vx,vy2,s2)
text(vx,vy3,s3)
text(vx,vy4,s4)
name=input('Data file name:','s')
vy4=1.02*v(4);
text(v(1),vy4,name)
shg
pause
v=[time(m1),time(m2),0,0.8];
axis(v)
plot(time,coin,':',time,n2o,'-')
xlabel('TIME, sec.')
ylabel('REACTOR %N2O AND FEED %CO (...)')
vy4=1.02*v(4);
text(v(1),vy4,name)
vx=v(1)+(v(2)-v(1))/5;
vy1=0.95*v(4);
vy2=0.90*v(4);
text(vx,vy1,s1)
text(vx,vy2,s4)
```

APPENDIX I

MATHEMATICAL MODEL FOR THE NO+CO REACTION TRANSIENT BEHAVIOR

I.1 Mass Balance Equations

In Chapter 4, the steady-state multiplicity behavior of the NO+CO reaction was described by a reaction mechanism consisting of the following seven reactions.

$$CO_{(g)} + M \rightleftharpoons M\text{-}CO \tag{I.1}$$

$$NO_{(g)} + M \rightleftharpoons M\text{-}NO \tag{I.2}$$

$$M\text{-}NO + M \rightarrow M\text{-}N + M\text{-}O \tag{I.3}$$

$$M\text{-}N + M\text{-}N \rightarrow N_{2(g)} + 2M \tag{I.4}$$

$$M\text{-}NO + M\text{-}N \rightarrow N_2O_{(g)} + 2M \tag{I.5}$$

$$N_2O_{(g)} + M \rightarrow N_{2(g)} + M\text{-}O \tag{I.6}$$

$$M\text{-}CO + M\text{-}O \rightarrow CO_{2(g)} + 2M \tag{I.7}$$

An additional process accounting for the reversible adsorption of CO_2 on the alumina support according to equation (I.8) is necessary to describe the reactor CO_2 transients. The adsorption of CO, NO and N_2O on the alumina support is negligible.

$$CO_2 + S \rightleftharpoons S\text{-}CO_2 \tag{I.8}$$

The recycle reactor can be considered as a CSTR because of the high recycle ratio. The internal and external mass transfer effects are negligible. Based on the above assumptions, the mass balance equations for the gas-phase species and surface species are described by equations (I.9) to (I.17). The CO self-exclusion effect described earlier in Chapters 2-4 has been considered in the development the following mass balance equations. In the following equations, the dimensionless gas-phase concentrations of NO, CO, N_2O and CO_2 are given by W, X, Y and Z respectively. All the symbols used in the equations are defined in the Notation section.

$$\frac{dW}{d\tau} = W_o - Q_n W - K_2 W\theta_V + K_{-2}\theta_{NO} \qquad (I.9)$$

$$\frac{dX}{d\tau} = X_o - Q_n X - K_1 X\theta_V \frac{(1-N_{CO}\theta_{CO})}{(1-\theta_{CO})} + K_{-1}\theta_{CO} \qquad (I.10)$$

$$\frac{dY}{d\tau} = Y_o - Q_n Y + K_5\theta_{NO}\theta_N - K_6 Y\theta_V \qquad (I.11)$$

$$\frac{dZ}{d\tau} = Z_o - Q_n Z + K_7\theta_{CO}\theta_O - K_8 Z(1-\xi_{CO_2}) + K_{-8}\xi_{CO_2} \qquad (I.12)$$

$$\frac{d\theta_{CO}}{d\tau} = \alpha_m[K_1 X\theta_V \frac{(1-N_{CO}\theta_{CO})}{(1-\theta_{CO})} - K_{-1}\theta_{CO} - K_7\theta_{CO}\theta_O] \qquad (I.13)$$

$$\frac{d\theta_O}{d\tau} = \alpha_m[K_3\theta_{NO}\theta_V + K_6\frac{2F_{NO}}{F_{CO}}Y\theta_V - K_7\theta_{CO}\theta_O] \qquad . (I.14)$$

$$\frac{d\theta_{NO}}{d\tau} = \alpha_m\frac{F_{NO}}{F_{CO}}[K_2 W\theta_V - K_{-2}\theta_{NO} - K_3\frac{F_{CO}}{F_{NO}}\theta_{NO}\theta_V - 2K_5\theta_{NO}\theta_N] \qquad (I.15)$$

$$\frac{d\theta_N}{d\tau} = \alpha_m[K_3\theta_{NO}\theta_V - 2K_4\theta_N^2 - \frac{2F_{NO}}{F_{CO}}K_5\theta_{NO}\theta_N] \qquad (I.16)$$

$$\frac{d\xi_{CO_2}}{d\tau} = \alpha_s[K_8 Z(1-\xi_{CO_2}) - K_{-8}\xi_{CO_2}] \tag{I.17}$$

where

$$Q_n = 1 - F_{CO}[K_1 X\theta_V \frac{(1-N_{CO}\theta_{CO})}{(1-\theta_{CO})} - K_{-1}\theta_{CO} - K_7\theta_{CO}\theta_O + K_8 Z(1-\xi_{CO_2}) - K_{-8}\xi_{CO_2} + K_4\theta_N^2] - F_{NO}[K_2 W\theta_V - K_{-2}\theta_{NO} - K_5\theta_{NO}\theta_N] \tag{I.18}$$

and

$$\theta_V = 1 - \theta_{CO} - \theta_O - \theta_{NO} - \theta_N \tag{I.19}$$

The cyclic conditions are similar to those described by equations (3.12) to (3.19) in Chapter 3 for the N_2O+CO reaction. To calculate the time-average conversions, the effect of the adsorption and desorption of CO_2 on the alumina support need not be considered. Therefore, it is sufficient to solve only eight differential equations (I.9) to (I.16) by setting the values of the rate constants K_8 and K_{-8} as zeroes. The value of Q_n can be assumed to be unity because the reactant concentrations used in this study are small and the volume change due to the reaction is negligible. The values of the rate constants have to be determined using iterative procedure. First, a set of rate constants, which describe the steady-state multiplicity data in Chapter 4 is obtained and then these values are used in the differential equations. This procedure is repeated until the solutions of the differential equations match the experimental values of the time-average conversions. The differential equations were solved using variable step 4th order Runge-Kutta-Fehlberg method for a particular case of cycling frequency of 2 mHz and NO phase lead of 180° and the solution is presented in Fig. 5.7. The MATLAB program for solving the differential equations is listed at the end of this appendix. To obtain the CO_2 response curve, the ninth equation (I.17) must also be considered.

I.2 Notation

a_m	total Pt surface area of supported catalyst, 9.4 m^2
a_s	total surface area of the support, 2092 m^2
[A]	instantaneous concentration of A (CO, CO_2, NO or N_2O) in the reactor, mol/m^3
$[A]_o$	time-average concentration of A (CO, CO_2, NO or N_2O) in feed, mol/m^3
F_{CO}	time-average mole fraction CO in feed
F_{NO}	time-average mole fraction NO in feed
k_i	rate constant for the i^{th} forward reaction
k_{-i}	rate constant for the i^{th} reverse reaction
K_1	dimensionless CO adsorption rate constant, $a_m L_m k_1 / Q_o$, 18740
K_{-1}	dimensionless CO desorption rate constant, $a_m L_m k_{-1} / Q_o [CO]_o$, 6.97
K_2	dimensionless NO adsorption rate constant, $a_m L_m k_2 / Q_o$, 18114
K_{-2}	dimensionless NO desorption rate constant, $a_m L_m k_{-2} / Q_o [NO]_o$, 967
K_3	dimensionless NO dissociation rate constant, $a_m L_m^2 k_{-3} / Q_o [NO]_o$, 846
K_4	dimensionless N_2 desorption rate constant, $a_m L_m^2 k_4 / Q_o [CO]_o$, 0.265
K_5	dimensionless N_2O formation rate constant, $0.5 a_m L_m^2 k_5 / Q_o [NO]_o$, 10.4
K_6	dimensionless N_2O dissociation rate constant, $a_m L_m k_6 / Q_o$, 80.75
K_7	dimensionless CO_2 formation rate constant, $a_m L_m^2 k_7 / Q_o [CO]_o$, 28.86
K_8	dimensionless CO_2 adsorption rate constant, $a_s L_s k_8 / Q_o$
K_{-8}	dimensionless CO_2 desorption rate constant, $a_s L_s k_{-8} / Q_o [CO]_o$.
L_m	adsorption capacity of platinum surface, $1.42 x 10^{-5}$ mol/m^2
L_s	CO_2 adsorption capacity of the alumina support, $1.2 x 10^{-6}$ mol/m^2
M	active site on the catalyst surface
M-A	adsorbed species of A (CO, NO, nitrogen or oxygen) on the catalyst surface
N_{CO}	CO self-exclusion factor, 1.05
Q_o	volumetric flow rate at reactor operating conditions, $5.39 x 10^{-6}$ m^3/s
Q_n	ratio of exit to feed volumetric flow rates

S	active site on alumina support
t	time, s
V	effective free volume of the reactor, 2.15x10^{-4} m^3
W	dimensionless reactor NO concentration, [NO]/$[NO]_o$
W_o	instantaneous dimensionless NO concentration in feed, 0 or 2
X	dimensionless reactor CO concentration, [CO]/$[CO]_o$
X_o	instantaneous dimensionless CO concentration in feed, 0 or 2
Y	dimensionless reactor N_2O concentration, $[N_2O]/2[NO]_o$
Y_o	instantaneous dimensionless N_2O concentration in feed, 0
Z	dimensionless reactor CO_2 concentration, $[CO_2]/[CO]_o$
Z_o	instantaneous dimensionless CO_2 concentration in feed, 0

Greek Letters

α_m	ratio of bulk volume to metal surface capacitances, $[CO]_o V/a_m L_m$, 0.487
α_m	ratio of bulk volume to support surface capacitances, $[CO]_o V/a_s L_s$, 0.026
θ_{CO}	fractional CO surface coverage
θ_O	fractional oxygen surface coverage
θ_{NO}	fractional NO surface coverage
θ_N	fractional nitrogen surface coverage
ξ_{CO_2}	fractional CO_2 surface coverage on the support
τ	dimensionless time based on the reactor residence time, $Q_o t/V$

I.3 MATLAB Program

```
%           Program 'NOCOD1.M'
%       This program solves the differential equations for the NO+CO
%       reaction. The equations are defined in a function file 'NODYN1.M'
%       The program further calculates the time average CO and NO conversion
%       for the specified number of cycles.
%
%       The program inputs include the model parameter values for the
%       differential equations, NO phase lead, Cycle period and the
%       number of cycles for integration.
```

```
%
global x10 x20
global k1 k11 k2 k21 k3 k4 k5 k6 k7 nco am fnc
diary noco2
% Enter the initial condition for integration  X0
x0=[1.9583 0.0001 0.0001 0.01048 0.50965 0.00004 0.00001 0.4233].’;
omgin=[2 2.5]; % vector containing the values of cycling frequencies
for ii=1:2
nop=1.2320;% time average NO in the feed
cop=1.2195;% time average CO in the feed
%       define the values of model parameters.
k1=18740;
k11=8.5/cop;
k2=18114;
k21=1195/nop;
k3=1032/cop;
k4=0.323/cop;
k5=12.82/nop;
k6=80.75;
k7=35.2/cop;
am=0.4*cop;
nco=1.05;
fnc=nop/cop;
omega=omgin(ii);
cycle=1000/omega;
angle=180;
%angle=input(’Phase lead for NO, degree’)
%num=input(’number of cycles for integration’)
%num1=input(’No. of steps per cycle’)
num1=1000.;
num=10;
%       The following values of v, q0, tk and p should
%       changed depending on experimental conditions
v=2.15*1e-4; % v=volume of the reactor cu.m.
tk=485; % temperature of the reactor K
p=103; % pressure in the reactor kPa
q0=185; %total feed flow to the reactor sccm
tt=(q0*1e-6/60)*(tk/273.15)*(101.325/p)*(cycle/v);tt
t0=0; tf=tt;nlead=(angle*tt)/360;
%tol    -accuracy used to calculate desirable error. A very low value
%       -value of ’tol’ will prevent integration of diff. equations
%       using Runge-Kutta-Fehlberg method
tol=0.0001;
%
%       Integrate a system of ordinary differential equations using
%       4th and 5th order Runge-Kutta formulas. The differential equations
%       are listed in a separate function file ’nodyn1.m’
% INPUT:
% t0    - Initial value of t.
% tf    - Final value of t.
% x0     - Initial value column-vector.
% tol   - The desired accuracy.
```

```
%
% OUTPUT:
% tout  - Returned integration time points (row-vector).
% xout  - Returned solution, one solution column-vector per tout-value.
%
% The Fehlberg coefficients:
%
alpha = [1/4  3/8  12/13  1  1/2]';
beta  = [ [    1       0       0     0       0    0]/4
          [    3       9       0     0       0    0]/32
          [ 1932  -7200    7296      0       0    0]/2197
          [ 8341 -32832   29440   -845       0    0]/4104
          [-6080  41040 -28352   9295   -5643     0]/20520 ]';
gamma = [ [902880  0  3953664  3855735  -1371249  277020]/7618050
          [ -2090  0     22528      21970    -15048  -27360]/752400 ]';
pow = 1/5;

% Initialization
t = t0;
% define the maximum and minimum step size for integration
hmax = (tf - t)/(5);
hmin=1e-2000;
h0 = (tf - t)/(num1) ;h=h0;
x00=[0 0 0 0 0 0 0 0 0 0];
% X00 stores the values at the beginning of each of the four
% quadrants of every cycle
flag=1;
if nlead>tt/2
nlead=tt-nlead;
flag=2; end
for i=1:num
sum1=0; sum2=0; sum3=0; sum4=0;
h=h0;
osold=x0(6);
nk=0;
tou1=0;
xou1=[0 0 0 0 0 0 0 0];
jk=1;
if (nlead==tt/2) | (angle==180)
jk=2; flag=3;end
for jj=1:jk:4, % perform integration for four quadrants of a cycle
if jj==1
x10=0;x20=2;t0=0;tf=nlead;
end
if jj==2
x10=2;x20=2;t0=nlead;tf=tt/2;
end
if jj==3
x10=2;x20=0;t0=tt/2;tf=t0+nlead;
end
if jj==4
x10=0;x20=0;t0=nlead+tt/2;tf=tt;
```

```
end
if flag==2
dummy=x20; x20=x10; x10=dummy; end
h=h0;
t=t0;
% correct the physically unreasonable values of initial condition X0
for jr=1:8
if (x0(jr)<=0), x0(jr)=0.000001; end
end
for jr=1:2
if (x0(jr)>=2), x0(jr)=1.999; end
end
for jr=5:8
if (x0(jr)>=1), x0(jr)=0.999; end
end
x00=[x00; i jj x0.’];
x = x0(:);
f = x*zeros(1,6);
tout = t0;
xout = x.’;
tout0=t0;
xout0=x.’;
tau = tol * max(norm(x, ’inf’), 1);
n=0;
% The main loop
  while (t < tf ) & (h >= hmin)
    if t + h > tf, h = tf - t; end
    n=n+1;
      nk=nk+1;
    % Compute the slopes
    temp = nodyn1(t,x);
    f(:,1) = temp(:);
    for j = 1:5
       temp = nodyn1( t+alpha(j)*h, x+h*f*beta(:,j));
       f(:,j+1) = temp(:);
    end

    % Estimate the error and the acceptable error
    delta = norm(h*f*gamma(:,2),’inf’);
    tau = tol*max(norm(x,’inf’),1.0);
    temp2=x+h*f*gamma(:,1);
    % Update the solution only if the error is acceptable
    if (delta <= tau)
       t = t + h;
       x = temp2;
yy=x.’;
sum1=sum1+(t-tout0)*(yy(1)+xout0(1))/2; % area under CO curve
sum2=sum2+(t-tout0)*(yy(2)+xout0(2))/2; % area under NO curve
sum3=sum3+(t-tout0)*(yy(3)+xout0(3))/2; % area under CO2 curve
sum4=sum4+(t-tout0)*(yy(4)+xout0(4))/2; % area under N2O curve
tout0=t;
xout0=yy;
```

```
xout=[xout; x.'];
tout=[tout; t];
         x0=x;
         h0=h;
       end
       % Update the step size
      if delta ~= 0.0
         h = min(hmax, 0.8*h*(tau/delta)^pow);
      end
    end;

    if (t < tf)
       disp('SINGULARITY LIKELY.')
       t
    end
          if (t < tf), break, end
     if (i > 8), if (i < 10),
          tou1=[tou1;tout];
          xou1=[xou1;xout];
      end, end
      end
          if (t<tf),break,end
          conv(i,1)=i;
          conv(i,2)=(tt-sum1)*100./tt;
          conv(i,3)=(tt-sum2-2*sum3)*fnc*100./tt;
          conv(i,4)=sum4*100./tt;
          conv(i,5)=(tt-sum2)*100/tt;
          conv(i,6)=sum3*nop*2/tt;
          pctos=(x0(6)-osold)*100/osold;
          conv(i,7)=pctos;
          conv(i,:)
       nk ,x0
 % save the output in an ASCII file for plotting
 if i==8
 save tou1 tou1 /ascii
 save xou1 xou1 /ascii
 end
 if i==9
 save tou2 tou1 /ascii
 save xou2 xou1 /ascii
 end

           end
       omega
           conv
 save xoo32 x00 /ascii
           end
 diary off
 exit
 %
 % *****************************************************
 %
```

```
% Function NODYN1.M
function xdot=nodyn1(t,x)
global x10 x20 k1 k11 k2 k21 k3 k4 k5 k6 k7 nco am fnc
%
% x(1)=dimensionless CO concentration
% x(2)=dimensionless NO concentration
% x(3)=dimensionless N2O concentration
% x(4)=dimensionless CO2 concentration
% x(5)=fractional CO surface coverage
% x(6)=fractional oxygen surface coverage
% x(7)=fractional NO surface coverage
% x(8)=fractional nitrogen surface coverage
%
xdot(1)=x10-x(1)-k1*x(1)*(1-x(5)-x(6)-x(7)-x(8)) ...
 *((1-nco*x(5))/(1-x(5)))+k11*x(5);
xdot(2)=x20-x(2)-k2*x(2)*(1-x(5)-x(6)-x(7)-x(8)) ....
   +k21*x(7);
xdot(3)=k5*x(7)*x(8)-x(3)-k6*x(3)* .....
   (1-x(5)-x(6)-x(7)-x(8));
xdot(4)=k7*x(5)*x(6)-x(4);
xdot(5)=am*(k1*x(1)*((1-nco*x(5))/(1-x(5))) ......
  *(1-x(5)-x(6)-x(7)-x(8))-x(5)*(k11+k7*x(6)));
xdot(6)=am*((1-x(5)-x(6)-x(7)-x(8))*(k3*x(7)+2*fnc*k6*x(3)) ...
  -k7*x(5)*x(6));
xdot(7)=fnc*am*((1-x(5)-x(6)-x(7)-x(8))*(k2*x(2) .....
  -k3*x(7)/fnc)-x(7)*(k21+2*k5*x(8)));
xdot(8)=am*(k3*x(7)*(1-x(5)-x(6)-x(7)-x(8)) ...
  -2*x(8)*(k4*x(8)+k5*fnc*x(7)));
```